The BUNYAVIRUS ENSEMBLE

Flexible Orchestration of Solo, Duo & Trio Acts

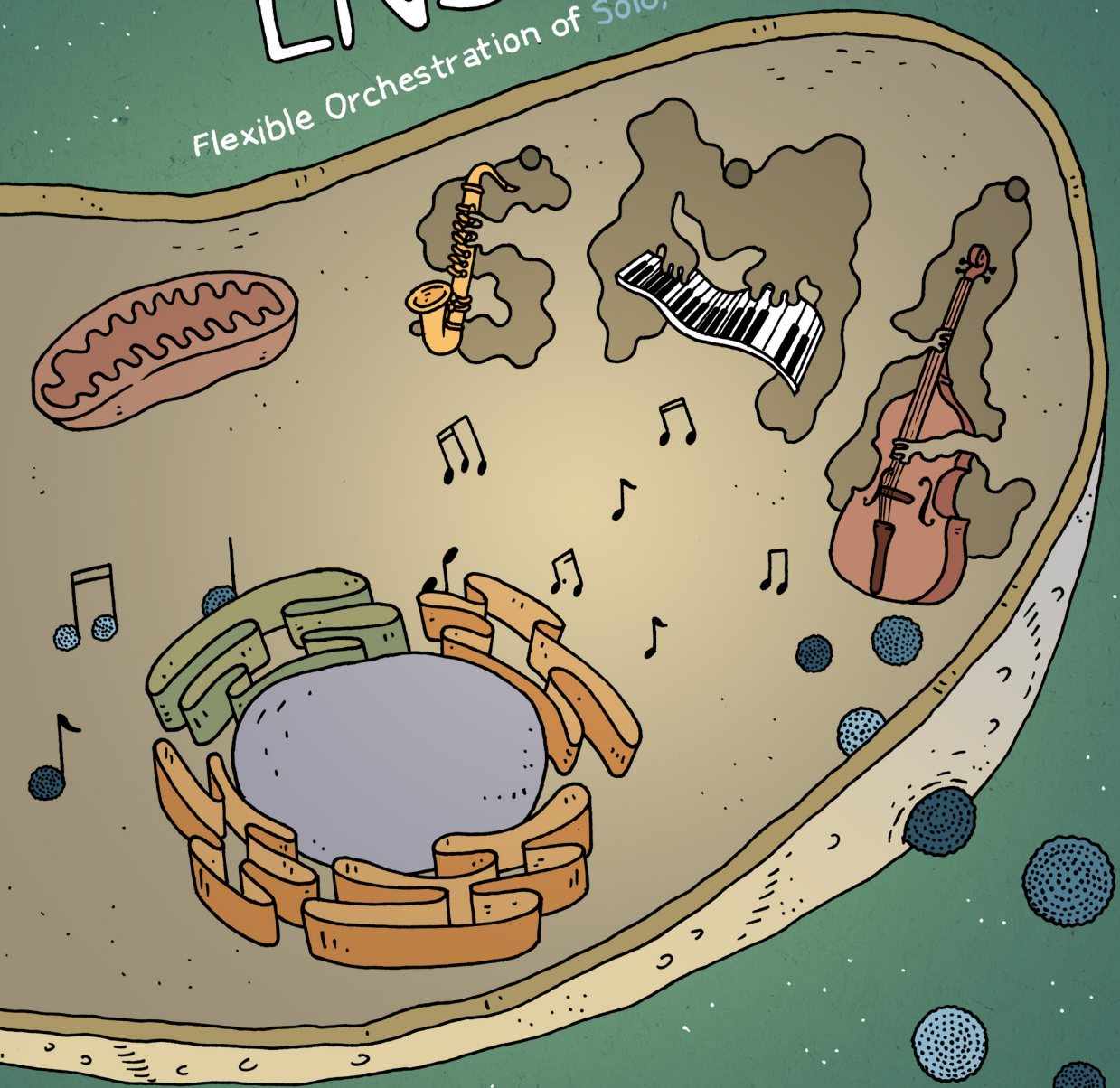

Erick Bermúdez Méndez

Propositions

1. Segmented viruses with random genome packaging are a bohemian form of multipartitism. (this thesis)

2. Incomplete particles contribute rather than interfere with the replication cycle of bunyaviruses. (this thesis)

3. Iterative speculation in research misleads the conceptualization of new scientific projects.

4. Predatory scientists are just as common as predatory journals.

5. Institutional claims about international diversity, equity and inclusion reflect political correctness instead of real practice.

6. Cell phone usage and true happiness are inversely correlated.

Propositions belonging to the thesis entitled:

The Bunyavirus Ensemble
Flexible Orchestration of Solo, Duo & Trio Acts

Erick Bermúdez Méndez
Wageningen, 21 November 2023

The Bunyavirus Ensemble

Flexible Orchestration of Solo, Duo & Trio Acts

Erick Bermúdez Méndez

Thesis committee

Promotors

Prof. Dr Monique M. van Oers
Professor of Virology
Wageningen University & Research

Prof. Dr Gorben P. Pijlman
Associate Professor, Laboratory of Virology
Wageningen University & Research

Co-promotor

Dr Paul J. Wichgers Schreur
Senior Scientist, Department of Virology & Molecular Biology
Wageningen Bioveterinary Research

Other members

Prof. Dr Wim H. M. van der Poel, Wageningen University & Research
Dr Benjamin Brennan, MRC-University of Glasgow, United Kingdom
Dr Izabela A. Rodenhuis-Zybert, University of Groningen and UMC Groningen
Dr Stéphane Blanc, Université Montpellier, France

This research was conducted under the auspices of The Graduate School for Production Ecology & Resource Conservation (PE&RC)

The Bunyavirus Ensemble

Flexible Orchestration of Solo, Duo & Trio Acts

Erick Bermúdez Méndez

Thesis

submitted in fulfilment of the requirements for the degree of doctor
at Wageningen University
by the authority of the Rector Magnificus,
Prof. Dr A. P. J. Mol,
in the presence of the
Thesis Committee appointed by the Academic Board
to be defended in public
on Tuesday 21 November 2023
at 11 a.m. in the Omnia Auditorium.

Erick Bermúdez Méndez

The Bunyavirus Ensemble
Flexible Orchestration of Solo, Duo & Trio Acts

230 pages

PhD thesis, Wageningen University, Wageningen, The Netherlands (2023)
With references, with summaries in English and Spanish

ISBN: 978-94-6447-880-8
DOI: https://doi.org/10.18174/638585

A mi familia

En las tierras verdes del volcán

Ahí se puede encontrar

El sonido húmedo tropical ♫

Bajando la Montaña, Señor Loop

Table of contents

Chapter 1

Introduction

Erick Bermúdez-Méndez

Department of Virology & Molecular Biology, Wageningen Bioveterinary Research, Lelystad, The Netherlands

Laboratory of Virology, Wageningen University & Research, Wageningen, The Netherlands

(Re-)emerging bunyaviruses: the threat is real

The order *Bunyavirales* comprises a large and expanding group of RNA viruses widely distributed across the globe[1]. The most recent report by the International Committee on Taxonomy of Viruses (ICTV 2022 Release MSL #38) classified them into 14 families, 63 genera and 552 species[2] (**Fig. 1**). The vast diversity of bunyaviruses is reflected in both their broad host range and variety of vectors. Within the *Bunyavirales* we find plant-, animal- and human-infecting viruses that can be transmitted by arthropods (e.g., mosquitoes, ticks, sand flies, midges, thrips, aphids) or rodents[3,4]. Recently, even fungi-infecting bunyaviruses have been discovered and started to be molecularly characterized[5].

In particular, members of the *Arenaviridae*, *Hantaviridae*, *Nairoviridae*, *Peribunyaviridae* and *Phenuiviridae* families are of major animal and public health concern for their known ability to cause severe disease in (farm) animals and/or humans[6]. Additionally, members of the *Tospoviridae* family and *Tenuivirus* genus (within the *Phenuiviridae* family) represent an important hazard for agricultural crops[4]. Besides the high toll on plant, animal and public health, bunyavirus outbreaks inevitably have a substantial negative socio-economic impact[7–9].

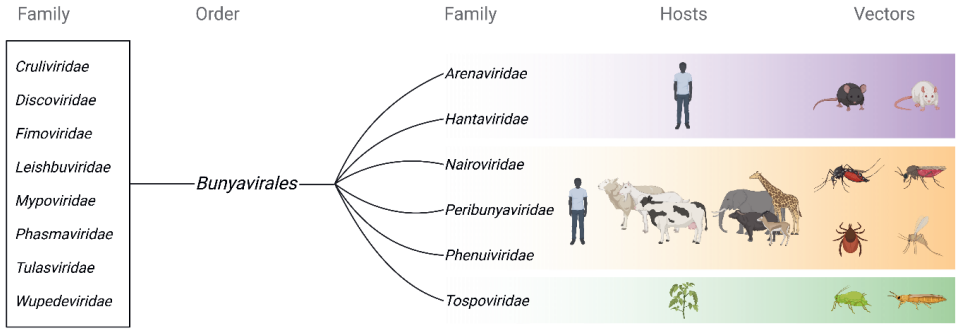

Figure 1. International Committee on Taxonomy of Viruses (ICTV) classification (release MSL #38, year 2022) of the order *Bunyavirales*. The order *Bunyavirales* is an expanding group of RNA viruses currently comprising 14 families. The most prominent hosts and vectors of the viruses in families that threaten human, animal and plant health are illustrated on the right side. Virus families less well studied are presented on the left side.

Although bunyavirus outbreaks are generally confined to particular geographic regions, the fact that competent vectors inhabit other latitudes highlights the risk of pathogen transmission to previously unaffected territories. This risk is especially relevant for arthropod-borne viruses, since

climate change, urbanization and international mobility are expanding the habitat of competent vectors[10–12]. Noteworthy, very limited vaccines and therapeutics are readily available to counteract the harmful effects of bunyavirus outbreaks. It then comes without surprise that in 2018 the World Health Organization (WHO) included three bunyaviruses on its Blueprint list of prioritized pathogens that require prompt research and development activities due to their potential to cause epidemics associated with severe disease[13].

Rift Valley fever virus

Rift Valley fever (RVF) was discovered in 1930 as a deadly viral disease in newborn lambs on a farm near Lake Naivasha in the Rift Valley of Kenya[14]. The disease-causing agent was named Rift Valley fever virus (RVFV), which turned out to be a mosquito-borne virus nowadays classified as a member of the genus *Phlebovirus* in the family *Phenuiviridae*[15]. Following the first recorded RVFV outbreak, multiple major outbreaks have been reported between 1950 and 2000 across numerous African countries[16]. In 2000, two outbreaks were recorded in Yemen and Saudi Arabia, marking the first reports of RVFV outside the African continent[17–19]. Since then, re-emergence of RVFV outbreaks keep being reported in previously affected African territories[16], along with reports of RVFV emergence in naïve territories like the French Island of Mayotte[20,21] (**Fig. 2**).

Figure 2. RVFV geographical distribution map. The virus is endemic in the African continent, the Arabian Peninsula and the Indian Ocean islands. The location where RVFV was discovered is pinned.

RVFV has been described to primarily infect domestic livestock (sheep, cattle, goats, camels), which act as amplifying hosts for the virus[22–24]. Of these, young lambs and pregnant ewes are the most susceptible hosts[25]. After an incubation period of about 24-36 h, animals become sick and present with high fever, loss of appetite, weakness, abdominal pain, diarrhea and a hemorrhagic syndrome that often leads to death[25,26]. Mortality in adult ruminant livestock ranges between 10-20%[27], whereas in newborn lambs this can be above 90%[25,26]. RVFV outbreaks typically feature sudden waves of abortion among pregnant animals, also called "abortion storms", with acutely infected pregnant ewes having nearly 100% chance of abortion[28]. Wild animals such as buffaloes, giraffes, rhinoceros, elephants, springboks and impalas can also become incidentally infected. However, their role in maintaining RVFV circulation remains disputed[25,27,29].

Transmission of RVFV between animals occurs typically via the bite of infected mosquitoes and is favored following periods of heavy rainfall in which mosquito populations explode[30,31]. More than 50 mosquito species, the majority belonging to the genera *Aedes*, *Anopheles*, *Culex* and *Eretmapodites*, have been found to be competent for RVFV transmission, as concluded from field isolations or experimental laboratory studies[31–36]. Although humans can also become infected via infected mosquito bites, most human infections occur through direct contact with infected animal tissues and body fluids[26,30] (**Fig. 3**).

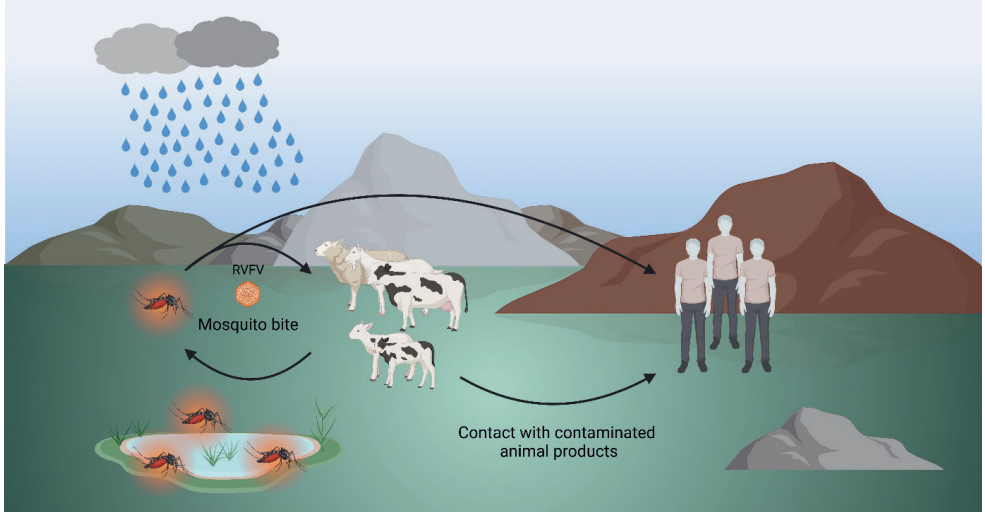

Figure 3. RVFV transmission cycle. Mosquitoes are vectors for transmitting RVFV. Following periods of heavy rainfall, mosquito populations expand and transmit RVFV primarily to domestic livestock, which serve as amplifying hosts. Humans can also become infected either by bites of infected mosquitoes or via direct contact with contaminated animal products.

The natural course of the infection in humans is characterized by a self-limiting febrile illness with headache, myalgia, arthralgia, nausea and abdominal pain[19,37–39]. Nonetheless, in a minority of cases, RVFV infection may show complications and progress to severe manifestations including hepatorenal failure, hemorrhagic fever, retinitis and encephalitis[18,19,39,40]. Overall, mortality in humans has been estimated at around 0.5-2%[30], but it can drastically increase above 30% in severe cases[18,40]. In both animals and humans, RVFV primarily targets the liver, rapidly inducing multifocal lesions and severe necrosis[37,38,41,42]. Placental transmission of RVFV in humans is considered plausible[43-45], which poses RVFV as a reasonable threat to pregnant women[46].

It is difficult to determine an accurate estimate of morbidity and mortality in livestock and humans caused by RVFV due to deficient documentation of epidemiological data during outbreaks. However, it is known that some of the largest outbreaks have accounted for tens of thousands of animal deaths and abortions, together with hundreds of human deaths from thousands of cases[47]. RVFV outbreaks also result in significant and wide-ranging socio-economic losses with influence beyond the agricultural sector[7,8]. The estimated losses during major outbreaks are in the order of tens of millions of US dollars[25,48].

Safe and efficacious vaccines might contribute to prevent the devastating effects caused by RVFV outbreaks. Nevertheless, to date, only a few veterinary RVFV vaccines with suboptimal safety or efficacy are in use in some African countries, and no specific RVFV vaccine or therapeutic for human use has been fully licensed[49]. Several joint efforts are pushing forward vaccine development, but they are still in early phase clinical trials.

Schmallenberg virus

In 2011, a previously unidentified disease in dairy cattle was reported by farmers and veterinarians in Germany and the Netherlands. Metagenomics combined with virus isolation from blood of affected cows determined that the disease-causing agent was a previously unknown bunyavirus. The virus was named Schmallenberg virus (SBV) after the town of Schmallenberg in North Rhine-Westphalia, Germany, where the first positive samples were collected[50].

SBV is a member of the Simbu serogroup within the genus *Orthobunyavirus* in the family *Peribunyaviridae*[15]. SBV is strictly a veterinary pathogen, primarily affecting domestic ruminants (cattle, sheep, goats)[51], although SBV has also been detected in wild ruminants such as bison, moose, alpacas, buffalos and deer[52]. The absence of SBV-neutralizing antibodies in potentially exposed people implies that there is no evidence that humans are susceptible to SBV infection[53,54].

However, other orthobunyaviruses within the Simbu serogroup like Oropouche virus[55], Iquitos virus[56] and Shuni virus[57] have been associated with human disease.

The clinical picture observed in acutely infected adult cattle typically includes transient fever, decreased milk production and diarrhea within a short viremia of 5-6 days[50,58]. Biting midges of the *Culicoides* genus are the vectors responsible for the transmission of SBV from one animal to another[59,60] (**Fig. 4**). Transplacental infection can also take place, frequently resulting in the birth of calves, lambs and goat kids with severe congenital malformations. Pathologically, neonatal SBV infection results in arthrogryposis, torticollis, scoliosis, kyphosis, brachygnathia inferior, hydranencephaly, and hypoplasia of the brain, cerebellum and spinal cord[53,61]. Additionally, infection during pregnancy can result in premature birth or stillbirth[62,63].

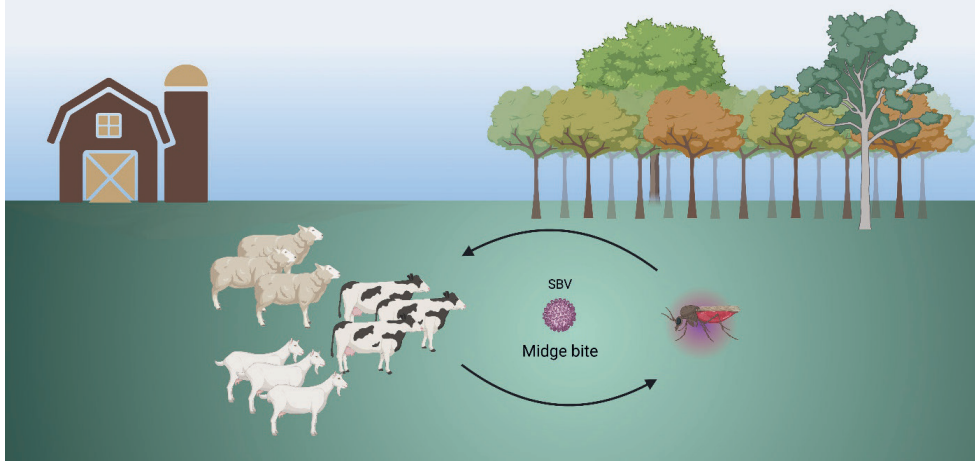

Figure 4. SBV transmission cycle. Transmission of SBV between domestic ruminants occurs through bites of infected midges.

The 2011 SBV outbreak marked the first recorded epidemic by a member of the Simbu serogroup in Europe. Soon after its discovery in Germany and the Netherlands, SBV rapidly spread over Belgium, France, Luxembourg, the United Kingdom, Italy, Spain, Denmark and Switzerland, causing a large epidemic in Europe between 2011-2012[64]. SBV kept spreading into naïve territories, with confirmed cases in at least 27 European countries by September 2013[63] (**Fig. 5**). Since then, SBV has established endemic re-circulation every 2-3 years[65].

Besides the negative consequences on animal welfare and economic losses due to SBV infections[9], the sudden emergence of the virus had an important impact on the international trade of susceptible animals and animal products[64]. Vaccination of livestock has proven as an efficacious measure to reduce or even prevent circulation of other vector-transmitted viruses. Nonetheless, although several inactivated SBV vaccines have reached the market, licensed SBV vaccines are not being used routinely due to high seroprevalence, unpredictable re-emergence and vaccine costs[66].

Figure 5. SBV geographical distribution map. The virus emerged and re-circulates in the European continent. The location where SBV was discovered is pinned.

Molecular biology of phlebo- and orthobunyaviruses

Mature phlebo- and orthobunyavirus particles (virions) generally are spherical or pleomorphic, enveloped by a lipid membrane and approximately 80-120 nm in diameter. Transmembrane glycoproteins protrude from the surface of the particles, resulting in characteristic virus-specific surface architectures[67–71]. For example, RVFV glycoproteins form cylindrical hollow structures that assemble into penta- and hexameric capsomeres[67,69,70], whereas SBV glycoproteins form tripod-like spikes[72,73] (**Fig. 6**). It is worth clarifying that while the descriptions given here and in the following paragraphs usually apply to most members of the genera *Phlebovirus* and *Orthobunyavirus*, there might be exceptions.

Phlebo- and orthobunyaviruses have a single-stranded RNA genome of negative polarity divided into three distinct segments, termed S, M and L, according to their length[74,75] (**Fig. 6**).

The L segment codes for an RNA-dependent RNA-polymerase (RdRp or L protein) responsible for viral genome transcription and replication[76,77]. The M segment codes for a polyprotein precursor that is co-translationally cleaved into two glycoproteins, Gn and Gc, and one non-structural protein (NSm). As stated above, the glycoproteins Gn and Gc are displayed on the surface of mature virus particles and are critical for virus entry, fusion with endosomal membranes and virion assembly in the Golgi complex[78,79]. The S segment codes for a nucleocapsid (N) protein and a non-structural (NSs) protein. The N protein encapsidates each viral genome segment preventing them from cellular degradation. Within the virion, the encapsidated viral genome segments associate with the RdRp to form so-called ribonucleoprotein (RNP) complexes. RNP complexes adopt a panhandle structure as a result of complementary base-pairing between the 3′ and 5′ termini of conserved, genus-specific untranslated regions (UTRs) present on each genome segment[80,81].

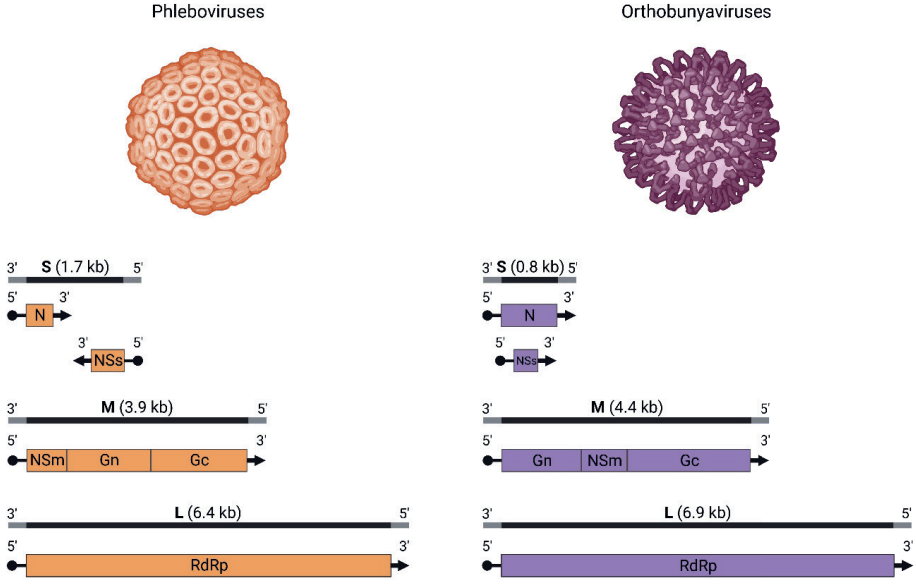

Figure 6. Virion morphology and typical genome organization of members of the genera *Phlebovirus* and *Orthobunyavirus*. 3D representations of spherical virus particles (80-120 nm in diameter) depicting the distinct surface topologies imparted by the envelope glycoproteins. The genome of bunyaviruses is divided into three unique segments termed S, M and L (depicted with black lines). Virus particles and sizes of genome segments represented in this figure correspond to RVFV (left) and SBV (right), as prototype phlebovirus and orthobunyavirus, respectively. Gray boxes represent the 3′ and 5′ untranslated regions. Viral proteins encoded by each segment are indicated in the coloured boxes. Phleboviruses employ an ambisense coding strategy to express the N and NSs proteins from the S segment, whereas orthobunyaviruses express N and NSs from a S segment overlapping reading frame.

Phleboviruses employ an ambisense coding strategy for the proteins encoded by the S segment, in which the N protein is transcribed from the negative-sense genomic RNA, and the NSs protein is transcribed from the positive-sense viral complementary RNA[74]. Orthobunyaviruses employ an overlapping reading frame coding strategy in which the N and NSs proteins are transcribed from the negative-sense genomic RNA using distinct AUG initiation codons[75]. In the M segment, NSm is transcribed as part of the polyprotein precursor from the negative-sense genomic RNA in both phlebo- and orthobunyaviruses, although the location of the NSm coding sequence differs between the genera[80,81] (**Fig. 6**).

NSs is the main virulence factor of bunyaviruses and contributes to their pathogenesis. In phlebo- and orthobunyaviruses, NSs is an interferon alpha/beta (IFN-α-β) antagonist that exerts its pro-viral effects via multiple mechanisms[82–85]. For example, RVFV NSs blocks IFN production by suppressing host gene transcription[86], which can be mediated by preventing the assembly of the TFIIH transcription factor[87]. Additionally, RVFV NSs prevents the antiviral activity of IFN through specific degradation of the double-stranded RNA-dependent protein kinase (PKR)[88,89]. The degradation of PKR inhibits the phosphorylation of eukaryotic initiation factor (eIF)2α, ultimately promoting viral translation[90]. On the other hand, SBV NSs antagonizes IFN by inhibiting host cell protein synthesis[91]. NSm has also been implicated with several accessory functions, even though its effects may seem less drastic than those of NSs. NSm has been shown to suppress apoptosis[92] and to facilitate mosquito infection in phleboviruses[93,94], while in orthobunyaviruses it was demonstrated to act as an auxiliary protein in virion assembly.[95].

The infectious cycle of bunyaviruses starts with entry into susceptible cells via receptor-mediated endocytosis. Fusion of the viral glycoproteins with the endosomal membrane at slightly acidic conditions releases the RNPs in the cytoplasm, where bunyavirus transcription and replication take place[96]. First, the virion-associated RdRp catalyzes the primary transcription of the incoming genomic negative-sense RNA. Viral mRNA synthesis is primed by 5′ end sequences from host cell mRNAs through a cap-snatching mechanism[77,97]. As opposed to host cell mRNAs, bunyaviral mRNAs are not polyadenylated. Viral transcription kicks-off the translation of viral proteins, after which synthesis of RNA shifts from transcription to replication of a complementary positive-sense RNA (anti-genome) that serves as a template for the synthesis of negative-sense genomic RNA. Secondary transcription of viral mRNAs occurs simultaneous to viral genome replication[76,77]. Newly synthesized genomic RNA gets encapsidated by multiple N proteins and traffics to the Golgi complex in the form of RNPs, where mature glycoproteins have been retained. Progeny virion assembly requires that the viral glycoproteins bud from Golgi complex membranes, while

incorporating the RNPs inside the newly formed virus particles. Lastly, the virions bud from Golgi inside vesicles that traffic to the cell surface and release the virus particles by exocytosis[76,98] (**Fig. 7**).

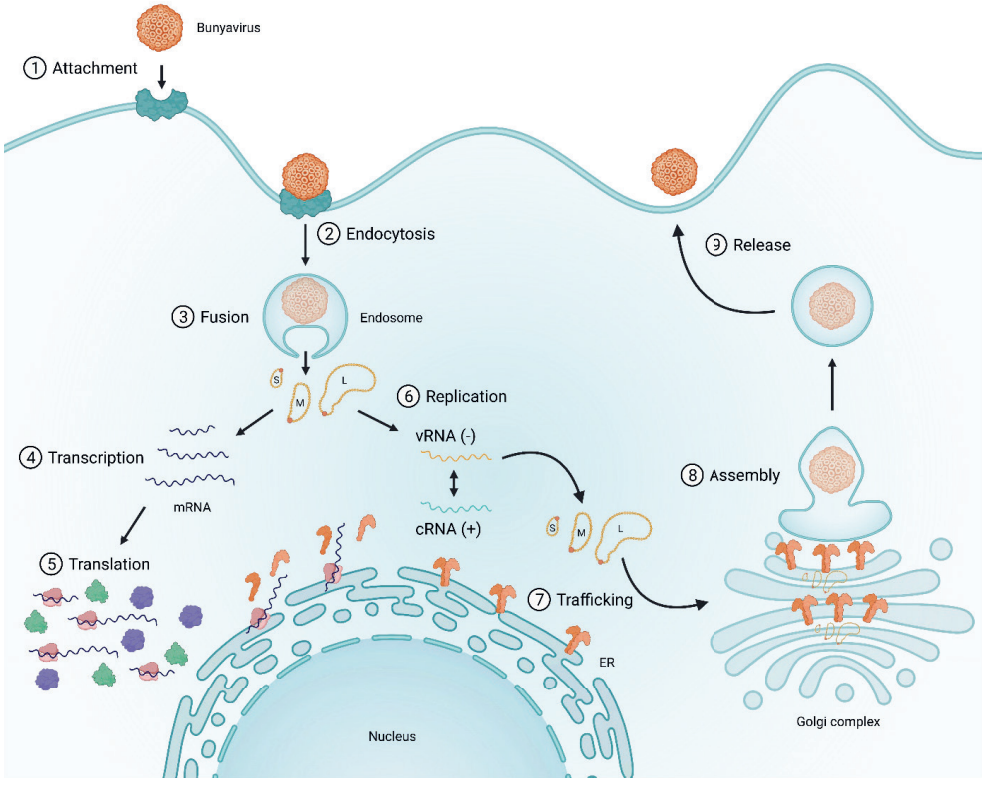

Figure 7. The bunyavirus life cycle. The viral glycoproteins on the surface of virus particles attach to host receptors (step 1). The virus enters the cell via receptor-mediated endocytosis (step 2). The viral glycoproteins mediate the fusion of the virus particle with the endosomal membrane, releasing the viral ribonucleoproteins (RNPs) in the cytoplasm (step 3). RNPs are transcribed by the virion-associated RNA-dependent RNA polymerase (step 4). Viral mRNAs are translated into viral proteins, including the synthesis of the viral glycoproteins by membrane-bound ribosomes (step 5). The viral genomic RNA (vRNA, negative-sense) is replicated through a complementary anti-genome RNA (cRNA, positive-sense) that serves as a template (step 6). Newly synthesized RNPs and viral glycoproteins traffic to the Golgi complex (with the glycoproteins first trafficking through the endoplasmic reticulum [ER]) (step 7). Progeny virions are assembled in the Golgi complex (step 8). Golgi-derived vesicles transport the progeny virions to the cellular membrane and release the infectious virus (step 9).

Genome packaging

Incorporating the viral genome inside newly formed virus particles, a process known as genome packaging, is a crucial step during progeny virion assembly to establish a productive infection

cycle. This process can be troublesome for viruses with a segmented genome, since all genome segments are essential and thus at least one copy of each segment should be incorporated inside individual virus particles. Failing to incorporate one or more genome segments would render the newly formed particle non-infectious, as the absence of part of the genome would hamper production of progeny virions[99].

The eight-segmented influenza A virus (family *Orthomyxoviridae*) and the eleven-segmented rotavirus (family *Sedoreoviridae*) are examples of viruses that overcome the genome packaging enigma by harnessing sequence-specific RNA-RNA or protein-RNA interactions that facilitate the incorporation of a complete set of genome segments into the majority of new virions[100–103]. Employing such a specific and selective mechanism seems imperative, as otherwise, the large number of segments would make it impossible to incorporate a complete genome just by chance.

Presuming that bunyaviruses might also need to employ a specific strategy to incorporate their segmented genome, pioneering studies aimed to study how genome packaging could be orchestrated in these viruses. The UTRs of bunyavirus genome segments have been shown to be critical for genome packaging[104–106]. Additionally, it has been demonstrated that interactions between the N protein and the cytoplasmic tails of the envelope glycoproteins mediate the packaging of RNPs into virions[107–110]. Furthermore, packaging of genomic RNA has been associated with the efficient release of progeny virions[111]. The possibility of specific intermolecular interactions between the viral RNA segments has also been proposed based on packaging assays[112].

Although the findings thus far hinted towards a selective packaging mechanism, no direct evidence for the formation of a supramolecular complex like the case for influenza A virus has been shown[113–115]. In fact, the ease by which the genome of RVFV could be manipulated to generate recombinant two-segmented and four-segmented viruses (instead of the typical three-segmented virus) or viruses with reconfigured genome segments, pointed to the notion of a very flexible genome and a packaging process that can tolerate significant changes[116–118].

Work by Wichgers Schreur and Kortekaas (2016) further challenged the previous conceptions and presented a somewhat discrepant hypothesis. In their single-molecule fluorescence *in situ* hybridization (smFISH) study, it was shown that RVFV S, M and L genome segments did not seem to colocalize to bundle into three-segmented SML complexes prior to virion assembly[119]. This observation suggested that RVFV does not employ a specific mechanism to incorporate a

complete genome inside virus particles. This finding set the stage to continue investigating the genome packaging process of bunyaviruses and answer the question of whether this process is governed by a selective or non-selective mechanism.

Dissecting host responses during viral infection

Apart from comprehending how bunyaviruses sustain a life cycle alternating between their mammalian hosts and vectors, understanding the processes by which bunyaviruses cause disease is of utmost relevance. Previous studies focusing on characterizing the virus-host interplay were extremely useful for generating a much-needed knowledge base. However, the ability to integrate the various findings and establish relationships between the underlying molecular mechanisms that lead to an observed phenotype was constrained by the research scope and tools available at that moment. Some limitations of preceding studies included analyzing data derived only from *in vitro* cell culture settings or focusing exclusively on a handful of interesting biological pathways while missing to analyze global host responses. Although extremely valuable, it is known that translating findings from the laboratory to real-life conditions usually is not straight-forward and that many subtle but important observations can go unnoticed if they are not given proper attention.

Nowadays, several high-throughput techniques have revolutionized the ways in which host responses during infection can be studied. One example of such techniques is RNA-sequencing (RNA-seq), a method in which the whole transcriptome of a host can be quantified and used to examine gene expression profiles under specific circumstances on a genome-wide level[120–122]. This approach has the potential to uncover new gene networks that drive the development of viral disease and therefore is now being used extensively for this purpose[123–125].

Studies combining RNA-seq with clinical and histopathological observations from biologically relevant systems (e.g., tissues of infected animals or circulating immune cells) can be used to infer genotype-phenotype associations[126,127]. Furthermore, RNA-seq performed at single-cell resolution allows exploring the heterogeneity in host cell responses within a cell population or tissue section[128,129]. This is especially interesting when specific host gene expression patterns can be explained by the infection status and/or viral load in a particular cell. Thus, obtaining detailed overviews of the host's transcriptional response upon infection is a worthy strategy to expand our knowledge on bunyavirus pathogenesis and to link experimental observations obtained by complementary means.

Thesis outline

Many medically-relevant bunyaviruses remain starkly understudied. A better comprehension of the fundamental biology of bunyaviruses is critical and can eventually facilitate the development of efficacious countermeasures. Here, RVFV and SBV were selected as prototypes of threatening zoonotic and veterinary pathogens, respectively, that deserve our attention in view of what they are currently causing, the risk of future epidemics/epizootics and the limited knowledge at hand. Research in the field of bunyaviruses has made significant progress in the last decades, but a constant and larger effort is still needed for greater preparedness. The overall aim of this thesis was to shed light on the genome packaging process of bunyaviruses and its implications for their life cycle, as well as unveiling molecular determinants underlying their pathogenesis.

In **Chapter 2**, state-of-the-art fluorescence microscopy was employed to examine the genome packaging process of the three-segmented RVFV and SBV at single-molecule resolution. The intracellular relative abundance of the viral genome segments was quantified in single cells and correlated with the genomic composition of individual virions assembled by each of those cells. Furthermore, the efficiency of genome packaging when the viruses replicated in mammalian cells or in insect cells was compared, considering that RVFV and SBV life cycles alternate between vertebrate and invertebrate hosts.

Studying genome packaging of bunyaviruses revealed a remarkably flexible and apparently inefficient process that raised additional questions regarding the mechanisms of within-host spread and between-host transmission. Intrigued by the puzzling role that particles with an incomplete set of viral genome segments could play in the life cycle of bunyaviruses, in **Chapter 3** it was investigated if the spread of RVFV could rely strictly on co-infection of particles with an incomplete but complementing genome. Populations of RVFV exclusively containing incomplete particles were generated using reverse genetics. Then, genome complementation was evaluated in a series of *in vitro* and *in vivo* (in mosquitoes) experiments. Moreover, the experimental findings were complemented with mathematical models that helped to realize under which biological circumstances this phenomenon could be relevant.

Understanding how RVFV causes disease in susceptible species under conditions that resemble a natural infection is equally important to understanding the molecular aspects of the RVFV replication cycle. **Chapter 4** presents how high-throughput sequencing technology was harnessed to study the whole transcriptomic profile in target organs (liver and spleen) of RVFV-infected lambs during acute infection. This analysis allowed to describe tissue-specific host responses upon

infection. In addition, the clinical presentation of the disease was linked to histological phenotypes with signature gene expression features, thereby contributing to unravelling RVFV pathogenesis.

Chapter 5 brings together the recently gained expertise on RNA-sequencing technologies with the intriguing role that incomplete particles might play during infection. Firstly, the host transcriptome differences between thousands of individual RVFV-infected and uninfected cells were explored. Conscious that an RVFV population consists of a mix of particles with different genomic compositions, it was then explored at single-cell resolution how the host transcriptome was influenced by the nature of the incoming infecting particle (i.e., complete or incomplete). By analyzing the effects of incomplete bunyavirus particles with replication capacity but unable to spread, this chapter fills in some knowledge gaps in the life cycle of bunyaviruses.

Finally, **Chapter 6** discusses the main findings of this thesis and places them into a broader context, highlighting differences, similarities and peculiarities of segmented viruses compared to monopartite and multipartite viruses. Emphasis is given to the still unanswered fundamental questions on the biology of bunyaviruses and to potential directions for future research.

Acknowledgements

Thanks to Paul J. Wichgers Schreur and Monique M. van Oers for providing valuable feedback on this chapter. Thanks also to Ingrid Cárdenas Rey for proofreading. Illustrations in **Figs. 1-7** were created with BioRender.com.

References

1. Abudurexiti A, Adkins S, Alioto D, Alkhovsky SV, Avšič-Županc T, Ballinger MJ, Bente DA, Beer M, Bergeron É, Blair CD, Briese T, Buchmeier MJ, *et al.* Taxonomy of the order *Bunyavirales*: update 2019. *Archives of Virology* **2019**, *164* (7), 1949–1965. https://doi.org/10.1007/s00705-019-04253-6.
2. International Committee on Taxonomy of Viruses (ICTV). *Virus Taxonomy: 2022 Release (MSL #38)*. https://ictv.global/taxonomy (accessed 2023-05-11).
3. Wichgers Schreur PJ, Kormelink R, Kortekaas J. Genome packaging of the *Bunyavirales*. *Current Opinion in Virology* **2018**, *33*, 151–155. https://doi.org/10.1016/j.coviro.2018.08.011.
4. Kormelink R, Verchot J, Tao X, Desbiez C. The Bunyavirales: The plant-infecting counterparts. *Viruses* **2021**, *13* (5), 842. https://doi.org/10.3390/v13050842.
5. Huang H, Hua X, Pang X, Zhang Z, Ren J, Cheng J, Fu Y, Xiao X, Lin Y, Chen T, Li B, Liu H, *et al.* Discovery and characterization of putative glycoprotein-encoding mycoviruses in the *Bunyavirales*. *Journal of Virology* **2023**, *97* (1), e01381-22. https://doi.org/10.1128/jvi.01381-22.

6. Leventhal SS, Wilson D, Feldmann H, Hawman DW. A look into Bunyavirales genomes: functions of non-structural (NS) proteins. *Viruses* **2021**, *13* (2), 314. https://doi.org/10.3390/v13020314.

7. Rich KM, Wanyoike F. An assessment of the regional and national socio-economic impacts of the 2007 Rift Valley fever outbreak in Kenya. *The American Journal of Tropical Medicine and Hygiene* **2010**, *83* (2_Suppl), 52–57. https://doi.org/10.4269/ajtmh.2010.09-0291.

8. Peyre M, Chevalier V, Abdo-Salem S, Velthuis A, Antoine-Moussiaux N, Thiry E, Roger F. A systematic scoping study of the socio-economic impact of Rift Valley fever: research gaps and needs. *Zoonoses Public Health* **2015**, *62* (5), 309–325. https://doi.org/10.1111/zph.12153.

9. Waret-Szkuta A, Alarcon P, Hasler B, Rushton J, Corbière F, Raboisson D. Economic assessment of an emerging disease: the case of Schmallenberg virus in France. *Rev. Sci. Tech. Off. Int. Epiz.* **2017**, *36* (1), 265–277. https://doi.org/10.20506/rst.36.1.2627.

10. Weaver SC, Reisen WK. Present and future arboviral threats. *Antiviral Research* **2010**, *85* (2), 328–345. https://doi.org/10.1016/j.antiviral.2009.10.008.

11. Weaver SC. Urbanization and geographic expansion of zoonotic arboviral diseases: mechanisms and potential strategies for prevention. *Trends in Microbiology* **2013**, *21* (8), 360–363. https://doi.org/10.1016/j.tim.2013.03.003.

12. Marklewitz M, Junglen S. Evolutionary and ecological insights into the emergence of arthropod-borne viruses. *Acta Tropica* **2019**, *190*, 52–58. https://doi.org/10.1016/j.actatropica.2018.10.006.

13. Friedrich MJ. WHO's blueprint list of priority diseases. *JAMA* **2018**, *319* (19), 1973–1973. https://doi.org/10.1001/jama.2018.5712.

14. Daubney R, Hudson JR, Garnham PC. Enzootic hepatitis or Rift Valley fever. An undescribed virus disease of sheep cattle and man from East Africa. *The Journal of Pathology and Bacteriology* **1931**, *34* (4), 545–579. https://doi.org/10.1002/path.1700340418.

15. Kuhn JH, Adkins S, Alkhovsky SV, Avšič-Županc T, Ayllón MA, Bahl J, Balkema-Buschmann A, Ballinger MJ, Bandte M, Beer M, Bejerman N, Bergeron É, *et al.* 2022 taxonomic update of phylum *Negarnaviricota* (*Riboviria*: *Orthornavirae*), including the large orders *Bunyavirales* and *Mononegavirales*. *Archives of Virology* **2022**, *167* (12), 2857–2906. https://doi.org/10.1007/s00705-022-05546-z.

16. Nanyingi MO, Munyua P, Kiama SG, Muchemi GM, Thumbi SM, Bitek AO, Bett B, Muriithi RM, Njenga MK. A systematic review of Rift Valley Fever epidemiology 1931–2014. *Infection Ecology & Epidemiology* **2015**, *5* (1), 28024. https://doi.org/10.3402/iee.v5.28024.

17. Ahmad K. More deaths from Rift Valley fever in Saudi Arabia and Yemen. *The Lancet* **2000**, *356* (9239), 1422. https://doi.org/10.1016/S0140-6736(05)74068-X.

18. Al-Hazmi M, Ayoola EA, Abdurahman M, Banzal S, Ashraf J, El-Bushra A, Hazmi A, Abdullah M, Abbo H, Elamin A, Al-Sammani E-T, Gadour M, *et al.* Epidemic Rift Valley fever in Saudi Arabia: a clinical study of severe illness in humans. *Clinical Infectious Diseases.* **2003**, *36* (3), 245–252. https://doi.org/10.1086/345671.

19. Madani TA, Al-Mazrou YY, Al-Jeffri MH, Mishkhas AA, Al-Rabeah AM, Turkistani AM, Al-Sayed MO, Abodahish AA, Khan AS, Ksiazek TG, Shobokshi O. Rift Valley Fever Epidemic in Saudi Arabia:

Epidemiological, Clinical, and Laboratory Characteristics. *Clinical Infectious Diseases* **2003**, *37* (8), 1084–1092. https://doi.org/10.1086/378747.

20. Sissoko D, Giry C, Gabrie P, Tarantola A, Pettinelli F, Collet L, D'Ortenzio E, Renault P, Pierre V. Rift Valley fever, Mayotte, 2007–2008. *Emerging Infectious Diseases* **2009**, *15* (4). https://doi.org/10.3201/eid1504.081045.

21. Youssouf H, Subiros M, Dennetiere G, Collet L, Dommergues L, Pauvert A, Rabarison P, Vauloup-Fellous C, Godais GL, Jaffar-Bandjee M-C, Jean M, Paty M-C, *et al.* Rift Valley fever outbreak, Mayotte, France, 2018–2019. *Emerging Infectious Diseases* **2020**, *26* (4). https://doi.org/10.3201/eid2604.191147.

22. Coetzer JA. The pathology of Rift Valley fever. II. Lesions occurring in field cases in adult cattle, calves and aborted foetuses. *The Onderstepoort Journal of Veterinary Research* **1982**, *49* (1), 11–17.

23. Munyua P, Murithi RM, Wainwright S, Githinji J, Hightower A, Mutonga D, Macharia J, Ithondeka PM, Musaa J, Breiman RF, Bloland P, Njenga MK. Rift Valley fever outbreak in livestock in Kenya, 2006-2007. *The American Journal of Tropical Medicine and Hygiene* **2010**, *83* (2_Suppl), 58–64. https://doi.org/10.4269/ajtmh.2010.09-0292.

24. Clark MHA, Warimwe GM, Nardo AD, Lyons NA, Gubbins S. Systematic literature review of Rift Valley fever virus seroprevalence in livestock, wildlife and humans in Africa from 1968 to 2016. *PLOS Neglected Tropical Diseases* **2018**, *12* (7), e0006627. https://doi.org/10.1371/journal.pntd.0006627.

25. Wright D, Kortekaas J, Bowden TA, Warimwe GM. Rift Valley fever: biology and epidemiology. *Journal of General Virology* **2019**, *100* (8), 1187–1199. https://doi.org/10.1099/jgv.0.001296.

26. Flick R, Bouloy M. Rift Valley fever virus. *Current Molecular Medicine* **2005**, *5* (8), 827–834. https://doi.org/10.2174/156652405774962263.

27. Bird BH, Ksiazek TG, Nichol ST, MacLachlan NJ. Rift Valley fever virus. *Journal of the American Veterinary Medical Association* **2009**, *234* (7), 883–893. https://doi.org/10.2460/javma.234.7.883.

28. Odendaal L, Clift SJ, Fosgate GT, Davis AS. Ovine fetal and placental lesions and cellular tropism in natural Rift Valley fever virus infections. *Veterinary Pathology* **2020**, *57* (6), 791–806. https://doi.org/10.1177/0300985820954549.

29. Dondona AC, Aschenborn O, Pinoni C, Gialleonardo LD, Maseke A, Bortone G, Polci A, Scacchia M, Molini U, Monaco F. Rift Valley fever virus among wild ruminants, Etosha National Park, Namibia, 2011. *Emerging Infectious Diseases* **2016**, *22* (1). https://doi.org/10.3201/eid2201.150725.

30. Pepin M, Bouloy M, Bird BH, Kemp A, Paweska J. Rift Valley fever virus (*Bunyaviridae*: *Phlebovirus*): an update on pathogenesis, molecular epidemiology, vectors, diagnostics and prevention. *Veterinary Research* **2010**, *41* (6), 61. https://doi.org/10.1051/vetres/2010033.

31. Linthicum KJ, Britch SC, Anyamba A. Rift Valley fever: an emerging mosquito-borne disease. *Annual Review of Entomology* **2016**, *61* (1), 395–415. https://doi.org/10.1146/annurev-ento-010715-023819.

32. Smithburn KC, Haddow AJ, Gillett JD. Rift Valley fever. Isolation of the virus from wild mosquitoes. *British Journal of Experimental Pathology* **1948**, *29* (2), 107–121.

33. Gear J, Meillo BD, Roux AFL, Kofsky R, Rose R, Steyn JJ, Oliff WD, Schulz KH. Rift Valley fever in South Africa: A study of the 1953 outbreak in the Orange Free State, with special reference to the vectors and possible reservoir hosts. *South African Medical Journal* **1955**, *29* (5).

34. Turell MJ, Dohm DJ, Mores CN, Terracina L, Wallette DL, Hribar LJ, Pecor JE, Blow JA. Potential for North American mosquitoes to transmit Rift Valley fever virus. *Journal of the American Mosquito Control Association* **2008**, *24* (4), 502–507. https://doi.org/10.2987/08-5791.1.

35. Turell MJ, Britch SC, Aldridge RL, Kline DL, Boohene C, Linthicum KJ. Potential for mosquitoes (Diptera: Culicidae) from Florida to transmit Rift Valley fever virus. *Journal of Medical Entomology* **2013**, *50* (5), 1111–1117. https://doi.org/10.1603/ME13049.

36. Brustolin M, Talavera S, Nuñez A, Santamaría C, Rivas R, Pujol N, Valle M, Verdún M, Brun A, Pagès N, Busquets N. Rift Valley fever virus and European mosquitoes: vector competence of *Culex pipiens* and *Stegomyia albopicta* (= *Aedes albopictus*). *Medical and Veterinary Entomology* **2017**, *31* (4), 365-372. https://doi.org/10.1111/mve.12254.

37. El-Din Abdel-Wahab KS, El Baz LM, El Tayeb EM, Omar H, Moneim Ossman MA, Yasin W. Rift Valley Fever virus infections in Egypt: Pathological and virological findings in man. *Transactions of The Royal Society of Tropical Medicine and Hygiene* **1978**, *72* (4), 392–396. https://doi.org/10.1016/0035-9203(78)90134-7.

38. van Velden DJJ, Meyer JD, Olivier J, Gear JHS, McIntosh B. Rift Valley fever affecting humans in South Africa - a clinicopathological study. *South African Medical Journal* **1977**, *51* (24), 867–871. https://doi.org/10.10520/AJA20785135_24734.

39. Laughlin LW, Meegan JM, Strausbaugh LJ, Morens DM, Watten RH. Epidemic Rift Valley fever in Egypt: observations of the spectrum of human illness. *Transactions of The Royal Society of Tropical Medicine and Hygiene* **1979**, *73* (6), 630–633. https://doi.org/10.1016/0035-9203(79)90006-3.

40. Hassan OA, Ahlm C, Sang R, Evander M. The 2007 Rift Valley fever outbreak in Sudan. *PLOS Neglected Tropical Diseases* **2011**, *5* (9), e1229. https://doi.org/10.1371/journal.pntd.0001229.

41. Odendaal L, Clift SJ, Fosgate GT, Davis AS. Lesions and cellular tropism of natural Rift Valley fever virus infection in adult sheep. *Veterinary Pathology* **2019**, *56* (1), 61–77. https://doi.org/10.1177/0300985818806049.

42. Odendaal L, Davis AS, Fosgate GT, Clift SJ. Lesions and cellular tropism of natural Rift Valley fever virus infection in young lambs. *Veterinary Pathology* **2020**, *57* (1), 66–81. https://doi.org/10.1177/0300985819882633.

43. Arishi HM, Aqeel AY, Al Hazmi MM. Vertical transmission of fatal Rift Valley fever in a newborn. *Annals of Tropical Paediatrics* **2006**, *26*, 251–253. https://doi.org/10.1179/146532806X120363.

44. Adam I, Karsany MS. Case report: Rift Valley Fever with vertical transmission in a pregnant Sudanese woman. *Journal of Medical Virology* **2008**, *80* (5), 929–929. https://doi.org/10.1002/jmv.21132.

45. Oymans J, Wichgers Schreur PJ, van Keulen L, Kant J, Kortekaas J. Rift Valley fever virus targets the maternal-foetal interface in ovine and human placentas. *PLOS Neglected Tropical Diseases* **2020**, *14* (1), e0007898. https://doi.org/10.1371/journal.pntd.0007898.

46. McMillen CM, Hartman AL. Rift Valley fever: a threat to pregnant women hiding in plain sight? *Journal of Virology* **2021**, *95* (9), e01394-19. https://doi.org/10.1128/JVI.01394-19.

47. Bron GM, Strimbu K, Cecilia H, Lerch A, Moore SM, Tran Q, Perkins TA, ten Bosch QA. Over 100 years of Rift Valley fever: a patchwork of data on pathogen spread and spillover. *Pathogens* **2021**, *10* (6), 708. https://doi.org/10.3390/pathogens10060708.

48. Muga GO, Onyango-Ouma W, Sang R, Affognon H. Sociocultural and economic dimensions of Rift Valley fever. *The American Journal of Tropical Medicine and Hygiene* **2015**, *92* (4), 730–738. https://doi.org/10.4269/ajtmh.14-0363.

49. Wichgers Schreur PJ, Bird BH, Ikegami T, Bermúdez-Méndez E, Kortekaas J. Perspectives of next-generation live-attenuated Rift Valley fever vaccines for animal and human use. *Vaccines* **2023**, *11* (3), 707. https://doi.org/10.3390/vaccines11030707.

50. Hoffmann B, Scheuch M, Höper D, Jungblut R, Holsteg M, Schirrmeier H, Eschbaumer M, Goller KV, Wernike K, Fischer M, Breithaupt A, Mettenleiter TC, *et al.* Novel orthobunyavirus in cattle, Europe, 2011. *Emerging Infectious Diseases* **2012**, *18* (3). https://doi.org/10.3201/eid1803.111905.

51. Wernike K, Elbers A, Beer M. Schmallenberg virus infection. *Rev. Sci. Tech. Off. Int. Epiz.* **2015**, *34* (2), 363–373. https://doi.org/10.20506/rst.34.2.2363.

52. European Food Safety Authority (EFSA). "Schmallenberg" virus: analysis of the epidemiological data (May 2013). *EFSA Supporting Publications* **2013**, *10* (5), 429E. https://doi.org/10.2903/sp.efsa.2013.EN-429.

53. Reusken C, van den Wijngaard C, van Beek P, Beer M, Bouwstra R, Godeke G-J, Isken L, van den Kerkhof H, van Pelt W, van der Poel W, Reimerink J, Schielen P, *et al.* Lack of evidence for zoonotic transmission of Schmallenberg virus. *Emerging Infectious Diseases* **2012**, *18* (11). https://doi.org/10.3201/eid1811.120650.

54. Ducomble T, Wilking H, Stark K, Takla A, Askar M, Schaade L, Nitsche A, Kurth A. Lack of evidence for Schmallenberg virus infection in highly exposed persons, Germany, 2012. *Emerging Infectious Diseases* **2012**, *18* (8). https://doi.org/10.3201/eid1808.120533.

55. Vasconcelos HB, Azevedo RSS, Casseb SM, Nunes-Neto JP, Chiang JO, Cantuária PC, Segura MNO, Martins LC, Monteiro HAO, Rodrigues SG, Nunes MRT, Vasconcelos PFC. Oropouche fever epidemic in Northern Brazil: Epidemiology and molecular characterization of isolates. *Journal of Clinical Virology* **2009**, *44* (2), 129–133. https://doi.org/10.1016/j.jcv.2008.11.006.

56. Aguilar PV, Barrett AD, Saeed MF, Watts DM, Russell K, Guevara C, Ampuero JS, Suarez L, Cespedes M, Montgomery JM, Halsey ES, Kochel TJ. Iquitos virus: a novel reassortant *Orthobunyavirus* associated with human illness in Peru. *PLOS Neglected Tropical Diseases* **2011**, *5* (9), e1315. https://doi.org/10.1371/journal.pntd.0001315.

57. Causey OR, Kemp GE, Causey CE, Lee VH. Isolations of Simbu-group viruses in Ibadan, Nigeria 1964-69, including the new types Sango, Shamonda, Sabo and Shuni. *Annals of Tropical Medicine & Parasitology* **1972**, *66* (3), 357–362. https://doi.org/10.1080/00034983.1972.11686835.

58. Muskens J, Smolenaars AJG, van der Poel WHM, Mars MH, van Wuijckhuise L, Holzhauer M, van Weering H, Kock P. Diarrhea and loss of production on Dutch dairy farms caused by the Schmallenberg virus. *Tijdschr Diergeneeskd* **2012**, *137* (2), 112–115.

59. Rasmussen LD, Kristensen B, Kirkeby C, Rasmussen TB, Belsham GJ, Bødker R, Bøtner A. Culicoids as vectors of Schmallenberg virus. *Emerging Infectious Diseases* **2012**, *18* (7). https://doi.org/10.3201/eid1807.120385.

60. Elbers ARW, Meiswinkel R, van Weezep E, van Oldruitenborgh-Oosterbaan MMS, Kooi EA. Schmallenberg virus in *Culicoides* spp. biting midges, The Netherlands, 2011. *Emerging Infectious Diseases* **2013**, *19* (1). https://doi.org/10.3201/eid1901.121054.

61. van den Brom R, Luttikholt SJM, Lievaart-Peterson K, Peperkamp NHMT, Mars MH, van der Poel WHM, Vellema P. Epizootic of ovine congenital malformations associated with Schmallenberg virus infection. *Tijdschr Diergeneeskd* **2012**, *137* (2), 106–111.

62. Garigliany M-M, Bayrou C, Kleijnen D, Cassart D, Jolly S, Linden A, Desmecht D. Schmallenberg virus: A new Shamonda/Sathuperi-like virus on the rise in Europe. *Antiviral Research* **2012**, *95* (2), 82–87. https://doi.org/10.1016/j.antiviral.2012.05.014.

63. Wernike K, Conraths F, Zanella G, Granzow H, Gache K, Schirrmeier H, Valas S, Staubach C, Marianneau P, Kraatz F, Höreth-Böntgen D, Reimann I, *et al.* Schmallenberg virus—Two years of experiences. *Preventive Veterinary Medicine* **2014**, *116* (4), 423–434. https://doi.org/10.1016/j.prevetmed.2014.03.021.

64. Beer M, Conraths FJ, van der Poel WHM. 'Schmallenberg virus' – a novel orthobunyavirus emerging in Europe. *Epidemiology & Infection* **2013**, *141* (1), 1–8. https://doi.org/10.1017/S0950268812002245.

65. Wernike K, Beer M. Re-circulation of Schmallenberg virus, Germany, 2019. *Transboundary and Emerging Diseases* **2020**, *67* (6), 2290–2295. https://doi.org/10.1111/tbed.13592.

66. Wernike K, Beer M. Schmallenberg virus: to Vaccinate, or not to vaccinate? *Vaccines* **2020**, *8* (2), 287. https://doi.org/10.3390/vaccines8020287.

67. Freiberg AN, Sherman MB, Morais MC, Holbrook MR, Watowich SJ. Three-dimensional organization of Rift Valley fever virus revealed by cryoelectron tomography. *Journal of Virology* **2008**, *82* (21), 10341–10348. https://doi.org/10.1128/JVI.01191-08.

68. Överby AK, Pettersson RF, Grünewald K, Huiskonen JT. Insights into bunyavirus architecture from electron cryotomography of Uukuniemi virus. *PNAS* **2008**, *105* (7), 2375–2379. https://doi.org/10.1073/pnas.0708738105.

69. Huiskonen JT, Överby AK, Weber F, Grünewald K. Electron cryo-microscopy and single-particle averaging of Rift Valley fever virus: evidence for Gn-Gc glycoprotein heterodimers. *Journal of Virology* **2009**, *83* (8), 3762–3769. https://doi.org/10.1128/JVI.02483-08.

70. Sherman MB, Freiberg AN, Holbrook MR, Watowich SJ. Single-particle cryo-electron microscopy of Rift Valley fever virus. *Virology* **2009**, *387* (1), 11–15. https://doi.org/10.1016/j.virol.2009.02.038.

71. Bowden TA, Bitto D, McLees A, Yeromonahos C, Elliott RM, Huiskonen JT. Orthobunyavirus ultrastructure and the curious tripodal glycoprotein spike. *PLOS Pathogens* **2013**, *9* (5), e1003374. https://doi.org/10.1371/journal.ppat.1003374.

72. Hellert J, Aebischer A, Wernike K, Haouz A, Brocchi E, Reiche S, Guardado-Calvo P, Beer M, Rey FA. Orthobunyavirus spike architecture and recognition by neutralizing antibodies. *Nature Communications* **2019**, *10*, 879. https://doi.org/10.1038/s41467-019-08832-8.

73. Hellert J, Aebischer A, Haouz A, Guardado-Calvo P, Reiche S, Beer M, Rey FA. Structure, function, and evolution of the *Orthobunyavirus* membrane fusion glycoprotein. *Cell Reports* **2023**, *42* (3), 112142. https://doi.org/10.1016/j.celrep.2023.112142.

74. Elliott RM, Brennan B. Emerging phleboviruses. *Current Opinion in Virology* **2014**, *5*, 50–57. https://doi.org/10.1016/j.coviro.2014.01.011.

75. Elliott RM. Orthobunyaviruses: recent genetic and structural insights. *Nature Reviews Microbiology* **2014**, *12* (10), 673–685. https://doi.org/10.1038/nrmicro3332.

76. Sun Y, Li J, Gao GF, Tien P, Liu W. Bunyavirales ribonucleoproteins: the viral replication and transcription machinery. *Critical Reviews in Microbiology* **2018**, *44* (5), 522-540. https://doi.org/10.1080/1040841X.2018.1446901

77. Malet H, Williams HM, Cusack S, Rosenthal M. The mechanism of genome replication and transcription in bunyaviruses. *PLOS Pathogens* **2023**, *19* (1), e1011060. https://doi.org/10.1371/journal.ppat.1011060.

78. Guardado-Calvo P, Rey FA. Chapter Three - The Envelope Proteins of the *Bunyavirales*. In *Advances in Virus Research*; Kielian M, Mettenleiter TC, Roossinck MJ, Eds.; Academic Press, 2017; Vol. 98, pp 83-118. https://doi.org/10.1016/bs.aivir.2017.02.002.

79. Hulswit RJG, Paesen GC, Bowden TA, Shi X. Recent advances in bunyavirus glycoprotein research: precursor processing, receptor binding and structure. *Viruses* **2021**, *13* (2), 353. https://doi.org/10.3390/v13020353.

80. Elliott RM, Weber F. Bunyaviruses and the type I interferon system. *Viruses* **2009**, *1* (3), 1003–1021. https://doi.org/10.3390/v1031003.

81. Walter CT, Barr JN. Recent advances in the molecular and cellular biology of bunyaviruses. *Journal of General Virology* **2011**, *92* (11), 2467–2484. https://doi.org/10.1099/vir.0.035105-0.

82. Bouloy M, Janzen C, Vialat P, Khun H, Pavlovic J, Huerre M, Haller O. Genetic evidence for an interferon-antagonistic function of Rift Valley fever virus nonstructural protein NSs. *Journal of Virology* **2001**, *75* (3), 1371–1377. https://doi.org/10.1128/JVI.75.3.1371-1377.2001.

83. Bridgen A, Weber F, Fazakerley JK, Elliott RM. Bunyamwera bunyavirus nonstructural protein NSs is a nonessential gene product that contributes to viral pathogenesis. *PNAS* **2001**, *98* (2), 664–669. https://doi.org/10.1073/pnas.98.2.664.

84. Weber F, Bridgen A, Fazakerley JK, Streitenfeld H, Kessler N, Randall RE, Elliott RM. Bunyamwera bunyavirus nonstructural protein NSs counteracts the induction of alpha/beta interferon. *Journal of Virology* **2002**, *76* (16), 7949–7955. https://doi.org/10.1128/JVI.76.16.7949-7955.2002.

85. Blakqori G, Delhaye S, Habjan M, Blair CD, Sánchez-Vargas I, Olson KE, Attarzadeh-Yazdi G, Fragkoudis R, Kohl A, Kalinke U, Weiss S, Michiels T, *et al.* La Crosse bunyavirus nonstructural protein NSs serves to suppress the type I interferon system of mammalian hosts. *Journal of Virology* **2007**, *81* (10), 4991–4999. https://doi.org/10.1128/JVI.01933-06.

86. Billecocq A, Spiegel M, Vialat P, Kohl A, Weber F, Bouloy M, Haller O. NSs protein of Rift Valley fever virus blocks interferon production by inhibiting host gene transcription. *Journal of Virology* **2004**, *78* (18), 9798–9806. https://doi.org/10.1128/JVI.78.18.9798-9806.2004.

87. Le May N, Dubaele S, De Santis LP, Billecocq A, Bouloy M, Egly J-M. TFIIH transcription factor, a target for the Rift Valley hemorrhagic fever virus. *Cell* **2004**, *116* (4), 541–550. https://doi.org/10.1016/S0092-8674(04)00132-1.

88. Habjan M, Pichlmair A, Elliott RM, Överby AK, Glatter T, Gstaiger M, Superti-Furga G, Unger H, Weber F. NSs protein of Rift Valley fever virus induces the specific degradation of the double-stranded RNA-dependent protein kinase. *Journal of Virology* **2009**, *83* (9), 4365–4375. https://doi.org/10.1128/JVI.02148-08.

89. Kainulainen M, Lau S, Samuel CE, Hornung V, Weber F. NSs virulence factor of Rift Valley fever virus engages the F-Box proteins FBXW11 and β-TRCP1 to degrade the antiviral protein kinase PKR. *Journal of Virology* **2016**, *90* (13), 6140–6147. https://doi.org/10.1128/JVI.00016-16.

90. Ikegami T, Narayanan K, Won S, Kamitani W, Peters CJ, Makino S. Rift Valley fever virus NSs protein promotes post-transcriptional downregulation of protein kinase PKR and inhibits eIF2alpha phosphorylation. *PLOS Pathogens* **2009**, *5* (2), e1000287. https://doi.org/10.1371/journal.ppat.1000287.

91. Elliott RM, Blakqori G, van Knippenberg IC, Koudriakova E, Li P, McLees A, Shi X, Szemiel AM. Establishment of a reverse genetics system for Schmallenberg virus, a newly emerged orthobunyavirus in Europe. *Journal of General Virology* **2013**, *94* (Pt 4), 851–859. https://doi.org/10.1099/vir.0.049981-0.

92. Won S, Ikegami T, Peters CJ, Makino S. NSm protein of Rift Valley fever virus suppresses virus-induced apoptosis. *Journal of Virology* **2007**, *81* (24), 13335–13345. https://doi.org/10.1128/JVI.01238-07.

93. Crabtree MB, Crockett RJK, Bird BH, Nichol ST, Erickson BR, Biggerstaff BJ, Horiuchi K, Miller BR. Infection and transmission of Rift Valley fever viruses lacking the NSs and/or NSm genes in mosquitoes: potential role for NSm in mosquito infection. *PLOS Neglected Tropical Diseases* **2012**, *6* (5), e1639. https://doi.org/10.1371/journal.pntd.0001639.

94. Kading RC, Crabtree MB, Bird BH, Nichol ST, Erickson BR, Horiuchi K, Biggerstaff BJ, Miller BR. Deletion of the NSm virulence gene of Rift Valley fever virus inhibits virus replication in and dissemination from the midgut of *Aedes aegypti* mosquitoes. *PLOS Neglected Tropical Diseases* **2014**, *8* (2), e2670. https://doi.org/10.1371/journal.pntd.0002670.

95. Shi X, Kohl A, Léonard VHJ, Li P, McLees A, Elliott RM. Requirement of the N-terminal region of orthobunyavirus nonstructural protein NSm for virus assembly and morphogenesis. *Journal of Virology* **2006**, *80* (16), 8089–8099. https://doi.org/10.1128/JVI.00579-06.

96. Albornoz A, Hoffmann AB, Lozach P-Y, Tischler ND. Early bunyavirus-host cell interactions. *Viruses* **2016**, *8* (5), 143. https://doi.org/10.3390/v8050143.

97. Olschewski S, Cusack S, Rosenthal M. The cap-snatching mechanism of Bunyaviruses. *Trends in Microbiology* **2020**, *28* (4), 293–303. https://doi.org/10.1016/j.tim.2019.12.006.

98. Barker J, da Silva LLP, Crump CM. Mechanisms of bunyavirus morphogenesis and egress. *Journal of General Virology* **2023**, *104* (4), 001845. https://doi.org/10.1099/jgv.0.001845.

99. Gerber M, Isel C, Moules V, Marquet R. Selective packaging of the influenza A genome and consequences for genetic reassortment. *Trends in Microbiology* **2014**, *22* (8), 446–455. https://doi.org/10.1016/j.tim.2014.04.001.

100. Goto H, Muramoto Y, Noda T, Kawaoka Y. The genome-packaging signal of the influenza A virus genome comprises a genome incorporation signal and a genome-bundling signal. *Journal of Virology* **2013**, *87* (21), 11316–11322. https://doi.org/10.1128/JVI.01301-13.

101. Borodavka A, Dykeman EC, Schrimpf W, Lamb DC. Protein-mediated RNA folding governs sequence-specific interactions between rotavirus genome segments. *eLife* **2017**, *6*, e27453. https://doi.org/10.7554/eLife.27453.

102. Dadonaite B, Gilbertson B, Knight ML, Trifkovic S, Rockman S, Laederach A, Brown LE, Fodor E, Bauer DLV. The structure of the influenza A virus genome. *Nature Microbiology* **2019**, *4* (11), 1781–1789. https://doi.org/10.1038/s41564-019-0513-7.

103. Le Sage V, Kanarek JP, Snyder DJ, Cooper VS, Lakdawala SS, Lee N. Mapping of influenza virus RNA-RNA interactions reveals a flexible network. *Cell Reports* **2020**, *31* (13). https://doi.org/10.1016/j.celrep.2020.107823.

104. Flick K, Katz A, Överby A, Feldmann H, Pettersson RF, Flick R. Functional analysis of the noncoding regions of the Uukuniemi virus (*Bunyaviridae*) RNA segments. *Journal of Virology* **2004**, *78* (21), 11726-11738. https://doi.org/10.1128/jvi.78.21.11726-11738.2004.

105. Kohl A, Lowen AC, Léonard VHJ, Elliott RM. Genetic elements regulating packaging of the Bunyamwera orthobunyavirus genome. *Journal of General Virology* **2006**, *87* (1), 177–187. https://doi.org/10.1099/vir.0.81227-0.

106. Murakami S, Terasaki K, Narayanan K, Makino S. Roles of the coding and noncoding regions of Rift Valley fever virus RNA genome segments in viral RNA packaging. *Journal of Virology* **2012**, *86* (7), 4034–4039. https://doi.org/10.1128/JVI.06700-11.

107. Överby AK, Pettersson RF, Neve EPA. The glycoprotein cytoplasmic tail of Uukuniemi virus (*Bunyaviridae*) interacts with ribonucleoproteins and is critical for genome packaging. *Journal of Virology* **2007**, *81* (7), 3198–3205. https://doi.org/10.1128/jvi.02655-06.

108. Ribeiro D, Borst JW, Goldbach R, Kormelink R. Tomato spotted wilt virus nucleocapsid protein interacts with both viral glycoproteins Gn and Gc *in planta*. *Virology* **2009**, *383* (1), 121–130. https://doi.org/10.1016/j.virol.2008.09.028.

109. Carnec X, Ermonval M, Kreher F, Flamand M, Bouloy M. Role of the cytosolic tails of Rift Valley fever virus envelope glycoproteins in viral morphogenesis. *Virology* **2014**, *448*, 1–14. https://doi.org/10.1016/j.virol.2013.09.023.

110. Tercero B, Narayanan K, Terasaki K, Makino S. Characterization of the molecular interactions that govern the packaging of viral RNA segments into Rift Valley fever phlebovirus particles. *Journal of Virology* **2021**, *95* (14), e00429-21. https://doi.org/10.1128/JVI.00429-21.

111. Piper ME, Sorenson DR, Gerrard SR. Efficient cellular release of Rift Valley fever virus requires genomic RNA. *PLOS ONE* **2011**, *6* (3), e18070. https://doi.org/10.1371/journal.pone.0018070.

112. Terasaki K, Murakami S, Lokugamage KG, Makino S. Mechanism of tripartite RNA genome packaging in Rift Valley fever virus. *PNAS* **2011**, *108* (2), 804–809. https://doi.org/10.1073/pnas.1013155108.

113. Noda T, Sagara H, Yen A, Takada A, Kida H, Cheng RH, Kawaoka Y. Architecture of ribonucleoprotein complexes in influenza A virus particles. *Nature* **2006**, *439* (7075), 490–492. https://doi.org/10.1038/nature04378.

114. Noda T, Sugita Y, Aoyama K, Hirase A, Kawakami E, Miyazawa A, Sagara H, Kawaoka Y. Three-dimensional analysis of ribonucleoprotein complexes in influenza A virus. *Nature Communications* **2012**, *3* (1), 1–6. https://doi.org/10.1038/ncomms1647.

115. Fournier E, Moules V, Essere B, Paillart J-C, Sirbat J-D, Isel C, Cavalier A, Rolland J-P, Thomas D, Lina B, Marquet R. A supramolecular assembly formed by influenza A virus genomic RNA segments. *Nucleic Acids Research* **2012**, *40* (5), 2197–2209. https://doi.org/10.1093/nar/gkr985.

116. Brennan B, Welch SR, McLees A, Elliott RM. Creation of a recombinant Rift Valley fever virus with a two-segmented genome. *Journal of Virology* **2011**, *85* (19), 10310–10318. https://doi.org/10.1128/JVI.05252-11.

117. Wichgers Schreur PJ, Oreshkova N, Moormann RJM, Kortekaas J. Creation of Rift Valley fever viruses with four-segmented genomes reveals flexibility in bunyavirus genome packaging. *Journal of Virology* **2014**, *88* (18), 10883–10893. https://doi.org/10.1128/JVI.00961-14.

118. Brennan B, Welch SR, Elliott RM. The consequences of reconfiguring the ambisense S genome segment of Rift Valley fever virus on viral replication in mammalian and mosquito cells and for genome packaging. *PLOS Pathogens* **2014**, *10* (2), e1003922. https://doi.org/10.1371/journal.ppat.1003922.

119. Wichgers Schreur PJ, Kortekaas J. Single-molecule FISH reveals non-selective packaging of Rift Valley fever virus genome segments. *PLOS Pathogens* **2016**, *12* (8), e1005800. https://doi.org/10.1371/journal.ppat.1005800.

120. Wang Z, Gerstein M, Snyder M. RNA-Seq: a revolutionary tool for transcriptomics. *Nature Reviews Genetics* **2009**, *10* (1), 57–63. https://doi.org/10.1038/nrg2484.

121. Stark R, Grzelak M, Hadfield J. RNA sequencing: the teenage years. *Nature Reviews Genetics* **2019**, *20* (11), 631–656. https://doi.org/10.1038/s41576-019-0150-2.

122. Aldridge S, Teichmann SA. Single cell transcriptomics comes of age. *Nature Communications* **2020**, *11* (1), 4307. https://doi.org/10.1038/s41467-020-18158-5.

123. Wyler E, Franke V, Menegatti J, Kocks C, Boltengagen A, Praktiknjo S, Walch-Rückheim B, Bosse J, Rajewsky N, Grässer F, Akalin A, Landthaler M. Single-cell RNA-sequencing of herpes simplex virus 1-infected cells connects NRF2 activation to an antiviral program. *Nature Communications* **2019**, *10* (1), 4878. https://doi.org/10.1038/s41467-019-12894-z.

124. Kozak RA, Fraser RS, Biondi MJ, Majer A, Medina SJ, Griffin BD, Kobasa D, Stapleton PJ, Urfano C, Babuadze G, Antonation K, Fernando L, *et al.* Dual RNA-Seq characterization of host and pathogen gene expression in liver cells infected with Crimean-Congo Hemorrhagic Fever Virus. *PLOS Neglected Tropical Diseases* **2020**, *14* (4), e0008105. https://doi.org/10.1371/journal.pntd.0008105.

125. Zheng Y, Li S, Li S-H, Yu S, Wang Q, Zhang K, Qu L, Sun Y, Bi Y, Tang F, Qiu H-J, Gao GF. Transcriptome profiling in swine macrophages infected with African swine fever virus at single-cell resolution. *PNAS* **2022**, *119* (19), e2201288119. https://doi.org/10.1073/pnas.2201288119.

126. Kotliar D, Lin AE, Logue J, Hughes TK, Khoury NM, Raju SS, Wadsworth MH, Chen H, Kurtz JR, Dighero-Kemp B, Bjornson ZB, Mukherjee N, *et al.* Single-cell profiling of Ebola virus disease in vivo reveals viral and host dynamics. *Cell* **2020**, *183* (5), 1383-1401.e19. https://doi.org/10.1016/j.cell.2020.10.002.

127. Neogi U, Elaldi N, Appelberg S, Ambikan A, Kennedy E, Dowall S, Bagci BK, Gupta S, Rodriguez JE, Svensson-Akusjärvi S, Monteil V, Vegvari A, *et al.* Multi-omics insights into host-viral response and pathogenesis in Crimean-Congo hemorrhagic fever viruses for novel therapeutic target. *eLife* **2022**, *11*, e76071. https://doi.org/10.7554/eLife.76071.

128. Russell AB, Trapnell C, Bloom JD. Extreme heterogeneity of influenza virus infection in single cells. *eLife* **2018**, *7*, e32303. https://doi.org/10.7554/eLife.32303.

129. Drayman N, Patel P, Vistain L, Tay S. HSV-1 single-cell analysis reveals the activation of anti-viral and developmental programs in distinct sub-populations. *eLife* **2019**, *8*, e46339. https://doi.org/10.7554/eLife.46339.

Chapter 2

Visualizing the ribonucleoprotein content of single bunyavirus virions reveals more efficient genome packaging in the arthropod host

Erick Bermúdez-Méndez [1,2], Eugene A. Katrukha [3], Cindy M. Spruit [1,4], Jeroen Kortekaas [1,2,5] & Paul J. Wichgers Schreur [1]

[1] Department of Virology & Molecular Biology, Wageningen Bioveterinary Research, Lelystad, The Netherlands

[2] Laboratory of Virology, Wageningen University & Research, Wageningen, The Netherlands

[3] Cell Biology, Department of Biology, Faculty of Science, Utrecht University, Utrecht, The Netherlands

[4] Present address: Department of Chemical Biology & Drug Discovery, Utrecht Institute for Pharmaceutical Sciences, Utrecht University, Utrecht, The Netherlands

[5] Present address: Boehringer Ingelheim Animal Health, Saint-Priest, France

Published:

Communications Biology (2021) 4, 345.

DOI: https://doi.org/10.1038/s42003-021-01821-y

Abstract

Bunyaviruses have a genome that is divided over multiple segments. Genome segmentation complicates the generation of progeny virus, since each newly formed virus particle should preferably contain a full set of genome segments in order to disseminate efficiently within and between hosts. Here, we combine immunofluorescence and fluorescence *in situ* hybridization techniques to simultaneously visualize bunyavirus progeny virions and their genomic content at single-molecule resolution in the context of singly infected cells. Using Rift Valley fever virus and Schmallenberg virus as prototype tri-segmented bunyaviruses, we show that bunyavirus genome packaging is influenced by the intracellular viral genome content of individual cells, which results in greatly variable packaging efficiencies within a cell population. We further show that bunyavirus genome packaging is more efficient in insect cells compared to mammalian cells and provide new insights on the possibility that incomplete particles may contribute to bunyavirus spread as well.

Introduction

Viruses from the genera *Phlebovirus* (family *Phenuiviridae*) and *Orthobunyavirus* (family *Peribunyaviridae*), belonging to the order *Bunyavirales*, are globally distributed and transmitted between vertebrate hosts by arthropods, such as mosquitoes, sandflies, ticks and midges[1–4]. Several members of these genera cause severe disease in livestock and humans, threatening animal and public health and economies[5,6]. Yet, several fundamental aspects of the viral life cycles remain poorly comprehended.

Phleboviruses and orthobunyaviruses have a tri-segmented genome of single-stranded RNA of negative-sense polarity. The small (S), medium (M) and large (L) segments, named according to their size, are encapsidated by multiple nucleocapsid (N) proteins to form viral ribonucleoprotein (vRNP) complexes that associate with the RNA-dependent RNA polymerase (RdRp or L protein). The N protein is encoded by the S segment, which also encodes a non-structural protein in antigenomic-sense orientation in phleboviruses and in genomic-sense orientation in orthobunyaviruses. The RdRp is encoded by the L segment, whereas the M segment encodes a polyprotein precursor that is cleaved into a non-structural protein and two glycoproteins (Gn and Gc) that protrude from the envelope of mature particles and facilitate entry into host cells[6–8]. Virions are enveloped, spherical particles of ~80–120 nm in diameter[9–11].

From a gene expression perspective, genome segmentation could theoretically facilitate control of viral gene transcription and translation without requiring various *cis*-acting elements as viruses with non-segmented genomes require. Moreover, genome segmentation is generally considered as an evolutionary advantage because it allows genetic reassortment events, which can potentially result in increased viral fitness and transmissibility[12]. However, partitioning of the genome complicates the genome packaging process of segmented viruses, since the packaging of at least one copy of each segment into a particle is thought to be essential to generate infectious progeny. Considering this, it could be expected that the packaging of segmented viral genomes is a highly selective process. The existence of a selective packaging mechanism has already been demonstrated for segmented RNA viruses of other families such as influenza virus and rotavirus[13-15]. Reverse genetics and electron microscopy studies on influenza virus showed that the eight genome segments use packaging signals to assemble into a supramolecular complex with a '7 + 1' configuration[16–19]. Fluorescence spectroscopy combined with pulsed interleaved excitation revealed that rotavirus genome segments form protein-mediated sequence-specific interactions[20]. In both cases, RNA–RNA interactions play an important role in the packaging of the complete genome inside newly formed particles.

Early reports based on mini-genome systems showed that the 5′ and 3′ untranslated regions (UTRs) of bunyavirus RNA segments are directly or indirectly involved in the genome packaging process[21]. Certain flexibility in the packaging process was demonstrated by the rescue of a recombinant Bunyamwera virus (BUNV, genus *Orthobunyavirus*) with an L segment open reading frame flanked by M-type UTRs[22]. Additional work with recombinant viruses revealed the flexibility in the packaging of Rift Valley fever virus (RVFV, genus *Phlebovirus*) genome segments, as evidenced by the creation of multiple two-segmented and four-segmented variants[23–25], as well as a variant with reconfigured coding orientation of the S segment[26]. More recently, by using single-molecule fluorescence *in situ* hybridization (smFISH) we showed that S, M and L vRNPs of RVFV do not co-localize in the cytoplasm during viral replication. Together with a codon shuffled M segment variant that retained similar growth characteristics, no evidence was found for the formation of a supramolecular RVFV vRNP complex, thereby suggesting that the packaging of RVFV genome segments is not a tightly regulated process[27]. Despite that the scarce evidence available has provided valuable insights into the genome packaging of bunyaviruses, our understanding of this process is still very limited. In particular, packaging of bunyaviruses has only been studied with a few virus species, and few studies have compared genome packaging in different hosts. Potential host differences in specific steps of the replication cycle may have important implications for virus transmission between vertebrates and invertebrates. In addition, the kinetics and efficiency of generating infectious particles have only been examined at a cell population level and the potential biological role of incomplete particles (i.e., particles lacking one or more genome segments) in within- and between-host transmission is currently unknown.

Here, we use RVFV and Schmallenberg virus (SBV, genus *Orthobunyavirus*) as prototypes of different bunyavirus families to study genome packaging in mammalian and insect cells. We describe a 5-channel FISH-immunofluorescence method that allows simultaneous visualization of progeny virions and each viral genome segment at single-molecule resolution, directly showing that only a small fraction of newly formed virus particles contains a full set of genome segments. We further show at a single-cell level that the packaging efficiency is highly heterogeneous within a cell population and provide direct evidence of the occasional incorporation of antigenomic-sense segments into virus particles. Finally, we report major differences between genome packaging efficiencies in mammalian and insect cells. Thus, the results of this study are in line with our previous suggestion that genome packaging of bunyaviruses is driven by a non-selective process and highlight host cell differences in bunyavirus life cycles.

Results

Viral RNA:infectivity ratios differ in mammalian and insect hosts

To study viral replication and the generation of infectious virus progeny in mammalian and insect cells, we infected Vero E6 (monkey), C6/36 (*Aedes albopictus*) and KC (*Culicoides sonorensis*) cells with RVFV or SBV, quantified in time intracellular and extracellular viral genome segments by RT-qPCR and determined the virus titer in the supernatant by endpoint titration (**Fig. 1A**). For both RVFV and SBV, the absolute genome segment copy numbers of all three segments were higher in lysates and supernatants of mammalian cells (Vero E6) compared to insect cells (C6/36 and KC) in the logarithmic viral growth phase (**Fig. 1B-E**). Remarkably, the higher genome copies in supernatants of Vero E6 cells did not always correspond proportionally with higher virus titers. For example, RVFV genome copies obtained at 48 h post-infection in Vero E6 cells were more than ten times higher than in C6/36 cells, whereas the virus titers in both host cell lines were equal (**Fig. 1F**). Another dissonance was observed with SBV at 24 h post-infection, where similar genome copies in supernatants of Vero E6 and KC cells resulted in a titer of infectious virus more than ten times higher in KC cells (**Fig. 1G**). After relating viral RNA copy numbers with virus titers of the supernatants in time, here referred to as vRNA:infectivity ratios, it became clear that for the generation of RVFV and SBV infectious units, fewer genome equivalents are needed in insect cells (**Fig. 1H, I**), suggesting that bunyavirus genome packaging efficiencies differ between hosts.

In addition to the *in vitro* comparison between hosts, to gain insight into vRNA:infectivity ratios *in vivo*, we analyzed plasma samples of lambs experimentally infected with RVFV within the scope of another study[28] (**Fig. 1J-L**). Briefly, lambs were inoculated via intravenous route with RVFV, followed by daily collection of plasma samples. In these plasma samples, vRNA:infectivity ratios increased over time, with the lowest ratio observed at 2 days post-infection (**Fig. 1M**), coinciding with peak viremia and the onset of symptoms[28], demonstrating that genome packaging efficiencies within a host may differ in time.

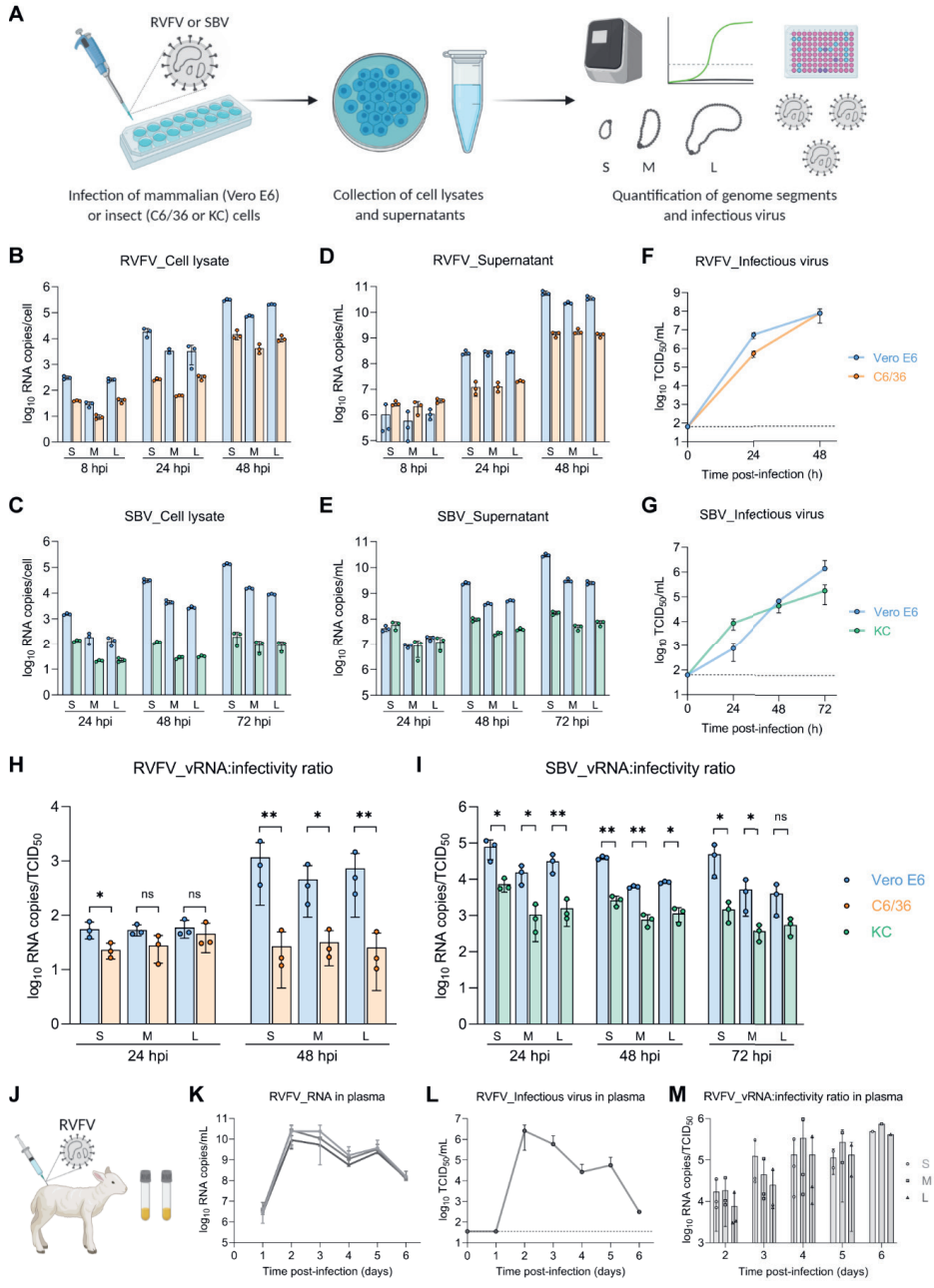

Figure 1. Viral RNA:infectivity ratios in mammalian and insect hosts. A Schematic representation of the *in vitro* experimental setup. Mammalian (Vero E6) and insect (C6/36 and KC) cells were infected with RVFV or SBV (MOI 0.01). Cell lysates and supernatants were collected at defined time points. Viral RNA was quantified with genome segment-specific RT-qPCRs and virus titers were determined by endpoint titration. **B-E** *In vitro* replication kinetics of RVFV and SBV. Bars show means with SD. Dots represent

biological replicates ($n = 3$ samples). Bar of RVFV cell lysate M segment at 24 h post-infection shows mean of two samples. **F, G** RVFV and SBV infectious titers in cell culture supernatants. Titers correspond to the same supernatant samples analyzed in **D, E**. Graphs show means with SD of $n = 3$ biological replicates. The dashed line indicates the limit of detection ($10^{1.80}$ $TCID_{50}$/mL). **H, I** RVFV and SBV vRNA:infectivity ratios calculated as viral genome copies per infectious unit in cell culture supernatants. Bars show means with SD. Dots represent individual ratios ($n = 3$). **J** Schematic representation of the animal samples from another study obtained for analysis. Lambs were experimentally infected via intravenous route with RVFV and plasma samples were collected daily[28]. **K** *In vivo* replication kinetics of RVFV. Graph shows means with SD of plasma samples ($n = 3$) analyzed by RT-qPCR. **L** RVFV infectious titers in plasma as determined with a virus isolation assay[28]. Graph shows means with SD of plasma samples ($n = 3$). The dashed line indicates the limit of detection ($10^{1.55}$ $TCID_{50}$/mL). **M** RVFV *in vivo* vRNA:infectivity ratios calculated as viral genome copies per infectious unit in plasma. Bars show means with SD. Dots represent individual ratios ($n = 3$). At early (1 day) and late (5–6 days) times post-infection, genome copies and infectious titers of some samples were below the limits of detection. In those cases, the reported values represent the mean of two samples or a single sample. Statistical analysis of vRNA:infectivity ratios was performed using an unpaired two-tailed Student's *t* test with Welch's correction (not assuming equal variances). $*p < 0.05$; $**p < 0.01$; ns, not significant ($p \geq 0.05$).

Visualization of newly formed progeny virions at single-particle resolution

To investigate the release kinetics of progeny virions from infected cells, we developed an immunofluorescence assay using antibodies targeting the surface glycoproteins of RVFV (Gn) and SBV (Gc). We infected Vero E6 cells, fixed the cells at defined time points and tracked the appearance of virus particles over time (**Fig. 2A**). For both RVFV and SBV, detection of the glycoproteins became evident around 5 ± 1 h post-infection. In the case of RVFV, the Gn glycoprotein signal started to accumulate in a perinuclear region (**Fig. 2B**, first panel), consistent with the Golgi apparatus being the site of virion assembly[29]. No accumulation of Gc in perinuclear regions was noticed in SBV-infected cells (**Fig. 2C**). Interestingly, around 7 ± 1 h post-infection with RVFV, localized clusters of symmetric spots, most likely portraying groups of virus particles trafficking simultaneously from the assembly site to the extracellular space in vesicles, were detected (**Fig. 2B**, second panel). As the infection progressed, a higher number of virus particles (hundreds to a few thousands) both inside and outside infected cells were detected (**Fig. 2B-E** and **Supplementary Movies 1, 2**). Of note, within an infected cell population, several cells showed lower glycoprotein levels and numbers of progeny virions despite being fixed at the same time point, probably representing the intrinsic variability in infection kinetics between cells. A plot of fluorescence intensities of individual spots shows a unimodal intensity distribution characteristic of single particles (**Fig. 2F**). Likewise, a histogram of the area of the spots also shows a unimodal distribution, denoting reproducible measurements of single spots within and between images (**Fig. 2G**). Importantly, the single-particle detection of newly formed progeny virions not only

allowed us to investigate the kinetics of virion release but also enabled us to determine the genomic composition of individual progeny virions.

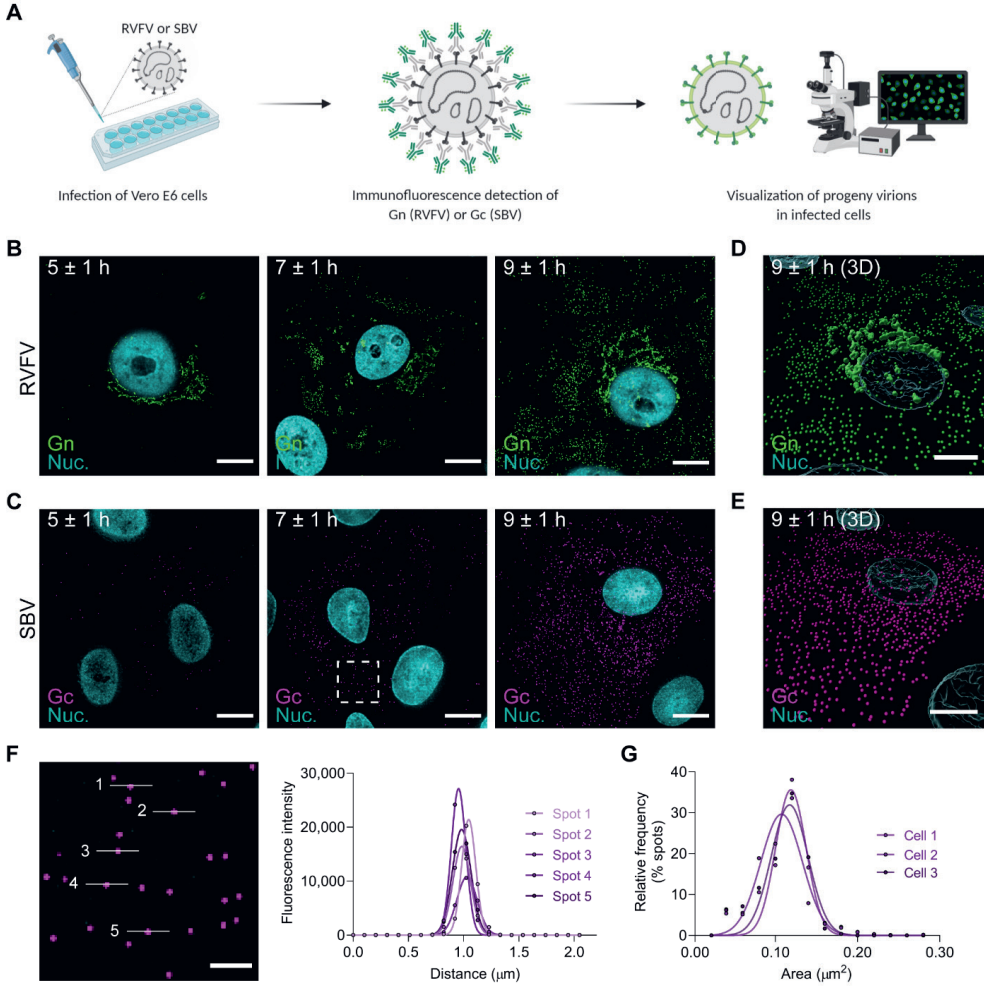

Figure 2. Immunofluorescence detection of newly formed bunyavirus progeny virions at single-particle resolution. A Schematic representation of the experimental setup. Vero E6 cells were infected with RVFV (MOI 1) or SBV (MOI 0.33) and cells were fixed at defined time points. Progeny virions were detected by immunofluorescence. Release kinetics of RVFV particles (green) (**B**) and SBV particles (magenta) (**C**). RVFV virions were detected with antibody 4-D4[48] targeting the Gn glycoprotein in combination with Alexa Fluor 488-conjugated secondary antibodies. SBV virions were detected with serum from an immunized rabbit[52] targeting the Gc glycoprotein in combination with FITC-conjugated secondary antibodies. Cell nuclei (cyan) were visualized with DAPI. RVFV Gn accumulates in a perinuclear region, the site of virion assembly. **D, E** Three-dimensional representations showing the spatial distribution of virions at the 9 ± 1 h time point created with Imaris using the Surfaces and Spots modes. **F** Magnification of a region of interest

(indicated as a dashed box in the second panel of **C**) and fluorescence intensity plot of the indicated spots. Dots represent data points and lines show Gaussian curves fitting the data. The unimodal distribution of fluorescence intensities along the lines crossing the spots is characteristic of single particles. **G** Histogram of the area of the spots detected in images of SBV-infected cells ($n = 3$ cells; more than 500 spots per image). Dots represent data points and lines show Gaussian curves fitting the data. The unimodal distribution denotes reproducible measurements of single spots within and between images. Images are merged maximum intensity projections of two channels. Scale bars, 10 μm (**B-E**), 2 μm (**F**).

Genome composition of newly formed virus particles

To investigate the genome content of newly formed RVFV and SBV virions in infected cells, we developed a 5-channel based combined RNA FISH-immunofluorescence method that allows the simultaneous visualization of virus particles and each viral genome segment at single-molecule resolution (**Fig. 3A**). Virions were detected as described in **Fig. 2** and specific FISH probe sets were designed to recognize the S, M and L viral RNAs (**Supplementary Figs. 1, 2** and **Supplementary Data 1**). The method enables the concomitant assessment of viral replication by quantification of the vRNPs in the cytoplasm (**Fig. 3D** and **Supplementary Fig. 3**), as well as the determination of the genome content of newly formed virus particles through co-localization analysis between the virions and the vRNPs (**Fig. 3B, C, E, F**, **Supplementary Figs. 3, 4** and **Supplementary Movies 3, 4**). Importantly, our assay facilitates linking the genomic content of the virions with the cytoplasmic vRNP content of the originative cell.

We used the assay to analyze individual RVFV- and SBV-infected cells fixed at 8 h post-infection, a stage in the infection cycle at which release of mature virions is clearly evident (**Fig. 3B, C, E, F** and **Supplementary Figs. 3, 4**) and virus genome replication has not proceeded long enough to impede the quantification of vRNPs in the cytoplasm due to an overcrowded signal detection (**Fig. 3D** and **Supplementary Fig. 3**). Following analysis, most RVFV and SBV particles were found to be empty, accounting on average for ~55% and 35% of total virions, respectively. In addition, the fraction of particles containing one segment was between ~30–35%, and the fraction containing two segments between about 10 and 20%. The fraction of particles containing a complete genomic set was below 10% (**Fig. 4C**). Remarkably, we observed great variability in packaging efficiencies within RVFV- and SBV-infected cell populations. Within both cell populations, a subpopulation of cells showed a striking inefficient packaging process, in some cases seemingly without generating a single infectious particle, whereas other cell subpopulations generated two or more times higher percentages of particles containing a complete genomic set than the average (**Fig. 4C**). Although the genome packaging process for both viruses is overall inefficient, packaging of SBV genome segments does occur more efficiently than for RVFV.

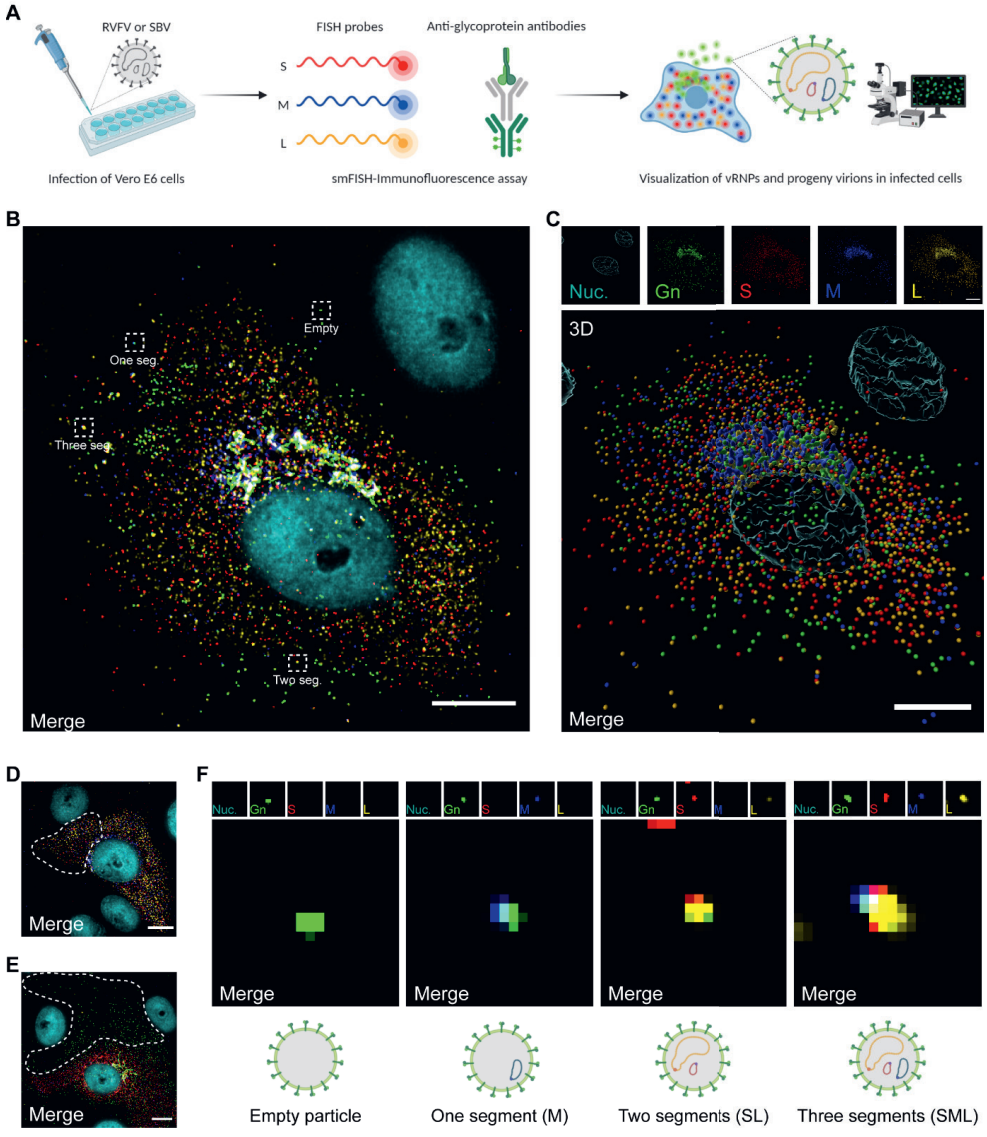

Figure 3. Single-molecule vRNA FISH-immunofluorescence of bunyavirus infected mammalian cells. **A** Schematic representation of the experimental setup. Vero E6 cells were infected with RVFV (MOI 0.50-0.75) or SBV (MOI 0.33) and cells were fixed at 8 h post-infection. The S segment (N gene; red), M segment (polyprotein gene; blue) and L segment (RdRp gene; yellow) were hybridized using probe sets labeled with CAL Fluor Red 610, Quasar 670 and Quasar 570, respectively. Progeny RVFV particles (green) were detected with antibody 4-D4[48] targeting the Gn glycoprotein in combination with Alexa Fluor 488-conjugated secondary antibodies. Progeny SBV particles (**Supplementary Figs. 3B, 4**) were detected with serum from an immunized rabbit[52] targeting the Gc glycoprotein in combination with FITC-conjugated secondary antibodies. Cell nuclei (cyan) were visualized with DAPI. Individual spots, each representing either a single vRNP or a virus particle were detected, counted and assessed for co-localization

in ImageJ with the plugin ComDet. **B** Visualization of vRNPs and progeny virions of a RVFV-infected cell. The dashed boxes highlight individual virus particles subjected to co-localization analysis for example purposes. The number of RVFV genome segments in each highlighted particle is indicated. **C** Three-dimensional representation showing the spatial distribution of vRNPs and virions of the image displayed in **B** created with Imaris using the Surfaces and Spots modes. Accumulation of vRNPs and co-localization to the same perinuclear region as Gn show active vRNP recruitment to the site of virion assembly. Co-localization of vRNPs and virions is depicted by merged spheres. **D, E** RVFV-infected cells. The dashed contours represent example regions of interest selected for the quantification of cytoplasmic vRNPs (**D**) and determining the genome composition of extracellular virions through co-localization analysis (**E**) (**Supplementary Fig. 3A**). Example regions of interest selected for the analysis of SBV-infected cells are shown in **Supplementary Fig. 3B**. **F** Magnification of regions of interest indicated by dashed boxes in **B**. The genome composition of each virion can be deduced from the spots detected on each individual channel. Images are merged maximum intensity projections of four (**D**) or five (**B, C, E, F**) channels. Due to a higher fluorescence intensity of the green channel compared to the other channels, spots co-localizing with the glycoprotein may sometimes appear masked and not entirely evident in merged images. Scale bars, 10 µm.

Intracellular vRNP content correlates with genome packaging efficiency

Seeking for an explanation to the high variability in genome packaging efficiency within cell populations, we looked into the vRNP content in the cytoplasm of the individual cells. Quantification of RVFV vRNPs in infected mammalian cells not only exposed a highly heterogenous cell-to-cell composition, but also an overall imbalanced content leaning towards higher abundances of the S (42%) and L (34%) segments compared to the M segment (24%). Quantification of SBV vRNPs in infected mammalian cells demonstrated that the overall vRNP content of the cytoplasm approached a theoretical balance, with abundances near the 33% for all three genome segments. Although the cytoplasm of some SBV-infected cells deviated from the average composition, the cell-to-cell heterogeneity in this population was less pronounced (**Fig. 4A, B**).

Next, we evaluated whether an imbalanced cytoplasmic content could be associated with a particular genome composition of the virions. The correlation analysis made evident that indeed, if a specific genome segment is more abundant intracellularly, it will be incorporated into a virus particle more often, and vice versa. A strong positive correlation (Pearson's coefficients of at least 0.5660 and $p < 0.01$) was found for all three genome segments of RVFV and SBV (**Fig. 4D**). The association between the cytoplasmic content and the efficiency of incorporating genome segments into virions was further assessed in a more integrative manner. Based on the frequencies of all three genome segments in the cytoplasm of individual cells and the fractions of empty, incomplete and complete particles, we generated a system to score the balance of the intracellular contents as well as the efficiency of genome packaging, normalizing the scores using

the extreme values present in our data set as reference (**Fig. 4E**). Surprisingly, our analysis revealed that a considerable number of cells with balanced intracellular genome contents exhibited an overall inefficient packaging. This indicates that, although the three different vRNPs will most likely be incorporated into particles in similar numbers if their intracellular abundance is similar, the three vRNPs are not necessarily co-packaged into the same particle. However, when we observed relatively efficient packaging, the vRNP content in the cytoplasm was balanced, implying that a balanced intracellular vRNP content is a pre-requisite for relatively efficient genome packaging. Accordingly, it also became clear that an imbalanced cytoplasmic vRNP content generally leads to inefficient genome packaging (**Fig. 4E, F**).

Differences in genome packaging efficiencies between mammalian and insect cells

Based on the different vRNA:infectivity ratios we found between mammalian and insect cells (**Fig. 1H, I**), we aimed to further evaluate potential host cell differences in genome packaging using our vRNA FISH-immunofluorescence method on RVFV-infected insect cells. Although we managed to visualize RVFV virions and vRNPs in insect cells (**Supplementary Fig. 5**), the image acquisition and analysis process at single-molecule resolution proved to be very challenging due to the elongated distribution in the *z*-axis of virion assembly sites. As an alternative, we applied our method to immobilized virions from virus stocks produced in different host cells and compared the genome composition of their virions (**Fig. 5A-F**). In general, virus stocks consist of a heterogeneous population of empty virions and virions with one, two or three genome segments (**Fig. 5E**). Interestingly, in mammalian cells (Vero E6) the S segment was packaged more often than the M and L segments, whereas in insect cells (C6/36) we observed the opposite (**Fig. 5F**). Consistent with the analysis of newly formed virions (**Fig. 4C**) and our own previous report[27], about 50% of total RVFV particles produced on Vero E6 cells were empty. On the other hand, empty particles of virus stocks produced on C6/36 cells accounted for a considerably lower fraction (~30% of total virions), indicating that despite bunyavirus genome packaging seems to be a largely stochastic process, the incorporation of genome segments into virions occurs more efficiently in insect cells than in mammalian cells. In addition, in insect cells the three different genome segments were incorporated into the same virion around three times more often than in mammalian cells (~23% vs. ~7%) (**Fig. 5E**), generating a higher percentage of complete particles and showing an overall more efficient genome packaging process.

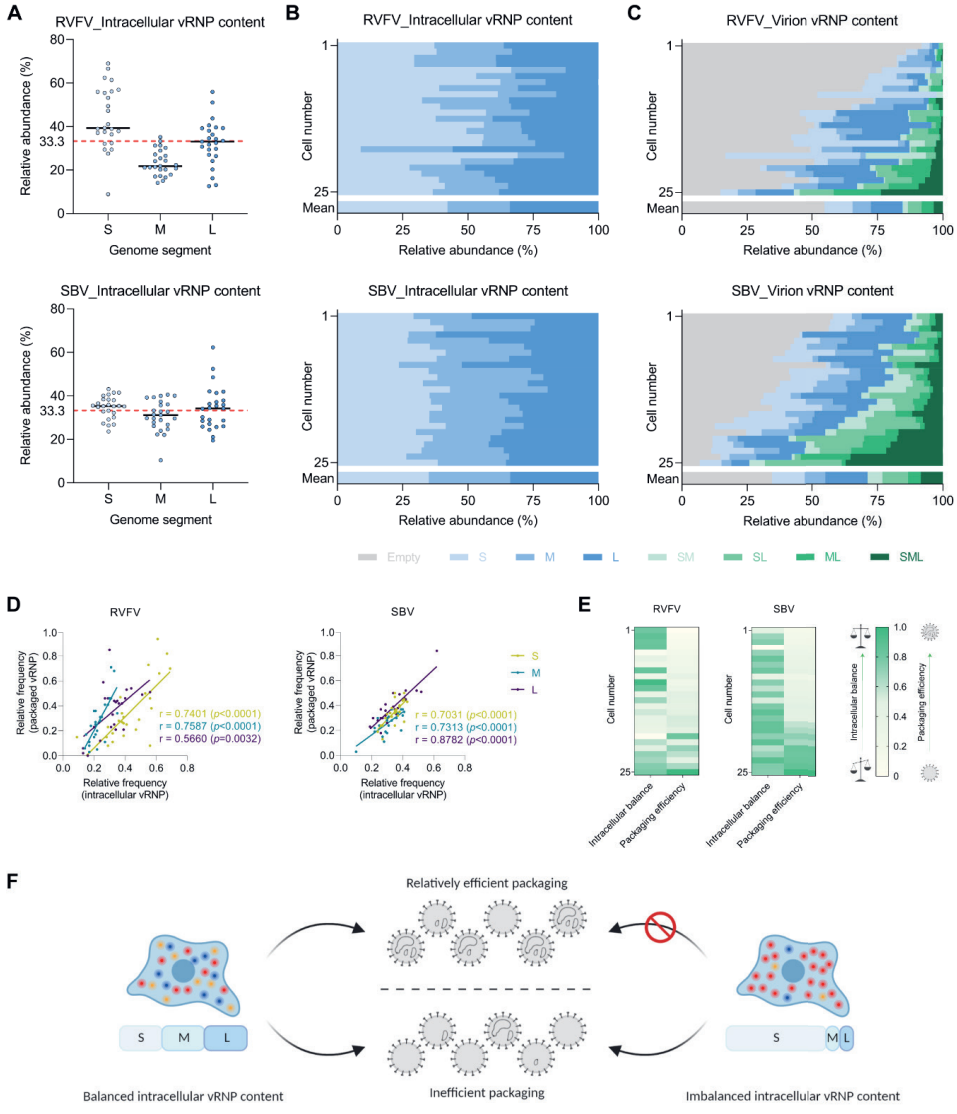

Figure 4. vRNP composition of the cytoplasm of bunyavirus infected mammalian (Vero E6) cells and their progeny virions at a single-cell level. RVFV- and SBV-infected cells were analyzed with a single-molecule vRNA FISH-immunofluorescence method as described in **Fig. 3**. **A** Quantification of RVFV and SBV S, M and L vRNPs in the cytoplasm of infected cells. Data are expressed as the relative intracellular abundance of each vRNP. The black lines represent the medians ($n = 25$ cells) and the red dotted line represents a theoretically balanced abundance of 33.33%. **B** Data shown in **A** presented per individual cell. **C** Quantification of RVFV and SBV S, M and L vRNPs in progeny virions. Data are expressed as the relative abundance of each of the eight different potential compositions of virions. Graphs **B** and **C** show the composition results of single cells ($n = 25$ cells; more than 5000 RVFV virions and more than 4500 SBV virions) and means. Cell numbers in **B** and **C** correspond. **D** Correlation analysis between the relative

intracellular frequency of a specific genome segment and the relative frequency of that genome segment being packaged. Pearson's correlation coefficients (r) and *p* values are shown for each genome segment. **E** Relationship between the intracellular content of vRNPs and the packaging efficiency of individual cells. A generic system to score the intracellular balance and the packaging efficiency was created. A frequency of 0.33 for each genome segment was considered as theoretically balanced. The balance score was calculated as the summatory of the absolute deviations from the theoretical frequency, normalized from 0 to 1, assigning the least balanced composition of the data set a score of 0. The packaging efficiency score was calculated taking into account the frequency of empty, incomplete and complete virus particles, normalized from 0 to 1, assigning the most efficient packaging value of the data set a score of 1. Scores are color coded from light green (lowest) to dark green (highest). **F** Proposed model on the efficiency of genome packaging based on the intracellular vRNP content. A balanced vRNP content in the cytoplasm seems to be a pre-requisite for relatively efficient genome packaging.

Visualization of viral complementary RNAs incorporated into newly formed progeny virions

Previous reports have found viral antigenomes, together with mRNA transcripts here referred to as viral complementary RNAs (cRNAs), in supernatants of bunyavirus infected cells or in purified virions preparations, as evidence for their incorporation into virus particles[26,30–32]. Here, we designed FISH probe sets to specifically recognize the cRNAs of RVFV and directly visualized their packaging using the vRNA FISH-immunofluorescence method (**Fig. 6A**, **Supplementary Fig. 6** and **Supplementary Data 1**). Due to a maximum capacity to properly filter light wavelengths up to five different channels, we assessed the packaging of one viral segment and the corresponding cRNA in pairs. Indeed, all three RVFV cRNAs were occasionally incorporated into virions (**Fig. 6B**). Interestingly, we again observed high cell-to-cell variability in packaging efficiency within the cell populations. Furthermore, the ratios between the frequencies of incorporation of the viral genomes and the respective cRNAs differed per segment, resulting in ratios of ~4:1, 9:1 and 14:1 for S/cS, M/cM and L/cL, respectively (**Fig. 6C**). Although the packaging of cRNAs occurs less frequently than that of viral genome segments, the direct visualization of virions containing cRNAs provides additional evidence of the absence of a selective mechanism that favors exclusively the incorporation of viral genome segments.

Discussion

The molecular mechanisms involved in the production of infectious bunyavirus progeny are yet to be discovered. Remarkably little is known about the principles that drive the genome packaging process of the multi-segmented bunyavirus genome into virions. Here, we combined smFISH and immunofluorescence assays to determine the genomic composition of RVFV and SBV virions at

single-particle resolution by simultaneous detection of individual virus particles and vRNPs (**Figs. 2, 3** and **Supplementary Figs. 3, 4**). Notably, we were able to link the intracellular abundance of specific vRNPs with the composition of progeny virions in individual infected cells and were able to show striking differences between genome packaging efficiencies in mammalian and insect cells.

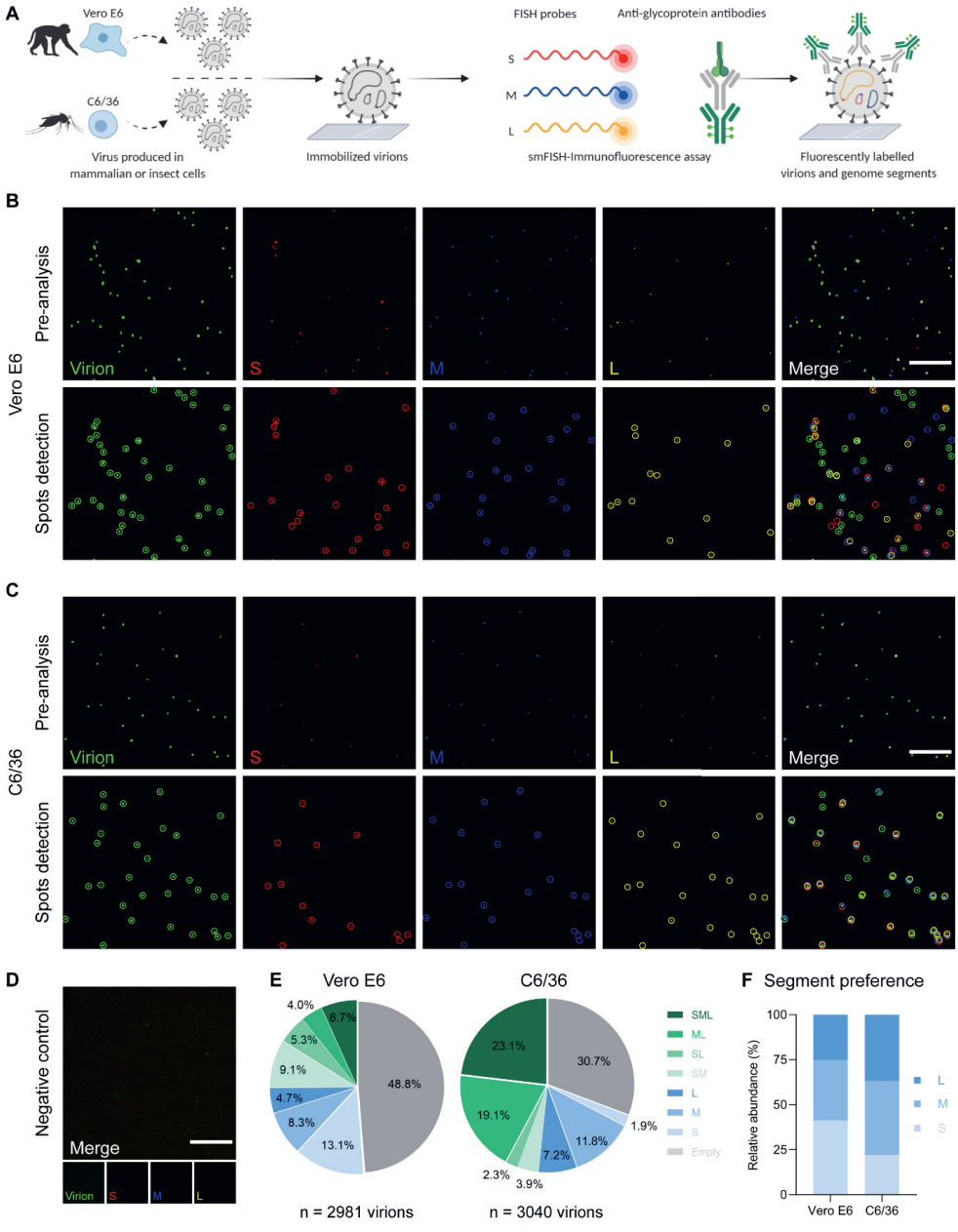

Figure 5. Genome segment composition of immobilized RVFV virions produced in mammalian and insect cells. A Schematic representation of the experimental setup. RVFV virions produced in Vero E6 cells or C6/36 cells were immobilized on coverglass by incubation for 5 h at 28 °C. The S segment (N gene; red), M segment (NSmGn and Gc genes separately; blue) and L segment (RdRp gene; yellow) were hybridized using probe sets labeled with CAL Fluor Red 610, Quasar 670 and Quasar 570, respectively. Progeny RVFV particles (green) were detected with antibody 4-D4[48] targeting the Gn glycoprotein in combination with Alexa Fluor 488-conjugated secondary antibodies. Individual spots, each representing either a single vRNP or a virus particle were detected, counted and assessed for co-localization in ImageJ with the plugin ComDet. Visualization of RVFV virions produced in Vero E6 cells (**B**) or C6/36 cells (**C**) (top rows). Merge images show the overlay of the four individual channels. Colored circles (bottom rows) display the spots detected on each channel and their co-localization in the merge image. Due to a higher fluorescence intensity of the green channel compared to the other channels, spots co-localizing with the glycoprotein may sometimes appear masked and not entirely evident in merged images. **D** Negative control sample using cell culture media instead of a virus stock preparation. Scale bars, 5 µm. **E** Relative abundance of the eight possible genome compositions of the virions produced in Vero E6 cells (left) or C6/36 cells (right). **F** Abundance of each genome segment incorporated into a virion relative to the total genome segment packaging events.

By analyzing individual infected cells and their progeny virions, we not only observed a high cell-to-cell variability in packaging efficiency, which leads to a highly diverse composition of the progeny virion population, but also learned that the relative intracellular abundance of the vRNPs can influence, at least partially, overall genome packaging efficiencies (**Fig. 4B, C**). Our observations, obtained from single-cell analysis, are consistent with previous reports on purified virions of RVFV studied at a population level by Northern blotting, which suggested that the relative abundance of each genome segment in virions roughly approximated their relative abundances intracellularly[33,34]. Likewise, we found that a low relative intracellular abundance of a particular genome segment correlates with a low packaging frequency of that segment and vice versa. Accordingly, when the overall intracellular vRNP content was imbalanced (i.e., S:M:L ratio moved away from the theoretical 1:1:1 ratio), virions produced from that cell rarely contained the three genome segments and packaging was most likely very inefficient (**Fig. 4D**). On the other hand, a balanced intracellular vRNP content appears to serve as an essential precondition for the generation of complete particles, although it does not ensure in all cases an overall efficient genome packaging (**Fig. 4E, F**). It is worth noting that an imbalanced intracellular vRNP composition can be the consequence of multiple factors, such as differential replication kinetics between the genome segments or an initially imbalanced co-infection of the same cell by a combination of complete and incomplete particles.

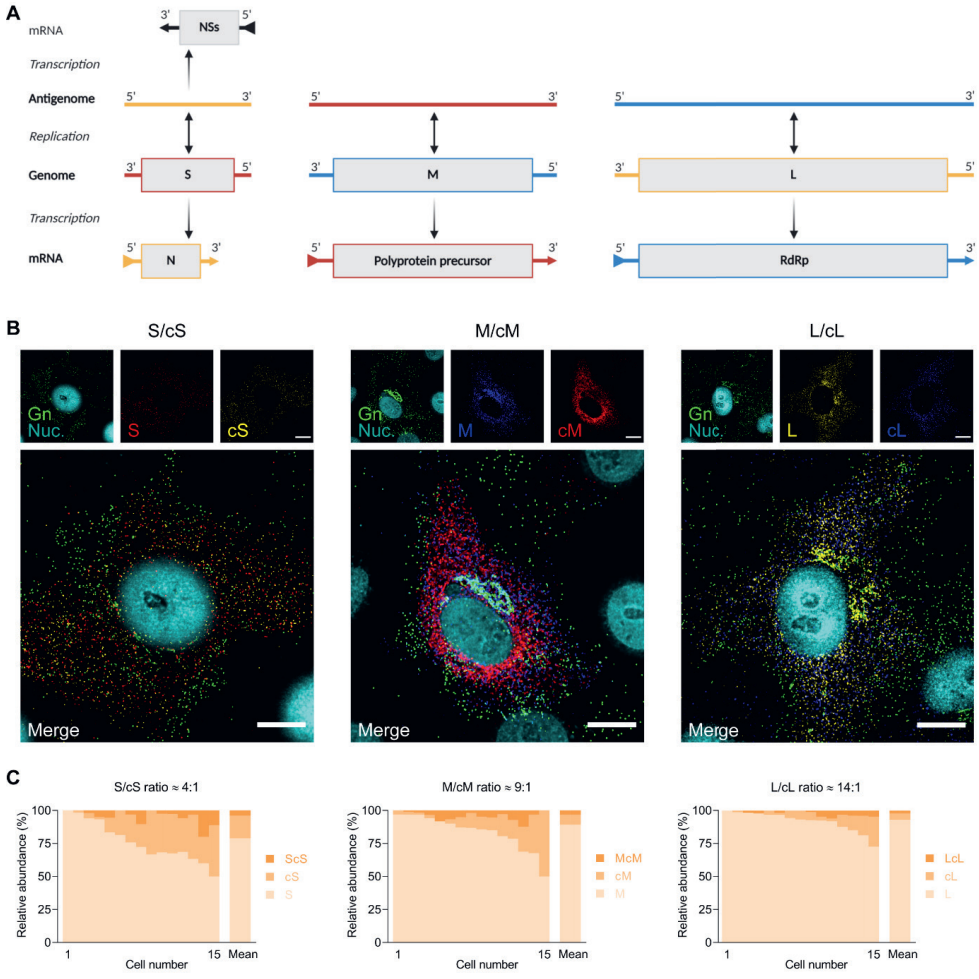

Figure 6. Single-molecule RNA FISH-immunofluorescence on vRNA-cRNA pairs of RVFV-infected mammalian cells. A Schematic representation of the replication and transcription of RVFV genome segments. Here, we refer to viral genome replication intermediates (antigenomes) and mRNA transcripts as cRNAs. RVFV S segment uses an ambisense coding strategy to generate mRNAs from both the genomic-sense and antigenomic-sense RNAs. **B** Visualization of vRNPs, cRNAs and progeny virions of RVFV-infected cells. Vero E6 cells were infected with RVFV (MOI 0.75-1.00) and cells were fixed at 8–10 h post-infection. Samples were hybridized against paired targets (i.e., S-cS segments, M-cM segments and L-cL segments). The S segment (N gene; red), M segment (polyprotein gene; blue) and L segment (RdRp gene; yellow) were hybridized using probe sets labeled with CAL Fluor Red 610, Quasar 670 and Quasar 570, respectively. The cS segment (N gene; yellow), cM segment (polyprotein gene; red) and cL segment (RdRp gene; blue) were hybridized using probe sets labeled with Quasar 570, CAL Fluor Red 610 and Quasar 670, respectively. Progeny RVFV particles (green) were detected with antibody 4-D4[48] targeting the Gn glycoprotein in combination with Alexa Fluor 488-conjugated secondary antibodies. Cell nuclei (cyan) were visualized with DAPI. Individual spots, each representing either a vRNP, a cRNA or a virus particle were detected, counted and assessed for co-localization in ImageJ with the plugin ComDet. Main

images are merged maximum intensity projections of four channels (individual channels shown on top). Due to a higher fluorescence intensity of the green channel compared to the other channels, spots co-localizing with the glycoprotein may sometimes appear masked and not entirely evident in merged images. Scale bars, 10 µm. **C** Quantification of the S, M, L vRNPs and their corresponding cRNAs in RVFV progeny virions. Genome compositions of the virions are expressed as their abundance relative to the amount of virions in which at least one vRNP or cRNA was detected. Graphs show the composition results of virions released by single cells (n = 15 cells per combination; more than 3900 virions per combination) and means. vRNA/cRNA ratios are indicated. cS complementary S segment, cM complementary M segment, cL complementary L segment.

Contrary to other segmented RNA viruses like influenza virus and rotavirus, in which specific RNA-RNA interactions facilitate co-packaging of all the different viral genome segments[20,35,36], a growing body of evidence supports the notion that bunyavirus genome packaging is rather flexible and non-selective[21]. Here, we show that less than 10% of RVFV and SBV progeny virions produced in mammalian cells contain the three genome segments, meaning that only a minor fraction of produced virus particles are infectious on their own (**Fig. 4C**). These results are in line with our previous report[27], which suggested that bunyavirus genome packaging occurs without a specific mechanism that guarantees a consistent incorporation of all three genome segments into the same particle. In addition, we showed that the incorporation of S, M and L cRNAs into virions does occur, but not frequently. Importantly, packaging of cRNAs occurs disregarding whether the corresponding vRNA segment has or not an ambisense coding strategy (**Fig. 6B, C**). Although we observed similar non-selective features regarding genome packaging of tri-segmented bunyaviruses that belong to two different families, the low particle-to-PFU ratios previously reported for BUNV[22] and Crimean-Congo Hemorrhagic fever virus[37] (family *Nairoviridae*, genus *Orthonairovirus*) imply that other bunyavirus species may have evolved towards a more efficient packaging process, but this remains to be studied.

Phleboviruses and orthobunyaviruses sustain a life cycle characterized by alternating productive infections between vertebrates and arthropod vectors[4], underscoring the importance of studying the virus biology in both hosts. In an experimental infection study in goats, the source of the virus was found to cause differences in the course of infection. Insect cell-derived RVFV appeared to be more infectious than mammalian cell-derived RVFV based on faster peak viremia, infection of peripheral blood mononuclear cells, induction of fever and cytokine levels[38]. From our *in vitro* virus replication experiments, we noticed that insect cells required fewer genome equivalents per infectious unit compared to mammalian cells (**Fig. 1H, I**). Furthermore, we found that in RVFV progeny derived from insect cells, the relative amount of particles containing a full set of genome

segments were about three times more compared to mature RVFV virions produced in mammalian cells (**Fig. 5E**). These observations strongly suggest that genome packaging occurs more efficiently in insect cells, which possibly contributes to maintain high viral loads during replication in the arthropod vector to enable efficient transmission to vertebrates. The reasons behind the more efficient genome packaging in insect cells are yet unknown, but could be related to the evolutionary origin of the viruses, which has been suggested to be of arthropod-specific ancestors[39].

In addition to host differences, the fact that the vRNA:infectivity ratio in plasma samples from experimentally infected lambs increased over time indicates that genome packaging efficiency may vary within a single host over the course of infection (**Fig. 1M**). To better evaluate changes in packaging efficiency over time, analysis of the vRNP content of virions present in plasma would be very informative. However, immobilizing virions from the plasma matrix has proven to be technically very challenging. Alternatively, single-cell analysis of vRNP packaging efficiencies at time points later than those evaluated in the present study could provide relevant information. Unfortunately, at a later stage of infection, such analysis is hampered by the increased intracellular vRNP density, which results in accumulated signal throughout the cytoplasm leading to loss of single-molecule resolution.

Interestingly, the bunyavirus genome packaging process investigated here gives rise to a large fraction of incomplete virus particles lacking one or two genome segments (**Figs. 4C, 5E**). Recently, a study with an influenza virus strictly dependent on genome complementation by co-infection demonstrated that incomplete influenza virus particles contributed to localized within-host spread[40]. This raises the intriguing question of whether co-infection by complementing incomplete particles may compensate for the inefficiency observed in bunyavirus genome packaging. In this hypothetical scenario, where complete particles are dispensable for a productive infection, bunyaviruses may resemble the life cycle of multipartite viruses, which establish a productive infection by independent transmission of a complementary ensemble of particles each containing a single genome segment[41,42].

Besides the potential role that incomplete particles may play in dissemination of bunyaviruses, additional strategies that would increase the flexibility also seem plausible as ways to overcome the bottleneck of an overall inefficient genome packaging process. Incorporating more than three genome segments per particle increases the probability of packaging at least one copy of S, M and L segments. Cryo-electron microscopy analyses of RVFV particles[43,44] suggest that

additional genome segments would fit within the intra-virion space. Another potential strategy involves the transmission of a large number of virions in structures known as collective infectious units, which result in a locally increased multiplicity of infection (MOI)[45]. It should also be noted, that a flexible packaging process may actually be best suited for the changing environments faced by the virus during its life cycle between vertebrates and arthropods. Finally, flexible packaging capabilities in terms of non-selectivity towards specific RNA sequences also facilitate the occurrence of reassortment events with related viruses, which increases genetic diversity and favors virus evolution.

In summary, here we studied genome replication and packaging of prototype bunyaviruses in mammalian and insect cells, both at a single-particle and single-cell level, as well as at a virion population and cell population level. Taken together, the evidence presented in this report further demonstrates that packaging of bunyavirus genome segments is a flexible, non-selective process and that genome packaging is more efficient in insect cells compared to mammalian cells.

Methods

Cell lines

Vero E6 cells (ATCC CRL-1586) were maintained in minimum essential medium (MEM) supplemented with 5% fetal bovine serum (FBS), 1% antibiotic/antimycotic, 1% MEM non-essential amino acids (MEM NEAA) and 2 mM L-glutamine at 37 °C and 5% CO_2. C6/36 cells (ATCC CRL-1660) were maintained in L-15 medium (Leibovitz) (Sigma-Aldrich) supplemented with 10% FBS, 1% antibiotic/antimycotic, 1% MEM NEAA and 2% tryptose phosphate broth at 28 °C. KC cells were maintained in Schneider's *Drosophila* medium supplemented with 10% FBS and 1% antibiotic/antimycotic at 28 °C. Cell culture media and supplements were purchased from Gibco, unless specified otherwise.

Viruses

Virus stocks of RVFV strain Clone 13[46] were obtained after infection of Vero E6 or C6/36 cells at a MOI of 0.005. Virus stocks of SBV isolate NL-F6[47] were obtained after infection of Vero E6 cells at a MOI of 0.01.

Genome segment-specific quantitative RT-PCR

Mammalian cells (Vero E6) or insect cells (C6/36 for RVFV and KC for SBV) were seeded in 6-well cell culture plates at 2×10^5 cells/well or 6×10^5 cells/well, respectively, and allowed to attach for 2–4 h. Cells were subsequently infected at a MOI of 0.01 and after incubation for 3.5 h, the inoculum was removed and substituted with fresh medium. At defined time points (varied per experiment), samples from the culture

supernatant and cells were collected. In addition to the *in vitro* experiments, plasma samples were obtained from another study (lambs #158, #160 and #162) in which lambs were experimentally infected via intravenous route with a 10^5 tissue culture infectious dose $(TCID)_{50}$ dose of RVFV strain 35/74[48].

From 1–2 mL of cell lysate, 200 µL of culture supernatant or 200 µL of plasma, total nucleic acid extractions were performed with the NucliSENS easyMAG system (bioMérieux) according to the manufacturer's instructions. Subsequently, viral cDNA was synthesized with the SuperScript IV First-Strand Synthesis System for RT-PCR (Invitrogen) using a combination of S, M and L segment-specific primers (**Supplementary Table 1**), according to the manufacturer's instructions. After the reverse transcription reaction, quantitative PCR amplifications were performed with the Power SYBR Green PCR Master Mix using 5 µL of 20- or 200-fold diluted cDNA preparations in a total volume of 25 µL, in combination with a 7500 Fast Real-Time PCR System (Applied Biosystems). Fragments from each segment were amplified using specific primers (**Supplementary Table 2**) under the following conditions: an initial denaturation step at 95 °C for 10 min; 40 cycles of denaturation at 95 °C for 15 s, annealing at 59 °C for 30 s and extension at 72 °C for 36 s; and a single cycle of denaturation at 95 °C for 15 s, annealing at 60 °C for 1 min, denaturation at 95 °C for 15 s and annealing at 60 °C for 15 s. Data were acquired and analyzed with the 7500 Fast System software version 1.5.1. (Applied Biosystems). Genome copies of each viral segment were finally calculated by intrapolation of the respective standard curve prepared with tenfold serial dilutions of the viral segment cloned in pUC57 plasmids starting at 0.1 ng/µL.

Virus titration

Infectious virus titers of samples from the *in vitro* replication experiments were determined with an immunoperoxidase monolayer assay. Vero E6 cells (2×10^4 cells/well) were incubated with tenfold serial dilutions (starting at 1:10) of cell culture supernatants for 72 h at 37 °C and 5% CO_2. After incubation, cells were fixed with 4% paraformaldehyde for 15 min, washed with PBS supplemented with 0.5% Tween 80 (PBST), and permeabilized with 1% Triton X-100 in PBS for 5 min. Next, samples were blocked with 100 µL/well of 5% horse serum in PBS and subsequently incubated in sequential steps with 100 µL/well of primary and secondary antibodies. Hybridoma 4-D4[48] supernatant (1:40 dilution) and serum from an experimentally infected sheep (1:1000 dilution), were used as primary antibodies against RVFV and SBV, respectively. As secondary antibodies, HRP-conjugated rabbit polyclonal anti-mouse immunoglobulins (1:500 dilution, Dako) and HRP-conjugated rabbit polyclonal anti-sheep IgG (1:500 dilution, ab6747 Abcam) were used. Incubations with the blocking solution, primary and secondary antibodies were each for 1 h at 37 °C. Plates were washed with PBST between the addition of primary and secondary antibodies. For staining, 100 µL/well of a 0.2 mg/mL amino ethyl carbazole solution in 500 mM acetate buffer pH 5.0, 88 mM H_2O_2 was added as substrate. Samples were analyzed in triplicate and the titer calculated as the median tissue culture infectious dose ($TCID_{50}$/mL) using the Spearman–Kärber method. Virus titers of plasma samples were determined with a virus isolation assay as reported[28].

Single-molecule RNA FISH-immunofluorescence

Experiments were performed with slight modifications to the Stellaris protocol for simultaneous FISH-immunofluorescence in adherent cells (Biosearch Technologies)[49–51]. Vero E6 cells (1.5×10^4 cells/well) or C6/36 cells (4.5×10^4 cells/well) were seeded on CultureWell 16 removable chambered coverglass (Grace Bio-Labs). Following overnight incubation at 37 °C and 5% CO_2 (Vero E6) or 28 °C (C6/36), cells were infected with RVFV or SBV at MOIs of 0.33–1.00. One hour post-infection, the medium was refreshed. At defined time points (varied per experiment), cells were fixed and permeabilized with a 3:1 mixture of methanol (Merck)—glacial acetic acid (Merck) for 10 min. Cells were subsequently washed twice with PBS and once with pre-hybridization buffer (10% deionized formamide [Millipore] in 2× concentrated SSC [Gibco]) for 5 min. Cells were then incubated for 12–16 h at 37 °C with 100 µL/well of virus-specific FISH probe sets (**Supplementary Data 1**) and primary antibodies in hybridization buffer (10% deionized formamide, 10% dextran sulfate [Sigma-Aldrich], 2 mM vanadyl ribonucleoside complexes [VRC, Sigma-Aldrich] in 2× SSC). Custom probe sets were designed using the RNA FISH Probe Designer tool (https://www.biosearchtech.com/support/tools/design-software/stellaris-probe-designer) and purchased from Biosearch Technologies (Petaluma, California and Risskov, Denmark). FISH probes were added at a final concentration of 250 nM for RVFV and 125 nM for SBV. Hybridoma 4-D4[48] supernatant (1:160 dilution) and serum from an immunized rabbit[52] (1:4000 dilution), were used as primary antibodies against RVFV and SBV, respectively. Following hybridization and incubation with primary antibodies, cells were extensively washed at 37 °C (twice with pre-hybridization buffer for 30 min and twice with 2× SSC for 15 min). Subsequently, cells were incubated with 100 µL/well of secondary antibodies for 1 h at 37 °C. A goat polyclonal anti-mouse IgG labeled with Alexa Fluor 488 (1:1000 dilution, A-11001 Invitrogen) or a goat polyclonal anti-rabbit IgG labeled with FITC (1:400 dilution, sc-2012 Santa Cruz Biotechnology) were used as secondary antibodies. Next, cells were washed twice with 2× SSC, and nuclei were stained by incubation with 100 µL/well of 1 µg/mL DAPI in 2× SSC for 5 min. Finally, cells were washed with 2× SSC and submerged in VectaShield antifade mounting medium H-1000 (Vector Laboratories). For analysis of virus stocks, 100 µL/well of virus stocks diluted 1:3 were added on CultureWell 16 removable chambered coverglass and virions were allowed to attach to the surface for 5 h at 28 °C. From the fixation step onwards, the same procedure as described for adherent cells was followed. The specificity of the FISH probes and antibodies was confirmed with single-color controls (**Supplementary Figs. 1, 2, 6**). Mock-infected samples and samples without primary antibodies were used as negative controls.

Image acquisition and analysis

Z-stacked images of infected cells and immobilized virions, with a fixed interval of 0.28–0.31 µm between slices, were acquired with an inverted widefield fluorescence microscope Axio Observer 7 (ZEISS, Germany) using appropriate filters and a 1.3 NA 100x EC Plan-NEOFLUAR oil objective in combination with an AxioCam MRm CCD camera. Exposure times were defined empirically and differed depending on the cell line, probe sets and fluorescent dyes. Raw images were deconvolved in standard mode using Huygens Professional version 19.10 (Scientific Volume Imaging B.V., The Netherlands). If required, raw images were Z-aligned in

ZEN 2.6 Pro (ZEISS, Germany) before deconvolution. For analysis, 3D data were converted to maximum intensity projections using Z-project within ImageJ[53]. Detection, quantification and co-localization analyses of individual spots, each representing a single virion, vRNP or cRNA, were performed in ImageJ in combination with the plugin ComDet version 0.5.0 (https://github.com/ekatrukha/ComDet). Spot detection thresholds for each channel were set empirically by individual examination of images. The threshold to define co-localized spots was set to a maximum distance of 3–4 pixels between the centers of the spots. Intracellular genome composition analysis considered a region of the cytoplasm representative of the overall composition, not including the Golgi apparatus where signal is generally overcrowded due to vRNP accumulation (**Fig. 3D** and **Supplementary Fig. 3**). Genome composition analysis of progeny virions only considered virus particles in selected regions of interest located distant from the nucleus of the infected cell (**Fig. 3E** and **Supplementary Fig. 3**). For visualization purposes, image brightness and contrast were manually adjusted in ImageJ. Finally, Imaris 9.5 software (Bitplane, Switzerland) was utilized to create optimal 3D representations of the data using the Surface and Spots modes.

Statistics and reproducibility

Prism 8 (GraphPad Software) was used to generate graphs and perform statistical analysis. Sample size varied per experiment and is indicated in each figure legend. Mean vRNA:infectivity ratios were compared using an unpaired two-tailed Student's *t* test with Welch's correction (not assuming equal variances). The correlation between the intracellular vRNP relative frequency and packaged vRNP relative frequency was calculated with the Pearson's correlation coefficient (r). p values ≥ 0.05 were considered not significant.

Ethics statement

The animal experiment within the scope of another study[28] from which plasma samples were obtained for analysis was conducted in accordance with European regulations (EU directive 2010/63/EU) and the Dutch Law on Animal Experiments (Wod, ID number BWBR0003081). Permissions were granted by the Dutch Central Authority for Scientific Procedures on Animals (Permit Number: AVD4010020185564). Specific procedures were approved by the Animal Ethics Committees of Wageningen Research.

Reporting summary

Further information on research design is available in the Nature Research Reporting Summary linked to this article.

Data availability

The authors declare that the data supporting the findings of this study are available within the paper and its supplementary information files. Source data underlying **Figs. 1B-I, 1K-M, 2F, 2G, 4A-E, 5E, 5F, 6C** are provided in the **Supplementary Data 2** file. Any remaining data are available from the corresponding author upon reasonable request.

Acknowledgements

EBM is a grateful recipient of scholarships from the Graduate School for Production Ecology & Resource Conservation (PE&RC) and Universidad de Costa Rica (OAICE-031-2019). We thank Corinne Geertsema (Laboratory of Virology, Wageningen University) for kindly providing the KC cells, Michèle Bouloy (Institut Pasteur, France) for kindly providing the RVFV strain Clone 13, Eduardo de Freitas Costa and Jose L. Gonzalez (Department of Epidemiology, Bioinformatics and Animal Studies, Wageningen Bioveterinary Research) for advice on statistics, Hélène Cecilia (UMR 1300 BIOEPAR, INRAE/Oniris) and Quirine ten Bosch (Quantitative Veterinary Epidemiology, Wageningen University) for stimulating discussions, and Richard Kormelink (Laboratory of Virology, Wageningen University) for critically reviewing the manuscript and providing feedback. Illustrations in **Figs. 1A, 1J, 2A, 3A, 3F, 4F, 5A, 6A** were created with BioRender.com.

Author contributions

PJWS and JK conceived the project. CMS contributed developing the 5-channel FISH-immunofluorescence method. EBM and PJWS designed the experiments. EBM performed the RT-qPCR, virus titration and FISH-immunofluorescence experiments. EAK developed and customized the plugin ComDet for image analysis. EBM and PJWS analyzed and interpreted the data with the contributions of JK and EAK. PJWS and JK supervised the project. EBM and PJWS wrote the manuscript, prepared the figures and movies with the contributions of JK.

Competing interests

The authors declare no competing interests.

References

1. Walter CT, Barr JN. Recent advances in the molecular and cellular biology of bunyaviruses. *Journal of General Virology* **2011**, *92* (11), 2467–2484. https://doi.org/10.1099/vir.0.035105-0.
2. Hughes HR, Adkins S, Alkhovskiy S, Beer M, Blair C, Calisher CH, Drebot M, Lambert AJ, de Souza WM, Marklewitz M, Nunes MRT, Shí (石晓宏) X, *et al.* ICTV Virus Taxonomy Profile: *Peribunyaviridae*. *Journal of General Virology*, **2020**, *101* (1), 1–2. https://doi.org/10.1099/jgv.0.001365.
3. Abudurexiti A, Adkins S, Alioto D, Alkhovsky SV, Avšič-Županc T, Ballinger MJ, Bente DA, Beer M, Bergeron É, Blair CD, Briese T, Buchmeier MJ, *et al.* Taxonomy of the order *Bunyavirales*: update 2019. *Archives of Virology* **2019**, *164* (7), 1949–1965. https://doi.org/10.1007/s00705-019-04253-6.
4. Horne KM, Vanlandingham DL. Bunyavirus-vector interactions. *Viruses* **2014**, *6* (11), 4373–4397. https://doi.org/10.3390/v6114373.

5. Elliott RM, Brennan B. Emerging phleboviruses. *Current Opinion in Virology* **2014**, *5*, 50–57. https://doi.org/10.1016/j.coviro.2014.01.011.

6. Elliott RM. Orthobunyaviruses: recent genetic and structural insights. *Nature Reviews Microbiology* **2014**, *12* (10), 673–685. https://doi.org/10.1038/nrmicro3332.

7. Elliott RM. Molecular biology of the *Bunyaviridae*. *Journal of General Virology* **1990**, *71* (3), 501–522. https://doi.org/10.1099/0022-1317-71-3-501.

8. Guardado-Calvo P, Rey FA. Chapter Three - The Envelope Proteins of the *Bunyavirales*. In *Advances in Virus Research*; Kielian, M., Mettenleiter, T. C., Roossinck, M. J., Eds.; Academic Press, 2017; Vol. 98, pp 83–118. https://doi.org/10.1016/bs.aivir.2017.02.002.

9. Överby AK, Pettersson RF, Grünewald K, Huiskonen JT. Insights into bunyavirus architecture from electron cryotomography of Uukuniemi virus. *PNAS* **2008**, *105* (7), 2375–2379. https://doi.org/10.1073/pnas.0708738105.

10. Freiberg AN, Sherman MB, Morais MC, Holbrook MR, Watowich SJ. Three-Dimensional Organization of Rift Valley Fever Virus Revealed by Cryoelectron Tomography. *Journal of Virology* **2008**, *82* (21), 10341–10348. https://doi.org/10.1128/JVI.01191-08.

11. Bowden TA, Bitto D, McLees A, Yeromonahos C, Elliott RM, Huiskonen JT. Orthobunyavirus Ultrastructure and the Curious Tripodal Glycoprotein Spike. *PLOS Pathogens* **2013**, *9* (5), e1003374. https://doi.org/10.1371/journal.ppat.1003374.

12. Briese T, Calisher CH, Higgs S. Viruses of the family *Bunyaviridae*: Are all available isolates reassortants? *Virology* **2013**, *446* (1), 207–216. https://doi.org/10.1016/j.virol.2013.07.030.

13. Gerber M, Isel C, Moules V, Marquet R. Selective packaging of the influenza A genome and consequences for genetic reassortment. *Trends in Microbiology* **2014**, *22* (8), 446–455. https://doi.org/10.1016/j.tim.2014.04.001.

14. Lakdawala SS, Fodor E, Subbarao K. Moving On Out: Transport and Packaging of Influenza Viral RNA into Virions. *Annual Review of Virology* **2016**, *3* (1), 411–427. https://doi.org/10.1146/annurev-virology-110615-042345.

15. Borodavka A, Desselberger U, Patton JT. Genome packaging in multi-segmented dsRNA viruses: distinct mechanisms with similar outcomes. *Current Opinion in Virology* **2018**, *33*, 106–112. https://doi.org/10.1016/j.coviro.2018.08.001.

16. Noda T, Sagara H, Yen A, Takada A, Kida H, Cheng RH, Kawaoka Y. Architecture of ribonucleoprotein complexes in influenza A virus particles. *Nature* **2006**, *439* (7075), 490–492. https://doi.org/10.1038/nature04378.

17. Noda T, Sugita Y, Aoyama K, Hirase A, Kawakami E, Miyazawa A, Sagara H, Kawaoka Y. Three-dimensional analysis of ribonucleoprotein complexes in influenza A virus. *Nature Communications* **2012**, *3* (1), 1–6. https://doi.org/10.1038/ncomms1647.

18. Fournier E, Moules V, Essere B, Paillart J-C, Sirbat J-D, Isel C, Cavalier A, Rolland J-P, Thomas D, Lina B, Marquet R. A supramolecular assembly formed by influenza A virus genomic RNA segments. *Nucleic Acids Research* **2012**, *40* (5), 2197–2209. https://doi.org/10.1093/nar/gkr985.

19. Goto H, Muramoto Y, Noda T, Kawaoka Y. The genome-packaging signal of the influenza A virus genome comprises a genome incorporation signal and a genome-bundling signal. *Journal of Virology* **2013**, *87* (21), 11316–11322. https://doi.org/10.1128/JVI.01301-13.

20. Borodavka A, Dykeman EC, Schrimpf W, Lamb DC. Protein-mediated RNA folding governs sequence-specific interactions between rotavirus genome segments. *eLife* **2017**, *6*, e27453. https://doi.org/10.7554/eLife.27453.

21. Wichgers Schreur PJ, Kormelink R, Kortekaas J. Genome packaging of the *Bunyavirales*. *Current Opinion in Virology* **2018**, *33*, 151–155. https://doi.org/10.1016/j.coviro.2018.08.011.

22. Lowen AC, Boyd A, Fazakerley JK, Elliott RM. Attenuation of Bunyavirus replication by rearrangement of viral coding and noncoding sequences. *Journal of Virology* **2005**, *79* (11), 6940–6946. https://doi.org/10.1128/JVI.79.11.6940-6946.2005.

23. Brennan B, Welch SR, McLees A, Elliott RM. Creation of a recombinant Rift Valley fever virus with a two-segmented genome. *Journal of Virology* **2011**, *85* (19), 10310–10318. https://doi.org/10.1128/JVI.05252-11.

24. Kortekaas J, Oreshkova N, Cobos-Jiménez V, Vloet RPM, Potgieter CA, Moormann RJM. Creation of a nonspreading Rift Valley fever virus. *Journal of Virology* **2011**, *85* (23), 12622–12630. https://doi.org/10.1128/JVI.00841-11.

25. Wichgers Schreur PJ, Oreshkova N, Moormann RJM, Kortekaas J. Creation of Rift Valley fever viruses with four-segmented genomes reveals flexibility in Bunyavirus genome packaging. *Journal of Virology* **2014**, *88* (18), 10883–10893. https://doi.org/10.1128/JVI.00961-14.

26. Brennan B, Welch SR, Elliott RM. The consequences of reconfiguring the ambisense S genome segment of Rift Valley fever virus on viral replication in mammalian and mosquito cells and for genome packaging. *PLOS Pathogens* **2014**, *10* (2), e1003922. https://doi.org/10.1371/journal.ppat.1003922.

27. Wichgers Schreur PJ, Kortekaas J. Single-Molecule FISH Reveals Non-selective packaging of Rift Valley fever virus genome segments. *PLOS Pathogens* **2016**, *12* (8), e1005800. https://doi.org/10.1371/journal.ppat.1005800.

28. Wichgers Schreur PJ, Vloet RPM, Kant J, van Keulen L, Gonzales JL, Visser TM, Koenraadt CJM, Vogels CBF, Kortekaas J. Reproducing the Rift Valley fever virus mosquito-lamb-mosquito transmission cycle. *Scientific Reports* **2021**, *11* (1), 1477. https://doi.org/10.1038/s41598-020-79267-1.

29. Carnec X, Ermonval M, Kreher F, Flamand M, Bouloy M. Role of the cytosolic tails of Rift Valley fever virus envelope glycoproteins in viral morphogenesis. *Virology* **2014**, *448*, 1–14. https://doi.org/10.1016/j.virol.2013.09.023.

30. Simons JF, Hellman U, Pettersson RF. Uukuniemi virus S RNA segment: ambisense coding strategy, packaging of complementary strands into virions, and homology to members of the genus Phlebovirus. *Journal of Virology* **1990**, *64* (1), 247–255. https://doi.org/10.1128/jvi.64.1.247-255.1990.

31. Kormelink R, de Haan P, Peters D, Goldbach R. Viral RNA synthesis in tomato spotted wilt virus-infected *Nicotiana rustica* plants. *Journal of General Virology* **1992**, *73 (Pt 3)*, 687–693. https://doi.org/10.1099/0022-1317-73-3-687.

32. Ikegami T, Won S, Peters CJ, Makino S. Rift Valley fever virus NSs mRNA is transcribed from an incoming anti-viral-sense S RNA Segment. *Journal of Virology* **2005**, *79* (18), 12106–12111. https://doi.org/10.1128/JVI.79.18.12106-12111.2005.

33. Gauliard N, Billecocq A, Flick R, Bouloy M. Rift Valley fever virus noncoding regions of L, M and S segments regulate RNA synthesis. *Virology* **2006**, *351* (1), 170–179. https://doi.org/10.1016/j.virol.2006.03.018.

34. Murakami S, Terasaki K, Narayanan K, Makino S. Roles of the coding and noncoding regions of Rift Valley fever virus RNA genome segments in viral RNA packaging. *Journal of Virology* **2012**, *86* (7), 4034–4039. https://doi.org/10.1128/JVI.06700-11.

35. Dadonaite B, Gilbertson B, Knight ML, Trifkovic S, Rockman S, Laederach A, Brown LE, Fodor E, Bauer DLV. The structure of the influenza A virus genome. *Nature Microbiology* **2019**, *4* (11), 1781–1789. https://doi.org/10.1038/s41564-019-0513-7.

36. Le Sage V, Kanarek JP, Snyder DJ, Cooper VS, Lakdawala SS, Lee N. Mapping of influenza virus RNA-RNA interactions reveals a flexible network. *Cell Reports* **2020**, *31* (13). https://doi.org/10.1016/j.celrep.2020.107823.

37. Weidmann M, Sall AA, Manuguerra J-C, Koivogui L, Adjami A, Traoré FF, Hedlund K-O, Lindegren G, Mirazimi A. Quantitative analysis of particles, genomes and infectious particles in supernatants of haemorrhagic fever virus cell cultures. *Virology Journal* **2011**, *8* (1), 81. https://doi.org/10.1186/1743-422X-8-81.

38. Nfon CK, Marszal P, Zhang S, Weingartl HM. Innate immune response to Rift Valley fever virus in goats. *PLOS Neglected Tropical Diseases* **2012**, *6* (4), e1623. https://doi.org/10.1371/journal.pntd.0001623.

39. Marklewitz M, Zirkel F, Kurth A, Drosten C, Junglen S. Evolutionary and phenotypic analysis of live virus isolates suggests arthropod origin of a pathogenic RNA virus family. *PNAS* **2015**, *112* (24), 7536-7541. https://doi.org/10.1073/pnas.1502036112.

40. Jacobs NT, Onuoha NO, Antia A, Steel J, Antia R, Lowen AC. Incomplete influenza A virus genomes occur frequently but are readily complemented during localized viral spread. *Nature Communications* **2019**, *10* (1), 1–17. https://doi.org/10.1038/s41467-019-11428-x.

41. Sicard A, Michalakis Y, Gutiérrez S, Blanc S. The strange lifestyle of multipartite viruses. *PLOS Pathogens* **2016**, *12* (11), e1005819. https://doi.org/10.1371/journal.ppat.1005819.

42. Lucía-Sanz A, Manrubia S. Multipartite viruses: adaptive trick or evolutionary treat? *npj Systems Biology and Applications* **2017**, *3* (1), 1–11. https://doi.org/10.1038/s41540-017-0035-y.

43. Huiskonen JT, Överby AK, Weber F, Grünewald K. Electron cryo-microscopy and single-particle averaging of Rift Valley fever virus: evidence for Gn-Gc glycoprotein heterodimers. *Journal of Virology* **2009**, *83* (8), 3762–3769. https://doi.org/10.1128/JVI.02483-08.

44. Sherman MB, Freiberg AN, Holbrook MR, Watowich SJ. Single-particle cryo-electron microscopy of Rift Valley fever virus. *Virology* **2009**, *387* (1), 11–15. https://doi.org/10.1016/j.virol.2009.02.038.

45. Sanjuán R. Collective infectious units in viruses. *Trends in Microbiology* **2017**, *25* (5), 402–412. https://doi.org/10.1016/j.tim.2017.02.003.

46. Muller R, Saluzzo JF, Lopez N, Dreier T, Turell M, Smith J, Bouloy M. Characterization of clone 13, a naturally attenuated avirulent isolate of Rift Valley fever virus, which is altered in the small segment. *The American Journal of Tropical Medicine and Hygiene* **1995**, *53* (4), 405–411. https://doi.org/10.4269/ajtmh.1995.53.405.

47. Hulst M, Kortekaas J, Hakze-van der Honing R, Vastenhouw S, Cornellissen J, van Maanen K, Bossers A, Harders F, Stockhofe N, van der Poel W. Genetic characterization of an atypical Schmallenberg virus isolated from the brain of a malformed lamb. *Virus Genes* **2013**, *47* (3), 505–514. https://doi.org/10.1007/s11262-013-0975-2.

48. Keegan K, Collett MS. Use of bacterial expression cloning to define the amino acid sequences of antigenic determinants on the G2 glycoprotein of Rift Valley fever virus. *Journal of Virology* **1986**, *58* (2), 263–270. https://doi.org/10.1128/jvi.58.2.263-270.1986.

49. Femino AM, Fay FS, Fogarty K, Singer RH. Visualization of single RNA transcripts in situ. *Science* **1998**, *280* (5363), 585–590. https://doi.org/10.1126/science.280.5363.585.

50. Raj A, van den Bogaard P, Rifkin SA, van Oudenaarden A, Tyagi S. Imaging individual mRNA molecules using multiple singly labeled probes. *Nature Methods* **2008**, *5* (10), 877–879. https://doi.org/10.1038/nmeth.1253.

51. Orjalo Jr. A, Johansson HE, Ruth JL. Stellaris™ fluorescence *in situ* hybridization (FISH) probes: a powerful tool for mRNA detection. *Nature Methods* **2011**, *8*, 884. https://doi.org/10.1038/nmeth.f.349.

52. Oymans J, Wichgers Schreur PJ, van Oort S, Vloet R, Venter M, Pijlman GP, van Oers MM, Kortekaas J. Reverse genetics system for Shuni virus, an emerging orthobunyavirus with zoonotic potential. *Viruses* **2020**, *12* (4), 455. https://doi.org/10.3390/v12040455.

53. Schneider CA, Rasband WS, Eliceiri KW. NIH Image to ImageJ: 25 years of image analysis. *Nature Methods* **2012**, *9* (7), 671–675. https://doi.org/10.1038/nmeth.2089.

Supplementary information

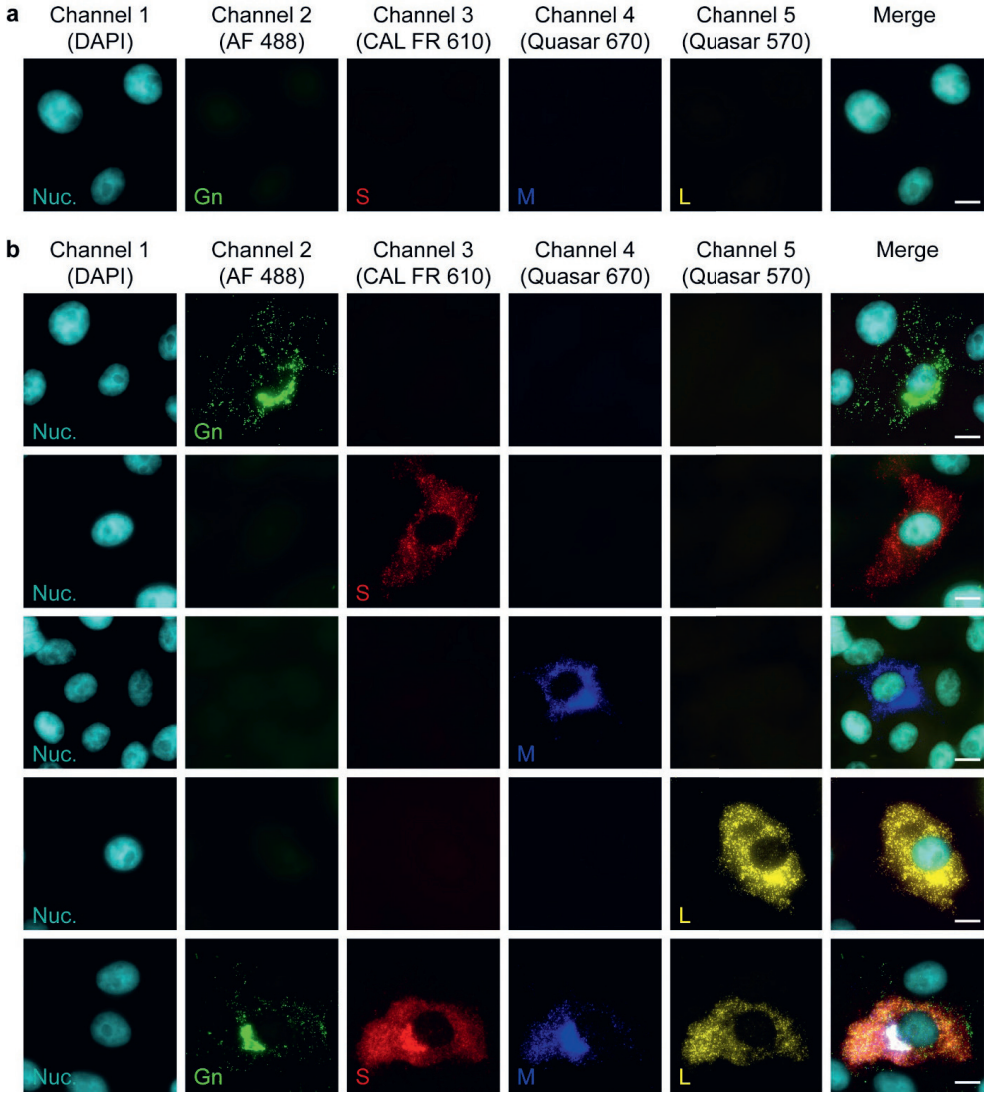

Supplementary Figure 1. Specificity of RVFV FISH probe sets and antibodies. A, B Vero E6 cells were mock-infected (**A**) or infected with RVFV (MOI 0.75) (**B**) and cells were fixed at 8 h post-infection. The S segment (N gene; red), M segment (polyprotein gene; blue) and L segment (RdRp gene; yellow) were hybridized using probe sets labelled with CAL Fluor Red 610, Quasar 670 and Quasar 570, respectively. Progeny RVFV particles (green) were detected with antibody 4-D4[48] targeting the Gn glycoprotein in combination with Alexa Fluor 488-conjugated secondary antibodies. Cell nuclei (cyan) were visualized with DAPI. Mock-infected cells (**A**) were treated simultaneously with the three probe sets and antibodies. RVFV infected cells (**B**) were treated with either one probe set or antibodies at a time as single-color controls (first four rows) or simultaneously with the three probe sets and antibodies (last row). Scale bars, 10 µm.

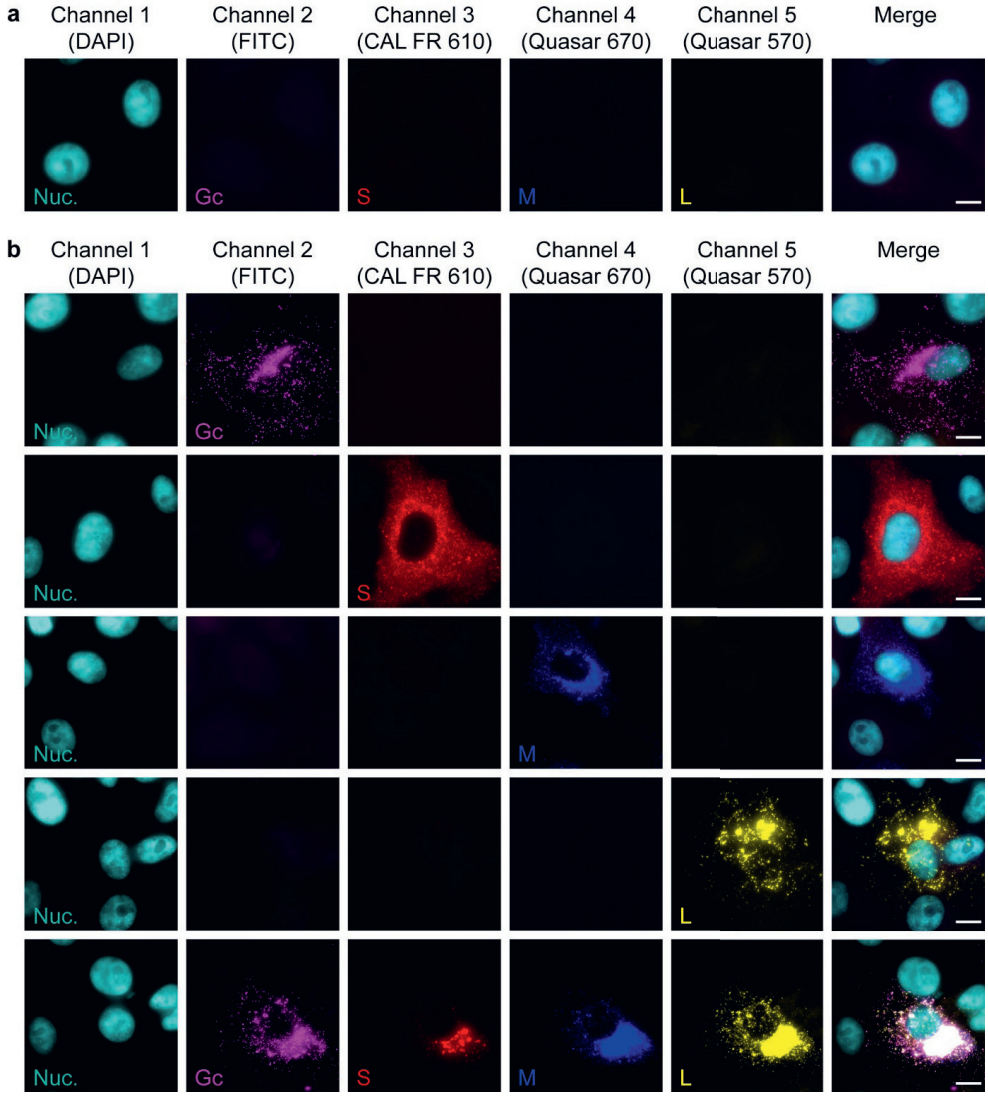

Supplementary Figure 2. Specificity of SBV FISH probe sets and antibodies. A, B Vero E6 cells were mock-infected (**A**) or infected with SBV (MOI 0.33) (**B**) and cells were fixed at 8 h post-infection. The S segment (N gene; red), M segment (polyprotein gene; blue) and L segment (RdRp gene; yellow) were hybridized using probe sets labelled with CAL Fluor Red 610, Quasar 670 and Quasar 570, respectively. Progeny SBV particles (magenta) were detected with serum from an immunized rabbit[52] targeting the Gc glycoprotein in combination with FITC-conjugated secondary antibodies. Cell nuclei (cyan) were visualized with DAPI. Mock-infected cells (**A**) were treated simultaneously with the three probe sets and antibodies. SBV infected cells (**B**) were treated with either one probe set or antibodies at a time as single-color controls (first four rows) or simultaneously with the three probe sets and antibodies (last row). Scale bars, 10 µm.

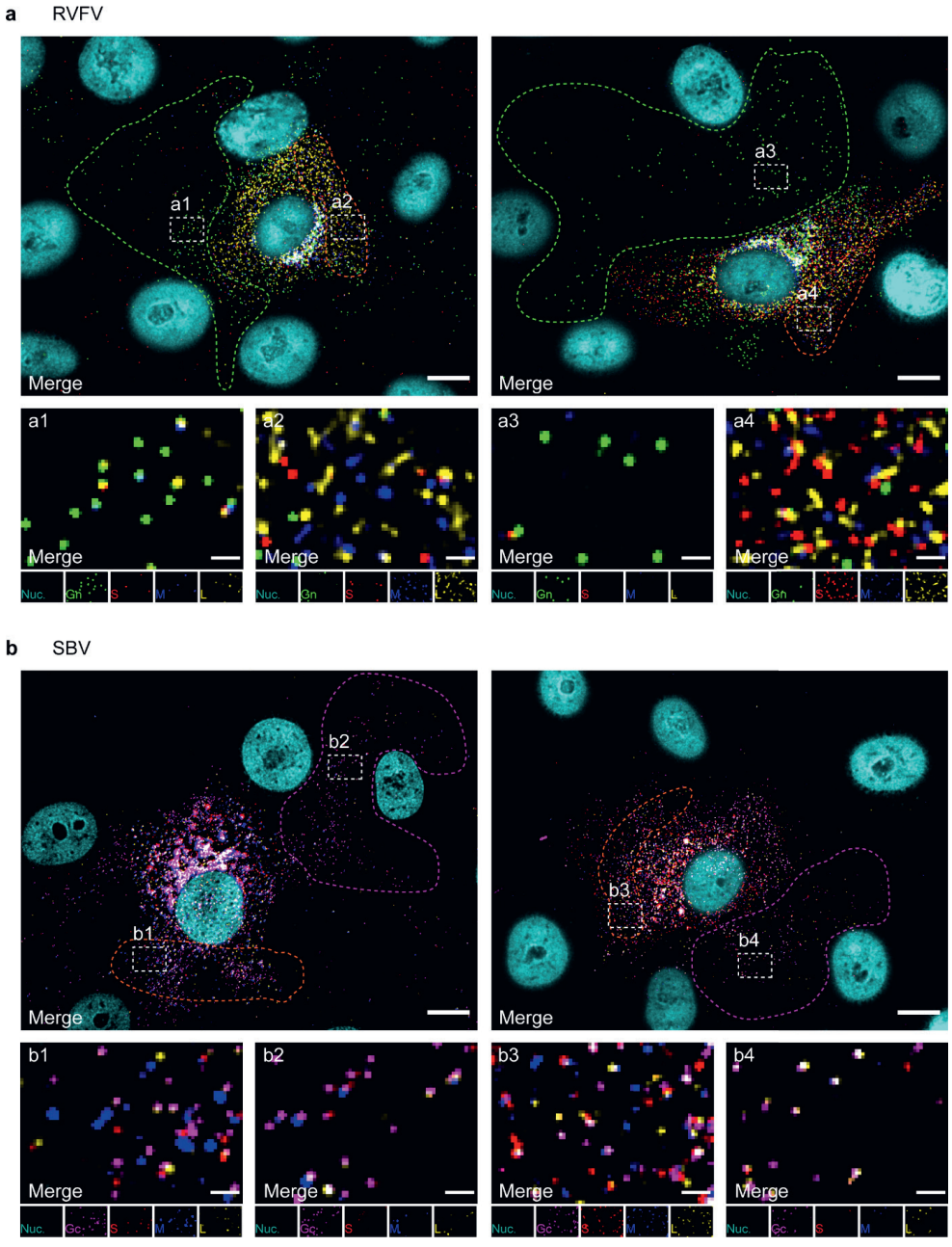

Supplementary Figure 3. Representative regions of interest for the analysis of bunyavirus infected mammalian cells and their progeny virions using single-molecule vRNA FISH-immunofluorescence. A, B Vero E6 cells were infected with RVFV (MOI 0.50-0.75) (**a**) or SBV (MOI 0.33) (**b**) and cells were fixed at 8 h post-infection. The S segment (N gene; red), M segment (polyprotein gene; blue) and L segment (RdRp gene; yellow) were hybridized using probe sets labelled with CAL Fluor Red 610, Quasar 670 and

Quasar 570, respectively. Progeny RVFV particles (green) were detected with antibody 4-D4[48] targeting the Gn glycoprotein in combination with Alexa Fluor 488-conjugated secondary antibodies. Progeny SBV particles (magenta) were detected with serum from an immunized rabbit[52] targeting the Gc glycoprotein in combination with FITC-conjugated secondary antibodies. Cell nuclei (cyan) were visualized with DAPI. The orange dashed contours depict representative regions of interest selected for quantification of cytoplasmic vRNPs. The green (**A**) and magenta (**B**) dashed contours depict representative regions of interest selected for determining the genome composition of RVFV and SBV extracellular virions, respectively, through co-localization analysis. Middle rows of **A** and **B** show magnifications of smaller regions of interest within the dashed contours (indicated in top rows as white dashed boxes and labelled as A1-4 and B1-4). Bottom rows of **A** and **B** show individual channels of the magnified regions of interest. Main images are merged maximum intensity projections of five channels. Due to a higher fluorescence intensity of the green and magenta channels compared to the other channels, spots co-localizing with the glycoprotein may sometimes appear masked and not entirely evident in merged images. Scale bars, 10 µm (top rows) and 1 µm (middle rows).

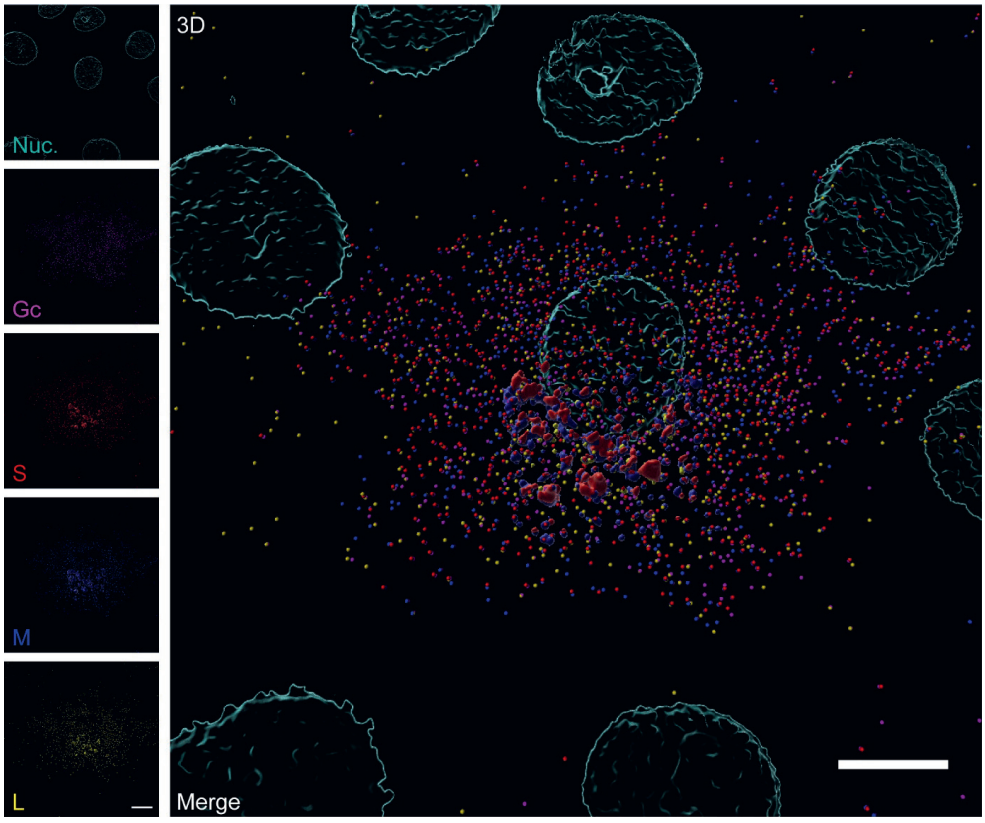

Supplementary Figure 4. Single-molecule vRNA FISH-immunofluorescence of SBV infected mammalian cells. Vero E6 cells were infected with SBV (MOI 0.33) and cells were fixed at 8 h post-infection. The S segment (N gene; red), M segment (polyprotein gene; blue) and L segment (RdRp gene; yellow) were hybridized using probe sets labelled with CAL Fluor Red 610, Quasar 670 and Quasar 570, respectively. Progeny SBV particles were detected with serum from an immunized rabbit[52] targeting the Gc glycoprotein in combination with FITC-conjugated secondary antibodies. Cell nuclei (cyan) were visualized with DAPI. The three-dimensional representation showing the spatial distribution of vRNPs and virions was created with Imaris using the Surfaces and Spots modes. Accumulation of vRNPs in a perinuclear region shows active vRNP recruitment to the site of virion assembly. Co-localization of vRNPs and virions is depicted by merged spheres. Scale bars, 10 µm.

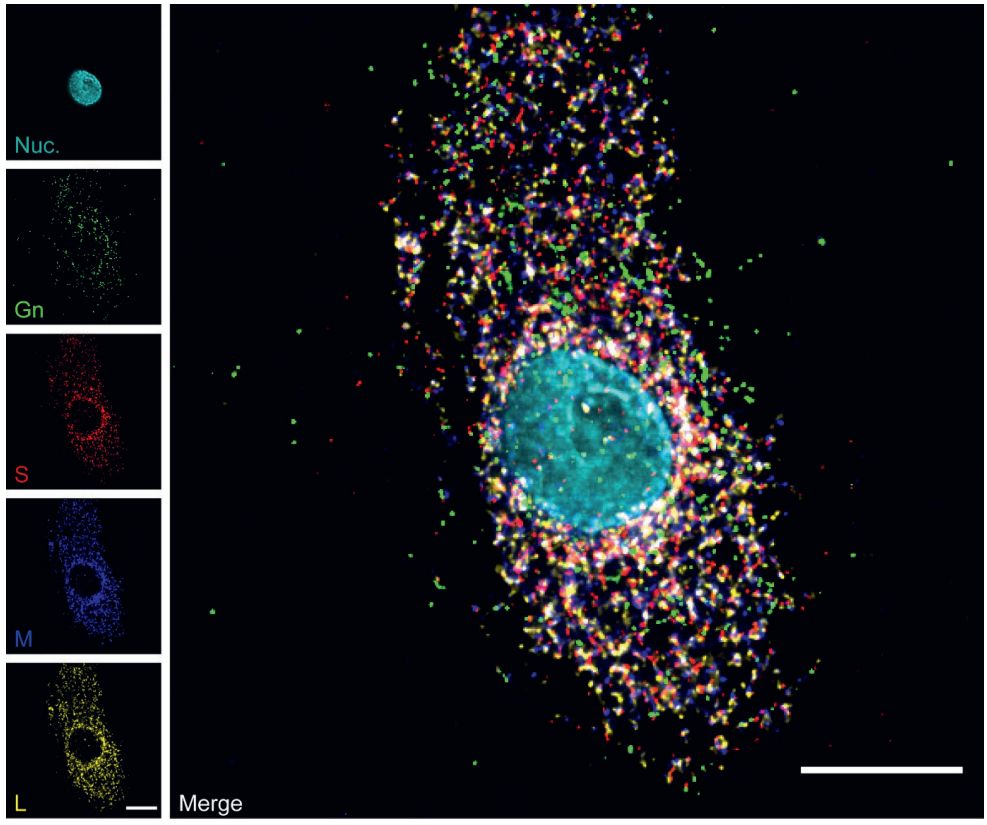

Supplementary Figure 5. Single-molecule vRNA FISH-immunofluorescence of a RVFV infected insect cell. C6/36 cells were infected with RVFV (MOI 0.75) and cells were fixed at 32 h post-infection. The S segment (N gene; red), M segment (polyprotein gene; blue) and L segment (RdRp gene; yellow) were hybridized using probe sets labelled with CAL Fluor Red 610, Quasar 670 and Quasar 570, respectively. Progeny RVFV particles (green) were detected with antibody 4-D4[48] targeting the Gn glycoprotein in combination with Alexa Fluor 488-conjugated secondary antibodies. Cell nuclei (cyan) were visualized with DAPI. The main image merges maximum intensity projections of five channels (shown on the left). Due to a higher fluorescence intensity of the green channel compared to the other channels, spots co-localizing with the glycoprotein may sometimes appear masked and not entirely evident in merged images. Scale bars, 10 µm.

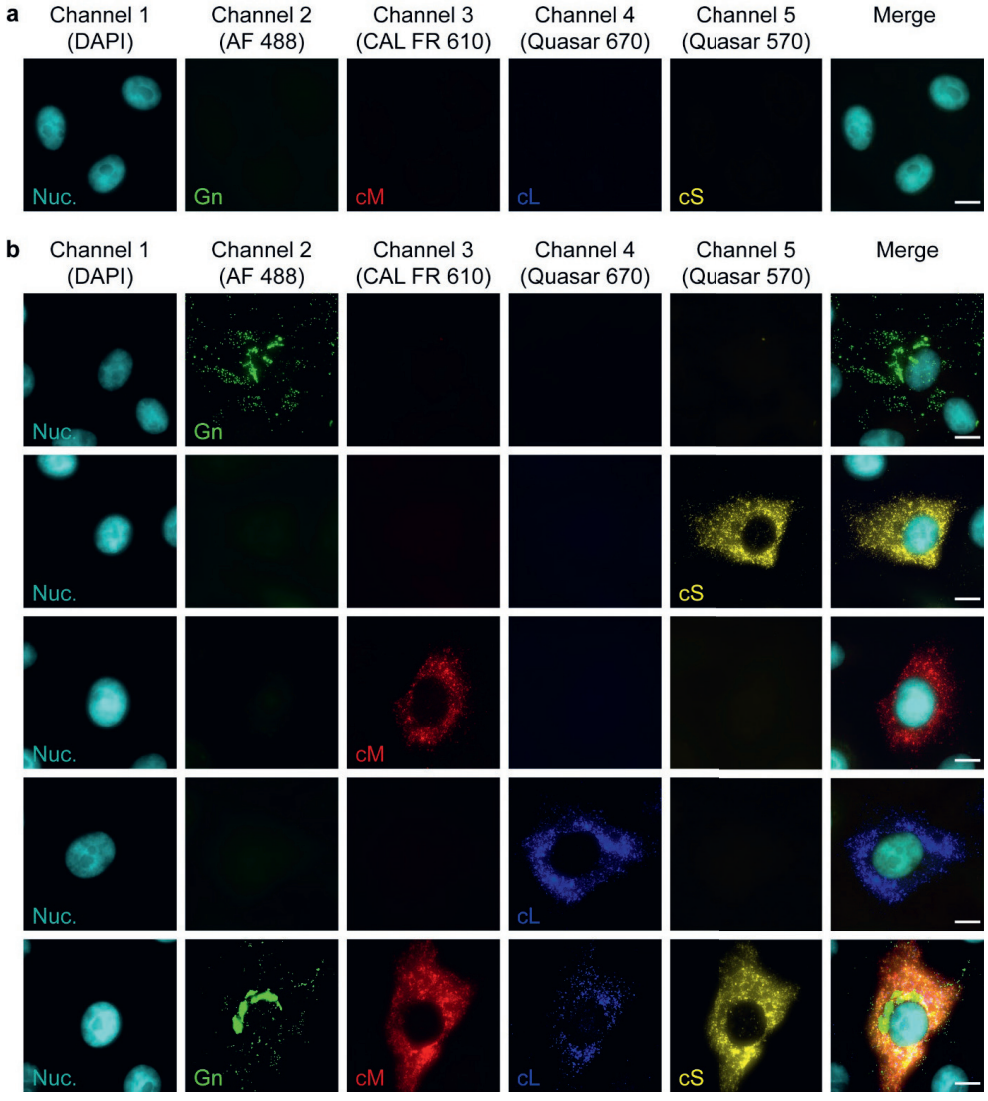

Supplementary Figure 6. Specificity of RVFV complementary RNAs (cRNAs) FISH probe sets and antibodies. **A, B** Vero E6 cells were mock-infected (**A**) or infected with RVFV (MOI 0.75) (**B**) and cells were fixed at 8 h post-infection. The S segment cRNA (N gene; yellow), M segment cRNA (polyprotein gene; red) and L segment cRNA (RdRp gene; blue) were hybridized using probe sets labelled with Quasar 570, CAL Fluor Red 610, Quasar 670, respectively. Progeny RVFV particles (green) were detected with antibody 4-D4[48] targeting the Gn glycoprotein in combination with Alexa Fluor 488-conjugated secondary antibodies. Cell nuclei (cyan) were visualized with DAPI. Mock-infected cells (**A**) were treated simultaneously with the three probe sets and antibodies. RVFV infected cells (**B**) were treated with either one probe set or antibodies at a time as single-color controls (first four rows) or simultaneously with the three probe sets and antibodies (last row). Scale bars, 10 µm.

Supplementary Table 1. Primers for cDNA synthesis of viral genome segments.

Target	Name	Sequence
RVFV-Clone 13-S and RVFV-35/74-S	JR860-For	ACAAAGCTCCCTAGAGATACA
RVFV-Clone 13-M and RVFV-35/74-M	JR861-For	GACACAAAGACGGTGCATTA
RVFV-Clone 13-L and RVFV-35/74-L	JR890-For	GACACAAAGGCGCCCAATC
SBV-NL-F6-S	JR875-For	GTGAACTCCACTATTAACTACAGA
SBV-NL-F6-M	JR891-For	GAGTAGTGAACTACCACAATCAA
SBV-NL-F6-L	JR892-For	GTAGTGTACCCCTAATTACAATCAC

Supplementary Table 2. Primers for RT-qPCR amplifications of viral genome fragments.

Target	Name	Sequence
RVFV-Clone 13-S and RVFV-35/74-S	JR907-For	TCCAGTTTGCTGCTCAA
	JR908-Rev	CTGCTTTAAGAGTTCGATAACC
RVFV-Clone 13-M and RVFV-35/74-M	JR909-For	GCTGATGGCTTGAACAAC
	JR910-Rev	GTCTCTCACACCGAACTATC
RVFV-Clone 13-L and RVFV-35/74-L	JR911-For	TCGATAGATGTGGAAGATATGG
	JR912-Rev	CGTCATTCATCATGGGAAAC
SBV-NL-F6-S	JR878-For	CGGGTATGTGGCATTTATTG
	JR879-Rev	GACCATCTTGGCCTTCTT
SBV-NL-F6-M	JR882-For	CGACGTGGATTGAAGATAATG
	JR883-Rev	GAGGCTCTGTGAATTGTTAAG
SBV-NL-F6-L	JR886-For	CCCTGGATTGATGAGGATAC
	JR887-Rev	GACTCATGGAATGTCAGTTTAG

Additional supplementary information files can be accessed online at:
https://doi.org/10.1038/s42003-021-01821-y

Supplementary Movie 1

Supplementary Movie 2

Supplementary Movie 3

Supplementary Movie 4

Supplementary Data 1

Supplementary Data 2

Chapter 3

Incomplete bunyavirus particles can cooperatively support virus infection and spread

Erick Bermúdez-Méndez [1,2], Kirsten F. Bronsvoort [1], Mark P. Zwart [3], Sandra van de Water [1], Ingrid Cárdenas-Rey [4,5], Rianka P. M. Vloet [1], Constantianus J. M. Koenraadt [6], Gorben P. Pijlman [2], Jeroen Kortekaas [1,2,7] & Paul J. Wichgers Schreur [1]

[1] Department of Virology & Molecular Biology, Wageningen Bioveterinary Research, Lelystad, The Netherlands

[2] Laboratory of Virology, Wageningen University & Research, Wageningen, The Netherlands

[3] Department of Microbial Ecology, The Netherlands Institute of Ecology, Wageningen, The Netherlands

[4] Department of Bacteriology, Host-Pathogen Interactions & Diagnostics Development, Wageningen Bioveterinary Research, Lelystad, The Netherlands

[5] Laboratory of Genetics, Wageningen University & Research, Wageningen, The Netherlands

[6] Laboratory of Entomology, Wageningen University & Research, Wageningen, The Netherlands

[7] Present address: Boehringer Ingelheim Animal Health, Saint-Priest, France

Published:

PLOS Biology (2022) 20(11): e3001870.

DOI: https://doi.org/10.1371/journal.pbio.3001870

Abstract

Bunyaviruses lack a specific mechanism to ensure the incorporation of a complete set of genome segments into each virion, explaining the generation of incomplete virus particles lacking one or more genome segments. Such incomplete virus particles, which may represent the majority of particles produced, are generally considered to interfere with virus infection and spread. Using the three-segmented arthropod-borne Rift Valley fever virus as a model bunyavirus, we here show that two distinct incomplete virus particle populations unable to spread autonomously are able to efficiently complement each other in both mammalian and insect cells following co-infection. We further show that complementing incomplete virus particles can co-infect mosquitoes, resulting in the reconstitution of infectious virus that is able to disseminate to the mosquito salivary glands. Computational models of infection dynamics predict that incomplete virus particles can positively impact virus spread over a wide range of conditions, with the strongest effect at intermediate multiplicities of infection. Our findings suggest that incomplete particles may play a significant role in within-host spread and between-host transmission, reminiscent of the infection cycle of multipartite viruses.

Introduction

Segmented and multipartite viruses have genomes divided over multiple segments. The classical paradigm in virology states that segmented viruses package all their genome segments into a single virus particle, whereas multipartite viruses package each genome segment into a distinct virus particle[1]. To ensure a productive infection, it is generally accepted that multipartite viruses (mainly found to infect plants and fungi) rely on co-infection of the same cell with a set of complementing particles, each particle containing a different genome segment[1,2]. Alternatively, complementation can occur at the tissue level, as proposed in a recent study with the plant-infecting faba bean necrotic stunt virus (FBNSV, family *Nanoviridae*). FBNSV was shown to complement its missing genome segments by exporting and distributing the viral mRNAs and proteins across interconnected neighboring cells[3]. By contrast, it has been thought that segmented viruses (mainly found to infect animals) solely rely on individual cells as units of viral replication and thus have to carry at least one copy of each genome segment within a single virus particle to ensure the delivery of a complete genome[4,5].

Under the traditional view on segmented viruses, it seems reasonable to expect a selective genome packaging strategy that facilitates the generation of progeny virus particles containing a complete set of genome segments. Influenza A virus (IAV, family *Orthomyxoviridae*) is the prime example of a segmented virus employing a highly selective genome packaging mechanism, in which intersegment interactions facilitate the assembly of its eight-segmented genome into a supramolecular complex that is incorporated inside new virus particles[6–12]. Despite employing a highly selective genome packaging mechanism, it has been shown that a fraction of IAV particles fails to express all its viral genes upon infection[13,14], either because of defective genome packaging[15], within-cell segment loss during trafficking[16], or erroneous gene transcription[17].

Challenging the classical paradigm, it has been demonstrated that genome segment complementation by co-infection of individual cells can lead to a productive infection[1,18,19]. To what extent these compensatory mechanisms play a role in IAV infection kinetics is not yet fully clear. Whether similar mechanisms are used by other segmented viruses that do not use a selective genome packaging strategy is also unknown. Remarkably, in the absence of a selective packaging process, an even higher proportion of particles containing an incomplete set of genome segments is produced. Guaico Culex virus (GCXV, clade Jingmenvirus related to family *Flaviviridae*)[1,20] and members of the order *Bunyavirales*[21,22] are examples of viruses that seem not to employ an orchestrated genome packaging process, leaving a gap in our understanding of their replication cycles.

Bunyaviruses are enveloped, negative- or ambi-sense, single-stranded RNA viruses with a genome divided over two to six segments. These viruses are transmitted by arthropods or rodents and can infect a wide variety of hosts, including mammals, birds, reptiles, and plants[23]. Recently, using a combined single-molecule fluorescence *in situ* hybridization (smFISH)-immunofluorescence approach, we showed that the genome packaging processes of two members of the *Bunyavirales*, Rift Valley fever virus (RVFV, family *Phenuiviridae*, genus *Phlebovirus*) and Schmallenberg virus (SBV, family *Peribunyaviridae*, genus *Orthobunyavirus*), are not tightly controlled. Such non-selective packaging mechanism results in mixed virus progeny populations that consist of a minor fraction (below 25%) of complete particles (i.e., containing a complete set of all three genome segments: S, M, and L) and a large fraction (above 75%) of empty and incomplete particles (i.e., lacking one or more genome segments)[21,22].

Despite the apparently inefficient genome packaging of RVFV and SBV, at least *in vitro*, these viruses can spread efficiently within and between their mammalian and arthropod hosts. RVFV and SBV can possibly compensate the theoretical fitness cost of employing a non-selective packaging strategy by benefits to viral replication or spread through yet unknown mechanisms. Due to the fact that bunyaviruses only generate a small fraction of complete particles, we hypothesize that similarly as demonstrated for IAV, bunyavirus particles with an incomplete set of genome segments may contribute to efficient virus spread by genetic complementation after co-infecting the same cell.

In this study, we used RVFV variants encoding fluorescent reporter proteins to investigate cell susceptibility to simultaneous infection by more than one virus particle. We then assessed whether within-host genome complementation could occur in mammalian and insect cells by generating different two-segmented incomplete virus particle populations that depend entirely on co-infection for the production of progeny virions. We further investigated whether particles with an incomplete set of genome segments can complement each other *in vivo* in the mosquito vector. Lastly, we mathematically modeled diverse infection scenarios to estimate under what conditions incomplete particles substantially contribute to virus spread. The results of our study point toward a significant role of incomplete particles in the bunyavirus life cycle, showing that incomplete virus particles can co-infect individual cells, resulting in the reconstitution of complete virus that contributes to within-host spread and potentially between-host transmission.

Results

Efficient co-infection of three- and two-segmented RVFV reporter viruses in both mammalian and insect cells

In vertebrates, genetic complementation of virus particles with a distinct genome composition strictly relies on their ability to co-infect the same cell. To assess if mammalian and insect cells are susceptible to RVFV co-infection, we generated two recombinant three-segmented RVFV variants encoding either eGFP or mCherry2 in place of the NSs gene, using a T7 polymerase-based reverse genetics system (**Fig. 1A**). Cells infected with the individual reporter viruses showed abundant expression of the respective fluorescent protein (**Fig. 1B**), providing a suitable strategy to track virus infection and identify co-infected cells through the detection of co-localized fluorescent signals. Moreover, RVFV-eGFP and RVFV-mCherry2 replicated with almost identical growth kinetics, reaching high titers already 24 h post-infection and peaking at 48 h post-infection (**Fig. 1C**). Upon simultaneous inoculation with RVFV-eGFP and RVFV-mCherry2, both BSR-T7/5 (hamster) and C6/36 (mosquito) cells were found to be susceptible to co-infection, as clearly evidenced by the co-localization of green and red fluorescent signal in a fraction of the cell population (**Fig. 1D, E**).

Simultaneous infections with RVFV-eGFP and RVFV-mCherry2 allowed us to qualitatively confirm cell susceptibility to co-infection (**Fig. 1E**). However, the fast spread of three-segmented RVFV impeded us from assessing accurately how often these co-infection events are actually taking place, since co-infections can occur over multiple infection cycles. To overcome this, we again used the T7 polymerase-based reverse genetics system to generate two non-spreading incomplete RVFV particle populations lacking the M segment and encoding a fluorescent protein (FP), either eGFP or mCherry2, in the S segment in place of the NSs gene (iRVFV-SL-FP) (**Fig. 2A**).

The non-spreading nature of iRVFV-SL particles allowed us to assess the extent of co-infection after a single cycle of infection (without the generation of virus progeny). The generation of iRVFV-SL-eGFP has been previously reported by our group (initially termed RRPs)[24], but the generation of iRVFV-SL-mCherry2 is first reported as part of this work. Both particle populations are produced following complementation with an expression plasmid encoding the structural glycoproteins (Gn and Gc) normally encoded by the M segment. Despite the absence of the M segment, the S and L genome segments encoding for the nucleocapsid (N) protein and the RNA-dependent RNA polymerase (RdRp or L protein), respectively, are sufficient to support the replication and transcription of the S and L segments upon infection of naive cells. Importantly,

because the M segment encoding for the Gn and Gc glycoproteins is absent in these naive cells, infection with iRVFV-SL particles does not lead to assembly and release of progeny virus. Direct fluorescence microscopy combined with an immunofluorescence assay to detect Gn clearly showed that cells infected with iRVFV-SL-eGFP or iRVFV-SL-mCherry2 have abundant expression of the respective FP but no expression of Gn (**Fig. 2B**). Furthermore, passaging the supernatant of cells infected with iRVFV-SL-FP to naive cells did not result in the expression of eGFP, mCherry2, or Gn, confirming that these particles are incomplete and not able to spread due to the lack of the M genome segment (**Fig. 2C**).

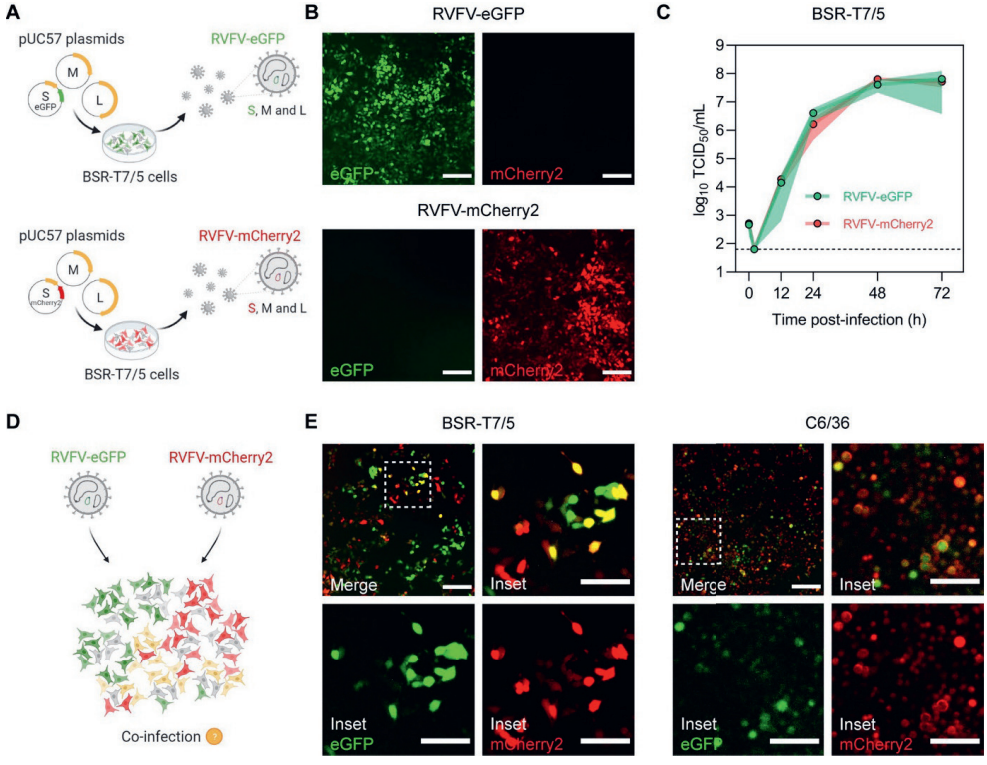

Figure 1. Co-infection of mammalian and insect cells with recombinant three-segmented RVFV reporter viruses. A Schematic representation of the T7 polymerase-based reverse genetics system. Fluorescently marked variants of RVFV were generated by simultaneous transfection of BSR-T7/5 cells with the transcription plasmids pUC57_S, pUC57_M, and pUC57_L encoding the RVFV-35/74 S, M and L genome segments, respectively, in antigenomic-sense orientation. The pUC57_S plasmid additionally encoded for either eGFP or mCherry2 in place of the NSs gene. **B** Direct fluorescence detection of BSR-T7/5 cells infected with either RVFV-eGFP (green) or RVFV-mCherry2 (red) (MOI 0.5) at 24 h post-infection. **C** Growth kinetics of RVFV-eGFP and RVFV-mCherry2 after infection of BSR-T7/5 cells at an MOI of 0.01. Virus titers were determined with an end-point dilution assay (fluorescence microscopy readout). Dots represent means of biological replicates (n = 3) at each time point, and the shaded area represents the standard deviation. The

dashed line indicates the limit of detection ($10^{1.8}$ $TCID_{50}$/mL). Source data are provided in **Supplementary Data 1**. **D** Schematic representation of the simultaneous infection of mammalian (BSR-T7/5) or insect (C6/36) cells with RVFV-eGFP and RVFV-mCherry2. **E** Direct fluorescence detection of BSR-T7/5 and C6/36 cells co-infected with RVFV-eGFP and RVFV-mCherry2 (MOI 0.5 for each virus) at 24 h (BSR-T7/5) or 72 h (C6/36) post-infection. Inset images are magnifications of a region of interest (indicated as a dashed box). Co-infected cells co-express eGFP (green) and mCherry2 (red) and thus appear yellow. Scale bars, 200 μm (inset images 100 μm). Illustrations in **Fig. 1A**, **D** were created with BioRender.com.

To quantify to what extent cells can be co-infected with the two different non-spreading fluorescent virus variants, we simultaneously infected BSR-T7/5 cells with iRVFV-SL-eGFP and iRVFV-SL-mCherry2 at increasing multiplicities of infection (MOIs, ranging from 0.1 to 2.5) (**Fig. 2D**). Through direct detection of co-localized eGFP and mCherry2 expression, we confirmed that these particles also could co-infect BSR-T7/5 cells (**Fig. 2E**). Next, using flow cytometry, we quantified the fraction of non-infected cells, singly-infected cells, and co-infected cells (**Fig. 2F**). Mock-infected cells and cells infected with only one population of incomplete particles were the basis to gate the flow cytometry data. A clear double (eGFP and mCherry2)-positive cell population was identified after co-infection with both populations of incomplete particles.

Interestingly, at each MOI tested, the percentage of infected and co-infected cells closely resembled that of a mathematical model of infection (model C), which assumes that genome segments are randomly packaged into virus particles and that host cell susceptibility is heterogeneous among the cell population (**Fig. 2G** and **Supplementary File 1**). Model selection based on the Akaike information criterion (AIC) indicated that model C is much better supported than two simpler models of infection (models A and B; **Supplementary Table 1**). Hence, model C was chosen for visualization here. The population of co-infected cells rose sharply with increasing MOI, showing a typical dose-response sigmoidal curve, suggesting no apparent mechanism leading to the exclusion of multiple particles entering the same cell in the present experimental setup. A reasonably good fit of the different models to the data suggests that co-infection is unrestricted upon simultaneous exposure to virus particles, as none of the models includes mechanisms of exclusion.

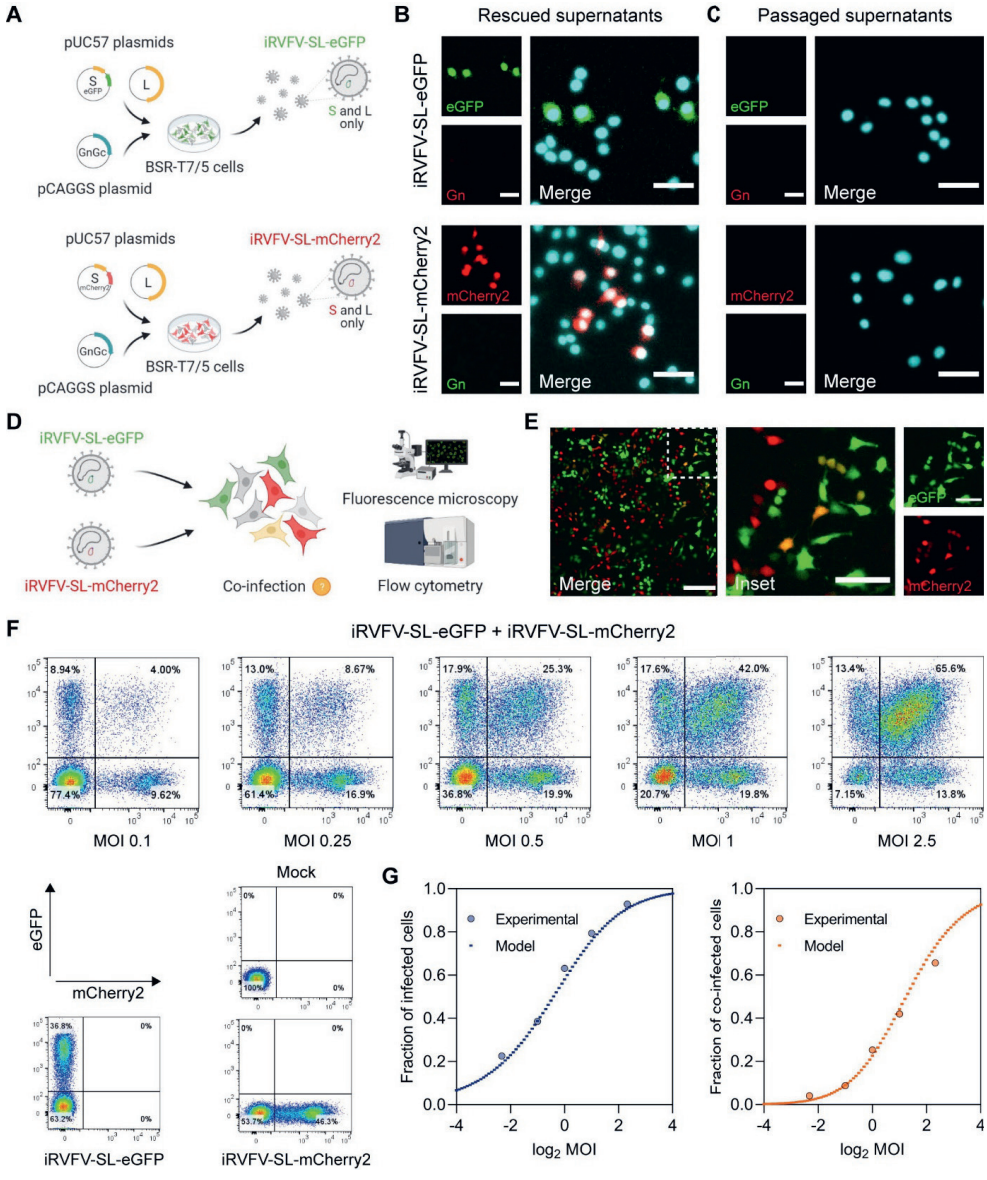

Figure 2. Quantitative assessment of mammalian cells co-infected with non-spreading two-segmented RVFV reporter viruses. A Schematic representation of the reverse genetics system used to create two-segmented RVFV reporter viruses. Incomplete RVFV-SL particles were generated by co-transfection of BSR-T7/5 cells with the transcription plasmids pUC57_S, encoding either eGFP or mCherry2 in place of the NSs gene, pUC57_L, and the protein expression plasmid pCAGGS_NSmGnGc. **B** Immunofluorescence assay for detection of BSR-T7/5 cells infected with iRVFV-SL-eGFP or iRVFV-SL-mCherry2 (MOI 0.5) at 24 h post-infection. **C** Supernatants from cells primarily infected with the incomplete RVFV particles in **B** were passaged onto naive BSR-T7/5 cells. Cells were examined at 24 h post-infection for expression of eGFP (green) and mCherry2 (red) by fluorescence microscopy. Expression of the Gn glycoprotein (green or red,

depending on the virus) was detected with rabbit polyclonal anti-Gn serum in combination with FITC-conjugated (green) or Alexa Fluor 568–conjugated (red) secondary antibodies. Cell nuclei (cyan) were visualized with DAPI. Scale bars, 50 μm. **D** Schematic representation of the simultaneous infection of mammalian (BSR-T7/5) cells with non-spreading iRVFV-SL-eGFP and iRVFV-SL-mCherry2 particles. Co-infections were done at increasing MOI (ranging from 0.1 to 2.5 for each virus). After 48 h, cells were examined by fluorescence microscopy and fixed for flow cytometry analysis. **E** Direct fluorescence detection of BSR-T7/5 cells co-infected (MOI of 0.5 for each virus) with the two-segmented incomplete particle populations. The inset image is a magnification of a region of interest (indicated as a dashed box). Co-infected cells co-express eGFP (green) and mCherry2 (red) and thus appear yellow. Scale bars, 200 μm (inset images 100 μm). **F** Cells expressing eGFP, mCherry2, or both were quantified by flow cytometry. Mock-infected cells and cells infected exclusively with only one population of incomplete particles (MOI 0.5) were used as controls. **G** Relationship between the fraction of infected (left) and co-infected (right) cells as a function of the MOI. Dots represent experimental data points. Dashed lines represent the predictions of a model based on the assumptions that genome segments are randomly packaged into virus particles and that host susceptibility is heterogeneous. The code required to reproduce the model predictions is provided as **Supplementary File 1**. Source data are provided in **Supplementary Data 1**. Illustrations in **Fig. 2A, D** were created with BioRender.com.

Successful generation of incomplete RVFV particles lacking the S genome segment

To study the potential role of incomplete particles in the bunyavirus life cycle, we needed at least two distinct populations of RVFV particles having incomplete but complementing genomes. Besides generating iRVFV-SL-FP particles, we also generated incomplete RVFV particles lacking the S segment (iRVFV-ML) by following a similar T7 polymerase-based reverse genetics strategy (**Fig. 3A**). Complete M and L genome segments were encoded in antigenomic-sense orientation by transcription plasmids, and the N protein was provided by an expression plasmid. Due to the absence of the S segment in the rescued particles and, consequently, the unavailability of N protein, infections with iRVFV-ML particles did not result in any appreciable viral genome replication. Accordingly, neither N nor Gn was detected in an immunofluorescence assay of cells infected with iRVFV-ML (**Fig. 3B**).

Due to the non-replicating nature of RVFV particles lacking the S genome segment, the infectious titer of iRVFV-ML stocks could not be determined with a conventional virus titration assay. Therefore, we confirmed the genomic composition of rescued iRVFV-ML particles by quantifying the S, M, and L genome segments via quantitative reverse transcription PCR (RT-qPCR) (**Fig. 3C**). In both batches of rescued iRVFV-ML particles, high copy numbers of only the M and L genome segments were detected, whereas the S segment was not detected. Similarly, in samples containing iRVFV-SL-eGFP particles, only the S and L genome segments were present at high

copy numbers, and the M segment was not detected. All three genome segments (S, M, and L) were detected in samples containing the three-segmented RVFV-eGFP used as control.

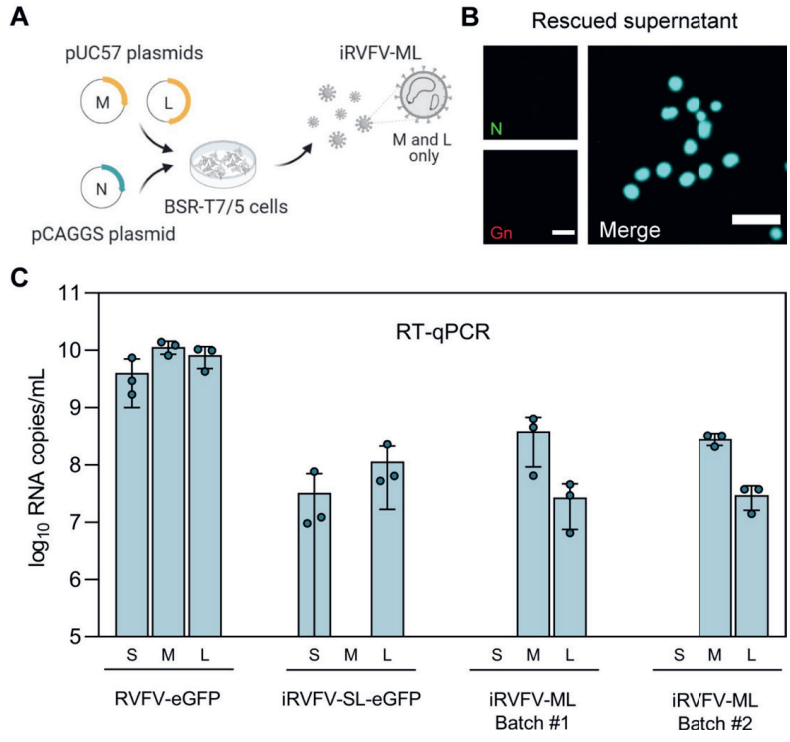

Figure 3. Generation of incomplete RVFV particles lacking the S genome segment. A Schematic representation of the reverse genetics system used to create incomplete RVFV-ML particles. iRVFV-ML particles were generated by co-transfection of BSR-T7/5 cells with the transcription plasmids pUC57_M, pUC57_L, and the protein expression plasmid pCAGGS_N. **B** Immunofluorescence assay for detection of BSR-T7/5 cells exposed to iRVFV-ML (MOI 0.5) at 24 h post-infection. Expression of the N protein (green) was detected with a mouse anti-N monoclonal hybridoma in combination with Alexa Fluor Plus 488-conjugated secondary antibodies. Expression of the Gn glycoprotein (red) was detected with rabbit polyclonal anti-Gn serum in combination with Alexa Fluor 568–conjugated secondary antibodies. Cell nuclei (cyan) were visualized with DAPI. Scale bars, 50 µm. **C** Segment-specific RT-qPCR quantification of the genomic composition of two batches of rescued iRVFV-ML particles. Stock preparations of RVFV-eGFP and iRVFV-SL-eGFP were included as reference for comparison. Bars show means with SD. Dots represent replicates (n = 3 samples). Source data are provided in **Supplementary Data 1**. Illustration in **Fig. 3A** was created with BioRender.com.

Co-infection with complementing incomplete RVFV particles results in efficient virus replication and spread among mammalian and insect cells

Having generated two distinct populations of two-segmented RVFV particles with an incomplete but complementing genome, we next investigated whether exposing cells to a mixture of these two populations would result in genome complementation (SL + ML = SML) and subsequent reconstitution of three-segmented (SML) infectious virus (**Fig. 4A**). Rescue of infectious virus following incubation of cells exclusively with virus populations with an incomplete set of genome segments would strongly suggest a role for incomplete particles in virus replication and spread. To this end, BSR-T7/5 and C6/36 cells were simultaneously inoculated with iRVFV-SL-eGFP and iRVFV-ML at different MOIs (ranging from 0.001 to 0.25 for each virus). As shown previously in **Figs. 2B, 3B**, incubating cells with only iRVFV-SL-eGFP or iRVFV-ML particles did not result in productive infections. Inoculation with iRVFV-SL-eGFP particles resulted in the expression of eGFP in single cells without spreading to neighboring cells, and inoculation with iRVFV-ML particles did not result in the production of viral proteins (**Fig. 4B, C**).

Remarkably, upon simultaneous inoculation with iRVFV-SL-eGFP and iRVFV-ML, abundant expression of eGFP but also of Gn was observed within the same cells, suggesting that particles from both populations can co-infect individual cells and together provide a complete set of genome segments encoding all the viral proteins. The co-expression of eGFP and Gn was accompanied by the detection of clusters of infected neighboring cells and a rapid increase in the percentage of infected cells over time, as was also observed after infection with the three-segmented RVFV-eGFP strain (**Fig. 4B, C** and **Supplementary Fig. 1**). This result strongly suggests that co-infection with complementing incomplete particles allows the reconstitution of a three-segmented virus. Notably, complementation by incomplete particles was efficient in both BSR-T7/5 and C6/36 cells even at low MOIs (≥0.1 and ≥0.01, respectively) (**Fig. 4D** and **Supplementary Fig. 1**). Next, to confirm whether cells simultaneously exposed to the two different populations of incomplete particles produce infectious progeny able to spread efficiently *in vitro*, we passaged the supernatants of both BSR-T7/5 and C6/36 cells to naive cells. The results showed that early after infection (24 hpi), a high proportion of the cell population abundantly co-expressed eGFP and Gn, with clusters of positive cells rapidly expanding, suggesting that infectious virus was rescued (**Fig. 4E**).

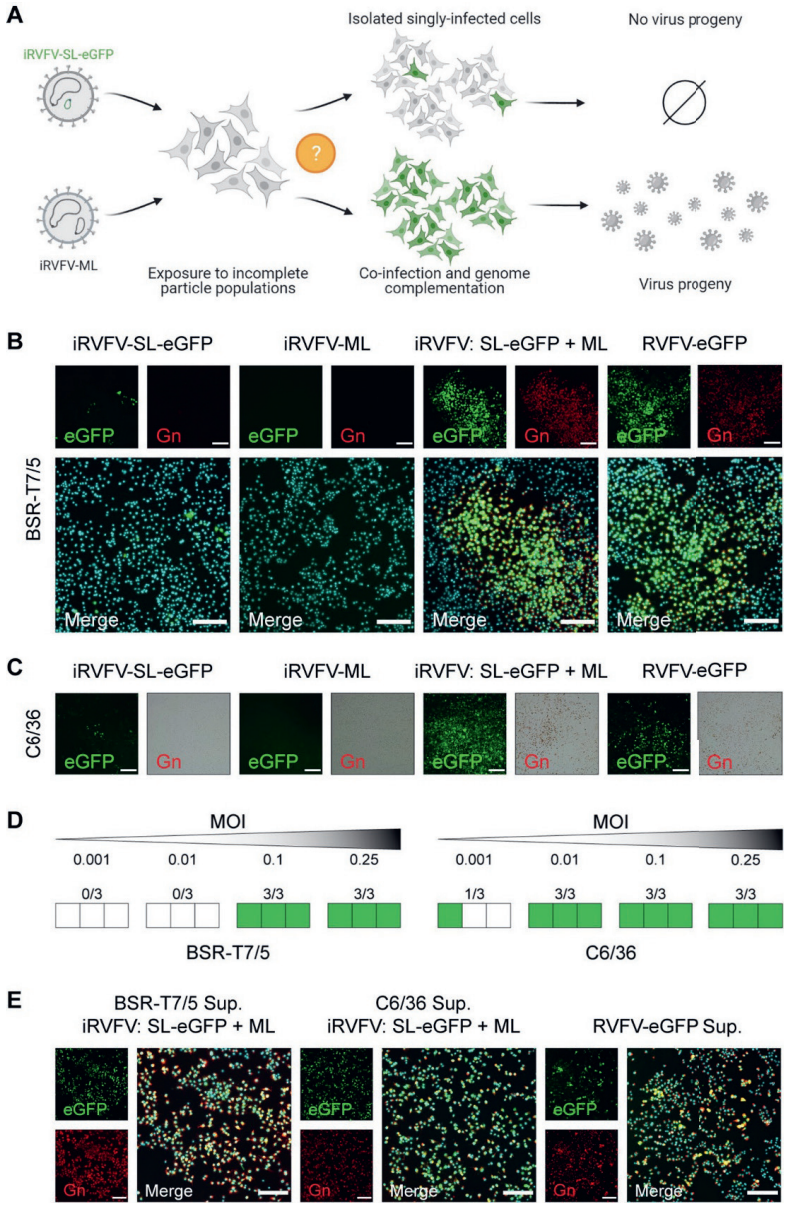

Figure 4. Co-infection with complementing incomplete RVFV particles results in efficient virus replication and spread among mammalian and insect cells. A Schematic representation of the individual or simultaneous exposure of mammalian (BSR-T7/5) and insect (C6/36) cells to non-spreading iRVFV-SL-eGFP and iRVFV-ML particles. If individual susceptible cells become co-infected by the two different incomplete particles, genome complementation could eventually allow virus replication and production of infectious progeny. **B, C** BSR-T7/5 cells (**B**) and C6/36 cells (**C**) were mock-infected, infected exclusively with one population of incomplete particles (MOI 0.1), or simultaneously infected with iRVFV-SL-eGFP and iRVFV-ML (MOI 0.1 for each virus). Cells infected with a three-segmented RVFV-eGFP (MOI 0.2) were used as a positive

control. In all cases, infected cells were analyzed at 24 h (BSR-T7/5 cells) or 72 h (C6/36 cells) post-infection by following the expression of eGFP (green) via direct fluorescence microscopy and the expression of Gn (red) via an immunofluorescence assay in BSR-T7/5 cells or an immunoperoxidase monolayer assay in C6/36 cells. For detection of Gn in C6/36 cells, the immunoperoxidase monolayer assay was chosen because the fluorescent signal got drastically reduced upon fixation of the cells. Expression of Gn was detected with rabbit polyclonal anti-Gn serum in combination with Alexa Fluor 568–conjugated secondary antibodies (immunofluorescence assay) or with HRP-conjugated secondary antibodies (immunoperoxidase monolayer assay). Cell nuclei (cyan) were visualized with DAPI. Scale bars, 200 μm. **D** Infections were also carried out at different MOIs (ranging from 0.001 to 0.25 for each virus, **Supplementary Fig. 1**) in triplicate. Green squares represent successful genome complementation leading to virus replication and spread. White squares represent absence of genome complementation. Source data are provided in **Supplementary Data 1**. **E** Supernatants from BSR-T7/5 and C6/36 co-infected cells or cells infected with RVFV-eGFP were passaged onto naive BSR-T7/5 cells. Cells were examined at 24 h post-infection combining direct fluorescence microscopy and immunofluorescence as described for panels in **B**. Scale bars, 200 μm. Illustration in **Fig. 4A** was created with BioRender.com.

Besides tracking the course of infection at the cell population level, we also analyzed the intracellular genome content of individual infected BSR-T7/5 cells using a combined smFISH-immunofluorescence method[22] (**Fig. 5A**). As expected, in cells exposed exclusively to iRVFV-SL-eGFP, we detected abundant copies of the S and L genome segments, while the M segment and the Gn glycoprotein were absent. No expression of eGFP or Gn was detected in cells exclusively exposed to iRVFV-ML particles, as the S genome segment is missing in this population, and thus no genome replication or transcription could take place. Contrary to cells exposed to only one population of incomplete particles, cells simultaneously exposed to both iRVFV-SL-eGFP and iRVFV-ML particles showed abundant copies of each of the three genome segments, similar to cells infected with the three-segmented RVFV-Clone 13 (**Fig. 5B**).

Finally, we used our smFISH-immunofluorescence method to obtain additional insights into the intravirion composition of the incomplete particle populations and the progeny virions released upon co-infection with these incomplete particles (**Fig. 5A**). Importantly, the M genome segment was not present in iRVFV-SL-eGFP particles, and the S genome segment was not present in iRVFV-ML particles, confirming the absence of the respective segment in each of the incomplete particle populations. Notably, just as in stocks of the three-segmented positive control RVFV-Clone 13, a fraction of the virions produced by co-infected cells was shown to contain the complete set of S, M, and L genome segments, ultimately confirming the reconstitution of infectious three-segmented virus upon co-infection with incomplete particles (**Fig. 5C**).

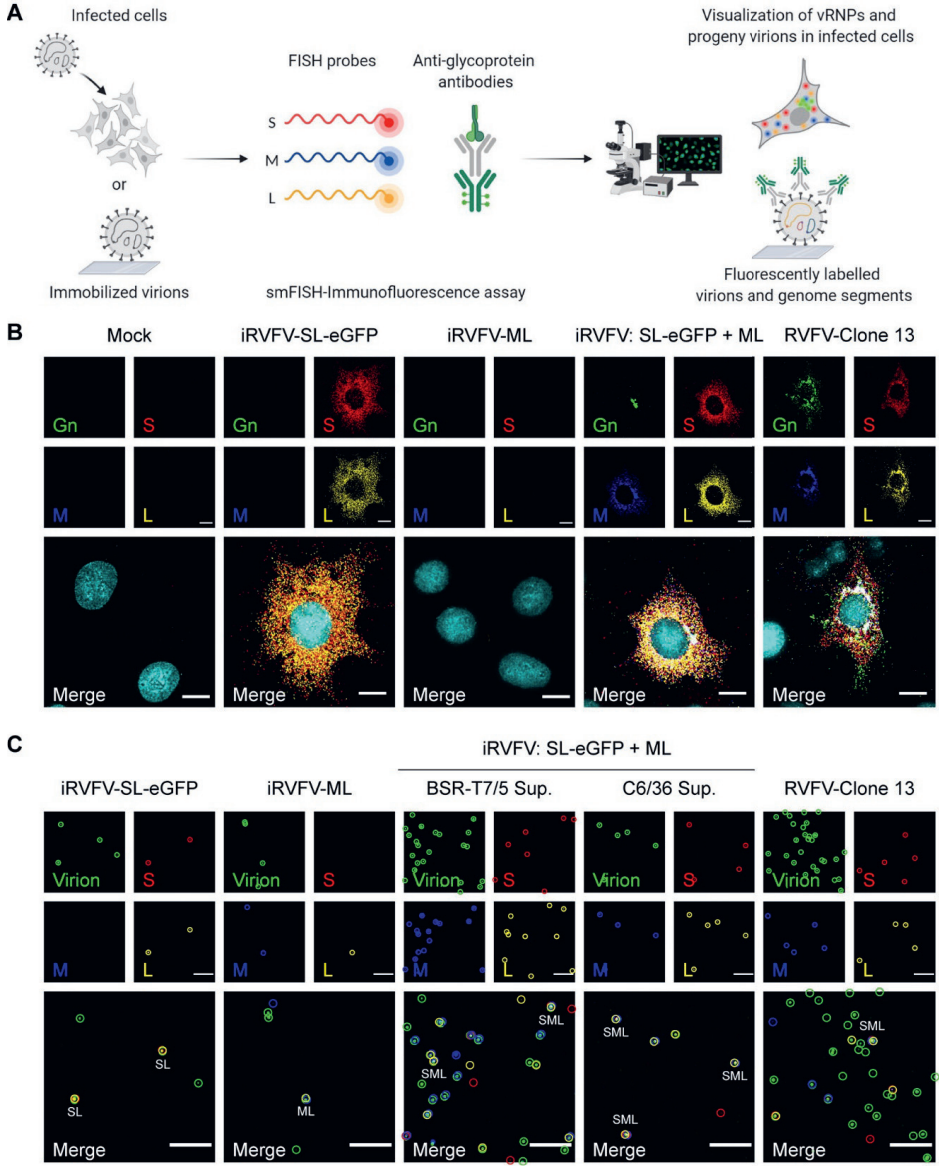

Figure 5. Visualization of viral genome segments in RVFV-infected cells and in immobilized RVFV virions from virus stocks and co-infection supernatants. A Schematic representation of the single-molecule viral RNA FISH-immunofluorescence method used to visualize the intracellular viral ribonucleoprotein (vRNP) composition of infected cells and the intravirion genomic composition of virus stocks and culture supernatants (illustration based on[22]). **B** BSR-T7/5 cells were mock infected, infected exclusively with one population of incomplete particles (MOI 1), or simultaneously infected with iRVFV-SL-eGFP and iRVFV-ML (MOI 1 for each virus), and fixed at 16 h post-infection. Cells infected with a three-segmented RVFV-Clone 13 (MOI 1) were used as positive control. **C** RVFV virions from incomplete particle stocks and supernatants of co-infected BSR-T7/5 and C6/36 cells were immobilized on coverglass by incubation for 5 h at 28°C. The

S segment (N gene, red), M segment (polyprotein gene, blue), and L segment (RdRp gene, yellow) were hybridized using probe sets labeled with CAL Fluor Red 610, Quasar 670, and Quasar 570, respectively. RVFV particles (green) were detected with antibody 4-D4[47] targeting the Gn glycoprotein in combination with Alexa Fluor 488–conjugated secondary antibodies. Cell nuclei (cyan) were visualized with DAPI. Merge images show the overlay of five (for cells) or four (for virions) individual channels. Individual spots, each representing either a single vRNP or a virus particle, were detected and assessed for co-localization in ImageJ with the plugin ComDet. Colored circles display the spots detected in each channel and their co-localization in the merge image. Scale bars, 10 μm (**B**), 5 μm (**C**). Illustration in **Fig. 5A** was created with BioRender.com.

Co-infection with complementing incomplete RVFV particles supports *in vivo* virus spread in mosquitoes

Having confirmed the ability of incomplete RVFV particles to generate a productive infection *in vitro* upon co-infection, we hypothesized that incomplete bunyavirus particles could also play a role in between-host virus transmission. To investigate this, groups of *Aedes aegypti* mosquitoes were fed with bovine blood meals spiked with diverse virus populations. Mosquitoes were exposed to a mock blood meal (group #1), a blood meal spiked with a single incomplete virus particle population (group #2 to iRVFV-SL-eGFP and group #3 to iRVFV-ML), a blood meal spiked with three-segmented RVFV-mCherry2 (group #4) or a blood meal spiked with a mixture of incomplete particles (iRVFV-SL-eGFP and iRVFV-ML, group #5). After incubation for 12 to 15 d post-feeding at 28°C, mosquitoes were analyzed for virus replication in their bodies and dissemination to the saliva (**Fig. 6A**). To this end, body homogenates and saliva samples were tested by virus isolation on BSR-T7/5 cells, using the expression of virus-encoded eGFP or mCherry2 (depending on the virus) as a readout.

All the mosquitoes fed on a mock blood meal (group #1, $n = 15$) or a blood meal spiked with only one population of incomplete virus particles (group #2, $n = 25$; and group #3, $n = 20$) were virus-negative in their bodies and saliva (**Fig. 6B**). No virus spread was observed in these groups, as iRVFV-SL-eGFP and iRVFV-ML both lack one genome segment, either the M or the S segment. In group #4, 33 out of 52 (63%) mosquitoes fed on a blood meal spiked with three-segmented RVFV-mCherry2 were virus-positive in their bodies, confirming the high vector competence of the mosquitoes for RVFV. Eleven of these 33 mosquitoes were also virus-positive in their saliva, implying that RVFV-mCherry2 had replicated in the mosquito midgut, disseminated throughout the body, reached the salivary glands, and was excreted in saliva. Strikingly, 24 out of 62 (39%) mosquitoes in group #5, which were fed on a blood meal spiked with a mixture of iRVFV-SL-eGFP and iRVFV-ML particles, were found to have virus-infected bodies. Of those 24, three mosquitoes

were virus-positive in their saliva (**Fig. 6B, C**). These results show that genome complementation via co-infection with two populations of RVFV exclusively comprising incomplete particles can also occur *in vivo*, supporting virus spread in mosquitoes and presumably contributing to virus transmission between hosts.

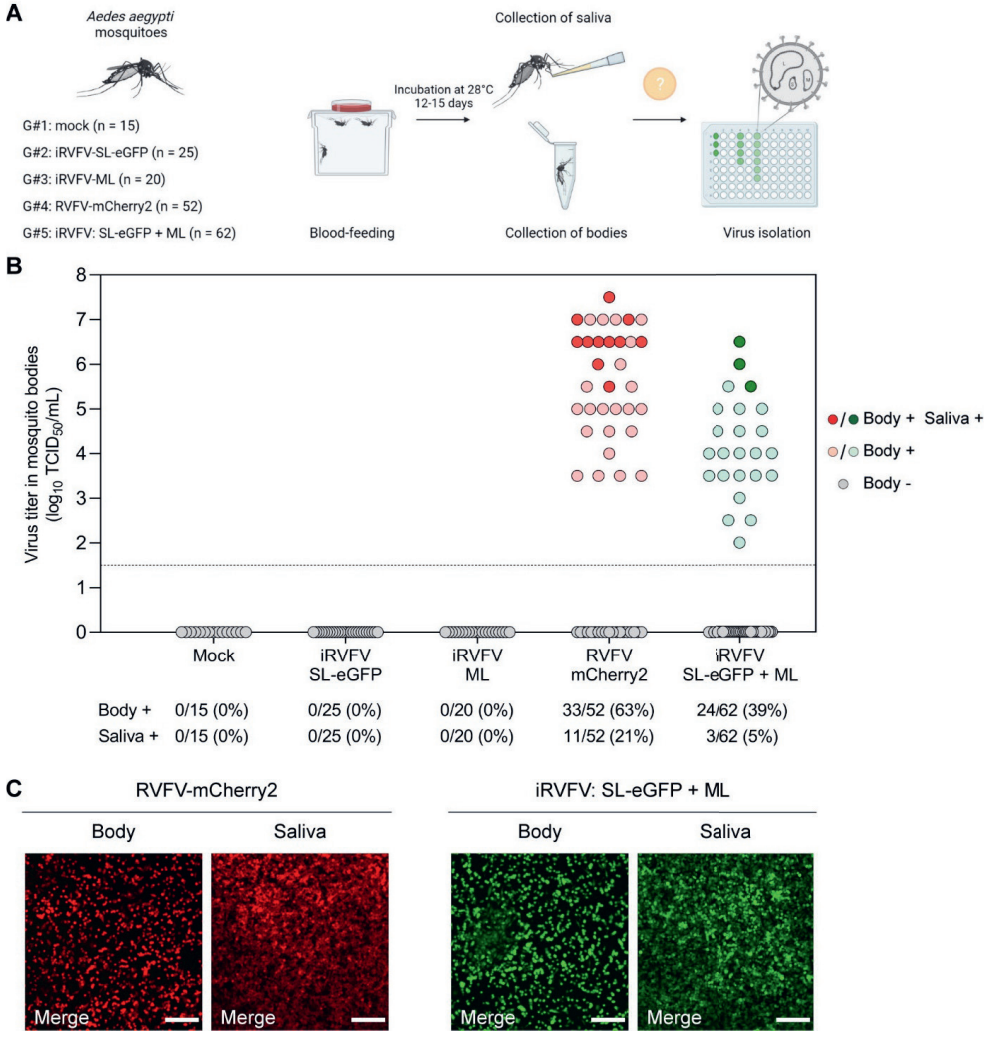

Figure 6. RVFV incomplete particles complement upon co-infection and allow virus replication and spread in mosquitoes. A Schematic representation of the experimental design. Five groups of *Aedes aegypti* mosquitoes (n = 15–62 per group) were fed a blood meal spiked with different RVFV preparations and housed at 28°C. After 12–15 d, mosquitoes were sedated with CO_2 and body and saliva samples were collected. RVFV infection of mosquito bodies and transmission to mosquito saliva were assessed via virus isolation with a fluorescence microscopy readout. **B** RVFV infectious titers in mosquito bodies. Dots

represent individual mosquitoes and are color-coded gray for negative bodies, light red (group #4) or light green (group #5) for positive bodies, and solid red (group #4) or solid green (group #5) for both body and saliva virus-positive mosquitoes. The dashed line indicates the limit of detection ($10^{1.5}$ $TCID_{50}$/mL). The incidence (in absolute numbers and percentages) of RVFV infection (bodies) and transmission (saliva) is indicated at the bottom for each group. Data corresponding to mosquitoes from groups #4 and #5 derive from two independent experiments. Source data are provided in **Supplementary Data 1**. **C** Representative fluorescence microscopy images of BSR-T7/5 cells inoculated with virus-positive body and virus-positive saliva samples from groups #4 (RVFV-mCherry2) and #5 (iRVFV: SL-eGFP + ML) at 48 h post-infection. Merge images show the overlay of two individual channels (eGFP and mCherry2). Scale bars, 200 μm. Illustration in **Fig. 6A** was created with BioRender.com.

Predicting the contribution of incomplete particles to virus spread

We showed that experimental co-infection with complementing two-segmented incomplete particles results in the rescue of spreading three-segmented virus both *in vitro* and *in vivo*. However, incomplete particles naturally co-exist within a mixed population of empty, incomplete, and complete particles. To know the relevance of incomplete virus particles for infection dynamics, it is important to measure to what extent incomplete particles actually contribute to virus spread. Ideally, this question should be addressed by comparing the performance of a natural virus population to a population in which infection by incomplete particles is blocked. Alternatively, this could be studied with experiments in which only complete virus particles are generated. As such experiments are technically not possible at present, we used a simulation model to compare RVFV infection dynamics in three different scenarios: (i) non-selective genome packaging without productive co-infection by incomplete virus particles; (ii) non-selective genome packaging with productive co-infection by incomplete virus particles; and (iii) selective genome packaging (**Fig. 7A** and **Supplementary File 2**).

In both the first and second scenarios, there is non-selective packaging, and the distribution of genome segments over virus particles approximately follows the empirical distribution. In the first scenario, the model assumes that the infection is driven exclusively by complete three-segmented particles, which only account for a small fraction of the particle population. By contrast, the second scenario allows the infection to progress by both complete particles and co-infecting incomplete particles, provided all segments are present in a single cell. Lastly, in the third scenario, it is assumed that all the particles are complete due to selective packaging, which serves as a reference point. Since there are differences in genome packaging efficiencies between mammalian and insect hosts[22], and, therefore, the exact ratio between empty, incomplete, and complete particles differs considerably depending on the host, we performed simulations with RVFV populations representative of those found in mammalian and insect hosts.

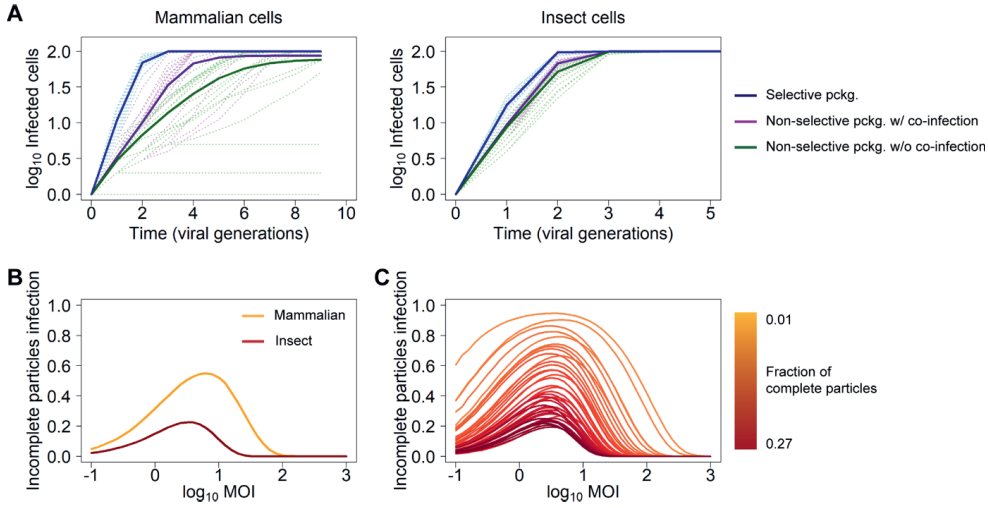

Figure 7. Predicting the contribution of incomplete particles to within-host virus spread. A Predicted RVFV infection dynamics in mammalian and insect cells in three different scenarios: selective genome packaging, non-selective genome packaging without co-infection by incomplete particles, and non-selective genome packaging with co-infection and productive complementation by incomplete particles. The low number of cells in the model is representative of localized virus spread. Solid lines represent the mean of n = 1,000 simulations per scenario, and the light-colored dashed lines represent 20 individual simulations. pckg.: packaging. **B** Contribution of incomplete particles to virus spread in mammalian and insect cells as a function of the MOI in a model representative of non-selective genome packaging allowing co-infection by incomplete particles. Lines represent the mean of n = 500–10^4 simulated cells, with a larger number of cells for the low MOI conditions where overall infection frequencies are low. **C** Contribution of incomplete particles to virus spread as a function of the MOI for starting inoculums with different frequencies of complete particles. Lines are color-coded in a gradient of dark yellow to dark red based on an increasing fraction of complete particles (ranging from 0.01 to 0.27) within the virus population. The code required to reproduce the plots of this figure is provided as **Supplementary File 2**.

Model parameters were defined to represent the conditions of localized virus spread (i.e., mean-field simulations in a small number of cells, for instance, 100), and the model predicts how the number of infected cells changes over time. In the first scenario, the number of infections increases the slowest, being limited by the small number of complete virus particles. In the second scenario, when the model considers that incomplete particles can generate a productive infection through complementation, the number of infected cells increases more rapidly, highlighting the contribution of incomplete particles to virus spread. However, the number of infected cells does not increase as quickly as in the third scenario in which all virus particles are complete, suggesting there is still a cost to non-selective packaging (**Fig. 7A** and **Supplementary File 2**). Importantly, the model is sensitive to the host in which the virus is replicating, suggesting that the contribution of

incomplete particles to virus spread is greater in mammalian cells than in insect cells due to the smaller fraction of complete particles in mammalian-derived virus.

When we considered how model parameter values affect the predictions, we found that the main trends noted here were also found over different conditions; there is often an advantage for the virus that allows complementation through co-infection over the non-complementing one, while the virus with selective genome packaging outperforms both viruses with non-selective packaging. Under some conditions, the performance of the virus with non-selective packaging but that allows genome complementation resembles that of a virus that employs selective packaging (**Supplementary Text 1**, **Supplementary Figs. 2, 3** and **Supplementary File 3**). Overall, these results suggest that incomplete virus particles can contribute to the spread of RVFV over a broad range of conditions but that non-selective packaging is generally costly and leads to inferior performance compared to a virus with selective packaging.

In both cases shown in **Fig. 7A**, the viruses employing non-selective packaging with or without complementation appear to perform the same initially. Later in the infection process, the complementing virus outperforms the non-complementing virus. As the MOI will increase over rounds of infection, these simulation results suggest an important role of the MOI in determining the relevance of incomplete particles to virus spread. We therefore explored the relationship between MOI and the contribution of incomplete particles more systematically. We calculated the fraction of infected cells comprising a complete set of genome segments as a result of co-infection with incomplete particles only, over a range of MOIs (**Fig. 7B** and **Supplementary File 2**).

The simulations show that the MOI has a pronounced effect on the contribution of incomplete particles to virus spread, with a limited contribution at extreme MOIs. At low MOIs, there is a low probability of particles co-infecting the same cell, and, consequently, complementation events are rare, whereas at high MOIs, in most cells, infection will be initiated by at least one complete particle, and complementation of incomplete particles is not required for virus spread. Notably, at intermediate MOIs, infection initiated by complementing incomplete particles is more common and plays an important role in virus spread (**Fig. 7B** and **Supplementary File 2**). Here again, the contribution of incomplete particles is estimated to be higher in the mammalian host than in the insect host, because insect-derived virus preparations contain a larger fraction of complete particles[22].

To gauge how general these model results are, we considered the relationship between MOI and the contribution of incomplete virus particles over a broad range of randomly selected genome segments frequencies for a three-segmented virus. Interestingly, the larger contribution of incomplete particles at intermediate MOIs appears to be a general feature over different virus particle compositions (**Fig. 7C** and **Supplementary File 2**). In line with what we observed for the mammalian- and insect-derived virus, this contribution becomes less relevant when the fraction of complete particles becomes larger.

Discussion

Mammalian-infecting viruses with an incomplete genome are unable to spread autonomously and have principally been considered as a source of interference in the course of an infection[25]. Segmented viruses with a non-selective genome packaging strategy are prone to generate large fractions of empty and incomplete particles[21,22], which in theory could detriment the fitness of the virus population as a whole. We hypothesized, however, that incomplete bunyavirus particles may contribute to virus spread by complementing their genomes inside cells co-infected with multiple particles, resembling the strategy that multipartite viruses use to replicate in plants and fungi. Using the three-segmented RVFV as a prototype bunyavirus with a non-selective genome packaging mechanism, we show here that incomplete bunyavirus particles can genetically complement upon co-infection and potentially contribute to within-host spread and between-host transmission. We cannot deduce from our experimental results how important genome complementation between incomplete particles is for virus spread. However, our modeling results suggest that complementation can have a significant effect on virus spread over a broad range of conditions, particularly when the distribution of genome segments over virus particles is similar to that observed in mammalian cells.

By creating fluorescently labeled RVFV variants, we were able to visualize infection of single cells by more than one virus particle and to show that mammalian and insect cells are prone to co-infection as a function of the MOI. Notably, the fractions of experimentally infected and co-infected cells coincided with model predictions, suggesting that the probability of (co-)infection does not depend on factors other than the intrinsic heterogeneous susceptibility within a host cell population. In our experiments, we exposed cells to two different RVFV variants simultaneously, as this represents a common scenario during a localized infection, in which non-infected cells are exposed to the burst of virus particles released by a neighboring infected cell. Nevertheless, it should be noted that susceptibility to co-infection may differ when cells are

exposed to the viruses at different time points due to innate immune responses and/or superinfection exclusion mechanisms, as has already been shown for other arthropod-borne viruses[26–29]. The frequency of co-infection events upon delayed exposure to a second virus is thus likely lower compared to simultaneous exposure. Additionally, it would be interesting to compare host cell responses following infection by a three-segmented virus, a two-segmented virus capable of replicating its genome, and a two-segmented virus unable to replicate its genome.

By generating two different incomplete virus particle populations entirely dependent on co-infection (iRVFV-SL-eGFP and iRVFV-ML), we showed at the cell population and single-cell levels that within-host genome complementation occurs readily in mammalian and insect cells, resulting in infectious progeny able to spread similarly as progeny resulting from infection with a virion containing all three genome segments. Importantly, by examining the genome composition of individual virions, we confirmed that cells simultaneously exposed to complementing incomplete particle populations can produce complete virus particles containing all three genome segments. As expected, the contribution of genome complementation to virus spread was found to depend on the MOI. Specifically, at both low and very high MOIs, the contribution to virus spread by incomplete particles was predicted to be negligible. The former is explained by the low probability of co-infection and the latter by the high probability of infection by a complete particle. Experimentally, we confirmed that at very low MOIs (≤0.01 for BSR-T7/5 cells and ≤0.001 for C6/36 cells), the chance of a co-infection event is rather low and consequently the probability of a productive infection is reduced (**Fig. 4D** and **Supplementary Fig. 1**). These results are in line with the mathematical models that predicted the contribution of incomplete particles to be highest at intermediate MOIs. It is worth noting that co-infection experiments were initially carried out in immune-deficient cell lines (BSR-T7/5 cells are interferon-deficient and C6/36 cells lack RNAi response), but having confirmed successful genome complementation *in vitro*, we proceeded to test our hypothesis *in vivo* in mosquitoes.

A previous report on the eight-segmented IAV showed that a virus entirely dependent on co-infection replicated efficiently in guinea pigs but was less infectious than the wild-type virus and was not able to transmit between animals[19]. Here, we show that *in vivo* bunyavirus genome complementation can occur in the mosquito vector. It should be noted that after a mosquito ingests an infectious blood meal, the resulting MOI is probably very low, which reduces the probability of multiple particles entering the same cell. To resemble the low probability of co-infection of midgut cells to that of a natural situation, we used virus titers in the blood meals that were comparable to virus titers observed in viremic lambs (approximately 10^7 $TCID_{50}$/mL)[30].

Despite the presumably low MOI, a fraction of the mosquitoes given a blood meal spiked with virus particles exclusively containing incomplete sets of genomes were found to be infected (both in bodies and saliva). Infected mosquito bodies can only be explained by complementing particles co-infecting the same midgut cell followed by the generation of a mixed virus progeny including three-segmented virus. Most likely, these co-infections occur in a small number of midgut epithelial cells that are highly susceptible to the virus, as reported previously for other arthropod-borne viruses[31–34].

Furthermore, the rescue of infectious virus from mosquito saliva indicates that the virus progeny was able to disseminate from the midgut cells to the hemocoel, generally considered a major bottleneck for virus dissemination in mosquitoes[35], and from the hemocoel to the salivary glands. Due to the absence of complete particles in the starting inoculum of the iRVFV-SL-eGFP and iRVFV-ML mixture, it was expected that the infectivity of this mixture was lower than the infectivity of the three-segmented RVFV-mCherry2. Although with lower efficiency, the fact that we rescued infectious virus from the saliva of mosquitoes fed with the mixture of incomplete particles suggests that incomplete particles may play a role in between-host virus transmission. Interestingly, we observed a positive correlation between the infectious virus titer in the body and the presence of infectious virus in saliva, with virus-positive saliva samples corresponding to mosquitoes with a high virus titer in their bodies. An *in vivo* experiment evaluating if it is possible to rescue infectious virus after exposing a mammalian host exclusively to a mixture of incomplete bunyavirus particles, either applied at the same skin site mimicking a mosquito bite or at distinct sites, would be valuable, but it remains subject of future research.

Several mechanisms have been proposed that may compensate for the fitness cost resulting from inefficient bunyavirus genome packaging. For instance, the incorporation of more than three genome segments per particle, which increases the likelihood of incorporating a complete set of segments[23]. Alternatively, groups of virions could be transmitted together in structures known as collective infectious units, jointly delivering multiple virions to target cells and drastically increasing the local MOI[36–39]. The latter, together with our finding that incomplete bunyavirus particles can genetically complement within co-infected cells, has important biological implications particularly for within-host virus spread, where following a primary infection of a target organ, neighboring cells become a local environment exposed to intermediate and high MOIs. In this study, we focused on co-infections by incomplete particles of the same virus. However, co-infections by incomplete particles of different but genetically related viruses could

give rise to reassortment events, adding to the potential roles of incomplete particles in the infection cycle and evolution of bunyaviruses.

Our data on localized virus spread driven by incomplete bunyavirus particles align with observations on IAV collectively delivering a complete genome upon simultaneous infection of individual cells with multiple virions[19]. Despite this similarity, a fundamental difference exists between the selective genome packaging process employed by IAV, which is facilitated by the formation of a supramolecular complex[6–9], and the non-selective process employed by RVFV[23]. As complete particles are scarce in populations of viruses that employ a non-selective packaging mechanism like RVFV, at least in theory, the dependence on genomic complementation by incomplete particles is likely much greater for bunyaviruses. Due to the large fraction of incomplete particles generated during bunyavirus infection and their potential to support virus spread, we hypothesize that the life cycle of bunyaviruses resembles to a certain degree that of multipartite viruses, which rely on co-infection with complementing particles to deliver a complete set of genome segments. Interestingly, a recent study with the octapartite FBNSV showed that the theoretical fitness cost of a multipartite genome can be reduced, at least partially, through non-concomitant acquisition of complementary sets of genome segments during between-host transmission[40]. Whether bunyaviruses can also reconstitute a complete genome through non-concomitant transmission awaits further investigation.

Altogether, the results of this study show that upon co-infection, incomplete bunyavirus particles can initially drive efficient progeny virus generation and spread, even in the absence of three-segmented RVFV infectious particles in the inoculum. In the context of natural infection with a mixed bunyavirus particle population, we propose that incomplete particles, instead of interfering, can support virus infection and spread, facilitating the dual life cycle of bunyaviruses in mammalian and insect hosts. At the tissue and organ levels, primary infected cells release a burst of complete and incomplete particles, generating a local intermediate to high MOI that can facilitate genome complementation within cells infected with complementing incomplete particles. Under these conditions, incomplete particles can directly contribute to localized secondary within-host virus spread (**Fig. 8A**). To facilitate between-host transmission, incomplete particles present in the blood of a mammalian host could be taken up by the mosquito and subsequently co-infect cells of the mosquito midgut. The reconstituted infectious virus could disseminate to the salivary glands, where the virus can then be transmitted back to a mammalian host via a mosquito bite (**Fig. 8B**). We hypothesize that the contribution of incomplete particles to virus infection and spread, predicted to be particularly important at intermediate MOIs

(**Fig. 8C**), partially compensates for the fitness cost of inefficient genome packaging. In conclusion, the present work stands out an important role of incomplete particles in the infection cycle of bunyaviruses, revealing parallels in the life cycles of segmented and multipartite viruses.

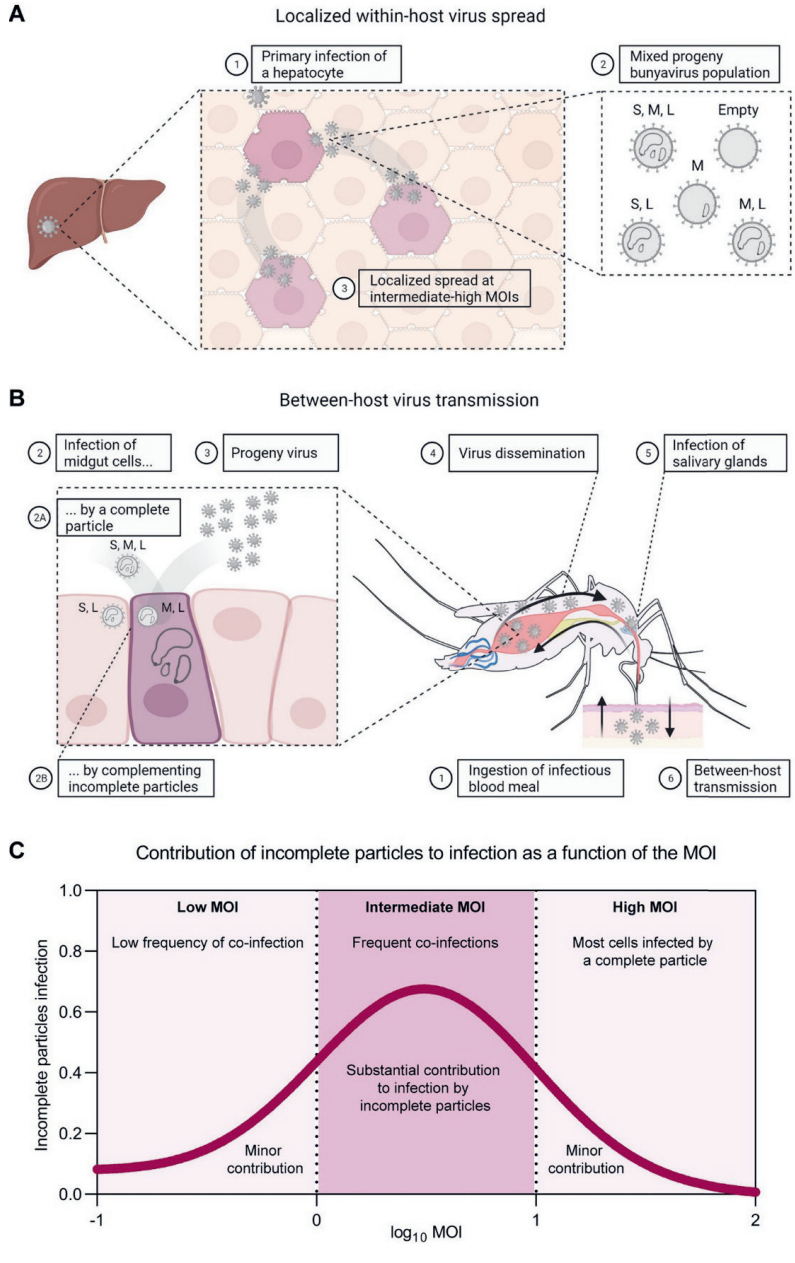

Figure 8. Schematic representation of the proposed model describing the contribution of incomplete virus particles to within-host spread and between-host transmission. A Localized within-host virus spread. (1) Most likely, a complete three-segmented particle derived from an infected mosquito vector starts a primary infection in a target organ (e.g., liver). (2) Due to a non-selective genome packaging mechanism, bunyavirus-infected cells give rise to a virus progeny population comprising a mixture of complete, incomplete, and empty virus particles. Although non-infectious on their own, incomplete particles with a complementing genome can co-infect the same cell and generate infectious progeny, contributing to localized secondary virus spread. (3) At the organ and tissue levels, the intermediate to high local MOI can greatly facilitate the occurrence of this phenomenon. **B** Between-host virus transmission. (1) The life cycle of bunyaviruses involves replication in both mammalian and insect hosts. For transmission, mosquitoes ingest an infectious blood meal from an infected animal. (2) Either through a complete three-segmented particle (2A) or through co-infection by complementing incomplete particles (2B), the virus infects a small group of highly susceptible cells of the mosquito midgut and (3) generates infectious progeny. (4) The virus disseminates from the midgut into the hemocoel and (5) reaches the salivary glands, where the virus also replicates. (6) To complete the cycle, the virus is excreted in the mosquito saliva and can be transmitted to a mammalian host through a mosquito bite (illustration inspired on[35]). Although perhaps at a lower frequency than in a localized environment, co-infection with incomplete particles can contribute to between-host virus transmission. Viruses transmitted as collective infectious units can facilitate the co-infection of a single cell by multiple particles. **C** Conceptual illustration of the relationship between the MOI and infections caused entirely by incomplete virus particles. At low MOIs (<1), infections caused by co-infection with incomplete particles are rare because, on average, less than a single virus particle will enter each cell. This situation is likely to represent the conditions of between-host transmission and early infection stages in a new host, where our data show that although incomplete particles have reduced infection potential, infection is still possible. At intermediate MOIs (1–10), infection via co-infecting incomplete particles becomes more common, as on average more virus particles enter each cell. This situation is likely to be representative of later infection stages within a host, when cells are exposed to larger numbers of virus particles. At high MOIs (>10), infection caused only by incomplete virus particles becomes rare, as most cells will also be infected by a complete virus particle. In this regime, incomplete particles can still contribute genetically to infection, but complementation between virus particles is no longer needed to establish infection. This latter situation may not be representative of conditions found in natural infections but can be generated in cell culture. Illustrations in **Fig. 8A, B** were created with BioRender.com.

Materials and methods

Cell lines

BSR-T7/5 cells (Golden hamster kidney, CVCL_RW96) stably expressing bacteriophage T7 RNA polymerase[41] were maintained in Glasgow minimum essential medium (G-MEM) supplemented with 5% fetal bovine serum (FBS), 1% antibiotic/antimycotic, 1% MEM non-essential amino acids (MEM NEAA), and 4% tryptose phosphate broth at 37°C and 5% CO_2. For stable maintenance of the cell line, the medium was supplemented with 1 mg/mL Geneticin (G-418 sulfate) every other passage. Vero E6 cells (African green

monkey kidney, ATCC CRL-1586) were maintained in MEM supplemented with 5% FBS, 1% antibiotic/antimycotic, 1% MEM NEAA, and 2 mM L-glutamine at 37°C and 5% CO_2. C6/36 cells (*Aedes albopictus* larva, ATCC CRL-1660) were maintained in L-15 medium (Leibovitz) (Sigma-Aldrich) supplemented with 10% FBS, 1% antibiotic/antimycotic, 1% MEM NEAA, and 2% tryptose phosphate broth at 28°C. Cell culture media and supplements were purchased from Gibco, unless specified otherwise.

Viruses

Virus stocks of RVFV strain Clone 13[42] were obtained following infection of Vero E6 cells at an MOI of 0.005. Recombinant fluorescently marked variants of RVFV strain 35/74 (accession numbers JF784386-88)[43], expressing either eGFP (RVFV-eGFP) or mCherry2 (RVFV-mCherry2), were generated by a pUC57 transcription plasmid-based reverse genetics system[24]. Briefly, BSR-T7/5 cells were seeded in 6-well cell culture plates at 1.5 to 2.0 × 10^5 cells/well (2 mL volume) and incubated for 18 to 24 h to generate a sub-confluent monolayer. Cells were subsequently co-transfected with the plasmids pUC57_S-FP (where FP corresponds to either eGFP or mCherry2 in place of the NSs gene), pUC57_M and pUC57_L, encoding the RVFV-35/74 S, M, and L genome segments, respectively, in antigenomic-sense orientation. Transfections were performed using *Trans*IT-LT1 transfection reagent (Mirus), with slight modifications to the manufacturer's instructions: 3 to 5 h prior to transfection, the seeding supplemented G-MEM was removed and substituted by 1 mL of Opti-MEM I Reduced-Serum medium. For transfection, 2,500 ng total plasmid/well (equal amounts per plasmid) with a 1:4 plasmid to transfection reagent ratio were used. At 3 to 5 h post-transfection, 1 mL of supplemented G-MEM was added. At 3 d post-transfection, culture supernatants were harvested and clarified by low-speed centrifugation. High-titer virus stocks of RVFV-eGFP and RVFV-mCherry2 were obtained following infection of BSR-T7/5 cells at an MOI of 0.001.

Generation of incomplete virus particles

Incomplete RVFV particles lacking either the S segment (iRVFV-ML) or the M segment (iRVFV-SL-FP) were generated by reverse genetics[24]. For the production of iRVFV-ML, BSR-T7/5 cells were co-transfected with pUC57_M, pUC57_L, and the protein expression plasmid pCAGGS_N (encoding for a codon-optimized RVFV-35/74 nucleocapsid protein). For the production of iRVFV-SL-FP, BSR-T7/5 cells were co-transfected with pUC57_S-FP (where FP corresponds to eGFP or mCherry2 in place of the NSs gene), pUC57_L, and the protein expression plasmid pCAGGS_NSmGnGc (encoding for the RVFV-35/74 polyprotein). Transfections were performed using *Trans*IT-LT1 transfection reagent (Mirus), following the protocol described for the generation of recombinant fluorescently marked RVFV-35/74 variants.

To obtain a high-titer stock of iRVFV-ML particles, the rescued supernatant from the transfection was concentrated by ultracentrifugation at 28,000 rpm, 4°C for 2 h (SW 32 Ti swinging-bucket rotor, Optima LE-80K Beckman Coulter) using a 25% w/v sucrose cushion. Furthermore, to obtain higher titers of iRVFV-SL-FP particles, cells initially transfected with the three plasmids were repeatedly transfected two additional times with the protein expression plasmid pCAGGS_NSmGnGc, resulting in a polyclonal cell line

replicating the S and L viral genome segments. New stocks of iRVFV-SL-FP particles were generated by a final transfection of the polyclonal cell line with pCAGGS_NSmGnGc. The latter transfections were performed using jetPEI transfection reagent (Polyplus) with a 1:3 plasmid to transfection reagent ratio. At 1 d post-transfection, culture supernatants were harvested and clarified by low-speed centrifugation.

Virus titration

Infectious titers of rescued virus and virus stocks were determined in an end-point dilution assay in combination with either an immunoperoxidase monolayer assay (IPMA, as described below) or direct microscopy detection of FP expression. BSR-T7/5 (3×10^4 cells/well) or C6/36 (6×10^4 cells/well) monolayers were incubated with 10-fold serial dilutions (starting at 1:10) of the samples for 72 h at 37°C and 5% CO_2 (BSR-T7/5) or 28°C (C6/36). Samples were analyzed in triplicate or quadruplicate, and the titer was calculated as the median tissue culture infectious dose ($TCID_{50}$/mL) using the Spearman–Kärber method.

Growth curves of fluorescent virus variants

BSR-T7/5 monolayers (3×10^6 cells/T75 flask) were infected with RVFV-eGFP or RVFV-mCherry2 at an MOI of 0.01. At 2 h post-infection, the inoculum was removed, cells were washed with PBS, and fresh medium was added. Cell culture supernatants were harvested at 0, 2, 12, 24, 48, and 72 h post-infection and were clarified by centrifugation at 2,500 rcf for 10 min. Virus titers of the clarified supernatants were determined with an end-point dilution assay (fluorescence microscopy readout) as described above. Growth curve determinations were performed with three biological replicates per time point.

Genome segment-specific quantitative RT-PCR

As a conventional end-point dilution assay is not suited for determining the titer of non-replicating particles, we estimated the titer of iRVFV-ML stocks through genome segment-specific quantification via RT-qPCR, followed by a comparison with the genome copies of iRVFV-SL-eGFP and three-segmented RVFV-eGFP preparations with known infectious titer determined with the end-point dilution assay. Total RNA extractions of 80 µL of virus stocks lyzed with 240 µL of TRIzol LS Reagent (Invitrogen) were performed in triplicate with the Direct-zol RNA MiniPrep kit (Zymo Research), largely according to the manufacturer's instructions, except for a more thorough in-column DNase I treatment. Namely, lyzed preparations were treated with 60 units of DNase I for 30 min. The extended DNase I treatment ensured the complete removal of residual plasmid DNA from the transfection. Total RNA was eventually eluted in 25 µL of DNase/RNase-free water (Zymo Research). Subsequently, viral cDNA was synthesized with the SuperScript IV First-Strand Synthesis System for RT-PCR (Invitrogen) using 100 units of SuperScript IV reverse transcriptase and a combination of S, M, and L segment-specific primers (**Supplementary Table 2**). After the reverse transcription reaction, quantitative PCR amplifications were performed with the Power SYBR Green PCR Master Mix using 5 µL of 50-, 250-, or 500-fold diluted cDNA preparations in a total volume of 25 µL, in combination with a 7500 Fast Real-Time PCR System (Applied Biosystems). Fragments from the three viral genome segments were amplified using specific primers (**Supplementary Table 3**) under the

following conditions: an initial denaturation step at 95°C for 10 min; 40 cycles of denaturation at 95°C for 15 s, annealing at 59°C for 30 s, and extension at 72°C for 36 s; and a single cycle of denaturation at 95°C for 15 s, annealing at 60°C for 1 min, denaturation at 95°C for 15 s, and annealing at 60°C for 15 s. Per sample, an additional reaction intended to detect residual plasmid DNA was carried out using primers designed to amplify a fragment of the ampicillin resistance gene (*ampR*) (**Supplementary Table 3**) present in pUC57 and pCAGGS plasmids used for generating the different RVFV variants. Data were acquired and analyzed with the 7500 Fast System software version 1.4. (Applied Biosystems). Genome copies of each viral segment were calculated by intrapolation of the respective standard curve prepared with 10-fold serial dilutions of the viral segment cloned in pUC57 plasmids starting at 0.1 ng/μL.

Flow cytometry

BSR-T7/5 cells were simultaneously co-infected with iRVFV-SL-eGFP and iRVFV-SL-mCherry2 at increasing MOIs (ranging from 0.1 to 2.5 for each virus). At 48 h post-infection, cells were trypsinized, spun down at 200 rcf for 5 min, fixed with 4% paraformaldehyde for 15 min, washed twice with PBS, and resuspended in sample buffer (PBS supplemented with 1% bovine serum albumin and 0.01% sodium azide). Mock-infected cells and cells infected exclusively with iRVFV-SL-eGFP or iRVFV-SL-mCherry2 at an MOI of 0.5 were used as negative and singly-infected controls, respectively. Flow cytometry was performed using a BD FACS Aria III (BD Biosciences) equipped with a standard laser and filter configuration. Cell subpopulations were categorized and quantified based on the expression of eGFP, mCherry2, both or none. Per sample, 50,000 events were recorded. Data were analyzed with FlowJo version 10.7.1. The gating strategy applied involved discriminating cells from debris, followed by selection of single cells and assessment of FP expression (**Supplementary Fig. 4**).

Co-infections with incomplete virus particles

BSR-T7/5 (5×10^4 cells/well) or C6/36 (1×10^5 cells/well) monolayers seeded in 24-well cell culture plates were simultaneously co-infected with iRVFV-SL-eGFP and iRVFV-ML particles at increasing MOIs (ranging from 0.001 to 0.25 for each virus). At 2 h post-infection, the inoculum was removed, cells were washed with PBS, and fresh medium was added. At defined time points post-infection (varied per cell line and ranged from 24 h to 72 h), cells were examined for expression of eGFP via direct fluorescence microscopy. Expression of Gn in BSR-T7/5 and C6/36 infected cells was examined via an IPMA or an immunofluorescence assay (as described below). The expression of eGFP was followed over the course of the infection as an indicator of viral spread. Co-infections at the different MOIs were performed with three biological replicates. Cells infected exclusively with either iRVFV-SL-eGFP or iRVFV-ML particles were used as singly-infected controls, whereas cells infected with a three-segmented RVFV-eGFP (MOIs ranging from 0.002 to 0.5) were used as positive control for virus spread. Mock-infected samples were used as negative control.

Immunostainings

BSR-T7/5 and C6/36 cells infected with different RVFV variants were subjected to an IPMA or an immunofluorescence assay to detect the expression of the viral proteins Gn and N. At defined time points post-infection (varied per experiment), cells were fixed with 4% paraformaldehyde for 15 min, washed with PBS supplemented with 0.5% Tween 80 (PBST), and permeabilized with 1% Triton X-100 in PBS for 5 min. Next, samples were blocked with 5% horse serum in PBS and subsequently incubated in sequential steps with primary and secondary antibodies diluted in blocking solution (**Supplementary Table 4**). Gn was detected with a polyclonal serum from a Gn-immunized rabbit (1:500 dilution, Thermo Fisher) as primary antibody. For the IPMA, HRP-conjugated goat polyclonal anti-rabbit immunoglobulin (1:500 dilution, P0448 Dako) was used as secondary antibody. For the immunofluorescence assay, goat polyclonal anti-rabbit IgG labeled with FITC (1:250 dilution, sc-2012 Santa Cruz Biotechnology) or donkey polyclonal anti-rabbit IgG labeled with Alexa Fluor 568 (1:500 dilution, A10042 Invitrogen) were used as secondary antibodies. N was detected with a monoclonal mouse hybridoma (1:100 dilution, F1D11 CISA-INIA) as primary antibody and a goat polyclonal anti-mouse IgG labeled with Alexa Fluor Plus 488 (1:500 dilution, A32723 Invitrogen) as secondary antibody. Sample incubations with the blocking solution, primary and secondary antibodies were each for 1 h at 37°C. Plates were washed with PBST after permeabilization, between the addition of primary and secondary antibodies, and prior to staining. In the IPMA, a 0.2-mg/mL amino ethyl carbazole solution in 500 mM acetate buffer (pH 5.0), 88 mM H_2O_2 was added as substrate. In the immunofluorescence assay, cell nuclei were stained by incubation with 1 μg/mL DAPI in PBS for 5 min. Mock-infected samples and samples without the addition of primary antibodies were used as negative controls.

Single-molecule RNA FISH-immunofluorescence

Experiments were performed with slight modifications to the Stellaris protocol for simultaneous FISH-immunofluorescence in adherent cells (Biosearch Technologies)[44–46]. BSR-T7/5 monolayers (1.5×10^4 cells/well) were seeded on CultureWell 16 removable chambered coverglass (Grace Bio-Labs) and allowed to attach for at least 2 h at 37°C and 5% CO_2. Cells were infected with the different RVFV variants at an MOI of 1. At 2 h post-infection, the inoculum was removed and the medium was refreshed. At 16 h post-infection, cells were fixed and permeabilized with a 3:1 mixture of methanol (Klinipath)-glacial acetic acid (Merck) for 10 min. Cells were subsequently washed twice with PBS and once with prehybridization buffer (10% deionized formamide [Millipore] in 2× concentrated SSC [Gibco]) for 5 min. Cells were then incubated for 4 to 16 h at 37°C with 100 μL/well of virus-specific FISH probe sets (**Supplementary Table 5**) and primary antibodies in hybridization buffer (10% deionized formamide, 10% dextran sulfate [Sigma-Aldrich], 2 mM vanadyl ribonucleoside complexes [VRC, Sigma-Aldrich] in 2× SSC). FISH probes were added at a final concentration of 250 nM. Gn was detected with hybridoma 4-D4[47] supernatant (1:160 dilution) as primary antibody (**Supplementary Table 4**). Following hybridization and incubation with primary antibodies, cells were extensively washed at 37°C (twice with prehybridization buffer for 30 min and twice with 2× SSC for 15 min). Subsequently, cells were incubated with 100 μL/well of

secondary antibody for 1 h at 37°C. A goat polyclonal anti-mouse IgG labeled with Alexa Fluor 488 (1:1,000 dilution, A-11001 Invitrogen) was used as secondary antibody (**Supplementary Table 4**). Next, cells were washed twice with 2× SSC, and nuclei were stained by incubation with 100 µL/well of 1 µg/mL DAPI in 2× SSC for 5 min. Finally, cells were washed with 2× SSC and submerged in VectaShield antifade mounting medium H-1000 (Vector Laboratories). For analysis of virus stocks, undiluted or 1:3 diluted virus stocks were added on CultureWell 16 removable chambered coverglass and virions were allowed to attach to the surface for 5 h at 28°C. The same procedure as described for adherent cells was followed from the fixation step onward. The specificity of the FISH probes and antibodies was reported previously[22]. Mock-infected samples and samples without primary antibodies were used as negative controls.

Image acquisition and analysis

Light microscopy images were acquired with a Leica Model DMi1 inverted microscope and 10× HI PLAN I or 20× HI PLAN I objectives. Fluorescence microscopy images were acquired with an inverted widefield fluorescence microscope Axio Observer 7 (ZEISS, Germany) using appropriate filters and a 10× EC Plan-NEOFLUAR objective or a 1.3 NA 100× EC Plan-NEOFLUAR oil objective in combination with an AxioCam MRm CCD camera. Exposure times were defined empirically and differed depending on the probe sets and fluorescent dyes. For the FISH-immunofluorescence assay, Z-stacked images of infected cells and immobilized virions were acquired with a fixed interval of 0.28 to 0.31 µm between slices. Raw images were deconvolved in standard mode using Huygens Professional version 21.04 (Scientific Volume Imaging B.V., the Netherlands). If required, raw images were Z-aligned in ZEN 2.6 Pro (ZEISS, Germany) before deconvolution. For analysis, 3D data were converted to maximum intensity projections using Z-project within ImageJ[48]. Detection, quantification and co-localization analyses of individual spots, each representing a single virion or vRNP, were performed in ImageJ in combination with the plugin ComDet version 0.5.0 (https://github.com/ekatrukha/ComDet). Spot detection thresholds for each channel were set empirically by individual examination of images. The threshold to define co-localized spots was set to a maximum distance of 3 to 4 pixels between the centers of the spots. For visualization purposes, image brightness and contrast were manually adjusted in ImageJ.

Mosquito experiment

Adult *Aedes aegypti* (Rockefeller strain) mosquitoes were reared in 30 × 30 × 30 cm cubic cages at 27 ± 1°C and a 12:12 h light:dark cycle, at the Laboratory of Entomology, Wageningen University & Research. Five groups of mosquitoes, housed independently in small cardboard buckets, were allowed to feed through a Parafilm M membrane for at least 1.5 h on 37°C-heated virus-spiked blood meals using a Hemotek PS5 membrane feeding system (Hemotek, United Kingdom). Virus-spiked blood meals were prepared by mixing virus stocks with bovine blood washed twice with DPBS in a 2:1 ratio (**Table 1**). Virus-blood mixtures were back-titrated as described above. After feeding, mosquitoes were anesthetized using a semi-permeable CO_2 pad. Engorged female mosquitoes were selected, placed into new cardboard buckets, and maintained at 28°C. Throughout the duration of the experiment, mosquitoes were provided with a cotton pad soaked

in a 6% sucrose solution *ad libitum*, except for the day before feeding and the day before forced salivation, in which mosquitoes were provided only with water *ad libitum*. To evaluate whether feeding on a blood meal spiked with a mixture of incomplete virus populations can result in virus infection and transmission by mosquitoes, body and saliva samples were collected and tested by virus isolation. Briefly, 12 to 15 d after the blood meal, mosquitoes were anesthetized using a semi-permeable CO_2 pad, wings and legs were removed with forceps, and mosquitoes were forced to salivate by inserting their proboscis inside a 20 µL filter tip pre-filled with 7 µL of a 1:1 FBS-50% sucrose mixture for at least 1 h. After salivation, mosquito bodies were collected and stored at −80°C until further processing. Data corresponding to mosquitoes from groups #1, #2, and #3 derive from a single biological experiment. Data corresponding to mosquitoes from groups #4 and #5 derive from two independent experiments.

Table 1. Description and mean titers of the virus stocks used for blood meals in the mosquito experiment.

Group	Virus stock	Blood-virus mixture titer (log_{10} $TCID_{50}$/mL)
Group #1	Mock	---
Group #2	iRVFV-SL-eGFP	8.1
Group #3	iRVFV-ML	Not determined*
Group #4	RVFV-mCherry2	8.1
Group #5	iRVFV-SL-eGFP + iRVFV-ML	7.0

* Virus stock prior to mixing with blood had an initial titer of $10^{7.1}$ $TCID_{50}$/mL.

Virus isolation

Saliva samples were directly added onto 3 × 10^4 BSR-T7/5 cells/well previously seeded in 96-well plates (groups #1, #2, and #3) or used to prepare four serial 10-fold dilutions, starting at 1:10 (groups #4 and #5). In the latter case, 50 µL of each dilution were added onto 3 × 10^4 BSR-T7/5 cells/well previously seeded in 96-well plates. Mosquito bodies were suspended in 100 µL of complete G-MEM supplemented with an extra 1% antibiotic/antimycotic, homogenized using a pellet pestle and handheld pellet pestle motor (Daigger Scientific, USA), and clarified by centrifugation at maximum speed. The supernatants were diluted with additional 200 µL of supplemented G-MEM and used to prepare eight serial dilutions (5-fold the first dilution and 10-fold the remaining dilutions). Of each dilution, 50 µL were added onto 3 × 10^4 BSR-T7/5 cells/well previously seeded in 96-well plates. For both saliva and body samples, the expression of the respective FP in plaques of infected cells was monitored by fluorescence microscopy 24 to 72 h post-infection and used as the readout method.

Modeling the fraction of infected and co-infected cells

To model the relationship between MOI and the fraction of (co-)infected cells, we considered predictions of three models. Here we describe the models briefly. A complete description of the models and the code are provided as **Supplementary File 1**. All three models use the MOI as utilized in the experiment (λ) and the relative inoculum frequency f of the two variants, denoted with G for iRVFV-SL-eGFP and C for

iRVFV-SL-mCherry2, to predict four frequencies: the fraction of uninfected cells, $P(\overline{G} \cap \overline{C})$; the two fractions of cells infected by one virus variant, $P(\overline{G} \cap C)$ and $P(G \cap \overline{C})$; the fraction of co-infected cells, $P(G \cap C)$. The sum of these four fractions is one, as they represent all possible infection outcomes in this setup. Note that for simplicity, we only plotted the total fraction of infected cells (i.e., $1 - P(\overline{G} \cap \overline{C})$) and co-infected cells $P(G \cap C)$ in the main figure (**Fig. 2G**). As there were no indications to the contrary, we assumed $f_G = f_C = 0.5$ for all models.

Model A predicts the four fractions based on the MOI following a previously described model based on the Poisson distribution[49]. This model has no free parameters to fit and assumes each virus particle has a complete set of genome segments. The four fractions are:

$$P(\overline{G} \cap \overline{C}) = e^{-\lambda} = e^{-\lambda_G - \lambda_C},$$
$$P(\overline{G} \cap C) = e^{-\lambda_G}(1 - e^{-\lambda_C}),$$
$$P(G \cap \overline{C}) = (1 - e^{-\lambda_G})e^{-\lambda_C},$$
$$P(G \cap C) = (1 - e^{-\lambda_G})(1 - e^{-\lambda_C}),$$

where $\lambda_G = f_G\lambda$ and $\lambda_C = f_C\lambda$.

Models B and C are both more complex and were not solved analytically, but model predictions were determined by an iterative approach (with 10^5 iterations of cellular infection performed for all model estimates). Model B introduces non-selective packaging of genome segments. For both virus variants, the number of infecting virus particles per cell (Λ_G or Λ_C) was drawn from a Poisson distribution with mean λ_G or λ_C (using the *rpois* function in R). However, here $\lambda_G = \psi f_G\lambda$ and $\lambda_C = \psi f_C\lambda$, where the free parameter ψ is the probability of infection per administered MOI unit. We introduced this parameter because incomplete particles cannot infect on their own, potentially giving rise to a discrepancy between the administered and actual MOI. Next, we drew the number of copies of genome segment S for each virus variant present in that cell ($\theta_{S,G}$ or $\theta_{S,C}$) from a binomial distribution with a probability of success set to 0.5 and a number of trials $3\Lambda_G$ or $3\Lambda_C$ (using the *rbinom* function in R). To justify these values for the binomial distribution, consider that (i) in the absence of quantitative information on the distribution of genome segments over virus particles for this particular experiment, we assume both segments (S and L) are present at equal frequencies in both virus populations (G and C) and (ii) that up to three genome segments can be loaded into a virus particle. The number of L genome segments present in a cell can then be determined by subtraction:

$$\theta_{L,G} = 3\Lambda_G - \theta_{S,G} \text{ and } \theta_{L,C} = 3\Lambda_C - \theta_{S,C}.$$

Based on the complete distribution of genome segments that has infected the cell, we can now determine the fate of the cell. $P(\overline{G} \cap \overline{C})$: At least one genome segment (S, L, or both) is not present. $P(G \cap \overline{C})$: Both

genome segments are present, but all copies of the S segment are from the *G* variant. $P(\overline{G} \cap C)$: Both genome segments are present, but all copies of the S segment are from the *C* variant. $P(G \cap C)$: Both genome segments are present, and S segments from the *G* and *C* variants are present, i.e., both fluorescent markers are present. To fit this model to data, the free parameter ψ needs to be estimated.

Model C is identical to model B, except that it adds heterogeneous susceptibility of host cells to RVFV. These differences in susceptibility are likely to arise for many reasons, for instance, differences in the cell growth phase. Heterogeneous susceptibility is introduced by allowing the probability of infection to follow a beta distribution over cells. The beta distribution is a versatile probability distribution that has been previously used for this purpose[50]. For this model, $\lambda_G = \zeta\psi f_G\lambda$ and $\lambda_C = \zeta\psi f_C\lambda$, where ζ is a stochastic variable that follows a beta distribution over cells, with shape parameters α and β (using the *rbeta* function in R to draw a new value for each iteration). To fit this model to data, the free parameters ψ, α, and β need to be estimated.

To estimate model parameters for models B and C, we minimized the negative log likelihood (NLL) using a stochastic hill climbing algorithm, with 100 independent runs initiated from randomly selected starting points in a larger parameter space. The NLL was determined from the multinomial likelihood of the four cell fractions for each dose using the *dmultinom* function in R, and then summing NLLs over all MOI values used in the experiment. Model selection was performed using the AIC.

Modeling virus spread and the relationship between MOI and co-infection

We generated a simple simulation model of viral spread to consider the impact of non-selective packaging and infection by incomplete virus particles on within-host dynamics. Here we provide a brief summary. A complete description of the model and the code are provided as **Supplementary File 2**. We modeled the number of infected cells over a total of g_{max} viral generations, in a fixed number of κ cells. Each cell produces φ virus particles and the probability that a virus particle will infect a cell in the next round of replication is ρ. Virus particles are assumed to remain infectious for a short period of time and therefore can only infect cells in the subsequent round of infection. At generation g_0, we assumed that only a single cell is infected. In the next round of infection, the mean number of infecting virus particles per cell (i.e., the MOI) will be $\lambda_{g+1} = \varphi\rho i_g / n_g$, where i is the number of infected cells and n is the number of uninfected cells. The MOI follows a Poisson distribution over cells, with a random value being drawn for each of the n_g cells (using the *rpois* function in R).

Next, the genome segment content of each infecting virus particle must be determined. For a non-selective random packager, there are eight genome segment contents possible {RNA1, RNA2, RNA3}: {0,0,0}, {1,0,0}, {0,1,0}, {0,0,1}, {1,1,0}, {1,0,1}, {0,1,1}, and {1,1,1}, with 0 indicating a segment is absent and 1 indicating it is present in one or more copies. The frequency of these eight types was set to values approximating the empirical distribution to model a virus with non-selective packaging that allows co-infection (for instance,

{0.5, 0.09, 0.09, 0.09, 0.06, 0.06, 0.06, 0.05} for mammalian cells). The *sample* function, set to sampling with replacement, was then used to determine the identity of each infecting virus particle, with the probabilities for each outcome weighted by the frequency of the virus particle type. Once the genome segment content of all virus particles infecting a cell is known, we can determine whether the cell will become productively infected and transition from *n* to *I*, which only occurs when three segment types are present.

To consider a virus employing non-selective packaging without co-infection using this model, we wanted to block the contribution of all incomplete virus particles to spread. We then simply reset the frequency of the eight virus particle types to {0.95, 0, 0, 0, 0, 0, 0, 0.05}, in effect making all incomplete virus particles empty and inert particles. To consider a virus employing a selective genome packaging strategy, we made all virus particles to have a complete set of genome segments. However, this raises a complication: making all virus particles complete could require a greater total number of genome segments than used in the viruses with non-selective packaging (i.e., if only one copy of each segment is present, then the incomplete particles will require appreciably fewer genome segments to assemble). To make the comparison fair, we therefore determined the minimal total number of genome segments present for the viruses with non-selective packaging and used this number to cap the production of virus particles for the virus with selective packaging (i.e., the same number of genome segments is allocated only to complete particles). For example, in the case of the virus employing selective packaging in mammalian cells, the frequency of virus particle types became {0.74, 0, 0, 0, 0, 0, 0, 0.26}. We then ran the model and plotted the frequency of infected cells over time to determine performance. Note that we also considered the effect of free parameter values, as described in **Supplementary Text 1**, **Supplementary Figs. 2, 3** and **Supplementary File 3.**

To consider the relationship between MOI and the fraction of cells infected only by incomplete particles, we first considered the trends for the simulations in a fixed number of cells described above. However, if we fix the mean MOI, we can consider model predictions systematically over a wide range of MOI values. To test the generality of the observations obtained, we randomly drew values for the frequency of each segment type from a uniform distribution using the *runif* function. Then, we normalized these values by the sum of all drawn values and considered model predictions (**Supplementary File 2**). To generate reproducible predictions and to limit the computational resources needed, the number of iterations (i.e., inoculated cells simulated) was dependent on the MOI (λ): $\lambda \leq 1$, $n = 10^4$; $1 < \lambda \leq 10$, $n = 5 \times 10^3$; $\lambda > 10$, $n = 500$.

Data analysis and visualization

All model predictions were performed and plotted in R Statistical Software[51] version 4.2.1. Prism 9 (GraphPad Software) was used to generate graphs of all the remaining results. Sample size varied per experiment and is indicated in each figure legend.

Data availability statement

All relevant data and code supporting the findings of this study are available within the paper and its Supplementary information files.

Acknowledgements

We thank Michèle Bouloy (Institut Pasteur, France), Karl-Klaus Conzelmann (Ludwig-Maximilians-Universität München), and Connie Schmaljohn (US Army Medical Research Institute of Infectious Diseases) for previously providing the RVFV strain Clone 13, the BSR-T7/5 cells, and the antibody 4-D4, respectively. We also thank Lars Ravesloot (Wageningen Bioveterinary Research), Hendrik de Buhr (Wageningen Bioveterinary Research), and Marcel H. Tempelaars (Shared Research Facilities, Wageningen University & Research) for technical assistance.

Funding

EBM is a grateful recipient of scholarships from the Graduate School for Production Ecology & Resource Conservation (PE&RC) and Universidad de Costa Rica (OAICE-031-2019). The funders had no role in study design, data collection and analysis, decision to publish, or preparation of the manuscript.

Author contributions

EBM, PJWS and JK conceived the project. EBM, PJWS and KFB designed the experiments. EBM and KFB performed the reverse genetics, infection and immunofluorescence experiments. EBM performed the growth curves, flow cytometry and smFISH-immunofluorescence experiments. KFB performed the IPMA and RT-qPCR experiments. CJMK provided the mosquitoes and bovine blood. EBM, KFB, SvdW, ICR, RPMV and PJWS performed the mosquito experiments. MPZ performed the mathematical modeling with contributions of EBM, JK and PJWS. EBM, KFB, MPZ and PJWS analyzed and interpreted the data with contributions of GPP and JK. PJWS, JK and GPP supervised the project. EBM and MPZ wrote the manuscript with contributions of PJWS. EBM and MPZ made the figures with contributions of KFB and PJWS. All authors reviewed the manuscript and provided feedback.

Competing interests

The authors have declared that no competing interests exist.

References

1. Michalakis Y, Blanc S. The curious strategy of multipartite viruses. *Annual Review of Virology* **2020**, *7* (1), 203–218. https://doi.org/10.1146/annurev-virology-010220-063346.
2. Sicard A, Yvon M, Timchenko T, Gronenborn B, Michalakis Y, Gutierrez S, Blanc S. Gene copy number is differentially regulated in a multipartite virus. *Nature Communications* **2013**, *4* (1), 1–8. https://doi.org/10.1038/ncomms3248.
3. Sicard A, Pirolles E, Gallet R, Vernerey M-S, Yvon M, Urbino C, Peterschmitt M, Gutierrez S, Michalakis Y, Blanc S. A multicellular way of life for a multipartite virus. *eLife* **2019**, *8*, e43599. https://doi.org/10.7554/eLife.43599.
4. Sicard A, Michalakis Y, Gutiérrez S, Blanc S. The strange lifestyle of multipartite viruses. *PLOS Pathogens* **2016**, *12* (11), e1005819. https://doi.org/10.1371/journal.ppat.1005819.
5. Lucía-Sanz A, Manrubia S. Multipartite viruses: adaptive trick or evolutionary treat? *npj Systems Biology and Applications* **2017**, *3* (1), 1–11. https://doi.org/10.1038/s41540-017-0035-y.
6. Noda T, Sagara H, Yen A, Takada A, Kida H, Cheng RH, Kawaoka Y. Architecture of ribonucleoprotein complexes in influenza A virus particles. *Nature* **2006**, *439* (7075), 490–492. https://doi.org/10.1038/nature04378.
7. Noda T, Sugita Y, Aoyama K, Hirase A, Kawakami E, Miyazawa A, Sagara H, Kawaoka Y. Three-dimensional analysis of ribonucleoprotein complexes in influenza A virus. *Nature Communications* **2012**, *3* (1), 1–6. https://doi.org/10.1038/ncomms1647.
8. Chou Y, Vafabakhsh R, Doğanay S, Gao Q, Ha T, Palese P. One influenza virus particle packages eight unique viral RNAs as shown by FISH analysis. *PNAS* **2012**, *109* (23), 9101–9106. https://doi.org/10.1073/pnas.1206069109.
9. Fournier E, Moules V, Essere B, Paillart J-C, Sirbat J-D, Isel C, Cavalier A, Rolland J-P, Thomas D, Lina B, Marquet R. A supramolecular assembly formed by influenza A virus genomic RNA segments. *Nucleic Acids Research* **2012**, *40* (5), 2197–2209. https://doi.org/10.1093/nar/gkr985.
10. Goto H, Muramoto Y, Noda T, Kawaoka Y. The genome-packaging signal of the influenza A virus genome comprises a genome incorporation signal and a genome-bundling signal. *Journal of Virology* **2013**, *87* (21), 11316–11322. https://doi.org/10.1128/JVI.01301-13.
11. Dadonaite B, Gilbertson B, Knight ML, Trifkovic S, Rockman S, Laederach A, Brown LE, Fodor E, Bauer DLV. The structure of the influenza A virus genome. *Nature Microbiology* **2019**, *4* (11), 1781–1789. https://doi.org/10.1038/s41564-019-0513-7.
12. Le Sage V, Kanarek JP, Snyder DJ, Cooper VS, Lakdawala SS, Lee N. Mapping of influenza virus RNA-RNA interactions reveals a flexible network. *Cell Reports* **2020**, *31* (13). https://doi.org/10.1016/j.celrep.2020.107823.
13. Brooke CB, Ince WL, Wrammert J, Ahmed R, Wilson PC, Bennink JR, Yewdell JW. Most influenza A virions fail to express at least one essential viral protein. *Journal of Virology* **2013**, *87* (6), 3155–3162. https://doi.org/10.1128/JVI.02284-12.
14. Brooke CB. Population diversity and collective interactions during influenza virus infection. *Journal of Virology* **2017**, *91* (22), e01164-17. https://doi.org/10.1128/JVI.01164-17.

15. Nakatsu S, Sagara H, Sakai-Tagawa Y, Sugaya N, Noda T, Kawaoka Y. Complete and incomplete genome packaging of influenza A and B viruses. *mBio* **2016**, *7* (5). https://doi.org/10.1128/mBio.01248-16.

16. Schelker M, Mair CM, Jolmes F, Welke R-W, Klipp E, Herrmann A, Flöttmann M, Sieben C. Viral RNA degradation and diffusion act as a bottleneck for the influenza A virus infection efficiency. *PLOS Computational Biology* **2016**, *12* (10), e1005075. https://doi.org/10.1371/journal.pcbi.1005075.

17. Russell AB, Trapnell C, Bloom JD. Extreme heterogeneity of influenza virus infection in single cells. *eLife* **2018**, *7*, e32303. https://doi.org/10.7554/eLife.32303.

18. Diefenbacher M, Sun J, Brooke CB. The parts are greater than the whole: the role of semi-infectious particles in influenza A virus biology. *Current Opinion in Virology* **2018**, *33*, 42–46. https://doi.org/10.1016/j.coviro.2018.07.002.

19. Jacobs NT, Onuoha NO, Antia A, Steel J, Antia R, Lowen AC. Incomplete influenza A virus genomes occur frequently but are readily complemented during localized viral spread. *Nature Communications* **2019**, *10* (1), 1–17. https://doi.org/10.1038/s41467-019-11428-x.

20. Ladner JT, Wiley MR, Beitzel B, Auguste AJ, Dupuis AP, Lindquist ME, Sibley SD, Kota KP, Fetterer D, Eastwood G, Kimmel D, Prieto K, *et al.* A multicomponent animal virus isolated from mosquitoes. *Cell Host & Microbe* **2016**, *20* (3), 357–367. https://doi.org/10.1016/j.chom.2016.07.011.

21. Wichgers Schreur PJ, Kortekaas J. Single-molecule FISH reveals non-selective packaging of Rift Valley fever virus genome segments. *PLOS Pathogens* **2016**, *12* (8), e1005800. https://doi.org/10.1371/journal.ppat.1005800.

22. Bermúdez-Méndez E, Katrukha EA, Spruit CM, Kortekaas J, Wichgers Schreur PJ. Visualizing the ribonucleoprotein content of single bunyavirus virions reveals more efficient genome packaging in the arthropod host. *Communications Biology* **2021**, *4* (1), 1–13. https://doi.org/10.1038/s42003-021-01821-y.

23. Wichgers Schreur PJ, Kormelink R, Kortekaas J. Genome packaging of the *Bunyavirales*. *Current Opinion in Virology* **2018**, *33*, 151–155. https://doi.org/10.1016/j.coviro.2018.08.011.

24. Kortekaas J, Oreshkova N, Cobos-Jiménez V, Vloet RPM, Potgieter CA, Moormann RJM. Creation of a nonspreading Rift Valley fever virus. *Journal of Virology* **2011**, *85* (23), 12622–12630. https://doi.org/10.1128/JVI.00841-11.

25. Manzoni TB, López CB. Defective (interfering) viral genomes re-explored: impact on antiviral immunity and virus persistence. *Future Virology* **2018**, *13* (7), 493–503. https://doi.org/10.2217/fvl-2018-0021.

26. Bara JJ, Muturi EJ. Effect of mixed infections of Sindbis and La Crosse viruses on replication of each virus in vitro. *Acta Tropica* **2014**, *130*, 71–75. https://doi.org/10.1016/j.actatropica.2013.10.016.

27. Pereira Abrao E, Lopes da Fonseca BA. Infection of mosquito cells (C6/36) by dengue-2 virus interferes with subsequent infection by yellow fever virus. *Vector-Borne and Zoonotic Diseases* **2016**, *16* (2), 124-130. https://doi.org/10.1089/vbz.2015.1804.

28. Wernike K, Brocchi E, Beer M. Effective interference between Simbu serogroup orthobunyaviruses in mammalian cells. *Veterinary Microbiology* **2016**, *196*, 23–26. https://doi.org/10.1016/j.vetmic.2016.10.007.

29. Boussier J, Levi L, Weger-Lucarelli J, Poirier EZ, Vignuzzi M, Albert ML. Chikungunya virus superinfection exclusion is mediated by a block in viral replication and does not rely on non-structural protein 2. *PLOS ONE* **2020**, *15* (11), e0241592. https://doi.org/10.1371/journal.pone.0241592.

30. Wichgers Schreur PJ, Oreshkova N, van Keulen L, Kant J, van de Water S, Soós P, Dehon Y, Kollár A, Pénzes Z, Kortekaas J. Safety and efficacy of four-segmented Rift Valley fever virus in young sheep, goats and cattle. *npj Vaccines* **2020**, *5* (1), 1–10. https://doi.org/10.1038/s41541-020-00212-4.

31. Olson KE, Myles KM, Seabaugh RC, Higgs S, Carlson JO, Beaty BJ. Development of a Sindbis virus expression system that efficiently expresses green fluorescent protein in midguts of *Aedes aegypti* following per os infection. *Insect Molecular Biology* **2000**, *9* (1), 57–65. https://doi.org/10.1046/j.1365-2583.2000.00162.x.

32. Scholle F, Girard YA, Zhao Q, Higgs S, Mason PW. *trans*-Packaged West Nile virus-like particles: infectious properties in vitro and in infected mosquito vectors. *Journal of Virology* **2004**, *78* (21), 11605–11614. https://doi.org/10.1128/JVI.78.21.11605-11614.2004.

33. Foy BD, Myles KM, Pierro DJ, Sanchez-Vargas I, Uhlířová M, Jindra M, Beaty BJ, Olson KE. Development of a new Sindbis virus transducing system and its characterization in three Culicine mosquitoes and two Lepidopteran species. *Insect Molecular Biology* **2004**, *13* (1), 89–100. https://doi.org/10.1111/j.1365-2583.2004.00464.x.

34. Smith DR, Adams AP, Kenney JL, Wang E, Weaver SC. Venezuelan equine encephalitis virus in the mosquito vector *Aedes taeniorhynchus*: Infection initiated by a small number of susceptible epithelial cells and a population bottleneck. *Virology* **2008**, *372* (1), 176–186. https://doi.org/10.1016/j.virol.2007.10.011.

35. Weaver SC, Forrester NL, Liu J, Vasilakis N. Population bottlenecks and founder effects: implications for mosquito-borne arboviral emergence. *Nature Reviews Microbiology* **2021**, *19* (3), 184–195. https://doi.org/10.1038/s41579-020-00482-8.

36. Cuevas JM, Durán-Moreno M, Sanjuán R. Multi-virion infectious units arise from free viral particles in an enveloped virus. *Nature Microbiology* **2017**, *2* (7), 1–7. https://doi.org/10.1038/nmicrobiol.2017.78.

37. Sanjuán R. Collective infectious units in viruses. *Trends in Microbiology* **2017**, *25* (5), 402–412. https://doi.org/10.1016/j.tim.2017.02.003.

38. Andreu-Moreno I, Sanjuán R. Collective infection of cells by viral aggregates promotes early viral proliferation and reveals a cellular-level allee effect. *Current Biology* **2018**, *28* (20), 3212-3219.e4. https://doi.org/10.1016/j.cub.2018.08.028.

39. Sanjuán R, Thoulouze M-I. Why viruses sometimes disperse in groups? *Virus Evolution* **2019**, *5* (vez014). https://doi.org/10.1093/ve/vez014.

40. Di Mattia J, Torralba B, Yvon M, Zeddam J-L, Blanc S, Michalakis Y. Nonconcomitant host-to-host transmission of multipartite virus genome segments may lead to complete genome reconstitution. *PNAS* **2022**, *119* (32), e2201453119. https://doi.org/10.1073/pnas.2201453119.

41. Buchholz UJ, Finke S, Conzelmann K-K. Generation of bovine respiratory syncytial virus (BRSV) from cDNA: BRSV NS2 is not essential for virus replication in tissue culture, and the human RSV leader region acts as a functional BRSV genome promoter. *Journal of Virology* **1999**, *73* (1), 251–259. https://doi.org/10.1128/JVI.73.1.251-259.1999.

42. Muller R, Saluzzo JF, Lopez N, Dreier T, Turell M, Smith J, Bouloy M. Characterization of clone 13, a naturally attenuated avirulent isolate of Rift Valley fever virus, which is altered in the small segment. *The American Journal of Tropical Medicine and Hygiene* **1995**, *53* (4), 405–411. https://doi.org/10.4269/ajtmh.1995.53.405.

43. Barnard BJH. Rift Valley fever vaccine - antibody and immune response in cattle to a live and an inactivated vaccine. *Journal of the South African Veterinary Associaton* **1979**, *50* (3), 155–157. https://doi.org/10.10520/AJA00382809_4630.

44. Femino AM, Fay FS, Fogarty K, Singer RH. Visualization of single RNA transcripts in situ. *Science* **1998**, *280* (5363), 585–590. https://doi.org/10.1126/science.280.5363.585.

45. Raj A, van den Bogaard P, Rifkin SA, van Oudenaarden A, Tyagi S. Imaging individual mRNA molecules using multiple singly labeled probes. *Nature Methods* **2008**, *5* (10), 877–879. https://doi.org/10.1038/nmeth.1253.

46. Orjalo Jr. A, Johansson HE, Ruth JL. Stellaris™ fluorescence *in situ* hybridization (FISH) probes: a powerful tool for mRNA detection. *Nature Methods* **2011**, *8*, 884. https://doi.org/10.1038/nmeth.f.349.

47. Keegan K, Collett MS. Use of bacterial expression cloning to define the amino acid sequences of antigenic determinants on the G2 glycoprotein of Rift Valley fever virus. *Journal of Virology* **1986**, *58* (2), 263–270. https://doi.org/10.1128/jvi.58.2.263-270.1986.

48. Schneider CA, Rasband WS, Eliceiri KW. NIH Image to ImageJ: 25 years of image analysis. *Nature Methods* **2012**, *9* (7), 671–675. https://doi.org/10.1038/nmeth.2089.

49. Zwart MP, Hemerik L, Cory JS, de Visser JAGM, Bianchi FJJA, van Oers MM, Vlak JM, Hoekstra RF, van der Werf W. An experimental test of the independent action hypothesis in virus–insect pathosystems. *Proceedings of the Royal Society B: Biological Sciences* **2009**, *276* (1665), 2233–2242. https://doi.org/10.1098/rspb.2009.0064.

50. van der Werf W, Hemerik L, Vlak JM, Zwart MP. Heterogeneous host susceptibility enhances prevalence of mixed-genotype micro-parasite infections. *PLOS Computational Biology* **2011**, *7* (6), e1002097. https://doi.org/10.1371/journal.pcbi.1002097.

51. R Core Team. R: A language and environment for statistical computing. Vienna, Austria: R Foundation for Statistical Computing **2022**. https://www.R-project.org/.

Supplementary information

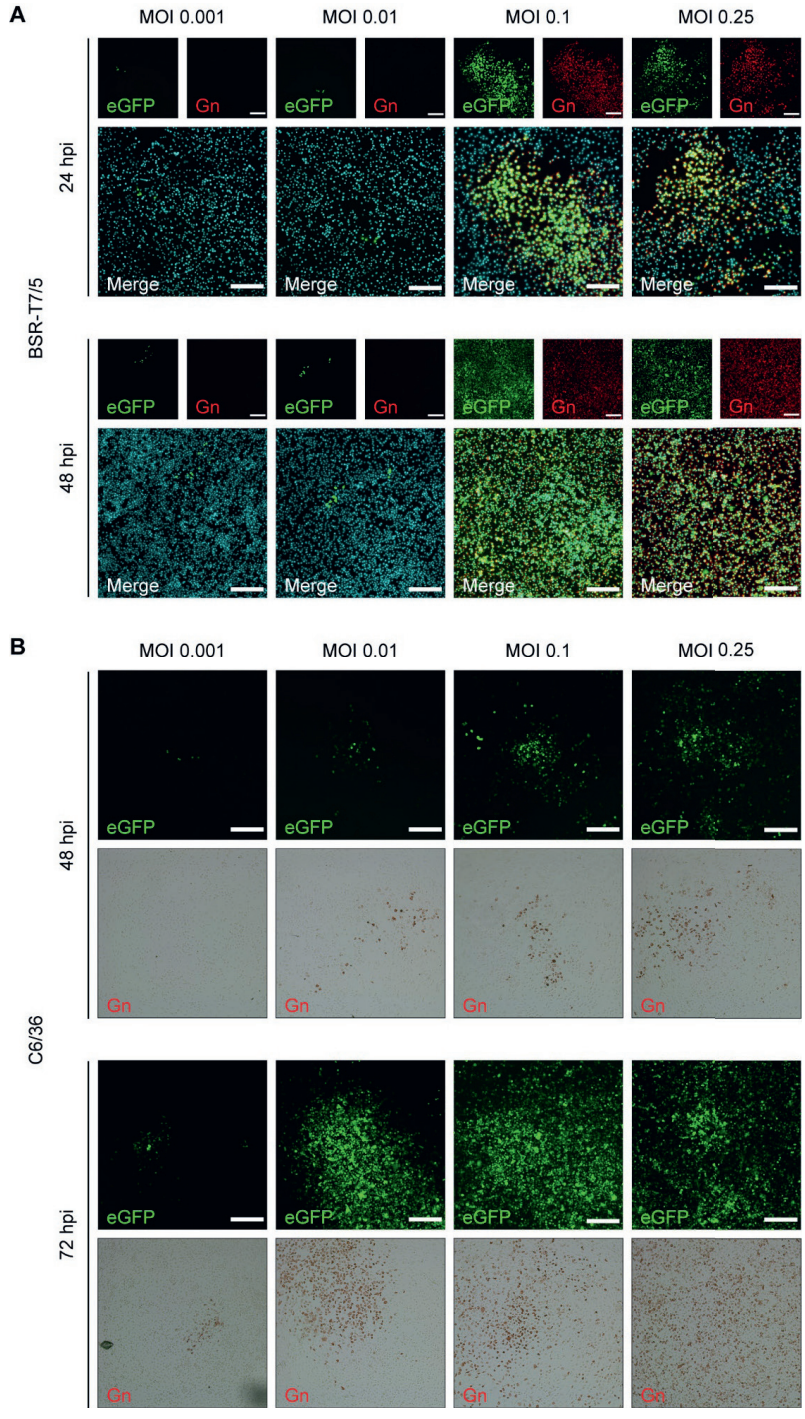

Supplementary Figure 1. Co-infection of mammalian and insect cells with complementing incomplete RVFV particles. A, B Mammalian (BSR-T7/5) (**A**) and insect (C6/36) (**B**) cells were simultaneously infected with non-spreading iRVFV-SL-eGFP and iRVFV-ML particles at increasing MOIs (ranging from 0.001 to 0.25 for each virus). Co-infection with the two populations of incomplete RVFV particles supports genome complementation, allows virus replication, production of infectious progeny, and virus spread. Infected cells were analyzed at 24–48 h (BSR-T7/5 cells) or 48–72 h (C6/36 cells) post-infection by following the expression of eGFP (green) via direct fluorescence microscopy examination and the expression of Gn (red) via an immunofluorescence assay in BSR-T7/5 cells or an immunoperoxidase monolayer assay in C6/36 cells. Expression of Gn was detected with rabbit polyclonal anti-Gn serum in combination with Alexa Fluor 568–conjugated secondary antibodies (immunofluorescence assay) or with HRP-conjugated secondary antibodies (immunoperoxidase monolayer assay). Cell nuclei (cyan) were visualized with DAPI. Of note, with the sole intention of depicting the outcome progression at increasing MOIs, images corresponding to co-infections (MOI of 0.1) at 24 h (BSR-T/5) and 72 h (C6/36) post-infection were purposely selected to be the exact same images as shown in **Fig. 4B, C**. Scale bars, 200 μm.

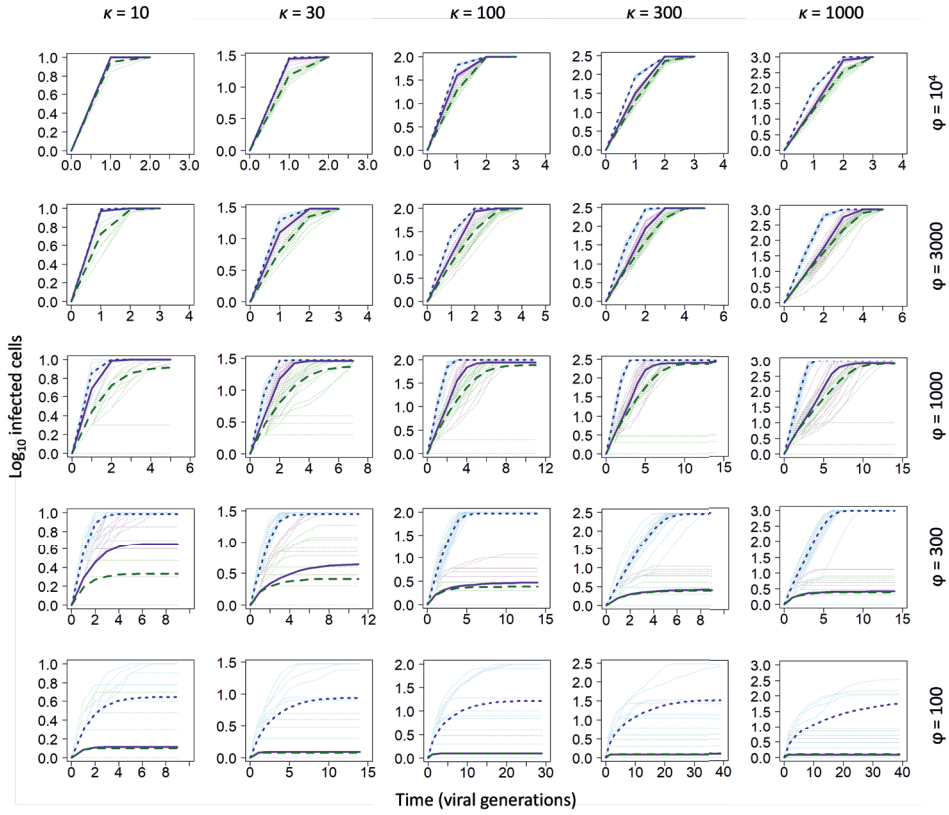

Supplementary Figure 2. Effects of model parameter values on predicted infection dynamics in mammalian cells. Predicted RVFV infection dynamics in mammalian cells for three different scenarios: selective genome packaging (finely dotted blue lines), non-selective genome packaging without co-infection by incomplete particles (coarsely dotted green lines), and non-selective genome packaging with co-infection and productive complementation by incomplete particles (solid magenta lines). The darker lines (each color corresponding to a different scenario) represent the mean values based on 1,000 simulations. The faint dotted lines (each color corresponding to a different scenario) represent trajectories for 20 individual simulations. In all panels, time is on the *x* axis and the number of infected cells is on the *y* axis. Note that the axes are scaled differently over panels. Values for the total number of cells (κ) and virus particle production (φ) were varied over panels, as indicated by the values at the top and right of the figure, respectively. Infection dynamics are clearly affected by parameter values, but under many conditions, the virus employing non-selective packaging but that allows co-infection has an advantage over the virus employing non-selective packaging without co-infection. The code required to reproduce the plots of this figure is provided as **Supplementary File 3**.

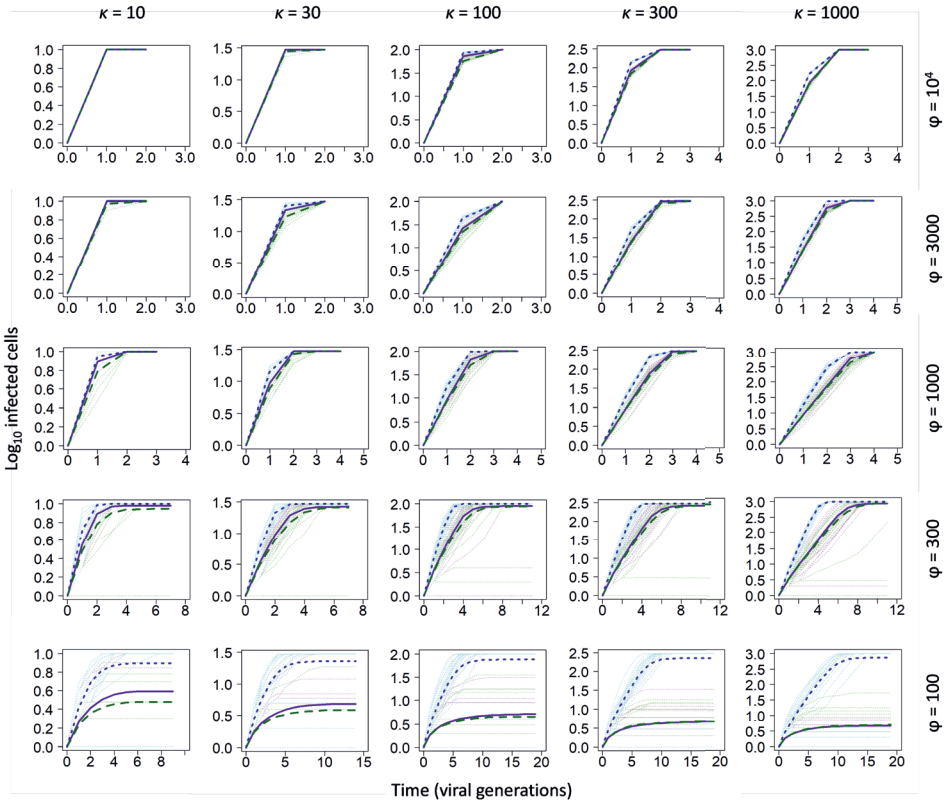

Supplementary Figure 3. Effects of model parameter values on predicted infection dynamics in insect cells. Predicted RVFV infection dynamics in insect cells for three different scenarios: selective genome packaging (finely dotted blue lines), non-selective genome packaging without co-infection by incomplete particles (coarsely dotted green lines), and non-selective genome packaging with co-infection and productive complementation by incomplete particles (solid magenta lines). The darker lines (each color corresponding to a different scenario) represent the mean values based on 1,000 simulations. The faint dotted lines (each color corresponding to a different scenario) represent trajectories for 20 individual simulations. In all panels, time is on the *x* axis and the number of infected cells is on the *y* axis. Note that the axes are scaled differently over panels. Values for the total number of cells (κ) and virus particle production (φ) were varied over panels, as indicated by the values at the top and right of the figure, respectively. Infection dynamics are clearly affected by parameter values, but the virus employing non-selective packaging with co-infection generally has a similar performance to the virus employing non-selective packaging without co-infection. The code required to reproduce the plots of this figure is provided as **Supplementary File 3**.

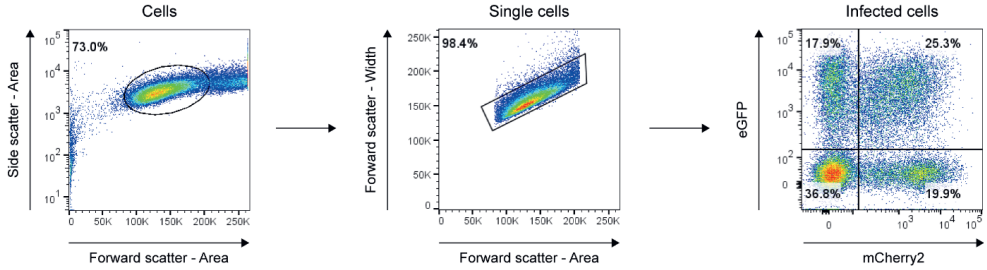

Supplementary Figure 4. Flow cytometry gating strategy. Illustrative example of the gating strategy employed for the analysis of flow cytometry data. BSR-T7/5 cells were mock-infected, singly-infected, or co-infected with non-spreading iRVFV-SL-eGFP and/or iRVFV-SL-mCherry2 particles. The cell population of interest was first discriminated from debris. Then, a gate was applied to select single cell events from doublets. Finally, we quantified the fraction of non-infected, singly-infected, or co-infected cells by determining the expression of eGFP, mCherry2, or both. The plots depicted here correspond to the co-infected sample (MOI of 0.5 for each virus population), as shown in **Fig. 2F**.

Supplementary Table 1. Model parameter estimates and model selection results for the co-infection assays.

Model[a]	Model parameter estimates[b]	NLL[c]	AIC	ΔAIC	AW
A	-	10,954.69	21,909.38	16,984.37	0.000
B	p = 0.03	8,891.86	17,785.72	12,860.71	0.000
C	p = 0.95, α = 0.13, β = 0.83	2,459.51	4,925.01	-	1.000

NLL: negative log likehood. AIC: Akaike information criterion. ΔAIC: delta AIC, the difference between this model and the best supported model in AIC. AW: Akaike weight, the likelihood that this model is the best-supported model within the set of models considered. [a] For a full description of the models, see the **Materials and methods** section and **Supplementary File 1**. [b] Note that model A has no free parameters that need to be estimated. [c] For a clarification of all terms used here, see this review (Johnson JB, Omland KS. Model selection in ecology and evolution. *Trends in Ecology & Evolution* **2004**, 19, 101-108. https://doi.org/10.1016/j.tree.2003.10.013).

Supplementary Table 2. Primers for cDNA synthesis of viral genome segments.

Target	Name	Sequence
RVFV-Clone 13-S and RVFV-35/74-S	JR860-For	ACAAAGCTCCCTAGAGATACA
RVFV-Clone 13-M and RVFV-35/74-M	JR861-For	GACACAAAGACGGTGCATTA
RVFV-Clone 13-L and RVFV-35/74-L	JR890-For	GACACAAAGGCGCCCAATC

Supplementary Table 3. Primers for RT-qPCR amplifications of viral genome fragments and *ampR*.

Target	Name	Sequence
RVFV-Clone 13-S and RVFV-35/74-S	JR907-For	TCCAGTTTGCTGCTCAA
	JR908-Rev	CTGCTTTAAGAGTTCGATAACC
RVFV-Clone 13-M and RVFV-35/74-M	JR909-For	GCTGATGGCTTGAACAAC
	JR910-Rev	GTCTCTCACACCGAACTATC
RVFV-Clone 13-L and RVFV-35/74-L	JR911-For	TCGATAGATGTGGAAGATATGG
	JR912-Rev	CGTCATTCATCATGGGAAAC
ampR	JR971-For	GCAGTGTTATCACTCATGG
	JR972-Rev	CACTATTCTCAGAATGACTTGG

Supplementary Table 4. Antibodies used in immunostaining assays.

Assay	Target	Antibody	Dilution	Source/reference
IPMA, IF (1^{ary})	RVFV Gn	Rabbit polyclonal serum	1:500	Thermo Fisher
IPMA (2^{ary})	Rabbit IgG	Goat polyclonal anti-rabbit IgG HRP-conjugated	1:500	P0448 Dako
IF (2^{ary})	Rabbit IgG	Goat polyclonal anti-rabbit IgG-FITC	1:250	sc-2012 Santa Cruz Biotechnology
IF (2^{ary})	Rabbit IgG	Donkey polyclonal anti-rabbit IgG-Alexa Fluor 568	1:500	A10042 Invitrogen
IF (1^{ary})	RVFV N	Monoclonal mouse hybridoma	1:100	F1D11 CISA-INIA
IF (2^{ary})	Mouse IgG	Goat polyclonal anti-mouse IgG-Alexa Fluor Plus 488	1:500	A32723 Invitrogen
FISH-IF (1^{ary})	RVFV Gn	Hybridoma 4-D4 supernatant	1:160	Ref. 47
FISH-IF (2^{ary})	Mouse IgG	Goat polyclonal anti-mouse IgG-Alexa Fluor 488	1:1000	A-11001 Invitrogen

IPMA: immunoperoxidase monolayer assay, IF: immunofluorescence, FISH-IF: fluorescence *in situ* hybridization-immunofluorescence.

Supplementary Text 1. Sensitivity analysis of the infection model parameters.

We generated an infection model to predict the infection kinetics of RVFV under three different scenarios and for two distributions of genome segments over virus particles (see **Fig. 7A**, **Materials and methods**, and **Supplementary File 3**). However, the models used have free parameters, so it is relevant to consider how parameter values affect model predictions. The infection model we have generated is relatively simple and has only three free parameters: the total number of cells (κ), virus particle production (φ) and the probability that a virus particle will infect a cell (ρ). As argued in the results section, we expect that parameter values will affect the prediction because the total number of cells available will determine how the multiplicity of infection (MOI) changes over time, i.e. all other things equal, the MOI will increase more rapidly in a small population of cells. It therefore makes sense to consider systematically how κ affects model predictions. We also expect that both φ and ρ will affect the model prediction, as they will determine how efficiently infection spreads between cells. However, the product $\varphi\rho$ determines the mean of the Poisson distribution describing the MOI, so it suffices to consider only one of these two parameters in this analysis, and we have chosen φ. Note that the model has two additional parameters: the total rounds of viral replication (g_{max}) and the number of infected cells in generation zero (i_0). Parameter g_{max} will not affect the prediction, provided that sufficient generations are given for all cells to become infected, and $i_0 = 1$, so that we can explore infection dynamics over the largest range in the frequency of infected cells and MOI values. In sum, to get an indication of how sensitive model predictions are to the chosen model parameters, we only need to consider parameters κ and φ.

We settled on values of $\kappa = 100$ and $\varphi = 1000$ *a priori* as reasonable values for these two parameters. Here, we therefore considered model predictions for all combinations of values of these parameters over two orders of magnitude to gauge how these model parameter values affect infection dynamics: κ = {10, 30, 100, 300, 1000} and φ = {100, 300, 1000, 3000, 10^4}. In particular, we are interested in how quickly the number of infected cells increases in a virus employing non-selective genome packaging but that allows co-infection compared to a virus employing non-selective packaging without co-infection.

First, we considered the predictions for mammalian cells (**Supplementary Fig. 2**). Here we found that the virus employing non-selective packaging with co-infection outperformed the virus employing non-selective

packaging without co-infection under most conditions. This effect was not seen when virus particle production was very low (φ = 100, both viruses with non-selective packaging perform very poorly) or very high (φ =10^4, both viruses perform so well that differences become negligible). For some conditions (e.g., κ = 10, φ = 300), the performance of the virus employing non-selective packaging with co-infection is much better than the virus employing non-selective packaging without co-infection. In some cases (e.g., κ = 10, φ = 1000), the performance of the virus employing non-selective packaging with co-infection is much closer to that of the virus employing selective packaging than to the virus employing non-selective packaging without co-infection. These results therefore clearly demonstrate that, for mammalian cells, the virus employing non-selective packaging with co-infection is predicted to have an advantage in spread over the virus employing non-selective packaging without co-infection under many conditions.

Second, we considered the predictions for insect cells (**Supplementary Fig. 3**), which differ only from the mammalian cell scenario in the distribution of genome segments over virus particles assumed. Recall that the model did not predict a large difference for the parameters values chosen (**Fig. 7A**). Here we found a similar pattern, as performance was the same or only marginally better for the virus that benefits from co-infection under most conditions. The advantage of the co-infecting virus over the non-co-infecting virus was greatest at low number of cells ($\kappa \leq 30$) and low virus particle production ($\varphi \leq 300$). Overall, these results suggest that the distribution of genome segments over virus particles may have a larger effect on whether co-infection contributes to enhanced spread than the exact conditions (κ and φ values) under which the virus is replicating.

Additional supplementary information files can be accessed online at:
https://doi.org/10.1371/journal.pbio.3001870

Supplementary Table 5. Oligonucleotide sequences of RNA FISH probe sets.

Supplementary File 1. Modeling the fraction of infected and co-infected cells.

Supplementary File 2. Modeling virus spread and the relationship between MOI and co-infection.

Supplementary File 3. Modeling virus spread: simple sensitivity analysis.

Supplementary Data 1. Source data underlying Figs. 1C, 2G, 3C, 4D, 6B.

Chapter 4

Transcriptomic profiling reveals intense host-pathogen dispute compromising homeostasis during acute Rift Valley fever virus infection

Erick Bermúdez-Méndez [1,2,3], Paolo Angelino [3,4], Lucien van Keulen [5], Sandra van de Water [1], Barry Rockx [1], Gorben P. Pijlman [2], Angela Ciuffi [3], Jeroen Kortekaas [1,2,6] & Paul J. Wichgers Schreur [1]

[1] Department of Virology & Molecular Biology, Wageningen Bioveterinary Research, Lelystad, The Netherlands

[2] Laboratory of Virology, Wageningen University & Research, Wageningen, The Netherlands

[3] Institute of Microbiology, Lausanne University Hospital and University of Lausanne, Lausanne, Switzerland

[4] Bioinformatics Core Facility, Swiss Institute of Bioinformatics, Lausanne, Switzerland

[5] Department of Bacteriology, Host-Pathogen Interactions & Diagnostics Development, Wageningen Bioveterinary Research, Lelystad, The Netherlands

[6] Present address: Boehringer Ingelheim Animal Health, Saint-Priest, France

Published:

Journal of Virology (2023) 97(6): e00415-23.

DOI: https://doi.org/10.1128/jvi.00415-23

Abstract

Rift Valley fever virus (RVFV) (family *Phenuiviridae*) can cause severe disease, and outbreaks of this mosquito-borne pathogen pose a significant threat to public and animal health. Yet many molecular aspects of RVFV pathogenesis remain incompletely understood. Natural RVFV infections are acute, characterized by a rapid onset of peak viremia during the first days post-infection, followed by a rapid decline. Although *in vitro* studies identified a major role of interferon (IFN) responses in counteracting the infection, a comprehensive overview of the specific host factors that play a role in RVFV pathogenesis *in vivo* is still lacking. Here, the host *in vivo* transcriptional profiles in the liver and spleen tissues of lambs exposed to RVFV are studied using RNA sequencing (RNA-seq) technology. We validate that IFN-mediated pathways are robustly activated in response to infection. We also link the observed hepatocellular necrosis with severely compromised organ function, which is reflected as a marked downregulation of multiple metabolic enzymes essential for homeostasis. Furthermore, we associate the elevated basal expression of *LRP1* in the liver with RVFV tissue tropism. Collectively, the results of this study deepen the knowledge of the *in vivo* host response during RVFV infection and reveal new insights into the gene regulation networks underlying pathogenesis in a natural host.

Importance

Rift Valley fever virus (RVFV) is a mosquito-transmitted pathogen capable of causing severe disease in animals and humans. Outbreaks of RVFV pose a significant threat to public health and can result in substantial economic losses. Little is known about the molecular basis of RVFV pathogenesis *in vivo*, particularly in its natural hosts. We employed RNA-seq technology to investigate genome-wide host responses in the liver and spleen of lambs during acute RVFV infection. We show that RVFV infection drastically decreases the expression of metabolic enzymes, which impairs normal liver function. Moreover, we highlight that basal expression levels of the host factor *LRP1* may be a determinant of RVFV tissue tropism. This study links the typical pathological phenotype induced by RVFV infection with tissue-specific gene expression profiles, thereby improving our understanding of RVFV pathogenesis.

Introduction

Rift Valley fever virus (RVFV) (family *Phenuiviridae*) is a single-stranded, three-segmented, negative-sense RNA virus transmitted by mosquitoes[1–3]. RVFV mainly affects ruminants such as sheep, goats, and cattle but can also affect camelids and humans[4–6]. Infected animals generally present with fever, anorexia, diarrhea, and overall weakness. Epizootic outbreaks are commonly characterized by abortion storms in sheep flocks and high mortality rates among newborns[1,7]. In humans, the clinical presentation of the disease is characterized by symptoms such as fever, headache, nausea, vomiting, abdominal pain, and diarrhea. In a minority of cases, the infection may progress to severe disease leading to hepato-renal failure, encephalitis, retinitis, and/or hemorrhagic manifestations[8–10].

In both animals and humans, the liver is the primary site of RVFV replication. Histopathological examinations of infected liver tissues revealed that diseased animals exhibit multifocal lesions and necrotic hepatitis[11,12]. The spleen is also commonly targeted during RVFV infection, with microscopic examination revealing various degrees of necrosis. Apart from the liver and the spleen, RVFV can occasionally be found in the kidneys, lungs, skin, brain, and placenta[11,13–15].

RVFV is endemic to most countries on the African Continent and the Arabian Peninsula. Nevertheless, as competent mosquito vectors already inhabit other geographical regions and are still expanding their territory, facilitated by climate change and international trade and transport, it is likely that the virus will be capable of invading previously unaffected areas[16–19]. RVFV outbreaks represent a significant threat to public health and can result in substantial economic losses[4,20,21], yet many key aspects of RVFV infection cycle and the molecular mechanisms underlying its pathogenesis are poorly comprehended.

High viremia peaking at 2 to 3 days post-infection followed by an abrupt decline from 4 to 5 days post-infection onward is a signature feature of acute RVFV infections in ruminants[22]. Generally, infected animals either succumb or fully recover during these days. Previous studies investigating RVFV virulence factors and pathogenesis revealed the predominant role of the non-structural protein NSs as an innate immune response antagonist. NSs acts primarily through the blockage of type I interferon (IFN) (IFN-α/β) production by inhibiting host cell transcription[23–25] and by inducing the degradation of the double-stranded RNA-dependent protein kinase (PKR)[26–28].

Recently, RNA sequencing (RNA-seq) technologies have enabled the transcriptome-wide analysis of host responses during virus infections. RNA-seq studies benefit from an exhaustive approach

to investigate the expression of the whole transcriptome using high-throughput sequencing instead of focusing on a short list of predicted genes of interest[29,30]. This broad analysis allows the detection of novel host factors playing an important role in the infection cycle that have escaped the radar of single-pathway-oriented investigations.

Two previous RVFV-mammalian host RNA-seq studies have been carried out with samples derived from infected cell cultures. The first study investigated the cellular response upon infection with the attenuated MP-12 strain and the virulent ZH548 strain in human small airway epithelial cells. In that study, the top pathways altered in response to infection with both RVFV strains included the regulation of the antiviral response, mitochondrial dysfunction, the DNA damage response, and integrin-linked kinase (ILK) signaling[31]. The second study investigated the response induced by MP-12 in HEK293 human embryonic kidney cells. The activation of innate immune signaling pathways and the upregulation of pro-inflammatory cytokines were observed, as were alterations in pathways associated with fatty acid metabolism and extracellular matrix receptor signaling[32].

Although these *in vitro* studies confirmed that IFN-mediated responses are crucial for fighting RVFV infection, our understanding of the tissue-specific host factors that play a role in *in vivo* pathogenesis is still very limited. To date, only one *in vivo* transcriptomic study on a RVFV-infected mammalian (surrogate) host has been performed. Investigation of the immune response in the brain of mice intranasally infected with RVFV revealed a protective response mediated by the mitochondrial antiviral-signaling protein (MAVS)[33]. A better understanding of the virus-host interface, especially in a natural RVFV host, would benefit the development of more effective outbreak control strategies.

In this work, we used RNA-seq technology to study *in vivo* the host transcriptional profiles in the liver and spleen tissues of lambs during RVFV peak viremia. We compared the gene expression profiles of infected lambs at 2 and 4 days post-infection with those of uninfected lambs and performed a genome-wide pathway analysis to identify biological processes that are affected during an acute infection. We revealed gene expression signatures underlying the observed histopathology phenotype, in addition to confirming the transcriptional responses to RVFV previously identified by *in vitro* experiments. Thus, this study improves our understanding of the *in vivo* host response to RVFV infection and uncovers new molecular features of RVFV pathogenesis.

Results

Selection of RVFV-infected ovine tissue samples for transcriptome analysis

Since sheep are the primary natural hosts of RVFV, and the liver and spleen are the two main target organs of the virus, we selected liver and spleen samples from lambs with moderate to high levels of viral RNA for host transcriptome analysis. For comparison, we selected samples from uninfected lambs. All the tissue samples were obtained from an experiment with Texel-Swifter lambs that were exposed to RVFV either via intravenous injection or via bites from infected mosquitoes[34] (**Fig. 1A**; see also **Materials and Methods** for additional details). Samples from group 1 belonged to lambs that were exposed to a low number of infected mosquitoes. These lambs did not develop any signs of disease, nor did they show detectable levels of infectious virus or viral RNA in the blood or the target organs (**Fig. 1B, C**). Group 1 was thus considered the control group. Samples from group 2 and group 3 belonged to lambs necropsied on days 2 and 4 post-infection, respectively, that presented with high levels of viral RNA (ranging between 10^7 and 10^{10} copies/mL on average) and infectious virus (ranging between 10^4 and 10^7 median tissue culture infectious doses [$TCID_{50}$]/mL on average) in the blood and the target organs (**Fig. 1B, C**). Noteworthy, the RNA copy numbers and infectious titers were slightly higher in the liver samples than in the spleen samples, without appreciable differences between lambs of groups 2 and 3.

Histological examination confirmed the infection status

Upon histological examination of tissue sections of the liver, acute necrosis of hepatocytes and an influx of neutrophils were observed in lambs from groups 2 and 3, clear indicators of acute hepatitis. In contrast, no histological alterations were observed in the liver tissues of the control lambs (group 1) (**Fig. 1D**). In line with the histological observations, immunohistochemistry detection of RVFV antigen revealed foci of infected cells in the livers of lambs from groups 2 and 3. The majority of the infected cells corresponded to necrotic hepatocytes, and a minority corresponded to endothelial cells. No virus-specific staining was observed in samples from group 1 (**Fig. 1E**).

RVFV infection status determines characteristic gene expression profiles

To determine the genome-wide gene expression profile in response to RVFV infection in the liver and spleen, total RNA from frozen tissue samples preserved in RNA*later* was isolated and subjected to poly(A)-enriched RNA-seq-based host transcriptome analysis. The integrity of the isolated RNA was confirmed by assessment of the RNA quality number (RQN) or the RNA integrity

number (RIN)[35], with RQN or RIN values >6 being found for the majority of the samples (see **Supplementary Table 1**). At least 20 million high-quality reads (average Phred score >30) per sample were obtained and mapped (ranging from 61.1% to 82.4% alignment) to the sheep (*Ovis aries*) NCBI reference genome (**Supplementary Fig. 1A-C**). A summary of the next-generation sequencing run and general statistics are provided in **Supplementary Table 2**. Initially, a total of 26,200 genes were detected across the different samples, of which 18,005 genes were retained for analysis after applying a filter to keep only genes with counts of 3 or higher in at least 2 of the samples. Of the input genes retained for the analysis, 83.8% were annotated in the reference genome (**Supplementary Fig. 1D**).

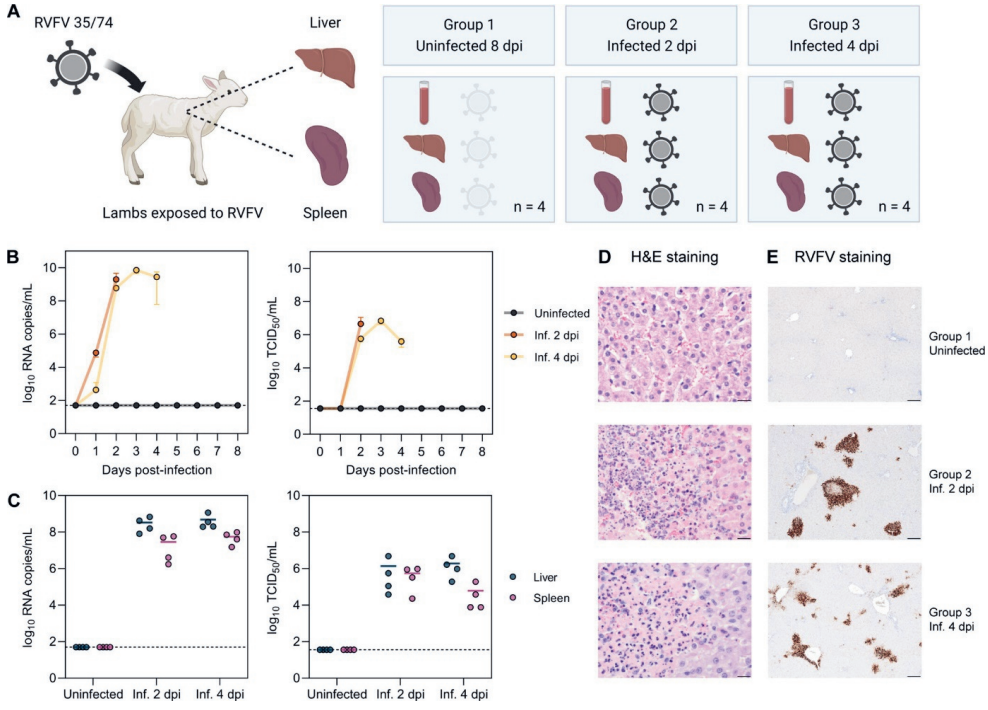

Figure 1. Selection of biologically relevant RVFV-infected samples. A Schematic representation of the selected animal samples. Liver and spleen samples of lambs exposed to RVFV strain 35/74 were selected from another study[34]. Group 1 consists of uninfected (non-responsive) lambs necropsied at 8 days post-exposure. Group 2 and group 3 consist of infected lambs necropsied at 2 and 4 days post-infection (dpi), respectively (n = 4 samples per group). **B, C** Viral RNA copy numbers and infectious titers in the blood (**B**) and target organs (**C**). Viral RNA was quantified by M-segment-specific RT-qPCR, and infectious titers were determined by an endpoint dilution virus isolation assay[34]. In panel B, graphs show the means with standard deviations (SD) at each time point. In panel C, dots represent individual replicates, and the horizontal lines represent the means. Dashed lines indicate the limits of detection (50 RNA copies/mL for RT-qPCR and 35.5 median tissue culture infectious doses [$TCID_{50}$]/mL for the virus isolation assay).

D Hematoxylin and eosin (H&E) staining of liver tissue sections. Group 1 shows no histological alterations in the liver, while groups 2 and 3 show acute hepatitis with necrosis of hepatocytes and an influx of polymorphonuclear cells. Bars, 20 µm. (E) Immunohistochemical detection of RVFV antigen in liver tissue. RVFV Gn glycoprotein (brown) was detected with antibody 4-D4[61] in combination with HRP-conjugated secondary antibodies. Bars, 200 µm. Inf., infected.

Separation mostly between liver and spleen samples was observed by both heat maps of the Euclidean distances and principal component analysis when all the samples were analyzed together (**Supplementary Fig. 2A, B**). As expected, this separation indicates that the gene expression profiles depend first on the host tissue rather than the infection status. We next performed similar analyses of each tissue separately. Heat maps of the Euclidean distances between samples revealed groupings into three distinct clusters (**Fig. 2A**). This clustering was also evident in the principal component analysis, where PC1 and PC2 represented 75% and 10% of the variance in the liver samples and 49% and 30% of the variance in the spleen samples, respectively (**Fig. 2B**). Notably, each cluster corresponded to either the uninfected lambs (group 1), the lambs at 2 days post-infection (group 2), or the lambs at 4 days post-infection (group 3), indicating that the infection status of the lamb determines a characteristic gene expression profile in each tissue.

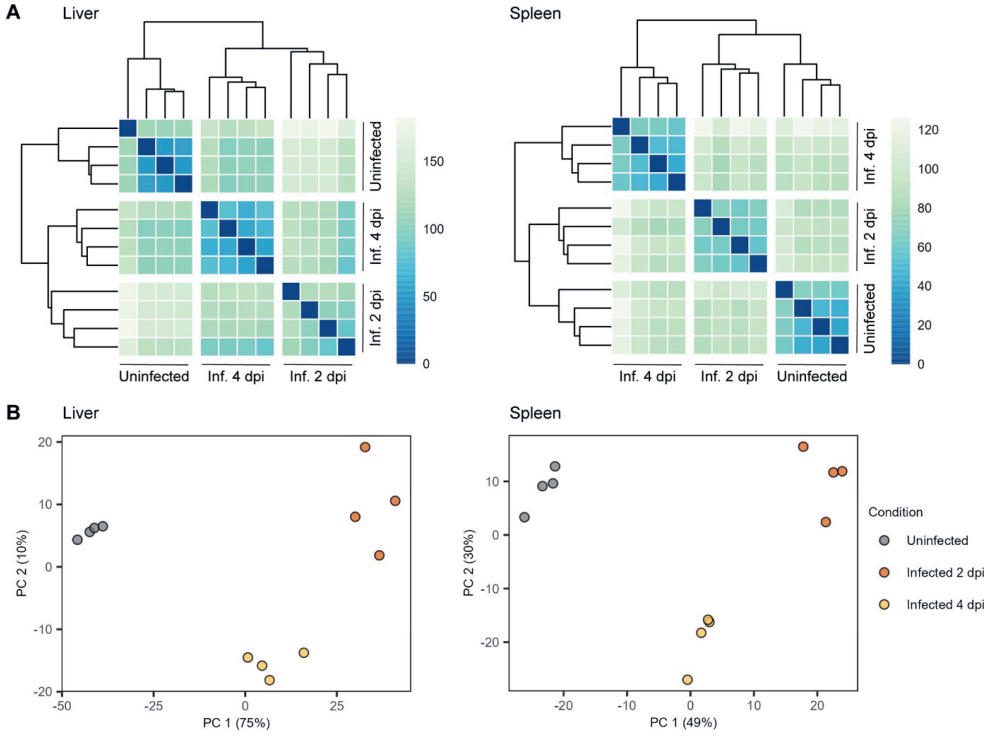

Figure 2. RVFV infection status determines characteristic gene expression profiles. A Heat maps of the Euclidean distances between liver (left) and spleen (right) tissue samples. Based on the calculated distance, each cell is color-coded in shades of a sequential gradient ranging from dark blue (close distance, implying similarity) to light green (far distance, implying dissimilarity). **B** Principal component analyses of liver (left) and spleen (right) tissue samples. Within each tissue type, samples cluster into three distinct well-defined clusters corresponding to a particular infection status. Abbreviations: Inf., infected; dpi, days post-infection.

RVFV infection induces extensive changes in liver and spleen gene expression

To examine how the infection status influenced the host liver and spleen responses upon RVFV infection, we performed pairwise differential gene expression analysis between the samples of each tissue type. Genes with an absolute $\log_2$ fold change of 1 and an adjusted p value <0.05 were considered significantly differentially expressed. In all of the paired comparisons, tens to hundreds of genes were differentially expressed (down- or upregulated), confirming that RVFV infection induced significant changes in the host liver and spleen transcriptomes (**Fig. 3A, B**). Lists of all of the differentially expressed genes with their corresponding $\log_2$ fold changes and adjusted p values are provided in **Supplementary Table 3**.

RVFV infection leads to immune response activation and decreased tissue-specific function

Within each tissue type, a fraction of differentially expressed genes were common to infected samples (groups 2 and 3) compared to uninfected samples (group 1), as depicted by the genes belonging to the intersection (overlap) of the corresponding gene lists (**Fig. 3C** and **Supplementary Table 4**). This commonality between the infected groups indicates that some genes remain either down- or upregulated during the peak phase (day 2) and the start of virus clearance (day 4) of an acute infection. Interestingly, when comparing samples between tissue types but at the same time points, there was a substantial intersection of genes upregulated in both the liver and the spleen. This intersection of upregulated genes in both tissues is mainly due to genes involved in the host's immune response against viral infection. On the contrary, the intersection of downregulated genes between both tissue types was minor, suggesting that downregulated gene expression changes are tissue specific (**Fig. 3D** and **Supplementary Table 4**).

A selection of the top 50 most variably expressed genes in the liver and spleen not only separated the different groups of samples based on infection status but also showed divergent patterns of expression in specific subsets of genes (**Supplementary Fig. 3**). In both liver and spleen tissues, the largest differences were observed between the uninfected (group 1) and the 2 days post-infection (group 2) samples. Remarkably, some of the most variably expressed genes

showing the largest divergences in expression patterns belonged to a set of 21 genes that were upregulated in the liver and spleen across all the infected samples (2 and 4 days post-infection) (**Fig. 4A-C**). Most of these genes, including *ISG15*, *ISG20*, *IFIT3*, *IFI6*, *USP18*, *XAF1*, *BST-2A*, *BST-2B*, *CCL2*, *DRAM1*, *FOLR3*, *IL18BP*, and *LGALS3BP*, are involved in the immune response of the host against viral infection, mainly via IFN-mediated signaling pathways. The remaining genes are involved in, among others, nucleosome assembly, apoptosis, and collagen biosynthesis.

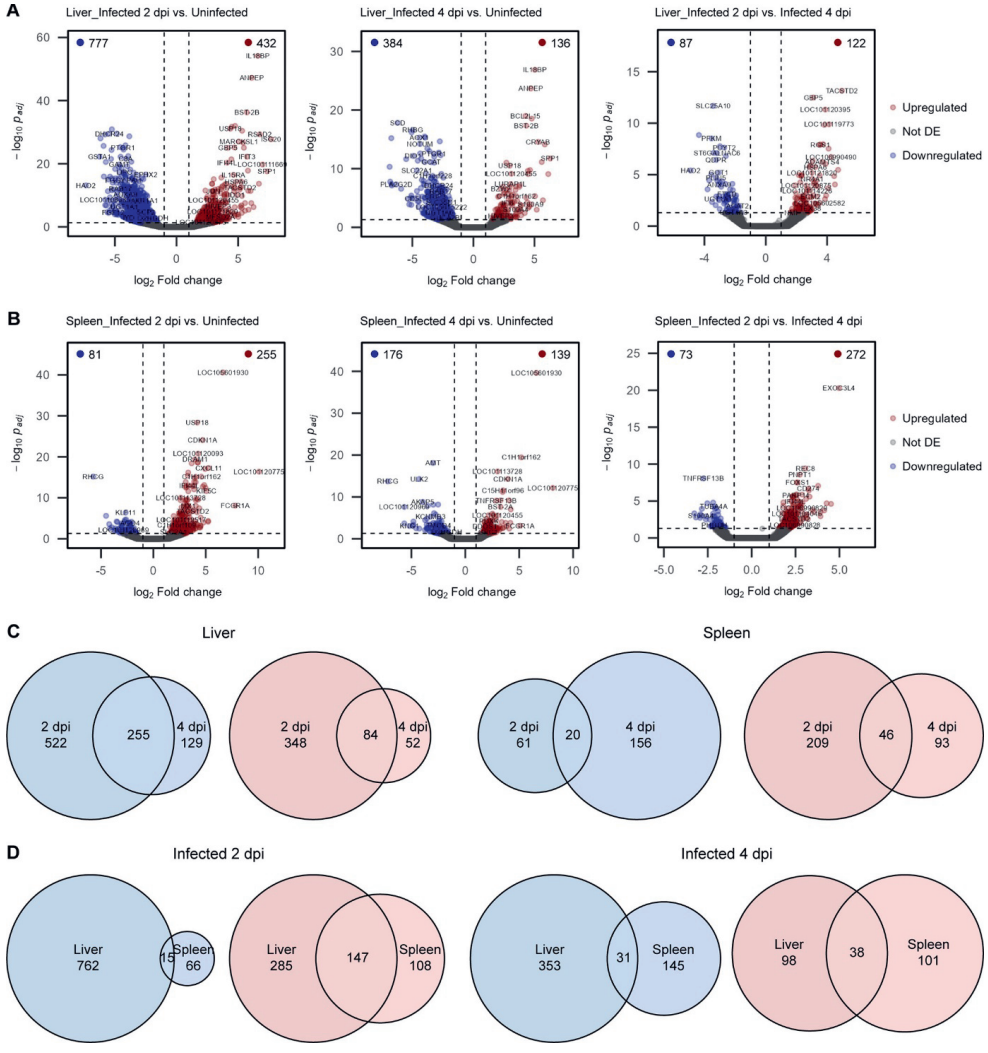

Figure 3. RVFV-induced changes in liver and spleen gene expression. A, B Volcano plots of differential gene expression analysis in liver (**A**) and spleen (**B**) tissues. Uninfected (group 1) and infected (groups 2 and 3) samples were compared pairwise. Dots represent individual genes. Genes with an absolute $\log_2$ fold change of 1 and a Wald test *p* value (adjusted by the Benjamini-Hochberg method) <0.05 were considered

significantly differentially expressed (DE). The vertical and horizontal dashed lines indicate the $\log_2$ fold changes and adjusted *p* value thresholds, respectively. The numbers of significantly downregulated (blue) and upregulated (red) genes are indicated at the top corners of each plot. **C, D** Euler diagrams representing the numbers of shared (intersection) and unique downregulated (blue) and upregulated (red) genes between infected groups 2 and 3 (compared to control group 1). Comparisons of time points for the same tissue type (**C**) and comparisons of tissues at the same time point (**D**) are shown. Abbreviation: dpi, days post-infection.

As initially noticed in the Euler diagram (**Fig. 3D**), the majority of the downregulated genes in RVFV-infected samples compared to uninfected samples are not common between the liver and spleen. The biological processes in which these genes are involved depend on the specific functions of these organs (**Fig. 5A-C**). The majority of the genes downregulated in the liver upon RVFV infection code for transporters (*ABCA10*, *AQP8*, *RHBG*, and genes encoding proteins of the *SLC* solute carrier family) and hepatic enzymes. These hepatic enzymes are involved in diverse metabolic processes, including the metabolism of lipids (*ALDH1A1*, *CYP2E1*, *FADS1*, *NOTUM*, and *SCD*), steroid hormones (*CYP7A1*, *CYP8B1*, *DHCR7*, *HSD17B2*, and *TM7SF2*), amino acids (*CSAD*, *GAMT*, *GCAT*, and *GLYAT*), vitamins (*FMO1* and *PDXP*), carbohydrates (*PFKB1* and *TKFC*), and xenobiotics (*AOX1*, *CYP1A2*, and *GSTA1*) (**Fig. 5A**). Genes downregulated in the spleen after RVFV infection were mostly those encoding structural proteins (*ACTG2*, *MYOM1*, *TNXB*, and *TCHH*), enzymes (*ATP2A1*, *ALDH1L2*, and *ULK2*), and proteins with ligand binding activity (*HMCN2*, *LGALS12*, and *PAMR1*) (**Fig. 5B**). In both the liver and spleen tissues, the downregulation trend of the underexpressed genes was maintained during both phases of the infection (2 and 4 days post-infection).

Host immune responses and metabolic pathways are markedly influenced by RVFV infection

Besides inspecting the profiles of individual differentially expressed genes, we also performed a functional analysis of gene sets of interest based on the Gene Ontology (GO) database. Over-representation analysis (ORA) determines if known biological processes or molecular functions are significantly over-represented in a particular list of differentially expressed genes[36], while gene set enrichment analysis (GSEA) determines if an *a priori*-defined set of genes shows significantly coordinated differences (i.e., detection of small but consistent changes in the same direction)[37].

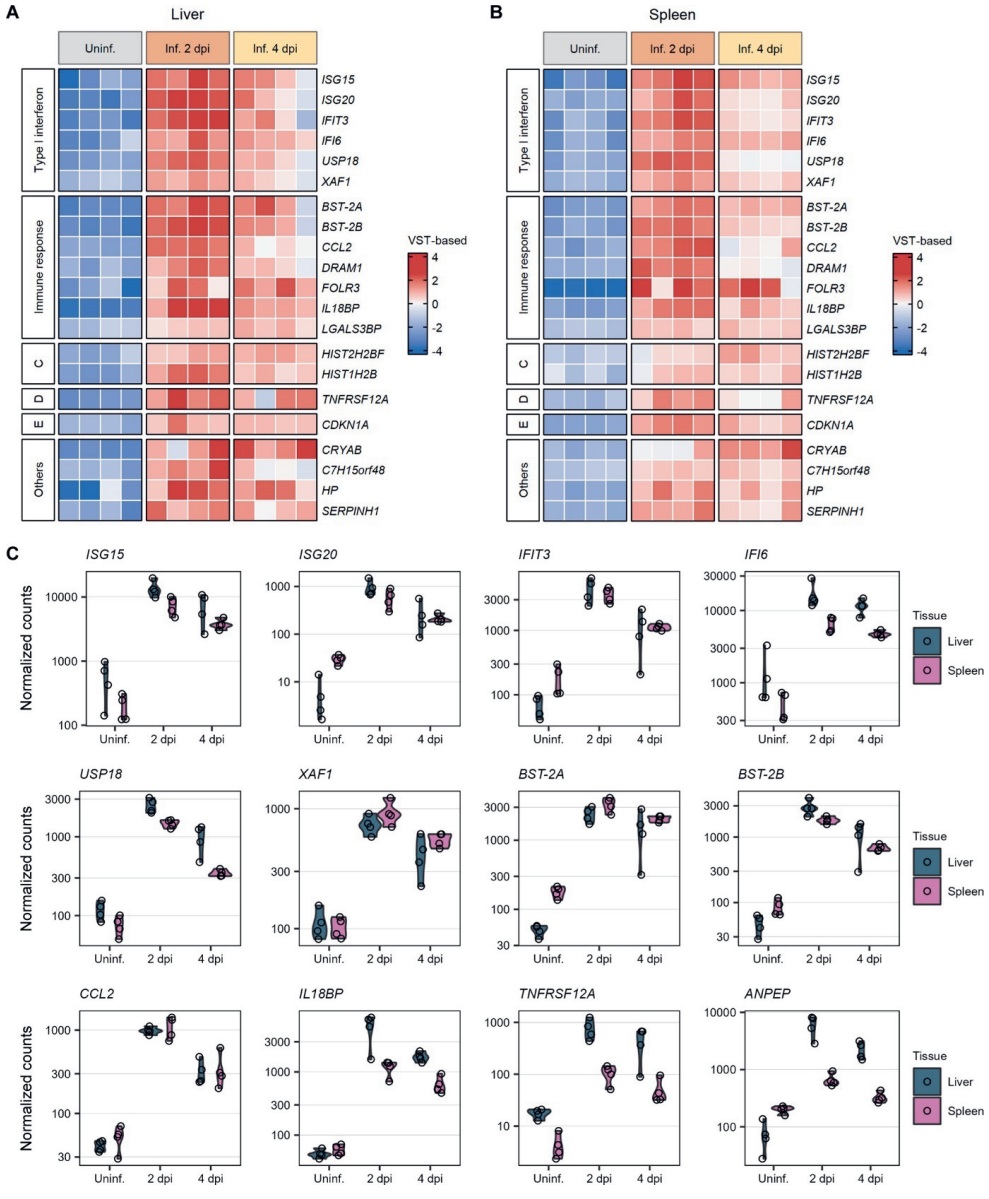

Figure 4. Commonly upregulated genes in the liver and spleen during peak RVFV infection. A, B Heat maps of a set of 21 genes commonly upregulated after RVFV infection in liver (**A**) and spleen (**B**) tissues. Samples were clustered based on their infection status, as indicated on top of the heat maps. Genes were clustered into categories based on their molecular function or biological process, as indicated at the left of the heat maps. To represent the magnitude of the $\log_2$ fold change of each gene compared to the mean gene expression level, cells are color-coded in shades of a gradient ranging from dark blue (low) to dark red (high). **C** Expression profiles of 12 selected genes commonly upregulated in RVFV-infected (Inf.) samples at 2 days post-infection (dpi) (group 2) and 4 days post-infection (group 3) compared to uninfected (Uninf.)

samples (group 1). Dots represent individual normalized gene counts (on a $\log_{10}$ scale), and the shaded area shows the distribution of the samples within each group. Abbreviations: VST, variance-stabilizing transformation; C, nucleosome assembly; D, cytokine receptor; E, apoptosis; Others, a chaperone and genes involved in metabolic processes such as collagen biosynthesis.

Specifically for the liver, in terms of biological processes, ORA and GSEA showed significant enrichment for GO terms related to the immune response, positive regulation of signaling, regulation of programmed cell death, and the metabolism of diverse molecules (e.g., lipids, organic acids, and nucleobase-containing molecules) at the peak of the infection (2 days post-infection). Molecular functions associated with these processes included cytokine activity, cytokine receptor binding, binding to other ligands (e.g., iron and vitamins), and enzymatic activity (e.g., oxidoreductase and hydrolase) (**Fig. 6A, B** and **Supplementary Table 5**). ORA and GSEA revealed very similar results for the 4 days post-infection time point (**Supplementary Fig. 4A, B** and **Supplementary Table 5**). Ridge plots **in Fig. 6B** depict that gene sets involved in the immune response were upregulated (positive normalized enrichment score), whereas gene sets involved in metabolic processes were downregulated (negative normalized enrichment score).

Similar to the liver, ORA and GSEA of the spleen data at the level of biological processes identified significant positive enrichment for GO terms involved in the immune response, regulation of the response to stress, regulation of programmed cell death, cytokine production, and the response to cytokines at 2 days post-infection. Regarding molecular functions, GO terms significantly enriched included cytokine activity, chemokine activity, signaling receptor binding, binding to other ligands (e.g., lipids and carbohydrates), and structural molecule activity (**Fig. 7A, B** and **Supplementary Table 5**). Furthermore, GSEA identified GO terms related to the upregulation of apoptotic signaling, protein heterodimerization activity, translation regulator activity, and the downregulation of ion transmembrane transporter activity specifically at the 4 days post-infection time point (**Supplementary Fig. 5** and **Supplementary Table 5**).

Additionally, ORA based on the Kyoto Encyclopedia of Genes and Genomes (KEGG) database corroborated the host's most influenced pathways upon RVFV infection. Pathways related to the metabolism of diverse molecules (e.g., xenobiotics, fatty acids, retinol, and arachidonic acid), peroxisome proliferator-activated receptor (PPAR) signaling, and the biosynthesis of steroid hormones and cofactors were identified in the liver samples (**Supplementary Fig. 6A** and **Supplementary Table 5**). Pathways involved in viral infection, cytokine receptor interaction, NF-κB

signaling, NOD-like receptor signaling, protein digestion, and apoptosis were identified in the spleen samples (**Supplementary Fig. 6B** and **Supplementary Table 5**).

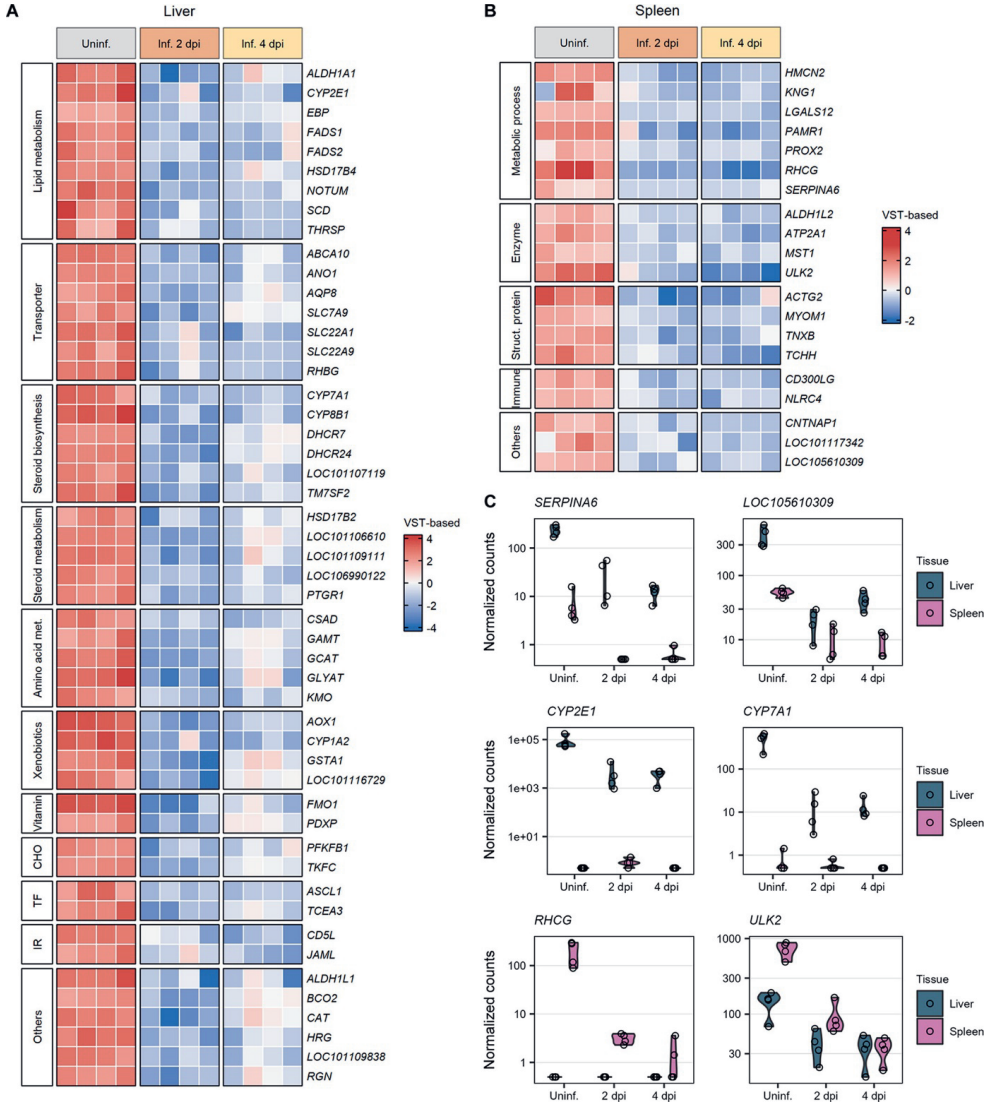

Figure 5. Downregulated genes in the liver and spleen during peak RVFV infection. A, B Heat maps of sets of genes significantly downregulated after RVFV infection in liver (**A**) and spleen (**B**) tissues. Samples were clustered based on their infection status, as indicated on top of the heat maps. Genes were clustered into categories based on their molecular function or biological process, as indicated at the left of the heat maps. To represent the magnitude of the $\log_2$ fold change of each gene compared to the mean gene expression level, cells are color-coded in shades of a gradient ranging from dark blue (low) to dark red (high). **C** Expression profiles of 6 selected genes significantly downregulated in RVFV-infected (Inf.) liver or spleen

samples at 2 days post-infection (dpi) (group 2) and 4 days post-infection (group 3) compared to uninfected (Uninf.) samples (group 1). Dots represent individual normalized gene counts (on a $\log_{10}$ scale), and the shaded area shows the distribution of the samples within each group. Abbreviations: VST, variance-stabilizing transformation; met., metabolism; CHO, carbohydrate metabolism; TF, transcription factor; IR, immune response; Struc., structural; Others, genes involved in folate metabolism, carotenoid metabolism, purine metabolism, signaling receptor activity, cell growth, hemostasis, and senescence.

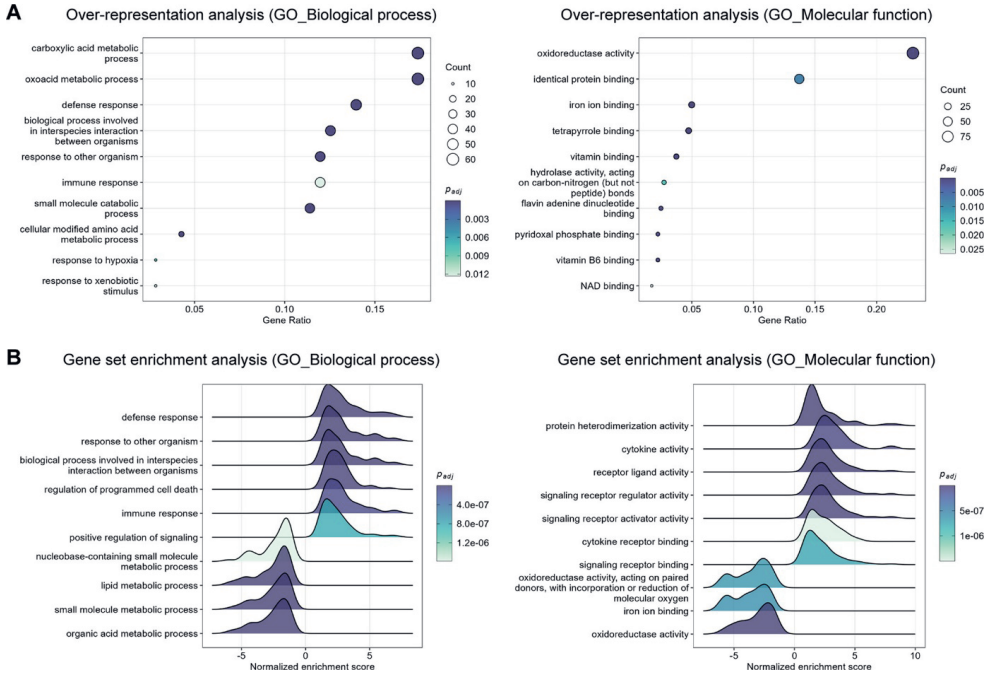

Figure 6. Top significantly enriched pathways altered in the liver in response to RVFV infection (2 days post-infection). **A** Gene Ontology (GO) biological process (left) and molecular function (right) over-representation analysis of genes differentially expressed in RVFV-infected liver tissue. The dot size represents the number of enriched genes associated with each GO term. Dots are color-coded according to their *p* values (adjusted by the Benjamini-Hochberg method). **B** GO biological process (left) and molecular function (right) gene set enrichment analysis in RVFV-infected liver tissue. Gene sets with positive normalized enrichment scores are upregulated, whereas gene sets with negative normalized enrichment scores are downregulated. Ridges are color-coded according to their *p* values (adjusted by the Benjamini-Hochberg method). The cutoff for significance for all the analyses was set to an adjusted *p* value <0.05. The top significantly enriched pathways altered in the liver in response to RVFV infection at 4 days post-infection are presented in **Supplementary Fig. 4**.

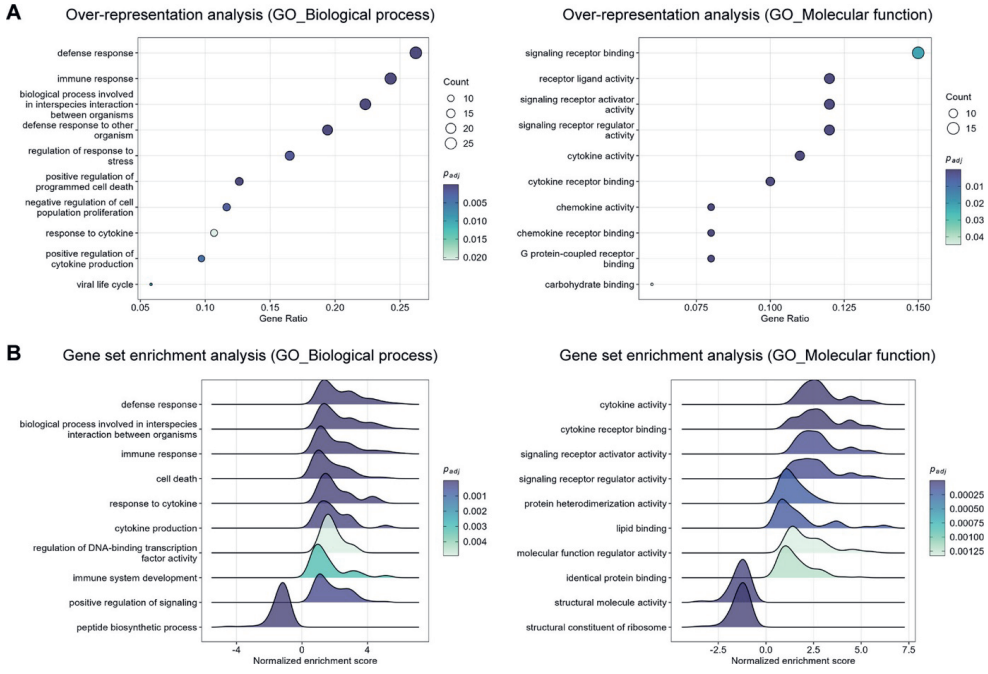

Figure 7. Top significantly enriched pathways altered in the spleen in response to RVFV infection (2 days post-infection). **A** Gene Ontology (GO) biological process (left) and molecular function (right) over-representation analysis of genes differentially expressed in RVFV-infected spleen tissue. The dot size represents the number of enriched genes associated with each GO term. Dots are color-coded according to their *p* values (adjusted by the Benjamini-Hochberg method). **B** GO biological process (left) and molecular function (right) gene set enrichment analysis in RVFV-infected spleen tissues. Gene sets with positive normalized enrichment scores are upregulated, whereas gene sets with negative normalized enrichment scores are downregulated. Ridges are color-coded according to their *p* values (adjusted by the Benjamini-Hochberg method). The cutoff for significance in all the analyses was set to an adjusted *p* value <0.05. The top significantly enriched gene sets altered in the spleen in response to RVFV infection at 4 days post-infection are presented in **Supplementary Fig. 5**.

Levels of the host factor *LRP1* correlate with RVFV tissue tropism

Recently, a genome-wide CRISPR screen identified low-density lipoprotein receptor-related protein 1 (LRP1) as a receptor for RVFV entry into host cells[38]. We took advantage of our in-depth RNA-seq analysis to investigate *LRP1* expression. We observed that the levels of *LRP1* expression in lambs clearly differed between organs but were not affected by the infection status. *LRP1* was more abundantly expressed in the liver than in the spleen (**Fig. 8A**). Such high basal expression levels of the entry factor *LRP1* in the liver correlated with the preference of RVFV for targeting this organ (**Fig. 8B**).

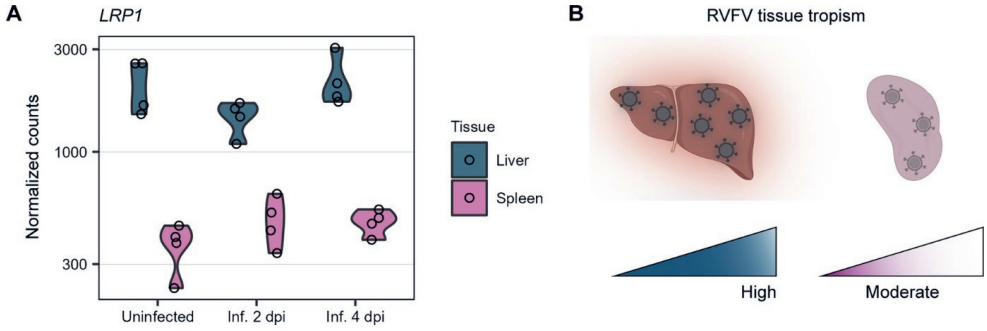

Figure 8. *LRP1* expression correlates with RVFV tissue tropism. A Expression profile of *LRP1* in the liver and spleen of lambs with different infection statuses. Dots represent individual normalized gene counts (on a $\log_{10}$ scale), and the shaded area shows the distribution of the samples within each group. **B** Schematic representation of RVFV tissue tropism. The elevated basal levels of *LRP1* in the liver correlated with the preference of RVFV for targeting this organ. Abbreviations: Inf., infected; dpi, days post-infection.

Discussion

The acute onset of clinical signs and rapid progression to severe disease are features of RVFV infection[39]. Experimental infections in rodents, ferrets, ruminants, and non-human primates have advanced our understanding of RVFV pathogenesis[22,40–45]. However, our knowledge of the underlying mechanisms is still rudimentary. Previous RNA-seq studies of *in vitro* infections and infections of non-target animals have unveiled important genes and pathways that are affected during RVFV infection[31–33]. Nevertheless, RNA-seq studies with primary target animals and tissues have not yet been performed. Here, we examined the *in vivo* genome-wide transcriptional responses in target organs (liver and spleen) of RVFV-infected lambs. This work provides a broad view of the host factors affected by RVFV to better understand the molecular basis of RVFV pathogenesis.

Our study harnessed preserved tissue samples from a previous animal trial in which lambs were exposed to RVFV[34]. Since this trial was not initially designed with the aim of performing a subsequent time course transcriptomic analysis, our study carries two inherent limitations. First, we did not have a conventional negative control group of uninfected lambs. To overcome this, we selected a specific set of samples from a group of lambs that were in theory exposed to the virus (through low-level exposure to mosquitoes) but that did not develop any signs of clinical disease and from which we could not detect infectious virus or viral RNA copies in the blood or the organs. In essence, these lambs had the same characteristics as those of lambs that have not

been exposed to the virus. Arguably, these samples also represent a good control for the potential effects of mosquito bites.

As a second limitation, lambs from the two RVFV-infected groups were exposed to the virus via different routes. Lambs from group 2 were infected via intravenous injection, while lambs from group 3 were infected via the bites of infected mosquitoes. While it can be argued that different routes of infection may lead to distinct infection outcomes, we previously observed that RVFV infection of lambs via intravenous injection or mosquito bites leads to highly similar levels of infectious virus in the blood, comparable histopathological changes, and the same clinical outcomes[22]. We are thus confident that these two above-mentioned limitations do not call into question the validity of our reported observations.

Previous studies by others on the host transcriptomic responses following RVFV infection reported the induction of defense responses[31–33]. Here, we confirmed that upon infection, RVFV induced a strong activation of innate immune and inflammatory responses in both the liver and spleen tissues of lambs, principally through the sharp upregulation of IFN-induced antiviral host restriction factors and cytokine-mediated signaling pathways. The immune and inflammatory activation explains the typical high fever steadily observed through the critical 2- to 4-day-post-infection phase, reflecting the quick and sustained counteraction of the host for clearing the virus.

Among the top upregulated genes, *ISG20* and *ISG15* are of special interest. Indeed, an *in vitro* IFN-stimulated gene (ISG) expression screening identified potent antibunyaviral effects of ISG20 against a diverse panel of members of the *Peribunyaviridae*, *Hantaviridae*, and *Nairoviridae* families through its RNase activity[46]. However, several members of the *Phenuiviridae* family (including RVFV) were described to resist the effects of ISG20[46]. We observed a significant upregulation of *ISG20* in infected tissues. This could mean either that RVFV may be susceptible to *ISG20*-mediated inhibition *in vivo* or that despite the high levels of *ISG20*, RVFV is indeed resistant to its antiviral effects (e.g., due to delayed kinetics of *ISG20* induction). *ISG15* has also been shown to exert antiviral activity against a wide range of viruses[47,48], including the bunyavirus Crimean-Congo hemorrhagic fever virus (CCHFV) (family *Nairoviridae*)[49,50]. The over-expression of *ISG15* during RVFV infection likely reflects its antiviral role.

Several other top upregulated genes in both RVFV-infected liver and spleen tissues have also previously been implicated as key factors in the host antiviral response. For instance, *IFIT3* has been associated with the inhibition of adenovirus[51], rabies virus[52], Japanese encephalitis virus, herpesviruses[53], and even RVFV[31]. *IFI6* was reported to block flavivirus replication[54], and *USP18* was reported to counteract infection by Sendai virus and encephalomyocarditis virus[55]. Similar broad antiviral activities have been described for *XAF1*[56] and *LGALS3BP*[57]. It is conceivable to think that the upregulation of these genes upon RVFV infection is the result of host cellular responses trying to limit viral replication. Thus, our results validate the role of commonly characterized antiviral host factors and expand the range of viruses against which they are known to exert restrictive activity.

The liver is the main target organ of RVFV, and infection generally leads to severe cellular damage that progresses to hepatic necrosis, often followed by inflammation with an infiltration of neutrophils[13,39]. Despite this tropism for the liver, we observed that only a small fraction of the tissue (approximately 10 to 20%) was infected in our samples. Most likely, RVFV-infected hepatocytes signal the viral threat to uninfected neighboring cells, inducing a strong antiviral state that counteracts the infection but compromises liver homeostasis for several days. Dozens of genes coding for enzymes involved in the metabolism of lipids, carbohydrates, proteins, nucleic acids, vitamins, and xenobiotics were markedly downregulated during peak viremia. In animals that recover from the infection, the generalized antiviral state, including transcriptional changes from uninfected neighboring cells, could explain the fast clearance of the virus. Once the levels of the virus decline, unaffected hepatocytes rapidly restore normal liver function.

The downregulation of oxidoreductases, hydrolases, transferases, and transporters, and overall liver failure are clear consequences of the observed tissue necrosis. Such a downregulation of hepatic enzymes responsible for essential metabolic processes possibly explains, for example, the icterus sometimes observed in RVFV-infected animals. Similarly, hemorrhage and coagulation disorders are likely to appear secondary to liver dysfunction due to the damaged liver's incapacity to synthesize proteins crucial for blood homeostasis.

Interestingly, previous *in vitro* RNA-seq studies investigating the mammalian host response upon RVFV infection did not decidedly identify the downregulation of many important metabolic enzymes[31,32]. This apparent discrepancy is most probably explained by the fact that those studies employed small airway epithelial cells and embryonic kidney cells instead of more biologically relevant cells. One additional difference relates to the expression levels of genes involved in ion

transport. Two solute carriers (*SLC24A2* and *SLC1A3*) were reported to be among the top upregulated genes upon RVFV infection[31], whereas we consistently found that several transporters from the same family (e.g., *SLC7A9*, *SLC22A1*, and *SLC22A9*) were significantly downregulated.

The spleen is a secondary target organ of RVFV. Necrosis of the spleen has been described as a common characteristic in naturally infected young lambs, often noticeable in both the red and white pulp[13]. Although less evident than in the liver, the downregulation of genes coding for cellular structural proteins and genes involved in metabolic processes also denotes that the function of the spleen was seriously compromised as a consequence of RVFV infection. Importantly, it might be that the transcriptomic changes observed in the spleen are a combination of direct effects on infected splenocytes and affected immune cells that trafficked to the spleen.

LRP1, a newly identified host entry factor for RVFV[38], is ubiquitously expressed in numerous human tissues, but its expression levels are higher in the liver, placenta, brain, adipose tissue, and fibroblasts (data available from https://www.proteinatlas.org/ENSG00000123384-LRP1)[58]. High expression levels of the LRP1 protein in these tissues can be associated with its natural function as a key molecule in intracellular lipoprotein metabolism (e.g., central cholesterol metabolism in the liver and progesterone biosynthesis in the placenta). In line with the human tissue-specific gene expression data, we found that the levels of *LRP1* expression in lambs were much higher in the liver than in the spleen. The high basal expression level of *LRP1* in the liver possibly explains, at least partially, the marked tropism of RVFV for human and ovine hepatocytes. RVFV also displays preferential tropism for placental cells in pregnant ewes[59], which normally leads to abortion storms during outbreaks[14]. Whether there also is elevated basal *LRP1* expression in the sheep placenta and whether this favors placental infection remain to be investigated. Confirmation of a good correlation between *LRP1* gene expression and its protein levels in lambs awaits further investigation as well.

In summary, the transcriptomic analysis of RVFV-infected liver and spleen tissues of lambs presented here revealed the most important genes and pathways that mediate the strong innate immune response upon infection and the drastic decrease in tissue-specific function. Our results validated that IFN-mediated signaling pathways are key regulators of RVFV infection. Moreover, we uncovered the severely damaged liver metabolic function underlying the acute hepatitis and necrosis induced by RVFV. In addition, we highlighted the elevated basal expression level of *LRP1* in liver cells as a potential factor influencing RVFV tissue tropism. Altogether, the results of this study shed light on the extensive perturbance of the *in vivo* host transcriptome during

critical phases of RVFV infection and provide new insights to better comprehend RVFV pathogenesis at the molecular level. Future studies could expand the current knowledge by concomitantly quantifying host and viral gene expression in individual cells. Transcriptomic profiling at single-cell resolution would make it possible to discriminate the innate immune responses of RVFV-infected cells from those of uninfected neighboring cells, ultimately improving our understanding of the molecular mechanisms employed by RVFV to overcome the host response.

Materials and methods

Tissue samples

Liver and spleen samples were selected from another study aimed at comparing RVFV infection in Texel-Swifter lambs after low-exposure (3 mosquitoes) and high-exposure (28 to 31 mosquitoes) challenges[34]. Mosquitoes used for the challenge were initially fed on lambs 2 days after the intravenous injection of 10^5 median tissue culture infectious doses ($TCID_{50}$) of RVFV strain 35/74[60]. For the purpose of the present study, 4 samples per group were selected from (i) non-responsive lambs (that did not develop viremia or disease) necropsied 8 days after low-level mosquito exposure (group 1), (ii) lambs presenting with high viremia necropsied 2 days after intravenous injection (group 2), and (iii) lambs presenting with high viremia necropsied 4 days after high-level mosquito exposure (group 3). A summary of the different groups is presented in **Table 1**. The group numbers and descriptions presented in **Table 1** belong exclusively to the present study, but to enable traceability, the original identification numbers of the selected samples are included. Within each group, samples were selected based on similar profiles of infectious titers and viral RNA copy numbers in the blood, liver, and spleen. The infectious titers and viral RNA copy numbers were determined by an endpoint dilution virus isolation assay and M-segment-specific quantitative reverse transcription PCR (RT-qPCR), respectively, as described previously[34]. Liver and spleen samples were long-term preserved in RNA*later* (Invitrogen) at ≤ −65°C.

Histology and immunohistochemistry

Tissue samples were fixed in 10% neutral buffered formalin for 48 h and processed routinely into paraffin blocks. Sections were cut on silane-coated glass slides and dried in a 37°C incubator for at least 48 h. After deparaffinization in xylene and rehydration in a series of graded alcohols, sections were stained routinely with hematoxylin and eosin (H&E) or immunostained for RVFV antigen. For immunostaining, heat-induced epitope retrieval was applied by autoclaving the sections for 15 min at 121°C in citrate buffer (pH 6) (Vector Laboratories). Monoclonal antibody 4-D4[61], directed against the Gn glycoprotein, was used as the primary antibody. Goat polyclonal anti-mouse horseradish peroxidase (HRP)-conjugated IgG (Invitrogen) was used as the secondary antibody, with diaminobenzidine (DAB^+) (Dako, Agilent) as the substrate. Sections were

counterstained with Mayer's hematoxylin and mounted permanently. Images were taken with an Olympus BX51 microscope equipped with a high-resolution digital camera.

Table 1. Description, route of exposure, identification number, sex, and age of the lambs from a previous animal study[a] selected for transcriptomic analysis.

Group	Description[b]	Route of exposure	Animal ID	Sex	Age (at challenge) (wks)
1	Uninfected	Mosquito bite (low exposure)	276	Female	10 weeks
			277	Male	
			278	Female	
			279	Female	
2	Infected 2 dpi	Intravenous injection	271	Female	10 weeks
			272	Female	
			273	Male	
			274	Female	
3	Infected 4 dpi	Mosquito bite (high exposure)	4618	Male	10 weeks
			4619	Female	
			4624	Male	
			4642	Female	

[a]See reference 34.

[b]dpi, days post-infection.

RNA isolation

Following thawing, liver and spleen tissue fragments of approximately 80 to 260 mg were washed once in 500 µL of Dulbecco's phosphate-buffered saline (DPBS) (Gibco) to remove excess RNA *later* and then placed into Lysing Matrix D tubes (MP Biomedicals) with 1 mL of TRIzol (Invitrogen). Tissue fragments were homogenized with at least 2 cycles in a FastPrep-24 homogenizer (MP Biomedicals) at 6 m/s for 50 s each cycle until complete homogenization was achieved. When required, to improve the homogenization of complex samples, 2 glass beads per tube were added. Homogenates were centrifuged at 20,800 relative centrifugal force (rcf) (Eppendorf 5417R) for 40 min at 4°C, and the cleared supernatants were kept. Total RNA extractions of 350 µL of lysed samples were performed with the Direct-zol RNA MiniPrep kit (Zymo Research), according to the manufacturer's instructions, with an additional centrifugation step after the addition of RNA wash buffer. Lysed preparations were treated with 30 U of DNase I for 15 min. Total RNA was eventually eluted in 30 µL of DNase/RNase-free water. The RNA concentration and purity were measured on a NanoDrop One instrument (Thermo Fisher Scientific), and samples were stored at ≤ −65°C until further use.

RNA-seq

Isolated RNA was sent for next-generation sequencing to GenomeScan B.V. (Leiden, The Netherlands). The RNA integrity was determined using a Fragment Analyzer system (Agilent) or a 2100 Bioanalyzer (Agilent). Samples were prepared using the NEBNext Ultra II Directional RNA Library Prep Kit for Illumina (catalog number E7760S/L; New England BioLabs [NEB]) according to the instructions of the manufacturer. Briefly, host poly(A) mRNA was isolated from total RNA using oligo(dT) magnetic beads. After the fragmentation of the mRNA, cDNA was synthesized, sequencing adapters were ligated, and the fragments were PCR amplified. The quality and yield of the sequencing library were determined using a Fragment Analyzer (Agilent). The resulting products had a size distribution with a broad peak between 300 and 500 bp. Clustering and sequencing of 1.1 nM DNA samples were performed using an Illumina NovaSeq 6000 instrument with NovaSeq control software NCS version 1.7, according to the instructions of the manufacturer. The sequence length of the short reads ranged between 151 and 159 bp.

RNA-seq data preprocessing

Raw sequencing reads were processed according to the nf-core/RNA-seq pipeline[62] version 3.4 (https://doi.org/10.5281/zenodo.1400710). Quality control was performed with FastQC[63] version 0.11.9 and MultiQC[64] version 1.10.1. Based on the high mean sequence quality (average Phred score >30) (see **Supplementary Fig. 1**), only soft trimming was required. Adapter sequences were removed with Cutadapt[65] version 3.4. Trimmed reads had an average length ranging between 131 and 150 bp. Reads were deduplicated based on unique molecular identifiers (UMIs) using UMI-tools[66] version 1.1.2. Unique reads were aligned to the sheep (*Ovis aries*) NCBI reference genome version 4.0 (Oar_v4.0) (https://www.ncbi.nlm.nih.gov/assembly/GCF_000298735.2/) with HISAT2[67] version 2.2.0 and quantified using featureCounts[68] (within the *Rsubread* package version 2.4.3). Unannotated genes were automatically assigned a *LOC* prefix gene identification nomenclature designation based on genomic position. However, the corresponding gene name, when available, was manually assigned for the plots presented in **Figs. 4A-C, 5A-C**.

Transcriptome analysis

The data set was filtered to remove low-count genes (at least 2 samples should have counts of 3 or higher for a gene to be kept). Pairwise differential gene expression analysis was performed with DESeq2[69] version 1.38.3 in R[70] version 4.2.2, using an absolute $\log_2$ fold change threshold of 1 and an alpha value of 0.05. DESeq2 models the count data with a negative binomial distribution using a generalized linear model. Wald test *p* values <0.05 (adjusted with the Benjamini-Hochberg method) were considered significant. For the initial exploration of the data, Euclidean distances between samples were calculated, and principal component analysis was conducted after applying a variance-stabilizing transformation to the data. For visualization and ranking purposes, the $\log_2$ fold change was shrunken using the adaptive shrinkage estimator from the *ashr* package[71] version 2.2-54. Heat maps were created with the R package *pheatmap* version 1.0.12 (https://CRAN.R-project.org/package=pheatmap) or *ComplexHeatmap*[72]

version 2.14.0. Euler diagrams were plotted with eulerr[73] version 6.1.1. Volcano plots were generated using *EnhancedVolcano*[74] version 1.16.0.

Functional ORA and GSEA were performed with *clusterProfiler*[75,76] version 4.6.0, based on the GO and KEGG databases. When required, the clusterProfiler function *simplify* was used to reduce the redundancy of enriched GO terms. *p* values <0.05 (adjusted by the Benjamini-Hochberg method) of a one-sided version of Fisher's exact test were considered significant for ORA. *p* values <0.05 (adjusted by the Benjamini-Hochberg method) of a permutation test were considered significant for GSEA.

Data analysis and visualization

Prism 9 (GraphPad Software) was used to generate graphs of infectious titer and viral RNA copy number data. Transcriptomic data were analyzed and plotted in R[70] version 4.2.2, using the above-mentioned R packages. Statistical tests differed per analysis and are indicated in the description of each analysis and the corresponding figure legends. *p* values ≥0.05 were considered not significant.

Ethics statement

The animal experiment carried out within the scope of another study[34], from which organ samples were obtained for analysis, was conducted in accordance with European regulations (European Union directive 2010/63/EU) and the Dutch Law on Animal Experiments (Wod, identification number BWBR0003081). Permissions were granted by the Dutch Central Authority for Scientific Procedures on Animals (permit numbers AVD4010020185564 and AVD4010020187168). Specific procedures were approved by the Animal Ethics Committees of Wageningen Research.

Data availability

Raw sequencing data were deposited at the NCBI Sequence Read Archive (SRA) under BioProject accession number PRJNA935986.

Acknowledgements

EBM is a grateful recipient of scholarships from the Graduate School for Production Ecology & Resource Conservation (PE&RC) and Universidad de Costa Rica (OAICE-031-2019). This work was supported in part by funds from the Rob Goldbach Fund to EBM for a laboratory training visit.

We thank Quirine ten Bosch (Quantitative Veterinary Epidemiology, Wageningen University & Research) for authorizing the utilization of samples from the RVFV animal trial[34]. We thank Ingrid Cárdenas Rey for proofreading. The illustrations in **Figs. 1A, 8B** were created with BioRender.com.

Author contributions

PJWS, EBM and JK conceived the project. EBM and SvdW performed the RNA isolation for RNA-seq. EBM and PA performed the RNA-seq data processing and bioinformatic analysis. EBM, PA and PJWS interpreted the RNA-seq data with contributions from BR, GPP, AC and JK. LvK performed the histology and immunohistochemistry experiments. PJWS, JK, AC and GPP supervised the project. EBM wrote the manuscript with contributions from PJWS and LvK. EBM made the figures with contributions from PA, LvK and PJWS. All authors reviewed the manuscript and provided feedback.

Competing interests

The authors declare no conflict of interest.

References

1. Flick R, Bouloy M. Rift Valley fever virus. *Current Molecular Medicine* **2005**, *5* (8), 827–834. https://doi.org/10.2174/156652405774962263.

2. Pepin M, Bouloy M, Bird BH, Kemp A, Paweska J. Rift Valley fever virus (*Bunyaviridae*: *Phlebovirus*): an update on pathogenesis, molecular epidemiology, vectors, diagnostics and prevention. *Veterinary Research* **2010**, *41* (6), 61. https://doi.org/10.1051/vetres/2010033.

3. Abudurexiti A, Adkins S, Alioto D, Alkhovsky SV, Avšič-Županc T, Ballinger MJ, Bente DA, Beer M, Bergeron É, Blair CD, Briese T, Buchmeier MJ, *et al.* Taxonomy of the order *Bunyavirales*: update 2019. *Archives of Virology* **2019**, *164* (7), 1949–1965. https://doi.org/10.1007/s00705-019-04253-6.

4. Nanyingi MO, Munyua P, Kiama SG, Muchemi GM, Thumbi SM, Bitek AO, Bett B, Muriithi RM, Njenga MK. A systematic review of Rift Valley Fever epidemiology 1931–2014. *Infection Ecology & Epidemiology* **2015**, *5* (1), 28024. https://doi.org/10.3402/iee.v5.28024.

5. Clark MHA, Warimwe GM, Nardo AD, Lyons NA, Gubbins S. Systematic literature review of Rift Valley fever virus seroprevalence in livestock, wildlife and humans in Africa from 1968 to 2016. *PLOS Neglected Tropical Diseases* **2018**, *12* (7), e0006627. https://doi.org/10.1371/journal.pntd.0006627.

6. Anywaine Z, Lule SA, Hansen C, Warimwe G, Elliott A. Clinical manifestations of Rift Valley fever in humans: Systematic review and meta-analysis. *PLOS Neglected Tropical Diseases.* **2022**, *16* (3), e0010233. https://doi.org/10.1371/journal.pntd.0010233.

7. Daubney R, Hudson JR, Garnham PC. Enzootic hepatitis or Rift Valley fever. An undescribed virus disease of sheep cattle and man from East Africa. *The Journal of Pathology and Bacteriology* **1931**, *34* (4), 545–579. https://doi.org/10.1002/path.1700340418.

8. Madani TA, Al-Mazrou YY, Al-Jeffri MH, Mishkhas AA, Al-Rabeah AM, Turkistani AM, Al-Sayed MO, Abodahish AA, Khan AS, Ksiazek TG, Shobokshi O. Rift Valley fever epidemic in Saudi Arabia: epidemiological, clinical, and laboratory characteristics. *Clinical Infectious Diseases* **2003**, *37* (8), 1084-1092. https://doi.org/10.1086/378747.

9. Al-Hazmi M, Ayoola EA, Abdurahman M, Banzal S, Ashraf J, El-Bushra A, Hazmi A, Abdullah M, Abbo H, Elamin A, Al-Sammani E-T, Gadour M, *et al.* Epidemic Rift Valley fever in Saudi Arabia: a clinical study of severe illness in humans. *Clinical Infectious Diseases* **2003**, *36* (3), 245–252. https://doi.org/10.1086/345671.

10. Hassan OA, Ahlm C, Sang R, Evander M. The 2007 Rift Valley fever outbreak in Sudan. *PLOS Neglected Tropical Diseases* **2011**, *5* (9), e1229. https://doi.org/10.1371/journal.pntd.0001229.

11. Odendaal L, Clift SJ, Fosgate GT, Davis AS. Lesions and cellular tropism of natural Rift Valley fever virus infection in adult sheep. *Veterinary Pathology* **2019**, *56* (1), 61–77. https://doi.org/10.1177/0300985818806049.

12. Wright D, Kortekaas J, Bowden TA, Warimwe GM. Rift Valley fever: biology and epidemiology. *Journal of General Virology* **2019**, *100* (8), 1187–1199. https://doi.org/10.1099/jgv.0.001296.

13. Odendaal L, Davis AS, Fosgate GT, Clift SJ. Lesions and cellular tropism of natural Rift Valley fever virus infection in young lambs. *Veterinary Pathology* **2020**, *57* (1), 66–81. https://doi.org/10.1177/0300985819882633.

14. Odendaal L, Clift SJ, Fosgate GT, Davis AS. Ovine fetal and placental lesions and cellular tropism in natural Rift Valley fever virus infections. *Veterinary Pathology* **2020**, *57* (6), 791–806. https://doi.org/10.1177/0300985820954549.

15. El-Din Abdel-Wahab KS, El Baz LM, El Tayeb EM, Omar H, Moneim Ossman MA, Yasin W. Rift Valley fever virus infections in Egypt: pathological and virological findings in man. *Transactions of The Royal Society of Tropical Medicine and Hygiene* **1978**, *72* (4), 392–396. https://doi.org/10.1016/0035-9203(78)90134-7.

16. Turell MJ, Dohm DJ, Mores CN, Terracina L, Wallette DL, Hribar LJ, Pecor JE, Blow JA. Potential for North American mosquitoes to transmit Rift Valley fever virus. *Journal of the American Mosquito Control Association* **2008**, *24* (4), 502–507. https://doi.org/10.2987/08-5791.1.

17. Turell MJ, Britch SC, Aldridge RL, Kline DL, Boohene C, Linthicum KJ. Potential for mosquitoes (Diptera: Culicidae) from Florida to transmit Rift Valley fever virus. *Journal of Medical Entomology* **2013**, *50* (5), 1111–1117. https://doi.org/10.1603/ME13049.

18. Brustolin M, Talavera S, Nuñez A, Santamaría C, Rivas R, Pujol N, Valle M, Verdún M, Brun A, Pagès N, Busquets N. Rift Valley fever virus and European mosquitoes: vector competence of *Culex pipiens* and *Stegomyia albopicta* (= *Aedes albopictus*). *Medical and Veterinary Entomology* **2017**, *31* (4), 365-372. https://doi.org/10.1111/mve.12254.

19. Kraemer MUG, Reiner RC, Brady OJ, Messina JP, Gilbert M, Pigott DM, Yi D, Johnson K, Earl L, Marczak LB, Shirude S, Davis Weaver N, *et al.* Past and future spread of the arbovirus vectors *Aedes aegypti* and *Aedes albopictus*. *Nature Microbiology* **2019**, *4* (5), 854–863. https://doi.org/10.1038/s41564-019-0376-y.

20. Rich KM, Wanyoike F. An assessment of the regional and national socio-economic impacts of the 2007 Rift Valley fever outbreak in Kenya. *The American Journal of Tropical Medicine and Hygiene* **2010**, *83* (2_Suppl), 52–57. https://doi.org/10.4269/ajtmh.2010.09-0291.

21. Peyre M, Chevalier V, Abdo-Salem S, Velthuis A, Antoine-Moussiaux N, Thiry E, Roger F. A systematic scoping study of the socio-economic impact of Rift Valley fever: research gaps and needs. *Zoonoses Public Health* **2015**, *62* (5), 309–325. https://doi.org/10.1111/zph.12153.

22. Wichgers Schreur PJ, Vloet RPM, Kant J, van Keulen L, Gonzales JL, Visser TM, Koenraadt CJM, Vogels CBF, Kortekaas J. Reproducing the Rift Valley fever virus mosquito-lamb-mosquito transmission cycle. *Scientific Reports* **2021**, *11* (1), 1477. https://doi.org/10.1038/s41598-020-79267-1.

23. Bouloy M, Janzen C, Vialat P, Khun H, Pavlovic J, Huerre M, Haller O. Genetic evidence for an interferon-antagonistic function of Rift Valley fever virus nonstructural protein NSs. *Journal of Virology* **2001**, *75* (3), 1371–1377. https://doi.org/10.1128/JVI.75.3.1371-1377.2001.

24. Billecocq A, Spiegel M, Vialat P, Kohl A, Weber F, Bouloy M, Haller O. NSs protein of Rift Valley fever virus blocks interferon production by inhibiting host gene transcription. *Journal of Virology* **2004**, *78* (18), 9798–9806. https://doi.org/10.1128/JVI.78.18.9798-9806.2004.

25. Le May N, Dubaele S, De Santis LP, Billecocq A, Bouloy M, Egly J-M. TFIIH transcription factor, a target for the Rift Valley hemorrhagic fever virus. *Cell* **2004**, *116* (4), 541–550. https://doi.org/10.1016/S0092-8674(04)00132-1.

26. Habjan M, Pichlmair A, Elliott RM, Överby AK, Glatter T, Gstaiger M, Superti-Furga G, Unger H, Weber F. NSs protein of Rift Valley fever virus induces the specific degradation of the double-stranded RNA-dependent protein kinase. *Journal of Virology* **2009**, *83* (9), 4365–4375. https://doi.org/10.1128/JVI.02148-08.

27. Ikegami T, Narayanan K, Won S, Kamitani W, Peters CJ, Makino S. Rift Valley fever virus NSs protein promotes post-transcriptional downregulation of protein kinase PKR and inhibits eIF2alpha phosphorylation. *PLOS Pathogens* **2009**, *5* (2), e1000287. https://doi.org/10.1371/journal.ppat.1000287.

28. Kainulainen M, Lau S, Samuel CE, Hornung V, Weber F. NSs virulence factor of Rift Valley fever virus engages the F-Box proteins FBXW11 and β-TRCP1 to degrade the antiviral protein kinase PKR. *Journal of Virology* **2016**, *90* (13), 6140–6147. https://doi.org/10.1128/JVI.00016-16.

29. Wang Z, Gerstein M, Snyder M. RNA-Seq: a revolutionary tool for transcriptomics. *Nature Reviews Genetics* **2009**, *10* (1), 57–63. https://doi.org/10.1038/nrg2484.

30. Stark R, Grzelak M, Hadfield J. RNA sequencing: the teenage years. *Nature Reviews Genetics* **2019**, *20* (11), 631–656. https://doi.org/10.1038/s41576-019-0150-2.

31. Pinkham C, Dahal B, de la Fuente CL, Bracci N, Beitzel B, Lindquist M, Garrison A, Schmaljohn C, Palacios G, Narayanan A, Campbell CE, Kehn-Hall K. Alterations in the host transcriptome *in vitro* following Rift Valley fever virus infection. *Scientific Reports* **2017**, *7* (1), 14385. https://doi.org/10.1038/s41598-017-14800-3.

32. Havranek KE, White LA, Lanchy J-M, Lodmell JS. Transcriptome profiling in Rift Valley fever virus infected cells reveals modified transcriptional and alternative splicing programs. *PLOS ONE* **2019**, *14* (5), e0217497. https://doi.org/10.1371/journal.pone.0217497.

33. Hum NR, Bourguet FA, Sebastian A, Lam D, Phillips AM, Sanchez KR, Rasley A, Loots GG, Weilhammer DR. MAVS mediates a protective immune response in the brain to Rift Valley fever virus. *PLOS Pathogens* **2022**, *18* (5), e1010231. https://doi.org/10.1371/journal.ppat.1010231.

34. Bron GM, Wichgers Schreur PJ, de Jong MCM, van Keulen L, Vloet RPM, Koenraadt CJM, Kortekaas J, ten Bosch QA. Quantifying Rift Valley fever virus transmission efficiency in a lamb-mosquito-lamb model. bioRxiv April 25, 2023, p 2023.04.25.538218. https://doi.org/10.1101/2023.04.25.538218.

35. Schroeder A, Mueller O, Stocker S, Salowsky R, Leiber M, Gassmann M, Lightfoot S, Menzel W, Granzow M, Ragg T. The RIN: an RNA integrity number for assigning integrity values to RNA measurements. *BMC Molecular Biology* **2006**, *7* (1), 1–14. https://doi.org/10.1186/1471-2199-7-3.

36. Boyle EI, Weng S, Gollub J, Jin H, Botstein D, Cherry JM, Sherlock G. GO::TermFinder—open source software for accessing Gene Ontology information and finding significantly enriched Gene Ontology terms associated with a list of genes. *Bioinformatics* **2004**, *20* (18), 3710–3715. https://doi.org/10.1093/bioinformatics/bth456.

37. Subramanian A, Tamayo P, Mootha VK, Mukherjee S, Ebert BL, Gillette MA, Paulovich A, Pomeroy SL, Golub TR, Lander ES, Mesirov JP. Gene set enrichment analysis: A knowledge-based approach for interpreting genome-wide expression profiles. *PNAS* **2005**, *102* (43), 15545–15550. https://doi.org/10.1073/pnas.0506580102.

38. Ganaie SS, Schwarz MM, McMillen CM, Price DA, Feng AX, Albe JR, Wang W, Miersch S, Orvedahl A, Cole AR, Sentmanat MF, Mishra N, *et al.* Lrp1 is a host entry factor for Rift Valley fever virus. *Cell* **2021**, *184* (20), 5163-5178.e24. https://doi.org/10.1016/j.cell.2021.09.001.

39. Terasaki K, Makino S. Interplay between the virus and host in Rift Valley fever pathogenesis. *Journal of Innate Immunity* **2015**, *7* (5), 450–458. https://doi.org/10.1159/000373924.

40. Scharton D, Wettere AJV, Bailey KW, Vest Z, Westover JB, Siddharthan V, Gowen BB. Rift Valley fever virus infection in golden Syrian hamsters. *PLOS ONE* **2015**, *10* (1), e0116722. https://doi.org/10.1371/journal.pone.0116722.

41. Lang Y, Henningson J, Jasperson D, Li Y, Lee J, Ma J, Li Y, Cao N, Liu H, Wilson W, Richt J, Ruder M, *et al.* Mouse model for the Rift Valley fever virus MP12 strain infection. *Veterinary Microbiology* **2016**, *195*, 70–77. https://doi.org/10.1016/j.vetmic.2016.09.009.

42. Albe JR, Boyles DA, Walters AW, Kujawa MR, McMillen CM, Reed DS, Hartman AL. Neutrophil and macrophage influx into the central nervous system are inflammatory components of lethal Rift Valley fever encephalitis in rats. *PLOS Pathogens* **2019**, *15* (6), e1007833. https://doi.org/10.1371/journal.ppat.1007833.

43. Barbeau DJ, Albe JR, Nambulli S, Tilston-Lunel NL, Hartman AL, Lakdawala SS, Klein E, Duprex WP, McElroy AK. Rift Valley fever virus infection causes acute encephalitis in the ferret. *mSphere* **2020**, *5* (5), e00798-20. https://doi.org/10.1128/mSphere.00798-20.

44. Wilson WC, Davis AS, Gaudreault NN, Faburay B, Trujillo JD, Shivanna V, Sunwoo SY, Balogh A, Endalew A, Ma W, Drolet BS, Ruder MG, *et al.* Experimental infection of calves by two genetically-distinct strains of Rift Valley fever virus. *Viruses* **2016**, *8* (5), 145. https://doi.org/10.3390/v8050145.

45. Smith DR, Bird BH, Lewis B, Johnston SC, McCarthy S, Keeney A, Botto M, Donnelly G, Shamblin J, Albariño CG, Nichol ST, Hensley LE. Development of a novel nonhuman primate model for Rift Valley fever. *Journal of Virology* **2012**, *86* (4), 2109–2120. https://doi.org/10.1128/JVI.06190-11.

46. Feng J, Wickenhagen A, Turnbull ML, Rezelj VV, Kreher F, Tilston-Lunel NL, Slack GS, Brennan B, Koudriakova E, Shaw AE, Rihn SJ, Rice CM, *et al.* Interferon-stimulated gene (ISG)-expression screening reveals the specific antibunyaviral activity of ISG20. *Journal of Virology* **2018**, *92* (13), e02140-17. https://doi.org/10.1128/JVI.02140-17.

47. Zhao C, Collins MN, Hsiang T-Y, Krug RM. Interferon-induced ISG15 pathway: an ongoing virus–host battle. *Trends in Microbiology* **2013**, *21* (4), 181–186. https://doi.org/10.1016/j.tim.2013.01.005.

48. Perng Y-C, Lenschow DJ. ISG15 in antiviral immunity and beyond. *Nature Reviews Microbiology* **2018**, *16* (7), 423–439. https://doi.org/10.1038/s41579-018-0020-5.

49. Scholte FEM, Zivcec M, Dzimianski JV, Deaton MK, Spengler JR, Welch SR, Nichol ST, Pegan SD, Spiropoulou CF, Bergeron É. Crimean-Congo hemorrhagic fever virus suppresses innate immune responses via a ubiquitin and ISG15 specific protease. *Cell Reports* **2017**, *20* (10), 2396–2407. https://doi.org/10.1016/j.celrep.2017.08.040.

50. Neogi U, Elaldi N, Appelberg S, Ambikan A, Kennedy E, Dowall S, Bagci BK, Gupta S, Rodriguez JE, Svensson-Akusjärvi S, Monteil V, Vegvari A, *et al.* Multi-omics insights into host-viral response and pathogenesis in Crimean-Congo hemorrhagic fever viruses for novel therapeutic target. *eLife* **2022**, *11*, e76071. https://doi.org/10.7554/eLife.76071.

51. Chikhalya A, Dittmann M, Zheng Y, Sohn S-Y, Rice CM, Hearing P. Human IFIT3 protein induces interferon signaling and inhibits adenovirus immediate early gene expression. *mBio* **2021**, *12* (6), e02829-21. https://doi.org/10.1128/mBio.02829-21.

52. Chai B, Tian D, Zhou M, Tian B, Yuan Y, Sui B, Wang K, Pei J, Huang F, Wu Q, Lv L, Yang Y, *et al.* Murine Ifit3 restricts the replication of Rabies virus both *in vitro* and *in vivo*. *Journal of General Virology* **2021**, *102* (7), 001619. https://doi.org/10.1099/jgv.0.001619.

53. Zhang W, Li Y, Xin S, Yang L, Jiang M, Xin Y, Wang Y, Cao P, Zhang S, Yang Y, Lu J. The emerging roles of IFIT3 in antiviral innate immunity and cellular biology. *Journal of Medical Virology* **2022**, *95* (1), e28259. https://doi.org/10.1002/jmv.28259.

54. Richardson RB, Ohlson MB, Eitson JL, Kumar A, McDougal MB, Boys IN, Mar KB, De La Cruz-Rivera PC, Douglas C, Konopka G, Xing C, Schoggins JW. A CRISPR screen identifies IFI6 as an ER-resident interferon effector that blocks flavivirus replication. *Nature Microbiology* **2018**, *3* (11), 1214–1223. https://doi.org/10.1038/s41564-018-0244-1.

55. Hou J, Han L, Zhao Z, Liu H, Zhang L, Ma C, Yi F, Liu B, Zheng Y, Gao C. USP18 positively regulates innate antiviral immunity by promoting K63-linked polyubiquitination of MAVS. *Nature Communications* **2021**, *12*, 2970. https://doi.org/10.1038/s41467-021-23219-4.

56. Han Y, Bai X, Liu S, Zhu J, Zhang F, Xie L, Liu G, Jiang X, Zhang M, Huang Y, Wang J, Li D, *et al.* XAF1 protects host against emerging RNA viruses by stabilizing IRF1-dependent antiviral immunity. *Journal of Virology* **2022**, *96* (17), e00774-22. https://doi.org/10.1128/jvi.00774-22.

57. Xu G, Xia Z, Deng F, Liu L, Wang Q, Yu Y, Wang F, Zhu C, Liu W, Cheng Z, Zhu Y, Zhou L, *et al.* Inducible LGALS3BP/90K activates antiviral innate immune responses by targeting TRAF6 and TRAF3 complex. *PLOS Pathogens* **2019**, *15* (8), e1008002. https://doi.org/10.1371/journal.ppat.1008002.

58. Uhlén M, Fagerberg L, Hallström BM, Lindskog C, Oksvold P, Mardinoglu A, Sivertsson Å, Kampf C, Sjöstedt E, Asplund A, Olsson I, Edlund K, *et al.* Tissue-based map of the human proteome. *Science* **2015**, *347* (6220), 1260419. https://doi.org/10.1126/science.1260419.

59. Oymans J, Wichgers Schreur PJ, van Keulen L, Kant J, Kortekaas J. Rift Valley fever virus targets the maternal-foetal interface in ovine and human placentas. *PLOS Neglected Tropical Diseases* **2020**, *14* (1), e0007898. https://doi.org/10.1371/journal.pntd.0007898.

60. Barnard BJH. Rift Valley fever vaccine - antibody and immune response in cattle to a live and an inactivated vaccine. *Journal of the South African Veterinary Association* **1979**, *50* (3), 155–157. https://doi.org/10.10520/AJA00382809_4630.

61. Keegan K, Collett MS. Use of bacterial expression cloning to define the amino acid sequences of antigenic determinants on the G2 glycoprotein of Rift Valley fever virus. *Journal of Virology* **1986**, *58* (2), 263–270.

62. Ewels PA, Peltzer A, Fillinger S, Patel H, Alneberg J, Wilm A, Garcia MU, Di Tommaso P, Nahnsen S. The nf-core framework for community-curated bioinformatics pipelines. *Nature Biotechnology* **2020**, *38* (3), 276–278. https://doi.org/10.1038/s41587-020-0439-x.

63. Andrews S. FastQC: a quality control tool for high throughput sequence data, 2010. http://www.bioinformatics.babraham.ac.uk/projects/fastqc.

64. Ewels P, Magnusson M, Lundin S, Käller M. MultiQC: summarize analysis results for multiple tools and samples in a single report. *Bioinformatics* **2016**, *32* (19), 3047–3048. https://doi.org/10.1093/bioinformatics/btw354.

65. Martin M. Cutadapt removes adapter sequences from high-throughput sequencing reads. *EMBnet.journal* **2011**, *17* (1), 10–12. https://doi.org/10.14806/ej.17.1.200.

66. Smith TS, Heger A, Sudbery I. UMI-tools: Modelling sequencing errors in Unique Molecular Identifiers to improve quantification accuracy. *Genome Research* **2017**, gr.209601.116. https://doi.org/10.1101/gr.209601.116.

67. Kim D, Paggi JM, Park C, Bennett C, Salzberg SL. Graph-based genome alignment and genotyping with HISAT2 and HISAT-genotype. *Nature Biotechnology* **2019**, *37* (8), 907–915. https://doi.org/10.1038/s41587-019-0201-4.

68. Liao Y, Smyth GK, Shi W. featureCounts: an efficient general purpose program for assigning sequence reads to genomic features. *Bioinformatics* **2014**, *30* (7), 923–930. https://doi.org/10.1093/bioinformatics/btt656.

69. Love MI, Huber W, Anders S. Moderated estimation of fold change and dispersion for RNA-seq data with DESeq2. *Genome Biology* **2014**, *15* (12), 550. https://doi.org/10.1186/s13059-014-0550-8.

70. R Core Team. R: A language and environment for statistical computing. R Foundation for Statistical Computing, Vienna, Austria 2022. https://www.R-project.org/.

71. Stephens M. False discovery rates: a new deal. *Biostatistics* **2017**, *18* (2), 275–294. https://doi.org/10.1093/biostatistics/kxw041.

72. Gu Z. Complex heatmap visualization. *iMeta* **2022**, *1* (3), e43. https://doi.org/10.1002/imt2.43.

73. Larsson J. eulerr: Area-Proportional Euler and Venn Diagrams with Ellipses, 2021. https://cran.r-project.org/package=eulerr.

74. Blighe K, Rana S, Myles L. EnhancedVolcano: publication-ready volcano plots with enhanced colouring and labeling, 2022. https://github.com/kevinblighe/EnhancedVolcano.

75. Yu G, Wang L-G, Han Y, He Q-Y. clusterProfiler: an R package for comparing biological themes among gene clusters. *OMICS* **2012**, *16* (5), 284–287. https://doi.org/10.1089/omi.2011.0118.

76. Wu T, Hu E, Xu S, Chen M, Guo P, Dai Z, Feng T, Zhou L, Tang W, Zhan L, Fu X, Liu S, *et al.* clusterProfiler 4.0: a universal enrichment tool for interpreting omics data. *The Innovation* **2021**, *2* (3), 100141. https://doi.org/10.1016/j.xinn.2021.100141.

Supplementary information

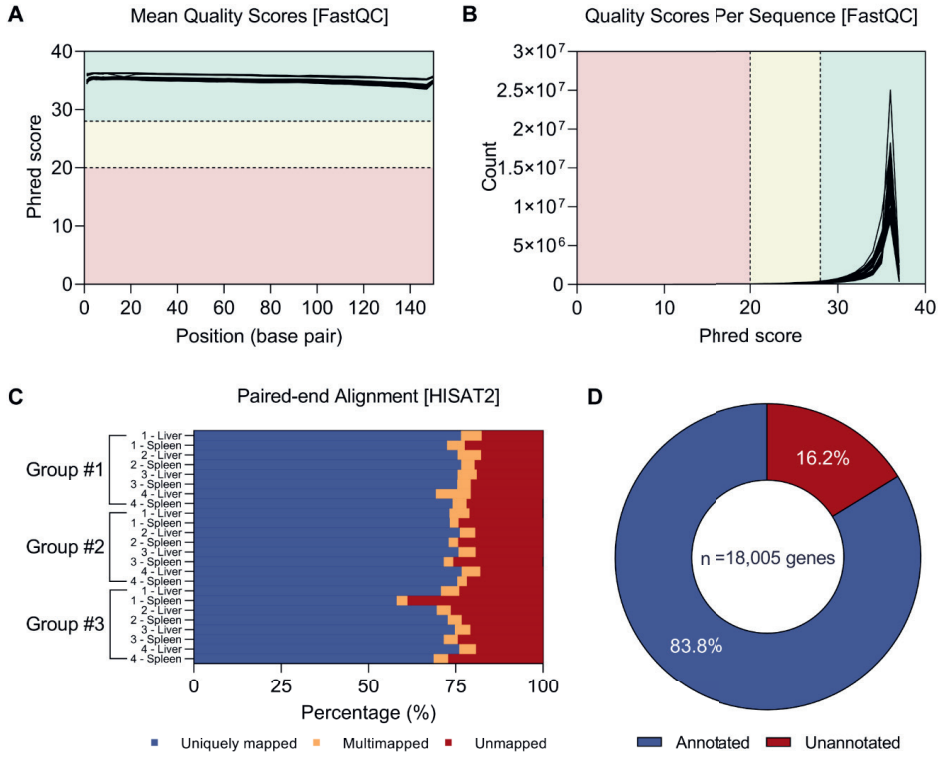

Supplementary Figure 1. RNA-seq raw data quality control and pre-processing. A Mean quality (Phred) scores across each position in the raw reads. **B** Histogram of per sequence quality (Phred) scores for the raw reads. Raw data quality control was performed with FastQC[1]. Individual lines represent the scores for each of the 48 raw reads. Dashed lines divide the plotting area into three regions according to the quality scores. Red indicates low quality (Phred score < 20), yellow indicates middle quality (20 ≤ Phred score < 28) and green indicates high quality (Phred score ≥ 28). **C** Alignment of unique reads to the sheep (*Ovis aries*) NCBI reference genome using HISAT2[2]. Single mate alignment counts were halved to tally with pair counts properly. **D** Fraction of input genes for analysis annotated in the reference genome.

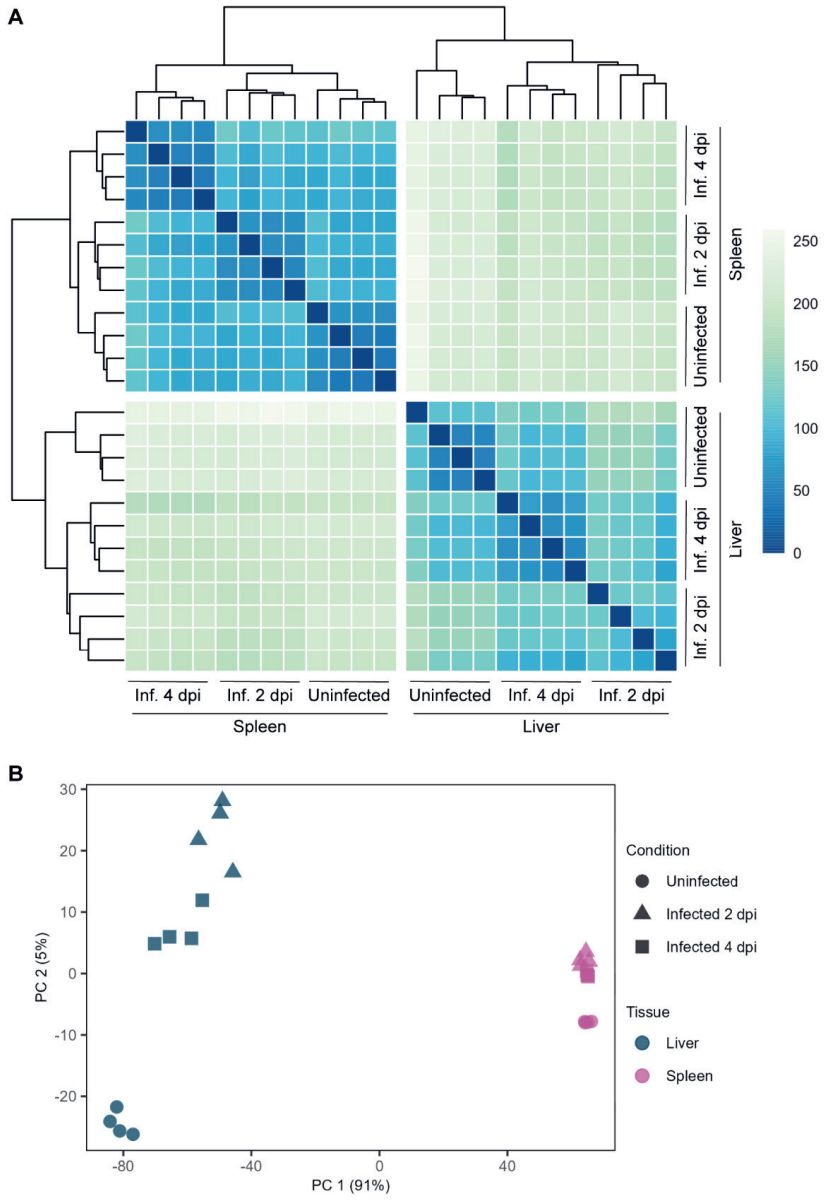

Supplementary Figure 2. Distinct tissue-specific gene expression profiles. A Heat map of euclidean distances between all the liver and spleen tissue samples. Based on the calculated distance, each cell is color-coded in shades of a sequential gradient ranging from dark blue (close distance, implying similarity) to light green (far distance, implying dissimilarity). **B** Principal component analysis of all the liver and spleen tissue samples. The sharp separation of the samples into two well-defined clusters indicates that gene expression profiles clearly differ between tissue types. Abbreviations: Inf., infected; dpi, days post-infection.

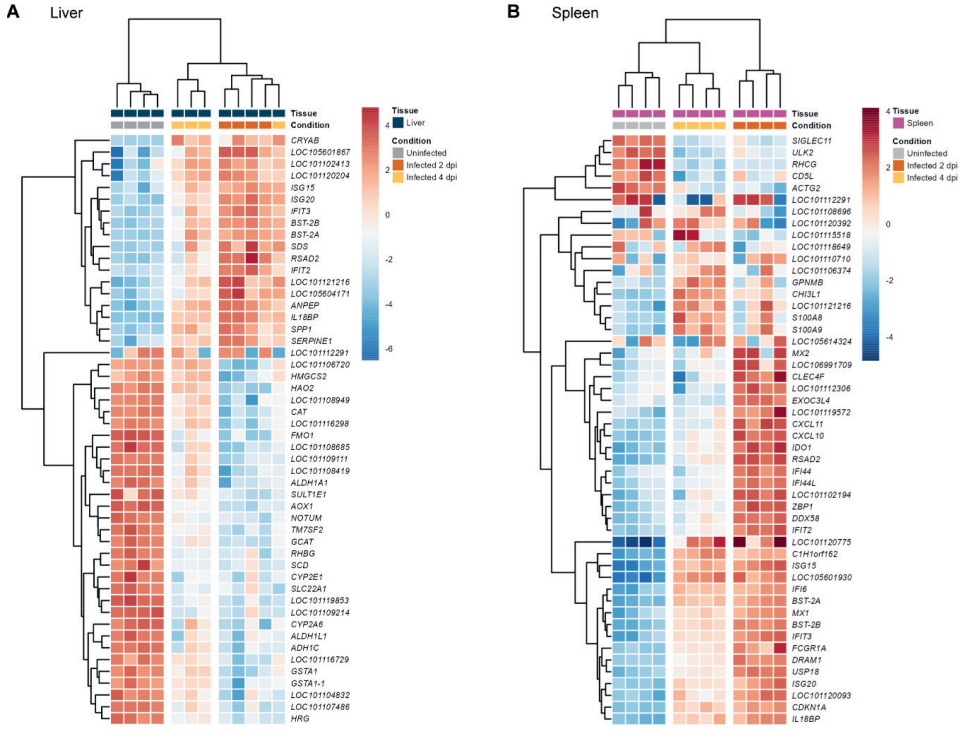

Supplementary Figure 3. Top variable genes differentially expressed upon RVFV infection. A, B Heat maps of the top 50 most variably expressed genes after RVFV infection in liver (**A**) and spleen (**B**) tissues. Based on the gene expression patterns of the most variably expressed genes, samples were hierarchically clustered into three groups. To represent the magnitude of the $\log_2$ fold change of each gene compared to the mean gene expression, cells are color-coded in shades of a gradient ranging from dark blue (low) to dark red (high). Abbreviation: dpi, days post-infection.

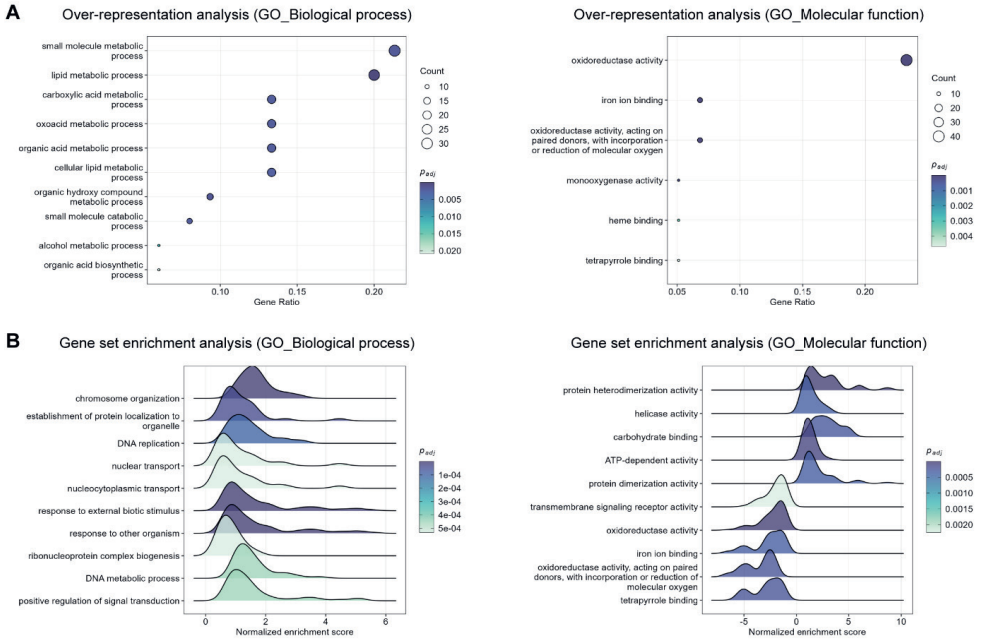

Supplementary Figure 4. Top significantly enriched pathways altered in the liver in response to RVFV infection (4 days post-infection). A Gene ontology (GO) biological process (left) and molecular function (right) over-representation analysis of genes differentially expressed in RVFV-infected liver tissue. Dot size represents the number of enriched genes associated to each GO term. Dots are color-coded according to their adjusted *p* value (Benjamini-Hochberg method). **B** GO biological process (left) and molecular function (right) gene set enrichment analysis in RVFV-infected liver tissue. Gene sets with positive normalized enrichment scores are upregulated, whereas gene sets with negative normalized enrichment scores are downregulated. Ridges are color-coded according to their adjusted *p* value (Benjamini-Hochberg method). Cut-off for significance in all the analyses was set to a *p* adjusted value < 0.05.

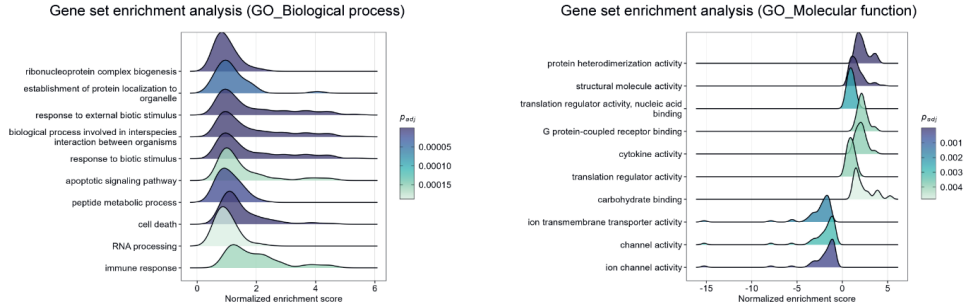

Supplementary Figure 5. Top significantly enriched gene sets altered in the spleen in response to RVFV infection (4 days post-infection). Gene ontology (GO) biological process (left) and molecular function (right) gene set enrichment analysis in RVFV-infected spleen tissue. Gene sets with positive normalized enrichment scores are upregulated, whereas gene sets with negative normalized enrichment scores are downregulated. Ridges are color-coded according to their adjusted *p* value (Benjamini-Hochberg method). Cut-off for significance in all the analyses was set to a *p* adjusted value < 0.05.

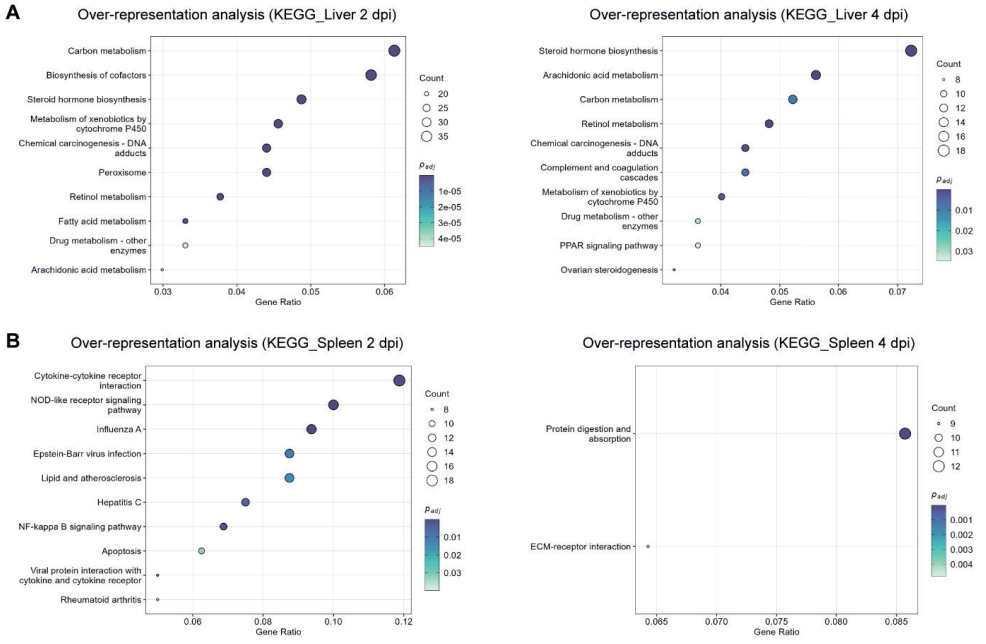

Supplementary Figure 6. Top significantly enriched KEGG pathways altered in the liver and spleen in response to RVFV infection. A, B Kyoto Encyclopedia of Genes and Genomes (KEGG) pathways over-representation analysis of genes differentially expressed in RVFV-infected liver (**A**) and spleen (**B**) tissues at 2 (left) and 4 (right) days post-infection. Dot size represents the number of enriched genes associated to each KEGG pathway. Dots are color-coded according to their adjusted *p* value (Benjamini-Hochberg method). Cut-off for significance in all the analyses was set to a *p* adjusted value < 0.05. Abbreviation: dpi, days post-infection.

Supplementary Table 1. Quality of isolated RNA used for next-generation sequencing.

Group	Sample ID	RNA quality number (RQN)*
Group #1	1 - Liver	7.1
	1 - Spleen	6.4
	2 - Liver	6.3
	2 - Spleen	6.2 (RIN)
	3 - Liver	6.1
	3 - Spleen	7.2
	4 - Liver	4.1 (RIN)
	4 - Spleen	6.3 (RIN)
Group #2	1 - Liver	5.2 (RIN)
	1 - Spleen	5.2
	2 - Liver	6.8
	2 - Spleen	7.3
	3 - Liver	6.3
	3 - Spleen	7.3
	4 - Liver	6.3
	4 - Spleen	7.0
Group #3	1 - Liver	6.2
	1 - Spleen	7.2
	2 - Liver	6.5
	2 - Spleen	7.5
	3 - Liver	7.3
	3 - Spleen	7.8
	4 - Liver	6.6
	4 - Spleen	7.1

* For some samples, the RNA integrity number (RIN) is reported instead of the RQN.

Supplementary Table 2. Summary of the next-generation sequencing run.

Group	Sample ID	Total reads (M) [FastQC]	Average Phred score [FastQC]	% Aligned [HISAT2]
Group #1	1 - Liver	21.7	35.4	82.4
	1 - Spleen	24.6	35.1	77.6
	2 - Liver	26.6	35.4	82.3
	2 - Spleen	23.3	35.3	80.4
	3 - Liver	24.1	35.3	81.0
	3 - Spleen	22.4	35.4	79.3
	4 - Liver	20.9	35.3	79.3
	4 - Spleen	25.7	35.5	78.2
Group #2	1 - Liver	28.6	35.2	79.0
	1 - Spleen	28.8	35.3	75.8
	2 - Liver	20.0	35.3	80.6
	2 - Spleen	21.8	35.3	75.7
	3 - Liver	27.9	35.3	80.7
	3 - Spleen	20.5	35.2	74.3
	4 - Liver	24.6	35.4	82.0
	4 - Spleen	38.7	35.5	78.2
Group #3	1 - Liver	23.2	35.1	76.0
	1 - Spleen	24.1	34.1	61.1
	2 - Liver	21.4	35.3	73.6
	2 - Spleen	25.2	35.5	76.7
	3 - Liver	22.5	35.3	79.2
	3 - Spleen	25.6	35.4	75.6
	4 - Liver	26.7	35.3	80.8
	4 - Spleen	25.8	35.1	72.8

In the column headings, the bioinformatic tool from which the information was extracted is specified within square brackets.

Additional supplementary information files can be accessed online at:
https://doi.org/10.1128/jvi.00415-23

Supplementary Table 3

Supplementary Table 4

Supplementary Table 5

Chapter 5

Single-cell transcriptomic profiling of ovine hepatocytes upon Rift Valley fever virus infection

Erick Bermúdez-Méndez [1,2,3], Paolo Angelino [3,4], Sandra van de Water [1], Gorben P. Pijlman [2], Angela Ciuffi [3] & Paul J. Wichgers Schreur [1]

[1] Department of Virology & Molecular Biology, Wageningen Bioveterinary Research, Lelystad, The Netherlands

[2] Laboratory of Virology, Wageningen University & Research, Wageningen, The Netherlands

[3] Institute of Microbiology, Lausanne University Hospital and University of Lausanne, Lausanne, Switzerland

[4] Bioinformatics Core Facility, Swiss Institute of Bioinformatics, Lausanne, Switzerland

Abstract

Bunyaviruses have a genome divided over multiple segments and the available evidence implies that these viruses package their genome through a random process. Both the segmentation of the genome and the randomness of genome packaging may play a role in the biology of bunyaviruses that goes beyond critical steps of the replication cycle and might influence the host's response upon infection. Here, we applied single-cell RNA-sequencing technology to dig deeper into complex virus-host interactions, using the three-segmented Rift Valley fever virus (RVFV) and ovine hepatocytes as a biologically relevant *in vitro* model of bunyavirus infection. Simultaneous quantification of the transcriptome of RVFV-exposed hepatocytes and their intracellular viral RNA showed that cells harboring a complete viral genome exhibit a starkly different transcriptome profile than uninfected cells. The infected phenotype is characterized by an upregulation of genes involved in the immune response and a downregulation of genes responsible for metabolic homeostasis. Additionally, we revealed extreme cell-to-cell variability in terms of the ratios at which the viral segments were present. This work characterizes the host's gene expression signatures following infection with RVFV at a single-cell resolution and provides a foundation to better understand the biological implications of replication and packaging of segmented bunyaviruses.

Introduction

Rift Valley fever virus (RVFV, family *Phenuiviridae*, order *Bunyavirales*)[1] is a mosquito-transmitted pathogen whose outbreaks have so far been endemic to the African continent and the Arabian peninsula[2]. Nonetheless, the transmission competence of RVFV arthropod vectors habiting in higher latitudes has become a threat due to the potential emergence of the virus in non-endemic territories[3–6]. RVFV is capable of causing severe disease, which can be fatal in livestock and humans[7,8]. In target ruminant species (sheep, cattle) and humans, RVFV primarily replicates in the liver, causing inflammation and multi-focal necrotic lesions[9]. Due to its potential to cause epidemics and the unavailability of antivirals and vaccines to counteract the virus in the event of an outbreak, RVFV has been included in the World Health Organization's R&D Blueprint list of prioritized pathogens[10].

Like in most bunyaviruses, the genome of RVFV is divided over three single-stranded RNA segments of negative polarity, termed S, M and L, according to their length. All three genome segments are essential for a productive infection, as each segment encodes for viral proteins required for viral genome replication and/or assembly of progeny virions[11]. Notably, in previous studies using single-molecule fluorescence *in situ* hybridization (smFISH), we found no evidence of a selective process to ensure the incorporation of a complete set of genome segments into individual virus particles. In fact, smFISH experiments revealed that the non-selective genome packaging of RVFV results in large fractions of empty and incomplete virus particles (i.e., particles lacking one or more genome segments) and only a minor fraction of complete three-segmented virus particles[12,13]. Generating virus particles with an incomplete set of genome segments might represent a cost for virus fitness. However, we recently showed that incomplete particles can complement each other and collectively contribute to RVFV infection and spread[14].

While additional insights into other aspects of RVFV biology are also being discovered, including identifying the host entry factor *LRP1*[15], many intricacies of the virus remain unexplored. Whole-genome transcriptomic studies have proven to be a powerful tool to unravel the complex dynamics of host-virus interactions[16]. Recently, we profiled the transcriptome of ovine liver and spleen tissue to determine the molecular basis underlying RVFV-induced pathogenesis[17]. This approach, particularly when performed at single-cell resolution, enables comparing gene expression patterns between infected and uninfected cells. Furthermore, it can reveal the direct and indirect effects of the infection and the potentially heterogeneous cellular responses often hidden in bulk measurements[18–21].

In this study, we employ single-cell RNA-sequencing (scRNA-seq) technology to investigate the transcriptomic response of ovine fetal liver cells during RVFV infection. In particular, we focus on how the viral load influences the host's response. Taking RVFV as a model three-segmented bunyavirus, this work expands our current knowledge on the bunyavirus-mammalian host interface and primes the journey to disentangle the biological implications of the random genome packaging of bunyaviruses on their life cycle.

Results

Single-cell transcriptomic profiling of ovine hepatocytes exposed to RVFV

We isolated and immortalized primary fetal ovine hepatocytes to study the host-virus interplay during RVFV infection (**Fig. 1A**), since lambs are a natural host of RVFV and the liver is the primary target organ of the virus. We confirmed that the immortalized cell clone, referred to as OHC-3, was susceptible to infection upon detection of RVFV antigen (N protein) in an immunohistochemical analysis of virus-exposed cells. The fraction of infected cells augmented with increasing multiplicities of infection (MOIs) and cytopathogenic effects became evident after only one day post-infection at the highest MOI (**Fig. 1B**).

OHC-3 cells exposed to RVFV at an MOI of 0.25 for 24 h were subsequently subjected to microfluidics-based partitioning and 5'-based RNA-seq to determine their genome-wide gene expression profile in response to RVFV infection at a single-cell level. We were especially interested in simultaneously quantifying the host's transcriptome and the expression of viral RNA. In theory, bunyaviral RNAs cannot be quantified using standard RNA-seq protocols (based on oligo-dT primers) because they lack a poly(A) tail. In an attempt to overcome this technical glitch, we modified the 10x Genomics' protocol by including different combinations of virus-specific primers to selectively capture genomic and anti-genomic RVFV RNAs (**Supplementary Tables 1, 2**). See the **Methods** section for details.

Four replicates ('S3' to 'S6') derived from a single infected sample were sequenced. At least 130 million high-quality reads (Q-score ≥ 30 in more than 90% of cell barcodes, RNA reads and UMI bases) per replicate were obtained and mapped (ranging from 88.6% to 94.8%) to the sheep (*Ovis aries*) and RVFV reference genomes. Mean reads per cell varied between samples from 28,612 up to 47,375, allowing to detect 2,722 to 4,492 median genes per cell. At least 20,000 genes

were detected in each sample. A summary of the high-throughput single-cell sequencing runs and pre-processed data is provided in **Supplementary Table 3**.

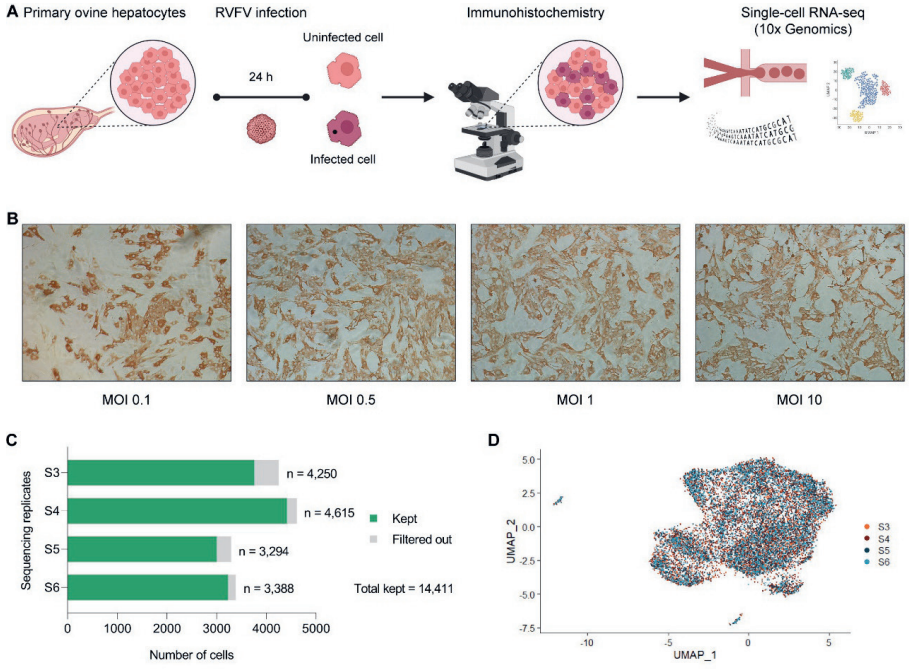

Figure 1. Transcriptomic profiling of ovine hepatocytes exposed to RVFV at single-cell resolution. **A** Schematic representation of the experimental approach. Primary hepatocytes were isolated from the liver of an ovine fetus. Cells were immortalized, and clone OHC-3 was expanded to generate a cell line. OHC-3 cells were exposed to RVFV for 24 h and were analyzed immunohistochemically and at a single-cell level (RNA-seq). A mock-infected sample was taken along the procedure as a negative control. **B** Immunohistochemical detection of RVFV antigen (N protein) in OHC-3 cells after infection at increasing MOIs. RVFV N protein was detected (red) with a polyclonal serum from an N-immunized rabbit in combination with HRP-conjugated secondary antibodies. **C** Number of cells per sequencing replicate (S3 to S6). Each sequencing replicate was derived from a single pool of infected cells. **D** UMAP of the integrated data set (14,411 cells in total).

A total of 14,411 cells derived from the sequencing replicates of the infected sample were retained for analysis after applying a filter to remove cells with low (≤ 1,500) or high (≥ 6,000) number of detected genes (**Fig. 1C**). The number of counts and genes detected per cell on each sample are shown in **Supplementary Fig. 1A**. The high correlation coefficient between the number of counts and genes detected is an expected measure of sequencing quality control (**Supplementary Fig. 1B**).

The rationale behind spiking-in different combinations of virus-specific primers was to validate that only viral RNAs for which primers were added could be captured. Unexpectedly, genomic and anti-genomic RVFV RNAs were detected in all the infected samples, including those in which no virus-specific primers were added. No virus-specific sequences were detected in a mock-infected sample that was taken along the procedure. Since spiking-in virus-specific primers did not have a large positive effect on the number of viral counts detected, we integrated the 14,411 cells derived from the sequencing replicates into a single data set for further analysis. The even distribution of the cells in a uniform manifold approximation and projection (UMAP) plot showed no batch-effect on the clustering of cells (**Fig. 1D**).

RVFV infection status dictates distinct gene expression profiles

A UMAP analysis of the integrated data set grouped the cells into three different clusters based on their gene expression profiles. Clustering displayed a small fraction of cells (cluster 1) deviating from the vast majority (cluster 0) and a minute group of cells (cluster 2) completely separated from the others (**Fig. 2**). Plotting the expression of the S, M and L segments of RVFV on the UMAP clearly revealed that cells harboring the viral segments belonged almost exclusively to cluster 1. This indicates that infection with RVFV leads to two distinct gene expression profiles corresponding to virus-infected (cluster 1) or uninfected (cluster 0) phenotypes (**Supplementary Fig. 2**). It is very little what can be deducted for cells that make up cluster 2, as this cluster consists only of a few cells, most of which are uninfected.

Viral load is a major factor influencing the gene expression landscape

To obtain a clearer picture of what is actually defining if a cell has an infected or uninfected phenotype, we calculated an average viral load per cell. We defined average viral load as the summation of the expression level of S, M and L segments divided by three. A UMAP featuring the average viral load per cell sharply shows that cells with a high viral load almost exclusively belong to cluster 1 (**Fig. 3A**). In other words, cells with an infected phenotype are characterized by a high expression of viral segments. The expression levels of each viral segment per cluster are presented in **Fig. 3B, C.**

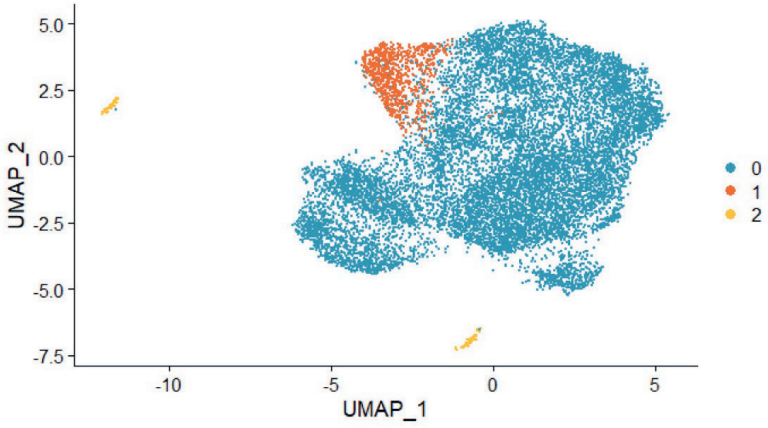

Figure 2. RVFV infection status dictates distinct gene expression profiles. UMAP based on gene expression profiling grouped cells into three clusters (0, 1 and 2). The vast majority of cells belong to cluster 0, a small fraction of cells belong to cluster 1 and a few cells comprise cluster 2.

The extent to which the viral load influences the gene expression landscape also becomes evident upon examining the pairwise correlation between the expression of the viral segments (S-M, S-L and M-L; **Supplementary Fig. 3A**). The correlation analysis showed that nearly all the cells with high expression of the two pair of compared segments belong to cluster 1 and that null or very low expression of both segments translates to cells belonging to cluster 0. In the case of cells expressing only one of the two segments, cells are grouped into cluster 1 only if the expression of that single segment is high. UMAPs featuring the pairwise viral segment expression are shown in **Supplementary Fig. 3B**.

Extreme heterogeneity in the relative abundance of viral RNAs within infected cells

Using single-molecule fluorescence *in situ* hybridization (smFISH), we previously showed that the relative abundance of RVFV segments per individual cell may differ largely[12,13]. To look into the dynamics of RVFV replication using scRNA-seq, we analyzed the relative abundance of each viral segment exclusively within SML-infected cells. Quantification of RVFV segments in infected ovine hepatocytes revealed an extreme cell-to-cell heterogeneity independent of the viral load (**Fig. 4A**). In general, the expression of viral segments appeared imbalanced towards higher abundances of the M segment compared to the S and L segments (**Fig. 4B, C**). Connecting the expression of the three viral segments per cell showed the extensive range of potential scenarios and the highly variable viral replication outcomes in an infected cell population (**Fig. 4D**).

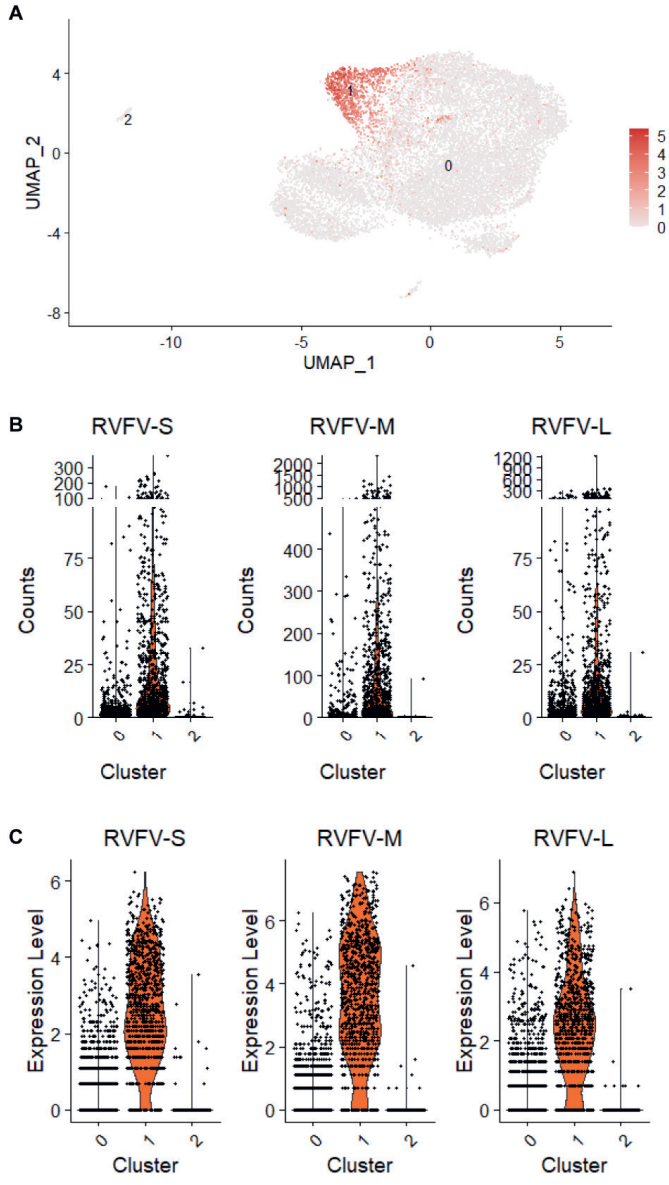

Figure 3. Viral load is a major factor influencing the gene expression landscape. A UMAP featuring the average viral load per cell. The average viral load was defined as the summation of the expression level of S, M and L segments divided by three. The average viral load on individual cells is color-coded in shades of a sequential gradient ranging from light grey (very low or no load) to dark red (high load). A high viral load is associated with cells grouping in cluster 1 (infected phenotype). **B, C** RVFV S, M and L segments expression levels per cell cluster. Expression levels are shown in counts (**B**) and normalized values (**C**). Dots represent data for individual cells. n = 14,411 cells.

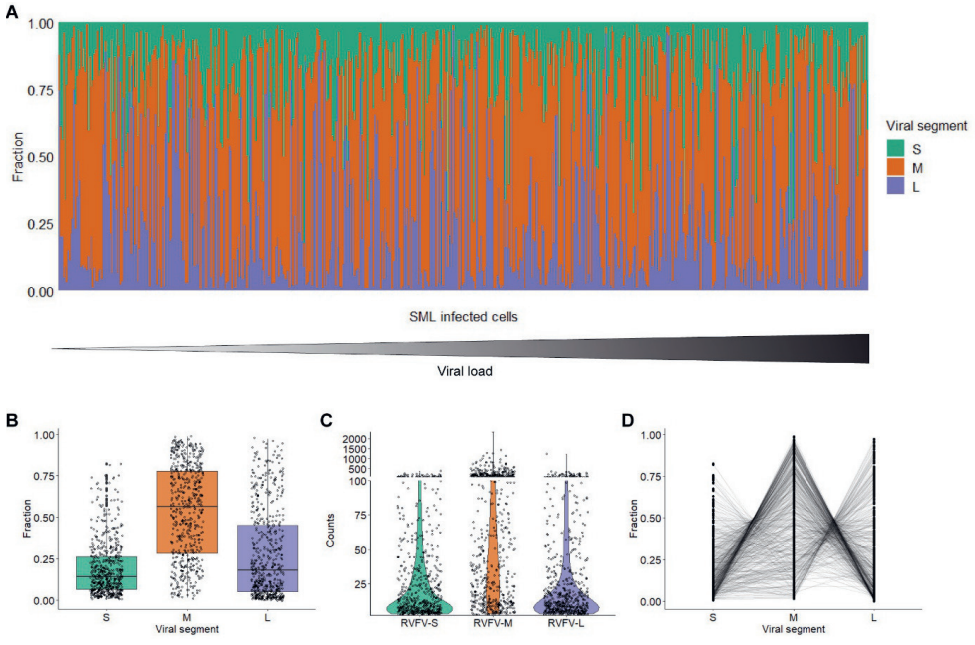

Figure 4. Extreme cell-to-cell variability of viral RNA expression within infected ovine hepatocytes. **A** Intracellular relative abundance of RVFV segments within individual SML-infected cells. Cells are sorted by increasing viral load from left to right. **B** Relative abundance of each viral segment. The boxes indicate the interquartile range (25^{th} – 75^{th} percentiles). The black lines represent the medians. **C** Distribution of the number of viral counts per segment. Dots represent data for individual cells. **D** Connected scatterplot depicting the extreme cell-to-cell heterogeneity in viral expression. Lines connect the S, M and L relative abundances for each cell. n = 557 SML-infected cells.

RVFV induces substantial changes in gene expression of ovine hepatocytes

We performed differential gene expression analysis between the three distinct cell populations (clusters 0, 1 and 2) to inspect how the infection status affected the gene expression landscape of ovine hepatocytes upon exposure to RVFV. Genes with an absolute $\log_2$ fold change of 0.5 and an adjusted p value < 0.05 were considered significantly differentially expressed. Several hundreds of genes were differentially expressed (down- or upregulated) between clusters, corroborating that RVFV infection promoted considerable shifts in the expression landscape of ovine hepatocytes. A summary of the top variably expressed genes per cell population is shown in **Fig. 5A**. A list with all the differentially expressed genes, including their corresponding $\log_2$ fold changes and adjusted p values, is provided in **Supplementary Table 4.**

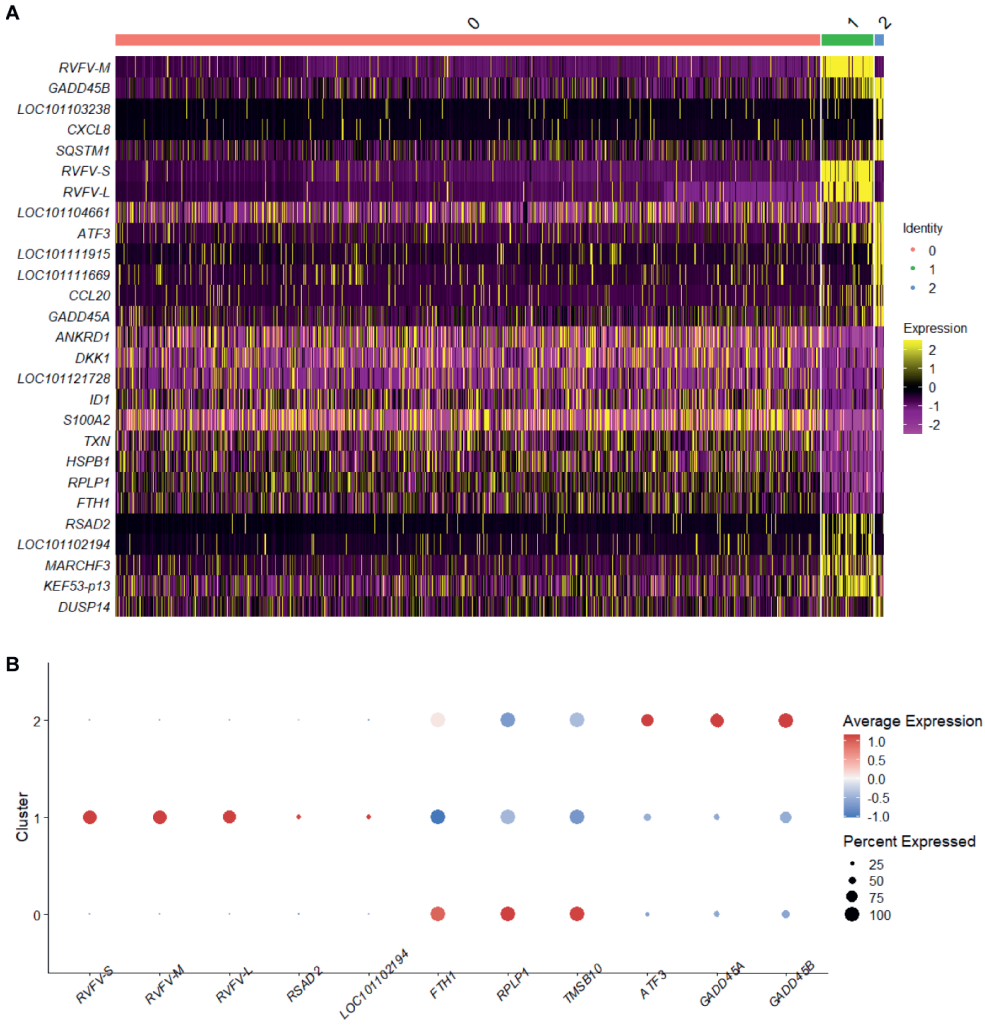

Figure 5. RVFV induces substantial changes in gene expression of ovine hepatocytes. A Heat map of the top differentially expressed genes per cluster after RVFV infection. Cells were clustered into distinct subpopulations (0, 1 and 2) based on their gene expression profiles, as indicated at the top of the graph. To represent the magnitude of the $\log_2$ fold change in expression, cells are color-coded in a bidirectional gradient departing from black (no change) to dark yellow (upregulated) or dark pink (downregulated). **B** Selected list of genes significantly differentially expressed per cluster after RVFV infection. To represent the magnitude of the average gene expression, dots are color-coded in shades of a gradient ranging from dark blue (downregulation) to dark red (upregulation). The dot size represents the percentage of cells in each cluster where the gene was detected.

Hepatic immune responses and metabolism are drastically affected by RVFV infection

We performed an additional differential gene expression analysis to focus on the differences between the infected and uninfected phenotypes, only comparing cells from cluster 1 against cells from cluster 0. More than 900 genes were found differentially expressed in this pairwise comparison. Most of these genes were downregulated in cluster 1 compared to cluster 0 (**Supplementary Table 5**). *FTH1*, *RPLP1* and *TMSB10* stood out among the downregulated genes, typically being involved in iron homeostasis, protein synthesis and cytoskeleton organization, respectively. On the other hand, *RSAD2* and *IFIT1* (*LOC101102194*) were among the few upregulated genes. *RSAD2* and *IFIT1* code for known interferon-inducible antiviral proteins (**Fig. 5B**). Intriguingly, the transcriptome of the few cells belonging to cluster 2 is characterized by a strong upregulation of *ATF3*, *GADD45A* and *GADD45B* ; all three genes often induced by stress signals associated with apoptosis/necroptosis (**Fig. 5B**).

We also employed the Gene Ontology (GO) and Kyoto Encyclopedia of Genes and Genomes (KEGG) databases to functionally analyze the transcriptomic data. We aimed to detect whether the genes most affected by RVFV infection were part of gene sets involved in particular host cell pathways. A GO over-representation analysis at the level of biological processes highlighted a significant enrichment for GO terms related to peptide metabolism, translation and electron transport chain (**Fig. 6A** and **Supplementary Table 6**). The same analysis but looking at molecular functions showed that differentially expressed genes serve as structural molecules and possess translation regulator, protein folding and antioxidant activities (**Fig. 6B** and **Supplementary Table 7**). Finally, over-representation analysis based on the KEGG database recapitulated the involvement of differentially expressed genes in metabolic pathways (amino acid metabolism, carbon metabolism, oxidative phosphorylation and glycolysis/gluconeogenesis), as well as in pathological conditions such as in fatty liver disease (**Supplementary Fig. 4** and **Supplementary Table 8**).

Relationship between the host's transcriptome and viral RNA segment diversity

Our main goal by simultaneously quantifying the host and viral RNA in individual cells was to investigate how the type and abundance of viral segments (S, M, L or combinations thereof) delivered by the infecting particle affect the host's response. Ideally, scRNA-seq would allow us to precisely define the presence or absence of each viral segment in individual cells. However, upon initial data exploration, we noticed that the assay offered us lower sensitivity than we hoped for. Our interpretation of suboptimal sensitivity is based on the overall relatively low RVFV-specific

counts per infected cell and prior knowledge on the biology of RVFV mostly gained through smFISH studies. Due to above-mentioned suboptimal sensitivity, we attempted to interpret the data presented below conservatively and invite the reader to consider our interpretations cautiously.

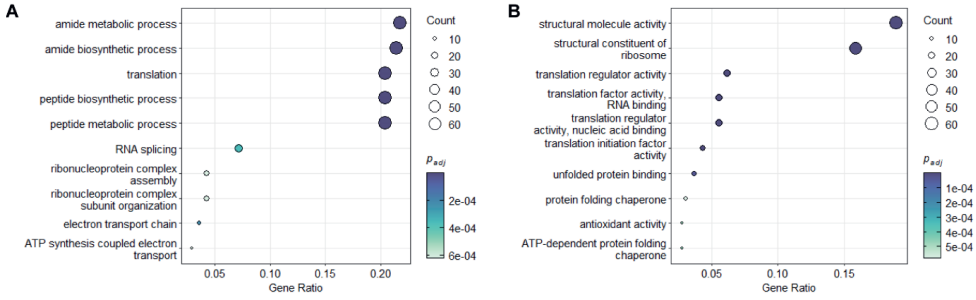

Figure 6. Top significantly enriched pathways altered in ovine hepatocytes in response to RVFV infection. A, B Gene Ontology (GO) biological process (**A**) and molecular function (**B**) over-representation analysis of genes differentially expressed in RVFV-infected ovine hepatocytes (24 h post-infection; pairwise comparison between cluster 1 and cluster 0). The dot size represents the number of enriched genes associated with each GO term. Dots are color-coded according to their *p* values (adjusted by the Benjamini-Hochberg method). The cutoff for significance was set to a *p* adjusted value < 0.05.

To discriminate between truly infected cells in which active viral replication is taking place from cells in which a viral segment was detected without clear evidence of its amplification, we empirically set a threshold of ≥ 3 viral segment counts for a cell to be considered positive for that specific segment. We also applied a coarse categorization and classified the cells into three groups: 'uninfected' (no viral RNAs), 'inf_incomplete' (one or two types of viral segments missing) or 'inf_SML' (complete SML genome) to distinguish between the different cells harboring viral segments (**Fig. 7A, B**).

Interestingly, a UMAP displaying each cell's infection status according to the three described categories revealed that cluster 1 mainly consists of either productively infected cells (classified as 'inf_SML') or cells harboring an incomplete genome (classified as 'inf_incomplete'). A careful look at the plot exposes that cells harboring an incomplete genome are distributed across the three different clusters (0, 1 and 2), but most of these cells belong to cluster 1 (**Fig. 7C**). The observation that cells harboring an incomplete genome may exhibit a transcriptome similar to that of SML-infected cells may seem like a notable revelation. However, considering the low sensitivity of the method for detecting intracellular viral RNAs, it should be noted that cells classified as

'inf_incomplete' could actually represent a subpopulation of productively infected cells at a very early stage of infection. Not surprisingly, 'uninfected' cells were almost exclusively part of cluster 0. The expression levels of each viral segment per cell category are presented in **Fig. 7D**.

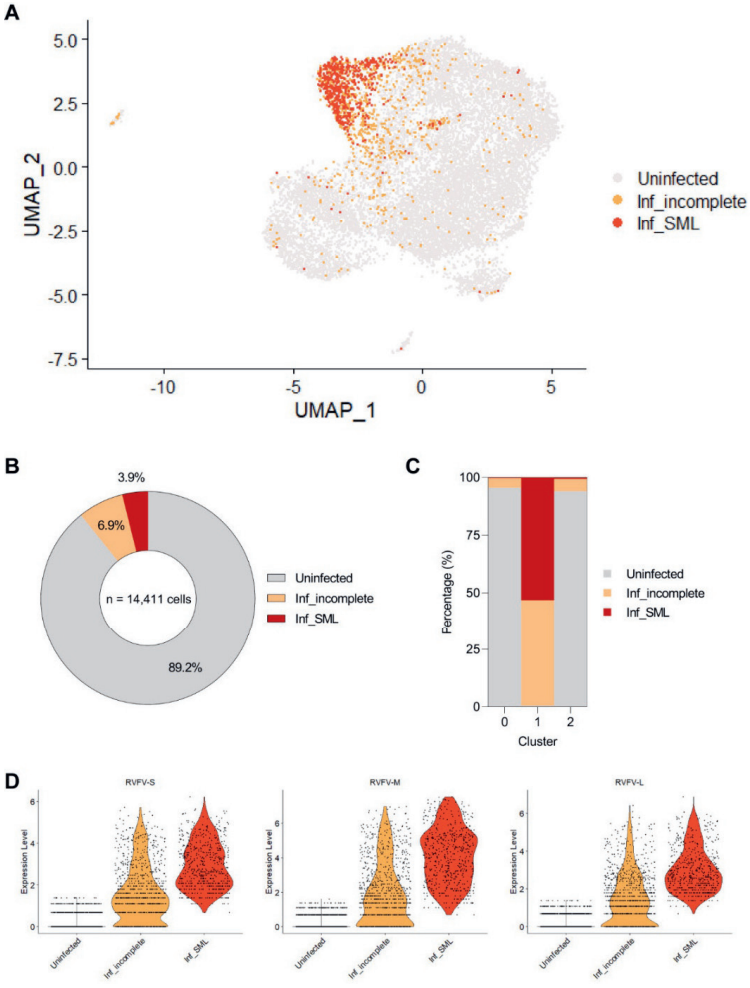

Figure 7. Relationship between the host's transcriptome and viral RNA segment diversity. A Gene expression-based UMAP in which cells are classified as 'uninfected', 'inf_incomplete', or 'inf_SML' according to the viral genome segments they harbor. Cluster 1 consists principally of 'inf_SML' and 'inf_incomplete' cells, indicating that RVFV infection leads to a signature gene expression profile distinct from that of uninfected cells. **B** Relative abundance of each cell category. **C** Relative abundance of each cell category per cluster. **D** Distribution of viral S, M and L expression levels per cell category. An empirical threshold of ≥ 3 counts was applied to determine if a cell was positive for the presence of a viral segment. This threshold explains why some cells appear positive for a viral segment even when classified as 'uninfected'. n = 14,411 cells.

In **Supplementary Fig. 5**, we present an alternative cell categorization simply to illustrate the type of analysis we hoped to achieve. In this case, we aimed for a more precise categorization in which cells were classified according to the number of different types of RVFV segments. **Supplementary Fig. 6** presents a classification in even greater detail, categorizing cells according to the presence or absence of each RVFV segment. These classifications were intended to highlight if the presence of a particular type of segment (S, M, L or combinations thereof) seems to drive a cell towards an uninfected (cluster 0) or an infected (cluster 1) phenotype. As explained above, the relatively low sensitivity of the method demanded us to be cautious in interpreting these results. However, we believe that the insights gained in this study provide valuable input to continue investigating how the type and abundance of viral segments might influence the host's response.

Discussion

An increasing number of studies are employing scRNA-seq technologies to investigate how the host's transcriptome varies across individual cells upon viral infection (reviewed in[22,23]). Studies linking transcriptome changes in an infected cell with a specific trend in the viral transcriptome add another layer of information to better understand the interplay between the host and the virus (for example[18,19,21,24–27]). Specifically for segmented viruses, linking the viral expression to a particular phenotype is highly desirable, as it allow us to examine on a single-cell basis the effect (if any), of differential replication of the viral segments on the host's response. Bunyaviruses are an excellent example to showcase the combined host-virus transcriptomic strategy, since they are not only segmented, but also produce incomplete particles, meaning that some infected cells will not receive a complete set of viral genome segments[14]. Here, we explore the potential of quantifying the host and viral transcriptome at single-cell resolution to investigate the effects of RVFV genome replication on fetal ovine hepatocytes.

We found that the viral load, understood as the summation of the viral S, M and L segments expression levels, is the main factor defining whether the phenotype of a cell harboring RVFV genome segments is starkly different from that of an uninfected cell. In other words, high viral loads result in an infected phenotype, whereas low viral loads result in an uninfected phenotype. Cells harboring the three viral segments are the result of an infection with a complete virus particle or a co-infection with incomplete particles that complement each other to reconstitute a complete genome. Thus, these cells represent the scenario of a typical productive infection, and it is reasonable that they contain a high viral load, which results in drastic host gene expression changes.

Most of the cells harboring only one type of viral segment had a low viral load and were often not distinguishable phenotypically from uninfected cells. This can be explained by one of the following reasons: (i) the cell was infected by an incomplete particle harboring only one viral segment, or (ii) the cell was also infected with other genome segment types, but the levels of these genome segments were below the detection limit. Cells with low viral load also may represent a subpopulation of cells at an early stage of the infection. In any case, cells with low viral load do not exhibit major changes in their transcriptome.

Apart from the new insights gained on how the viral load and diversity of viral segments affect the host cell transcriptome, we observed extreme cell-to-cell variability in viral segment expression between SML-infected cells. This intracellular heterogeneity of RVFV-infected cells confirms our prior results from single-molecule fluorescence *in situ* hybridization studies[13] and expands the observation by noting that the heterogeneity is independent of the viral load. Which factors or conditions cause differential viral segment replication to vary so much across cells is unknown. One possibility is that individual incomplete virus particles co-infecting a cell do not do so simultaneously, delivering the viral segments with delay and impacting the replication kinetics. Another possibility is that cells receive multiple copies of the same viral segment type from multiple particles or from a single particle that carries more than one copy of the same segment. This initial imbalanced content can possibly drive an imbalanced viral replication. Finally, it is also possible that viral segment ratios within infected cells are dynamic over time and equilibrate at a certain stage.

Importantly, our study also corroborates mainstream observations from previous and our own RVFV transcriptomic studies. Here, we also show that the most drastic transcriptomic changes upon RVFV infection include the upregulation of genes involved in interferon-mediated immune responses[17,28,29]. Furthermore, we show that RVFV infection induces the downregulation of genes related to the hepatic metabolism of various substrates and genes coding for structural molecules[17]. These results suggest that the OHC-3 ovine liver cell line described here serves as a biologically relevant *in vitro* RVFV infection model. In future studies, it would be worth to develop an *in vitro* model co-culturing OHC-3 cells with liver sinusoidal endothelial cells, which have been described to have a fundamental role in maintaining immune homeostasis of the liver[30].

This pioneering study applying scRNA-seq technology on a segmented virus that synthesizes non-poly(A) mRNAs has four technical limitations that demand a cautious examination of the conclusions made with respect to absence and ratios of genome segments. First, the

quantification method offered suboptimal sensitivity. Direct visualization of RVFV genome segments using smFISH has shown that an infected cell can harbor thousands of viral RNAs within hours of becoming infected[12,13]. The relatively low levels of viral RNAs detected through scRNA-seq imply that the absence of a viral segment could not be called out confidently. Second, the assay was not able to discriminate between viral genomic RNA (negative-sense), anti-genomic RNA (positive-sense) and mRNA. This issue arises from conventional scRNA-seq data pre-processing pipelines not being designed to count reads mapped to the reference genome separately based on their polarity. Moreover, viral anti-genomic RNA and mRNA have identical sequences to a large extent, which further complicates discriminating between the two molecules. Thus, what we here referred to as viral RNA for each RVFV S, M and L segments, consists of an undistinguishable mixture of genomic RNA, anti-genomic RNA and mRNA. Third, we observed a bias in viral segment quantification towards the M segment. Although adding virus-specific primers did not seem to have a substantial effect on capturing RVFV RNAs, all the samples contained an M-specific primer that possibly explains the overall higher levels of M segment detected compared to the S and L segments. Fourth, samples were analyzed only after a single time point. A time-course experiment would provide valuable additional information.

In spite of the limitations, our study provides a starting point to dissect further the intricacies of RVFV replication and its influence in a host/vector cell population at a single-cell level. We uncovered that cells receiving an incomplete RVFV genome, although unable to generate infectious progeny, might respond similarly to an SML-infected cell or an uninfected cell, depending on the level of viral expression. Future studies performing infections exclusively with populations of incomplete virus particles could produce valuable findings to comprehend better the effects on the host's transcriptome associated to viral segment abundance and diversity. Alternatively, other processes closely related to virus replication and genome packaging, such as the production of progeny virions or the induction of a generalized antiviral state, can be studied by combining different single-cell technologies. For instance, a recent study combined scRNA-seq and viral barcoding to reveal that viral transcription and progeny virion generation were not correlated[31]. Another study demonstrated that the changes induced by a virus in an infected cell could influence the susceptibility to viral infection of neighboring uninfected cells[32]. The particularities of the life cycle of RVFV, and bunyaviruses in general, make exploring similar experimental strategies in the future appealing.

Methods

Cell line

BHK-21 cells (baby Syrian golden hamster kidney fibroblasts, ATCC CCL-10) were maintained in Glasgow minimum essential medium (G-MEM) supplemented with 5% fetal bovine serum (FBS), 4% tryptose phosphate broth, 1% MEM non-essential amino acids and 1% antibiotic/antimycotic at 37 ºC and 5% CO_2. Cell culture media and supplements were purchased from Gibco, unless specified otherwise.

Primary ovine hepatocytes

Primary ovine hepatocytes were isolated from the fetus of a Texel-Swifter pregnant ewe in the second trimester of its pregnancy. Briefly, blood was rinsed away from the fetus's liver by injecting Hanks' Balanced Salt Solution (HBSS) at 37 ºC with a syringe through the portal vein. Liver slices were cut and injected with 0.1% collagenase IV in HBSS. Liver slices were further chopped and incubated in 0.1% collagenase IV in HBSS for 30 min at 37 ºC. Dissociated cells were filtered through a 70 µm cell strainer to remove cell aggregates, and the cell suspension was centrifuged at 1200 rpm (5699-R rotor) for 5 min. Cell pellets were resuspended in 5 mL of ammonium-chloride-potassium (ACK) lysing buffer and incubated for 5 min at room temperature. Cells were washed twice with an excess of HBSS, pelleted by centrifugation at 1200 rpm (5699-R rotor) for 5 min and resuspended in Dulbecco's modified eagle medium (DMEM) supplemented with 10% FBS, 4% cell maintenance cocktail-B, 20 ng/mL epidermal growth factor (EGF) and 1% antibiotic/antimycotic. For culturing, plates and flasks were coated with 100 µg/mL collagen I in 0.02 M acetic acid for at least 2 h, washed with Dulbecco's phosphate-buffered saline (DPBS) and dried for 4 h. Cells were maintained at 37 ºC and 5% CO_2.

Primary ovine hepatocytes were sent for immortalization to InSCREENex[33] (Braunschweig, Germany). Briefly, 12-well plates were coated with a 1:10-1:40 diluted collagen solution (InSCREENex) in DPBS for at least 2 h. The collagen solution was aspirated prior to seeding the cells. Primary ovine hepatocytes resuspended in DMEM supplemented with 10% FBS, 4% cell maintenance cocktail-B and 1% antibiotic/antimycotic were seeded in the collagen-coated 12-well plates (50,000 cells/well) and maintained at 37 ºC and 5% CO_2. Three-days post-seeding, cell monolayers reached about 80% confluence and were infected using InSCREENex's lentiviral gene bank. Lentiviral infections were performed overnight in the presence of 8 µg/mL Polybrene. The following day, the virus-containing media was removed, and the media was replenished. For the establishment of individual hepatocyte clones, the cells were split two days post-infection and the selection started using 0.2 mg/mL Geneticin (G-418 sulfate) until robustly proliferating colonies arose. The cells were further cultivated for up to ten weeks on collagen-coated plates. Mock-infected cells were included as a control. Mock-infected cells stopped proliferation after ten days of selection with 0.2 mg/mL Geneticin (G-418 sulfate). From the different immortalized clones generated, ovine hepatocytes clone # 3 (termed OHC-3 cells from now on) were employed in this study.

For virus infection experiments, immortalized OHC-3 cells were maintained in William's E medium supplemented with 10% FBS, 4% cell maintenance cocktail-B, 1.4 µM dexamethasone and 1% antibiotic/antimycotic at 37 ºC and 5% CO_2. OHC-3 cells were initially grown (for at least the first two passages) in collagen-coated tissue-culture flasks (as described above).

Virus

Wild-type RVFV strain 35/74 was originally isolated from the liver of a sheep that died during an RVFV outbreak in the Free State province of South Africa in 1974[34]. The parental virus was passaged four times in suckling mouse brain and then four times in BHK cells. Stocks of RVFV 35/74 for infection experiments were obtained after further virus propagation in BHK-21 cells at low multiplicity of infection (MOI). The virus titer was determined with an end-point dilution assay. Briefly, BHK-21 (15,000 cells/well) monolayers were incubated with 5-fold serial dilutions (starting at 1:10) of virus at 37 ºC and 5% CO_2. Samples were analyzed in triplicate, scoring for cytopathic effect after 7 days post-infection. The virus titer was calculated as the median tissue culture infectious dose ($TCID_{50}$/mL) using the Spearman-Kärber method. RVFV 35/74 was handled at BSL-3 containment.

Infections to confirm susceptibility

OHC-3 cells were seeded in 24-well cell culture plates at 1 x 10^5 cells/well and allowed to attach for at least 2 h. Cells were infected at MOIs of 0.1, 0.5, 1 and 10. The infection was allowed to proceed for a period of 24 h.

Immunostaining

RVFV-infected OHC-3 cells were subjected to an immunoperoxidase monolayer assay (IPMA) to detect the expression of the viral N protein. At one day post-infection, cells were fixed with 4% paraformaldehyde for 15 min, washed with PBS supplemented with 0.5% Tween 80 (PBST), and permeabilized with 1% Triton X-100 in PBS for 5 min. Next, samples were blocked with 5% horse serum in PBS and subsequently incubated in sequential steps with primary and secondary antibodies diluted in blocking solution. The N protein was detected with a polyclonal serum from a N-immunized rabbit (1:500 dilution, GenScript) as primary antibody. Horse radish peroxidase (HRP-conjugated goat polyclonal anti-rabbit immunoglobulin (1:500 dilution, P0448 Dako) was used as secondary antibody. Sample incubations with the blocking solution, primary and secondary antibodies were each for 1 h at 37˚C. Plates were washed with PBST after permeabilization, between the addition of primary and secondary antibodies, and prior to staining. A 0.2 mg/mL amino ethyl carbazole solution in 500 mM acetate buffer (pH 5.0), 88 mM H_2O_2 was added as substrate. Light microscopy images were acquired with a Leica Model DMi1 inverted microscope and 10× HI PLAN I or 20× HI PLAN I objectives.

Infections for transcriptomics

OHC-3 cells were seeded in 6-well collagen-coated cell culture plates at 2 x 10^5 cells/well and allowed to attach overnight. Coating of plates was done prior seeding cells with 1 mL/well of collagen (InSCREENex) and incubated at 37 °C for at least 1 h. The next day, the cells were infected at an MOI of 0.25. After incubation for 1 h, the inoculum was removed and substituted with fresh medium. At 24 h post-infection, the culture supernatant was removed, and samples of the cells were collected after a wash with PBS, trypsinization with TrypLE Express and resuspension in 0.22 µm-filtered complete William's E medium. Mock-infected cells were used as a negative control.

Single-cell RNA-seq

Cell suspensions at a density of 1,000 cells/µL were prepared for single-cell RNA-seq using a Chromium Controller (10x Genomics) and the Chromium Next GEM Single Cell 5' Kit version 2 (Dual Index; 10x Genomics) according to the manufacturer's instructions. Briefly, 10,000 cells/sample were loaded for single-cell partitioning and gel beads-in-emulsion (GEM) generation. Following GEM generation, mRNAs were reverse transcribed using poly(dT) primers to produce full-length cDNAs tagged with unique 16 nucleotides 10x Genomics barcodes, 10 nucleotides unique molecular identifiers (UMIs) and a 13 nucleotides template switch oligo (TSO). The resulting cDNAs were amplified, fragmented enzymatically, selected by size and subjected to adaptor ligation and sample index PCR to construct 5' gene expression libraries. The resulting products had a size distribution with a broad peak between ~ 500-3,000 base pairs.

Reverse transcription and PCR reactions were performed using a Veriti 96-Well Thermal Cycler (Applied Biosystems). Gene expression libraries were sequenced on an Illumina NovaSeq 6000 instrument by the Lausanne Genomic Technologies Facility (University of Lausanne). The quality and yield of the amplified cDNA and gene expression libraries were determined on a 5200 Fragment Analyzer (Agilent) using ProSize software version 4.0.0.3.

Initially, the infected sample was split into 5 sub-samples designated with consecutive numbers from 'S2' to 'S6'. The standard Chromium Next GEM Single Cell 5' Kit version 2 (10x Genomics) protocol was modified by spiking virus-specific primers, each with an adapter identical to the adapter sequence present in the poly-dT RT primer from 10x Genomics (**Supplementary Tables 1, 2**), following the strategy reported in previous studies[35–38]. Virus-specific primers were spiked-in to selectively capture RVFV-specific RNAs. The mock-infected sample was designated as 'S1'.

Single-cell RNA-seq raw data pre-processing

FASTQ files were pre-processed following the Cell Ranger (10x Genomics) pipeline version 7.1.0. Sequencing reads were aligned to a concatenation of the sheep (*Ovis aries*; ARS-UI-Ramb-v2.0, https://www.ncbi.nlm.nih.gov/datasets/genome/GCF_016772045.1/)[39] and RVFV (accession numbers:

JF784386.1, JF784387.1 and JF784388.1) reference genomes. The resulting UMI count matrices were first processed for each sample individually in R[40] version 4.3.0 using Seurat[41,42] version 4.3.0.

Cells with ≤ 1,500 or ≥ 6,000 detected genes were filtered from the data set and excluded from the analysis. Genes that were detected in < 3 cells also were excluded. These thresholds were defined empirically upon data examination for each sample. Data from sample 2 (RVFV-infected, without the addition of primers) was dropped out due to suboptimal sample preparation that resulted in lower sequencing quality. Since the infected samples naturally comprise both infected and uninfected cells, including S1 (mock) was unnecessary and thus not included in the downstream analysis.

Following an exploratory individual sample analysis, it became evident that reads mapping to all the RVFV genome and anti-genome RNAs were detected in all the infected samples, regardless of the addition or not of virus-specific primers. Since the protocol modification did not have the intended impact, it was decided to combine all the data from the remaining RVFV-infected samples (S3 to S6) for further analysis.

Filtered data from S3 to S6 was normalized with Seurat's function *SCTransform* version 2 and integrated into a combined data set using *IntegrateData* based on 3,000 variable genes. A principal component analysis (n = 50) was performed for data exploration. The non-linear dimensional reduction technique uniform manifold approximation and projection (UMAP) was applied (including principal component 1 to principal component 50) for visualization purposes. Optimal clustering of cells was achieved with a resolution parameter of 0.04.

Cell categorization

Individual cells were categorized according to their infection status with three different approaches. In the first approach, cells were coarsely categorized as 'uninfected', 'inf_incomplete' or 'inf_SML', according to the viral segments harbored per cell. In the second approach, cells were classified according to the number of different viral segments detected (0 = "uninfected", 1 = "infected_1_seg", 2 = "infected_2_seg" and 3 = "infected_3_seg"), disregarding the type of viral segment detected (S, M or L). In the third approach, cells were classified according to the exact type of viral segments detected ("uninfected", "S", "M", "L", "SM", "SL", "ML" and "SML"). In all the approaches, we applied an empirically defined threshold of ≥ 3 counts for each viral segment to discriminate truly infected cells with active viral replication from cells harboring very few viral RNAs without clear evidence of viral replication.

The proportion of viral RNA per cell was calculated as the counts aligned to the viral genome divided by the total counts. The average expression level of viral RNA per cell ('viral load') was calculated as the summation of the expression level of all viral RNAs divided by three. The relative abundance of each viral RNA on SML-infected cells was calculated as the counts per viral segment (S, M or L) divided by the total viral counts. Spearman correlation analysis was performed between the expression level of the different viral RNAs.

Transcriptome analysis

Downstream analyses were performed with Seurat[41,42] version 4.3.0 in R[40] version 4.3.0. Differentially expressed genes per cluster or cell category were identified with the functions *FindAllMarkers* or *FindMarkers* based on a non-parametric Wilcoxon rank sum test, using a $\log_2$ fold change threshold of 0.5 and a minimum percentage of cells argument of 0.25. Wilcoxon test *p* values adjusted with the Bonferroni method < 0.05 were considered significant. Functional over-representation analysis (ORA) was performed with *clusterProfiler*[43,44] version 4.8.1, based on the Gene Ontology (GO) and Kyoto Encyclopedia of Genes and Genomes (KEGG) databases. When required, the clusterProfiler function *simplify* was used to reduce the redundancy of enriched GO terms. A one-sided version of Fisher's exact test *p* values adjusted with the Benjamini-Hochberg method < 0.05 were considered significant.

Data analysis and visualization

Prism 9 (GraphPad Software) was used to generate graphs of sequencing statistics and cell categorization according to infection status. Transcriptomic data were analyzed and plotted in R[40] version 4.3.0, using the above-mentioned R packages. Statistical tests differed per analysis and are indicated in the description of each in the corresponding figure legends. *p* values ≥ 0.05 were considered not significant.

Data availability

Raw sequencing data are available through the authors upon reasonable request.

Acknowledgements

EBM is a grateful recipient of scholarships from the Graduate School for Production Ecology & Resource Conservation (PE&RC) and Universidad de Costa Rica (OAICE-031-2019). This work was supported in part by funds from the 'Rob Goldbach Fund' to EBM for a laboratory training visit. The fetal ovine hepatocyte cells (OHC-3) were developed within the Veterinary Biocontained Research Facility Network (VetBioNet) of the European Union's Horizon 2020 research and innovation programme under grant agreement No 731014. We thank Judith Oymans, Jet Kant (Wageningen Bioveterinary Research) and Raquel Martínez Tenreiro (Lausanne University Hospital and University of Lausanne) for technical assistance. We thank Alex Bossers (Wageningen Bioveterinary Research) for providing access to a high performance computing server. Thanks also to Ingrid Cárdenas Rey for proofreading. The illustration in **Fig. 1A** was created with BioRender.com.

Author contributions

EBM and PJWS conceived the project. SvdW performed the initial infections and the immunostaining. EBM performed the infection, sample processing and library preparation for the single-cell RNA-seq

experiment. EBM and PA performed the single-cell RNA-seq data processing and bioinformatic analysis. EBM, PA and PJWS interpreted the data with contributions of GPP and AC. PJWS, GPP and AC supervised the project. EBM wrote the manuscript with contributions of PJWS. EBM made the figures with contributions of PA and PJWS.

Competing interests

The authors declare no competing interest.

References

1. Kuhn JH, Adkins S, Alkhovsky SV, Avšič-Županc T, Ayllón MA, Bahl J, Balkema-Buschmann A, Ballinger MJ, Bandte M, Beer M, Bejerman N, Bergeron É, *et al.* 2022 taxonomic update of phylum *Negarnaviricota* (*Riboviria*: *Orthornavirae*), including the large orders *Bunyavirales* and *Mononegavirales*. *Archives of Virology* **2022**, *167* (12), 2857–2906. https://doi.org/10.1007/s00705-022-05546-z.

2. Nanyingi MO, Munyua P, Kiama SG, Muchemi GM, Thumbi SM, Bitek AO, Bett B, Muriithi RM, Njenga MK. A systematic review of Rift Valley Fever epidemiology 1931–2014. *Infection Ecology & Epidemiology* **2015**, *5* (1), 28024. https://doi.org/10.3402/iee.v5.28024.

3. Turell MJ, Dohm DJ, Mores CN, Terracina L, Wallette DL, Hribar LJ, Pecor JE, Blow JA. Potential for North american mosquitoes to transmit Rift Valley fever virus. *Journal of the American Mosquito Control Association* **2008**, *24* (4), 502–507. https://doi.org/10.2987/08-5791.1.

4. Turell MJ, Britch SC, Aldridge RL, Kline DL, Boohene C, Linthicum KJ. Potential for mosquitoes (Diptera: Culicidae) from Florida to transmit Rift Valley fever virus. *Journal of Medical Entomology* **2013**, *50* (5), 1111–1117. https://doi.org/10.1603/ME13049.

5. Brustolin M, Talavera S, Nuñez A, Santamaría C, Rivas R, Pujol N, Valle M, Verdún M, Brun A, Pagès N, Busquets N. Rift Valley fever virus and European mosquitoes: vector competence of *Culex pipiens* and *Stegomyia albopicta* (= *Aedes albopictus*). *Medical and Veterinary Entomology* **2017**, *31* (4), 365-372. https://doi.org/10.1111/mve.12254.

6. Kraemer MUG, Reiner RC, Brady OJ, Messina JP, Gilbert M, Pigott DM, Yi D, Johnson K, Earl L, Marczak LB, Shirude S, Davis Weaver N, *et al.* Past and future spread of the arbovirus vectors *Aedes aegypti* and *Aedes albopictus*. *Nature Microbiology* **2019**, *4* (5), 854–863. https://doi.org/10.1038/s41564-019-0376-y.

7. Clark MHA, Warimwe GM, Nardo AD, Lyons NA, Gubbins S. Systematic literature review of Rift Valley fever virus seroprevalence in livestock, wildlife and humans in Africa from 1968 to 2016. *PLOS Neglected Tropical Diseases* **2018**, *12* (7), e0006627. https://doi.org/10.1371/journal.pntd.0006627.

8. Anywaine Z, Lule SA, Hansen C, Warimwe G, Elliott A. Clinical manifestations of Rift Valley fever in humans: Systematic review and meta-analysis. *PLOS Neglected Tropical Diseases* **2022**, *16* (3), e0010233. https://doi.org/10.1371/journal.pntd.0010233.

9. Odendaal L, Davis AS, Venter EH. Insights into the pathogenesis of viral haemorrhagic fever based on virus tropism and tissue lesions of natural Rift Valley fever. *Viruses* **2021**, *13* (4), 709. https://doi.org/10.3390/v13040709.

10. Friedrich MJ. WHO's blueprint list of priority diseases. *JAMA* **2018**, *319* (19), 1973–1973. https://doi.org/10.1001/jama.2018.5712.

11. Wright D, Kortekaas J, Bowden TA, Warimwe GM. Rift Valley fever: biology and epidemiology. *Journal of General Virology* **2019**, *100* (8), 1187–1199. https://doi.org/10.1099/jgv.0.001296.

12. Wichgers Schreur PJ, Kortekaas J. Single-molecule FISH reveals non-selective packaging of Rift Valley fever virus genome segments. *PLOS Pathogens* **2016**, *12* (8), e1005800. https://doi.org/10.1371/journal.ppat.1005800.

13. Bermúdez-Méndez E, Katrukha EA, Spruit CM, Kortekaas J, Wichgers Schreur PJ. Visualizing the ribonucleoprotein content of single bunyavirus virions reveals more efficient genome packaging in the arthropod host. *Communications Biology* **2021**, *4* (1), 1–13. https://doi.org/10.1038/s42003-021-01821-y.

14. Bermúdez-Méndez E, Bronsvoort KF, Zwart MP, van de Water S, Cárdenas-Rey I, Vloet RPM, Koenraadt CJM, Pijlman GP, Kortekaas J, Wichgers Schreur PJ. Incomplete bunyavirus particles can cooperatively support virus infection and spread. *PLOS Biology* **2022**, *20* (11), e3001870. https://doi.org/10.1371/journal.pbio.3001870.

15. Ganaie SS, Schwarz MM, McMillen CM, Price DA, Feng AX, Albe JR, Wang W, Miersch S, Orvedahl A, Cole AR, Sentmanat MF, Mishra N, *et al.* Lrp1 is a host entry factor for Rift Valley fever virus. *Cell* **2021**, *184* (20), 5163-5178.e24. https://doi.org/10.1016/j.cell.2021.09.001.

16. Svensson V, Vento-Tormo R, Teichmann SA. Exponential scaling of single-cell RNA-seq in the past decade. *Nature Protocols* **2018**, *13* (4), 599–604. https://doi.org/10.1038/nprot.2017.149.

17. Bermúdez-Méndez E, Angelino P, van Keulen L, van de Water S, Rockx B, Pijlman GP, Ciuffi A, Kortekaas J, Wichgers Schreur PJ. Transcriptomic profiling reveals intense host-pathogen dispute compromising homeostasis during acute Rift Valley fever virus infection. *Journal of Virology* **2023**, *97* (6), e00415-23. https://doi.org/10.1128/jvi.00415-23.

18. Wyler E, Franke V, Menegatti J, Kocks C, Boltengagen A, Praktiknjo S, Walch-Rückheim B, Bosse J, Rajewsky N, Grässer F, Akalin A, Landthaler M. Single-cell RNA-sequencing of herpes simplex virus 1-infected cells connects NRF2 activation to an antiviral program. *Nature Communications* **2019**, *10* (1), 4878. https://doi.org/10.1038/s41467-019-12894-z.

19. Drayman N, Patel P, Vistain L, Tay S. HSV-1 single-cell analysis reveals the activation of anti-viral and developmental programs in distinct sub-populations. *eLife* **2019**, *8*, e46339. https://doi.org/10.7554/eLife.46339.

20. Kotliar D, Lin AE, Logue J, Hughes TK, Khoury NM, Raju SS, Wadsworth MH, Chen H, Kurtz JR, Dighero-Kemp B, Bjornson ZB, Mukherjee N, *et al.* Single-cell profiling of Ebola virus disease in vivo reveals viral and host dynamics. *Cell* **2020**, *183* (5), 1383-1401.e19. https://doi.org/10.1016/j.cell.2020.10.002.

21. Zheng Y, Li S, Li S-H, Yu S, Wang Q, Zhang K, Qu L, Sun Y, Bi Y, Tang F, Qiu H-J, Gao GF. Transcriptome profiling in swine macrophages infected with African swine fever virus at single-cell resolution. *PNAS* **2022**, *119* (19), e2201288119. https://doi.org/10.1073/pnas.2201288119.

22. Cristinelli S, Ciuffi A. The use of single-cell RNA-Seq to understand virus–host interactions. *Current Opinion in Virology* **2018**, *29*, 39–50. https://doi.org/10.1016/j.coviro.2018.03.001.

23. Suomalainen M, Greber UF. Virus infection variability by single-cell profiling. *Viruses* **2021**, *13* (8), 1568. https://doi.org/10.3390/v13081568.

24. Russell AB, Trapnell C, Bloom JD. Extreme heterogeneity of influenza virus infection in single cells. *eLife* **2018**, *7*, e32303. https://doi.org/10.7554/eLife.32303.

25. O'Neal JT, Upadhyay AA, Wolabaugh A, Patel NB, Bosinger SE, Suthar MS. West Nile virus-inclusive single-cell RNA sequencing reveals heterogeneity in the type I interferon response within single cells. *Journal of Virology* **2019**, *93* (6), e01778-18. https://doi.org/10.1128/JVI.01778-18.

26. Kelly JN, Laloli L, V'kovski P, Holwerda M, Portmann J, Thiel V, Dijkman R. Comprehensive single cell analysis of pandemic influenza A virus infection in the human airways uncovers cell-type specific host transcriptional signatures relevant for disease progression and pathogenesis. *Frontiers in Immunology* **2022**, *13*. https://doi.org/10.3389/fimmu.2022.978824.

27. Schwartz M, Shnayder M, Nachshon A, Arazi T, Kitsberg Y, Levi Samia R, Lavi M, Kuint R, Tsabari R, Stern-Ginossar N. Molecular characterization of human cytomegalovirus infection with single-cell transcriptomics. *Nature Microbiology* **2023**, *8* (3), 455–468. https://doi.org/10.1038/s41564-023-01325-x.

28. Pinkham C, Dahal B, de la Fuente CL, Bracci N, Beitzel B, Lindquist M, Garrison A, Schmaljohn C, Palacios G, Narayanan A, Campbell CE, Kehn-Hall K. Alterations in the host transcriptome *in vitro* following Rift Valley fever virus infection. *Scientific Reports* **2017**, *7* (1), 14385. https://doi.org/10.1038/s41598-017-14800-3.

29. Havranek KE, White LA, Lanchy J-M, Lodmell JS. Transcriptome profiling in Rift Valley fever virus infected cells reveals modified transcriptional and alternative splicing programs. *PLOS ONE* **2019**, *14* (5), e0217497. https://doi.org/10.1371/journal.pone.0217497.

30. Shetty S, Lalor PF, Adams DH. Liver sinusoidal endothelial cells — gatekeepers of hepatic immunity. *Nature Reviews Gastroenterology & Hepatology* **2018**, *15* (9), 555–567. https://doi.org/10.1038/s41575-018-0020-y.

31. Bacsik DJ, Dadonaite B, Butler A, Greaney AJ, Heaton NS, Bloom JD. Influenza virus transcription and progeny production are poorly correlated in single cells. *eLife* **2023**, *12*. https://doi.org/10.7554/eLife.86852.

32. Song B, Sheng X, Justice JL, Lum KK, Metzger PJ, Cook KC, Kostas JC, Cristea IM. Intercellular communication within the virus microenvironment affects the susceptibility of cells to secondary viral infections. *Science Advances* **2023**, *9* (19), eadg3433. https://doi.org/10.1126/sciadv.adg3433.

33. Lipps C, Klein F, Wahlicht T, Seiffert V, Butueva M, Zauers J, Truschel T, Luckner M, Köster M, MacLeod R, Pezoldt J, Hühn J, *et al.* Expansion of functional personalized cells with specific transgene combinations. *Nature Communications* **2018**, *9* (1), 994. https://doi.org/10.1038/s41467-018-03408-4.

34. Barnard BJH. Rift Valley fever vaccine - antibody and immune response in cattle to a live and an inactivated vaccine. *Journal of the South African Veterinary Association* **1979**, *50* (3), 155–157. https://doi.org/10.10520/AJA00382809_4630.

35. Mimitou EP, Cheng A, Montalbano A, Hao S, Stoeckius M, Legut M, Roush T, Herrera A, Papalexi E, Ouyang Z, Satija R, Sanjana NE, *et al.* Multiplexed detection of proteins, transcriptomes, clonotypes and CRISPR perturbations in single cells. *Nature Methods* **2019**, *16* (5), 409–412. https://doi.org/10.1038/s41592-019-0392-0.

36. Replogle JM, Norman TM, Xu A, Hussmann JA, Chen J, Cogan JZ, Meer EJ, Terry JM, Riordan DP, Srinivas N, Fiddes IT, Arthur JG, *et al.* Combinatorial single-cell CRISPR screens by direct guide RNA capture and targeted sequencing. *Nature Biotechnology* **2020**, *38* (8), 954–961. https://doi.org/10.1038/s41587-020-0470-y.

37. Stadtmauer EA, Fraietta JA, Davis MM, Cohen AD, Weber KL, Lancaster E, Mangan PA, Kulikovskaya I, Gupta M, Chen F, Tian L, Gonzalez VE, *et al.* CRISPR-engineered T cells in patients with refractory cancer. *Science* **2020**, *367* (6481), eaba7365. https://doi.org/10.1126/science.aba7365.

38. Sanborn MA, Li T, Victor K, Siegfried H, Fung C, Rothman AL, Srikiatkhachorn A, Fernandez S, Ellison D, Jarman RG, Friberg H, Maljkovic Berry I, *et al.* Analysis of cell-associated DENV RNA by oligo(dT) primed 5′ capture scRNAseq. *Scientific Reports* **2020**, *10* (1), 9047. https://doi.org/10.1038/s41598-020-65939-5.

39. Davenport KM, Bickhart DM, Worley K, Murali SC, Salavati M, Clark EL, Cockett NE, Heaton MP, Smith TPL, Murdoch BM, Rosen BD. An improved ovine reference genome assembly to facilitate in-depth functional annotation of the sheep genome. *GigaScience* **2022**, *11*, giab096. https://doi.org/10.1093/gigascience/giab096.

40. R Core Team. R: A language and environment for statistical computing. R Foundation for statistical computing, Vienna, Austria 2022. https://www.R-project.org/.

41. Satija R, Farrell JA, Gennert D, Schier AF, Regev A. Spatial reconstruction of single-cell gene expression data. *Nature Biotechnology* **2015**, *33* (5), 495–502. https://doi.org/10.1038/nbt.3192.

42. Hao Y, Hao S, Andersen-Nissen E, Mauck WM, Zheng S, Butler A, Lee MJ, Wilk AJ, Darby C, Zager M, Hoffman P, Stoeckius M, *et al.* Integrated analysis of multimodal single-cell data. *Cell* **2021**, *184* (13), 3573-3587.e29. https://doi.org/10.1016/j.cell.2021.04.048.

43. Yu G, Wang L-G, Han Y, He Q-Y. clusterProfiler: an R package for comparing biological themes among gene clusters. *OMICS* **2012**, *16* (5), 284–287. https://doi.org/10.1089/omi.2011.0118.

44. Wu T, Hu E, Xu S, Chen M, Guo P, Dai Z, Feng T, Zhou L, Tang W, Zhan L, Fu X, Liu S, *et al.* clusterProfiler 4.0: A universal enrichment tool for interpreting omics data. *The Innovation* **2021**, *2* (3), 100141. https://doi.org/10.1016/j.xinn.2021.100141.

Supplementary information

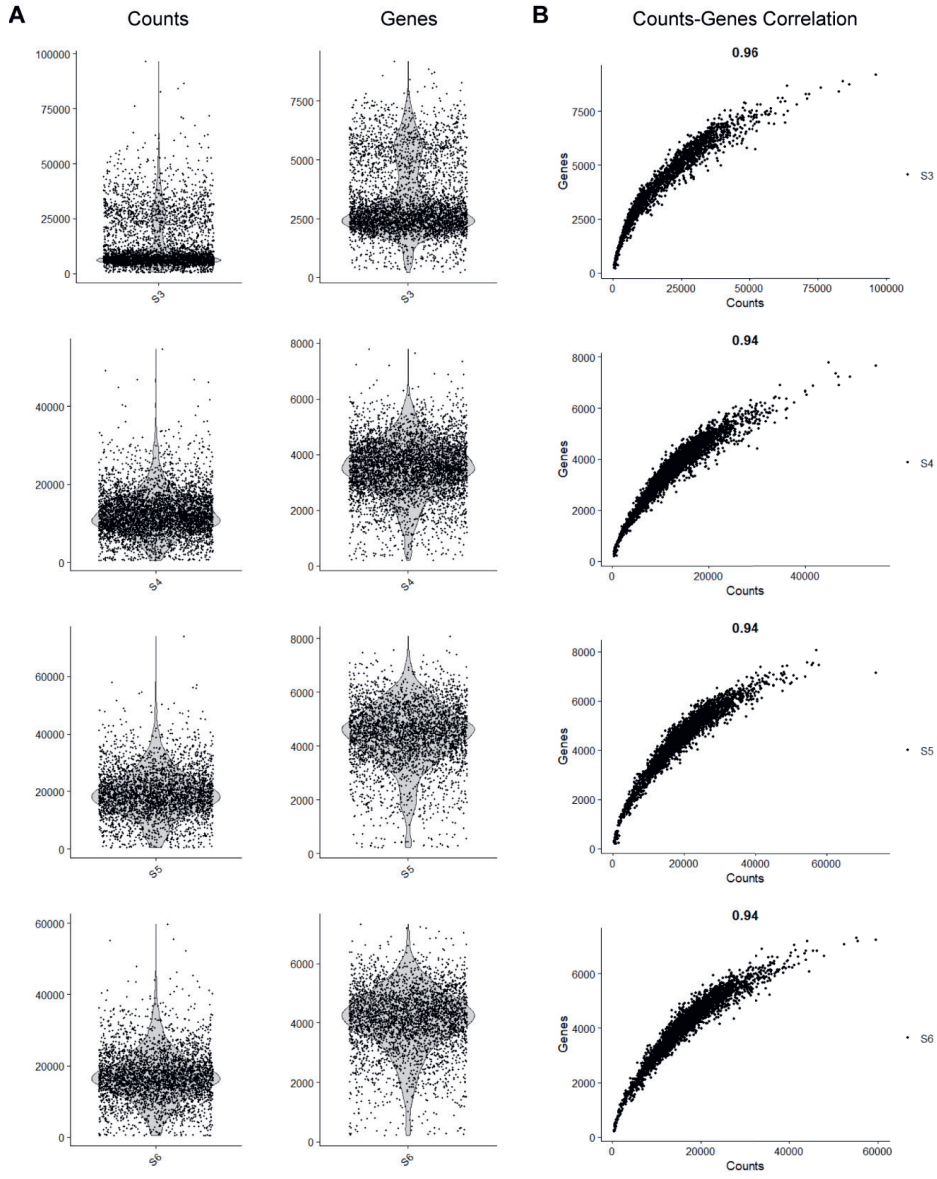

Supplementary Figure 1. Preliminary exploration of the data. A Distribution of the counts and genes detected on each sequencing replicate ('S3' to 'S6'). Dots represent data for individual cells. **B** Correlation analysis between the number of counts and genes detected per individual cell. The correlation coefficient is shown on top of the plot for each sequencing replicate. n = 15,547 cells (pre-filtered data).

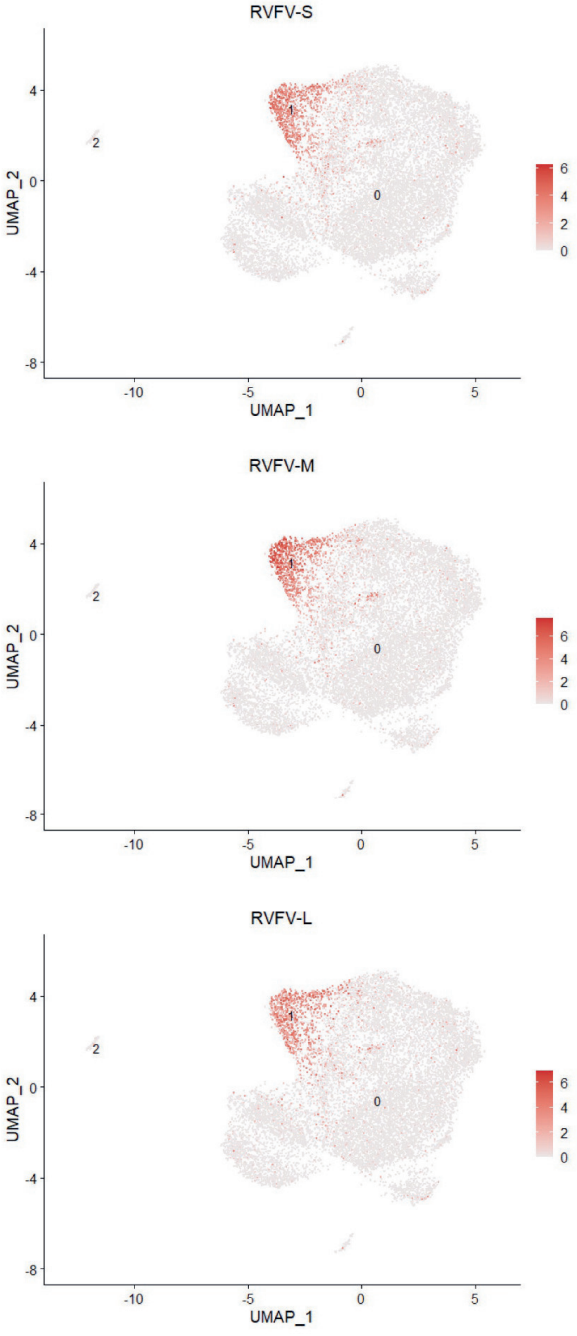

Supplementary Figure 2. Expression of RVFV segments at a single-cell level. UMAP featuring the expression of RVFV S, M and L segments. Expression of each viral segment on individual cells is color-coded in shades of a sequential gradient ranging from light grey (very low or no expression) to dark red (very high expression). High viral expression levels are almost exclusively present in cells grouped to cluster 1.

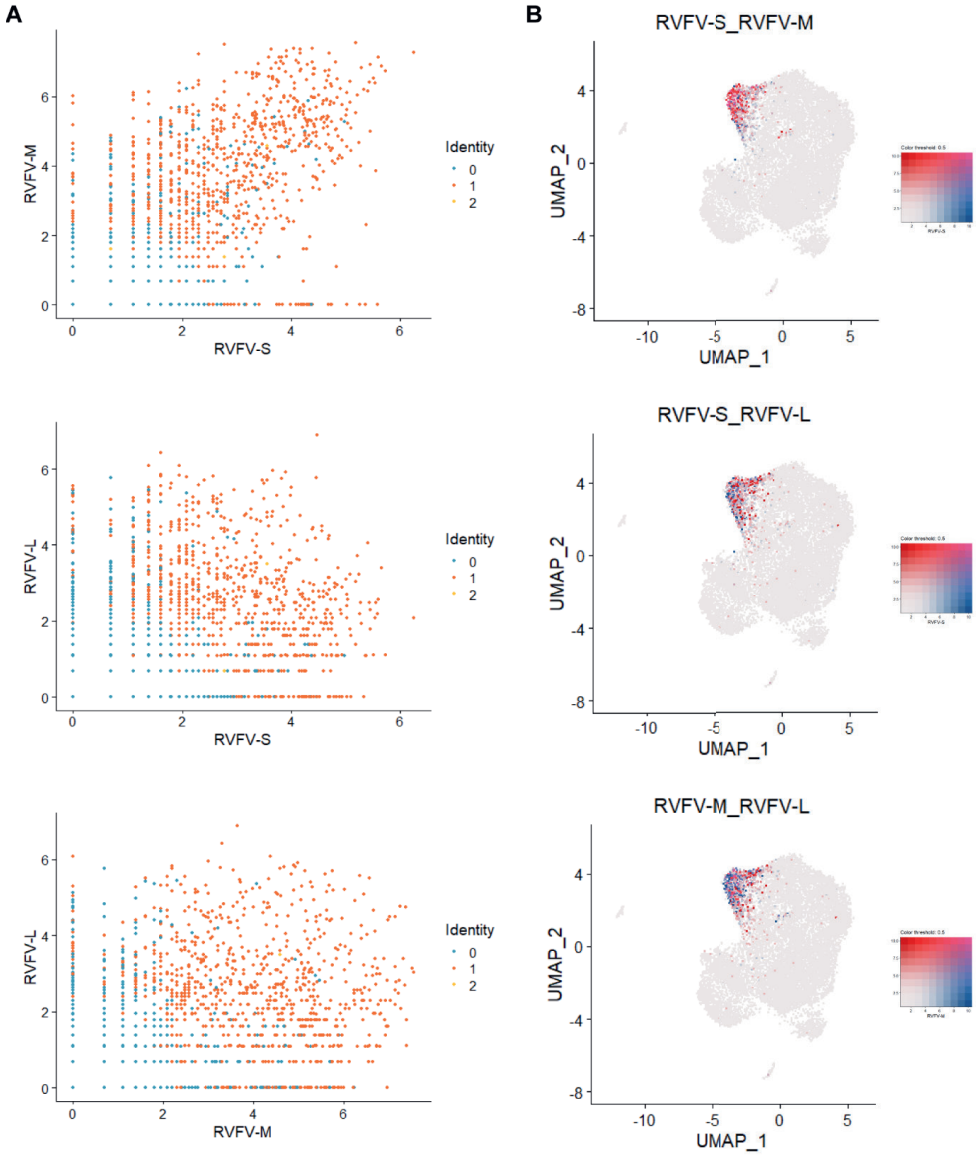

Supplementary Figure 3. Pairwise viral segment expression analysis. A Pairwise correlation analysis between the expression level of two viral segments per individual cell. **B** UMAPs featuring pairwise viral segment expression. The expression of viral segments is color-coded in shades of a combined sequential gradient ranging from light grey (very low or no expression) to dark blue (high expression of the first segment), dark red (high expression of the second segment) or dark purple (high expression of both segments).

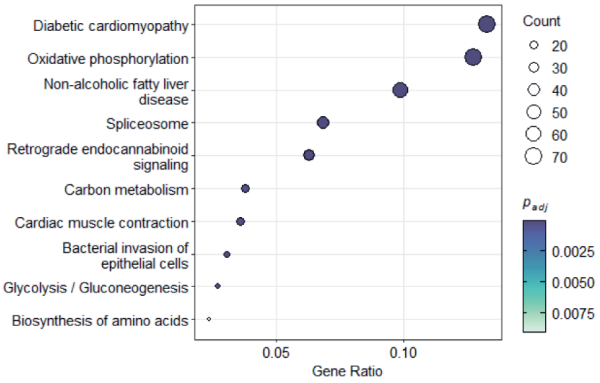

Supplementary Figure 4. Top significantly enriched KEGG pathways altered in ovine hepatocytes in response to RVFV infection. Kyoto Encyclopedia of Genes and Genomes (KEGG) pathways over-representation analysis of genes differentially expressed in RVFV-infected ovine hepatocytes (24 h post-infection; pairwise comparison between cluster 1 and cluster 0). Dot size represents the number of enriched genes associated with each KEGG pathway. Dots are color-coded according to their adjusted *p* value (Benjamini-Hochberg method). Cut-off for significance was set to a *p* adjusted value < 0.05.

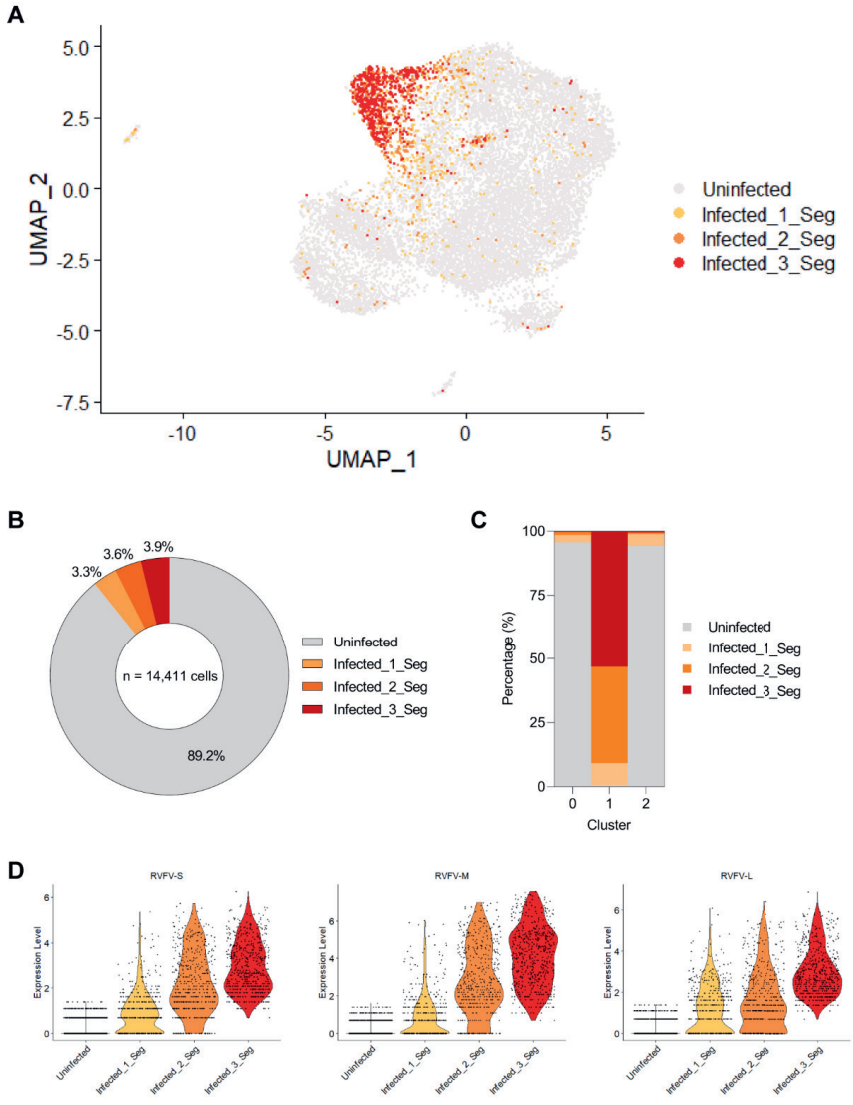

Supplementary Figure 5. The number of different RVFV segment types influences gene expression profiles. **A** UMAP based on the infection status. Cells are classified according to the number of different RVFV segments present or absent as 'uninfected', 'infected_1_seg', 'infected_2_seg', or 'infected_3_seg'. Cluster 1 consist principally of 'infected_3_seg' and 'infected_2_seg' cells. **B** Relative abundance of each cell category, classified according to the number of different RVFV segments. **C** Relative abundance of each cell category per cluster. **D** Distribution of viral S, M and L expression levels per cell category according to the number of different RVFV segment types. An empirical threshold of ≥ 3 counts was applied to determine if a cell was positive for the presence of a viral segment. This threshold explains why some cells appear positive for a viral segment even when classified as 'uninfected'. n = 14,411 cells.

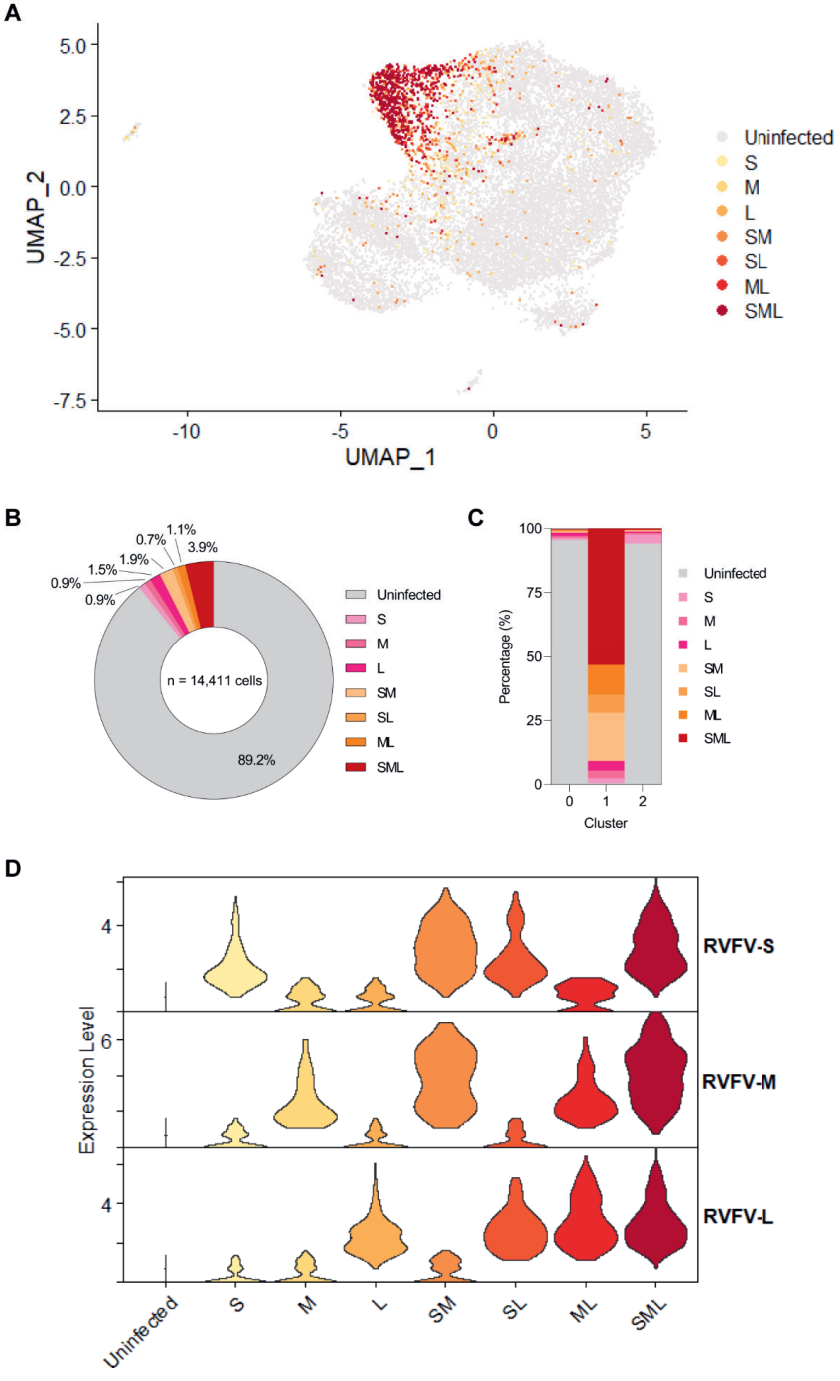
A
UMAP_2
UMAP_1
Uninfected
S
M
L
SM
SL
ML
SML
B
n = 14,411 cells
89.2%
0.9%
1.5%
1.9%
0.7%
1.1%
3.9%
0.9%
C
Percentage (%)
Cluster
D
Expression Level
RVFV-S
RVFV-M
RVFV-L
Uninfected
S
M
L
SM
SL
ML
SML

Supplementary Figure 6. RVFV infection status dictates distinct gene expression profiles. A UMAP based on the infection status. Cells are classified according to the presence or absence of RVFV segments as 'uninfected', 'S', 'M', 'L', 'SM', 'SL', 'ML' or 'SML'. Cluster 1 consist principally of SML-infected cells, indicating that RVFV infection leads to a signature gene expression profile distinct from that of uninfected cells. **B** Relative abundance of each cell category, classified according to the presence or absence of RVFV segments. **C** Relative abundance of each cell category per cluster. **D** Distribution of viral S, M and L expression levels per cell category. An empirical threshold of ≥ 3 counts was applied to determine if a cell was positive for the presence of a viral segment. This threshold explains why some cells appear positive for a viral segment even when classified as 'uninfected'. n = 14,411 cells.

Supplementary Table 1. Sequences of virus-specific primers spiked-in to modify the standard Chromium Next GEM Single Cell 5′ Kit version 2 protocol for single-cell RNA-seq.

Name	Target	Sequence
EB14	RVFV-S genome	AAGCAGTGGTATCAACGCAGAGTACTCCAGTTTGCTGCTCAA
EB15	RVFV-S anti-genome	AAGCAGTGGTATCAACGCAGAGTACCTGCTTTAAGAGTTCGATAACC
EB16	RVFV-M genome	AAGCAGTGGTATCAACGCAGAGTACGCTGATGGCTTGAACAAC
EB17	RVFV-M anti-genome	AAGCAGTGGTATCAACGCAGAGTACGTCTCTCACACCGAACTATC
EB18	RVFV-L genome	AAGCAGTGGTATCAACGCAGAGTACTCGATAGATGTGGAAGATATGG
EB19	RVFV-L anti-genome	AAGCAGTGGTATCAACGCAGAGTACCGTCATTCATCATGGGAAAC

Supplementary Table 2. Distribution of virus-specific primers spiked-in to modify the standard Chromium Next GEM Single Cell 5′ Kit version 2 protocol for single-cell RNA-seq.

Samples	Status	Primers					
		EB14	EB15	EB16	EB17	EB18	EB19
S1	Mock						
S2	RVFV-infected						
S3	RVFV-infected			✓			
S4	RVFV-infected			✓	✓		
S5	RVFV-infected	✓		✓		✓	
S6	RVFV-infected	✓	✓	✓	✓	✓	✓

Supplementary Table 3. Summary statistics of the next-generation single-cell sequencing runs and data pre-processing.

	S3	S4	S5	S6
Number of reads	177,440,000	132,245,517	157,520,806	135,966,726
Mean reads per cell	41,526	28,612	47,375	39,967
Fraction reads in cells	97.3%	98.5%	98.4%	98.3%
Median genes per cell	2,722	3,550	4,492	4,193
Total genes detected	20,888	20,903	21,545	20,719
Valid barcodes	91.9%	92.1%	93.3%	93.6%
Valid UMIs	99.6%	99.8%	99.3%	99.8%
Sequencing saturation	53.3%	33.7%	35.9%	37.0%
Q30 bases in barcode	94.3%	94.3%	94.6%	94.3%
Q30 bases in RNA read	92.2%	91.9%	90.4%	91.4%
Q30 bases in UMI	93.9%	93.9%	94.1%	93.9%
Reads mapped to genome	94.8%	93.6%	88.6%	92.9%

Pipeline: Cell Ranger version 7.1.0 (chemistry: single-cell 5′ R2-only).

Additional supplementary information files are available through the authors upon reasonable request:

Supplementary Table 4. Differentially expressed genes per cluster (0, 1 and 2) in ovine hepatocytes upon RVFV infection (Excel file).

Supplementary Table 5. Differentially expressed genes between infected (cluster 1) and uninfected (cluster 0) phenotypes in ovine hepatocytes upon RVFV infection (Excel file).

Supplementary Table 6. Significantly enriched Gene Ontology pathways (biological processes) altered in ovine hepatocytes upon RVFV infection (Excel file).

Supplementary Table 7. Significantly enriched Gene Ontology pathways (molecular functions) altered in ovine hepatocytes upon RVFV infection (Excel file).

Supplementary Table 8. Significantly enriched KEGG pathways altered in ovine hepatocytes upon RVFV infection (Excel file).

Chapter 6

Discussion

Erick Bermúdez-Méndez

Department of Virology & Molecular Biology, Wageningen Bioveterinary Research, Lelystad, The Netherlands

Laboratory of Virology, Wageningen University & Research, Wageningen, The Netherlands

Deepening our knowledge of the biology of arthropod-borne viruses has proven instrumental in the development and improvement of outbreak control strategies, such as vaccines and therapeutics. Although the discoveries made through fundamental research might not be immediately applicable, they often set the ground for solutions developed later on. The work presented in this thesis concentrated on two fundamental aspects of the biology of bunyaviruses: genome packaging and the host's response during acute infection. This final chapter aims to establish connections between the different pieces of work described in this thesis (**Chapters 2-5**) and to interpret the most important findings in a broader sense. In addition, the limitations of the chosen experimental approaches are presented, as well as perspectives on research questions that remain open and how future research might address these.

Word of caution: Rift Valley fever virus (RVFV), and in some cases Schmallenberg virus (SBV), were employed as prototype bunyaviruses belonging to different families (*Phenuiviridae* and *Peribunyaviridae*, respectively) throughout this thesis. It is worth pointing out that, although there is a tendency to generalize the results for the sake of simplicity, the findings described here might not be representative of all members of the order *Bunyavirales*.

Genome packaging of segmented bunyaviruses: a first glimpse

Segmentation of viral genomes has long raised questions about genome packaging and the subsequent spread of the virus, mainly considering the potential pros and cons for virus fitness[1,2]. In theory, genome segmentation could be beneficial as it may allow for better control over viral gene expression levels[3]. Furthermore, genome segmentation can facilitate the occurrence of genome exchange events (reassortments) between related viruses, potentially favoring virus evolution[4]. On the other hand, having a genome split over multiple segments appears to be a logistics problem per se. At least one copy of each genome segment must be incorporated inside a single virus particle for it to be infectious on its own. Otherwise, the lack of one or more genome segments would impede the virus from generating infectious progeny[2]. This logistics issue can be especially problematic for viruses with a large number of segments[5], unless the virus employs a highly specific mechanism to ensure the incorporation of a complete set of segments (**Fig. 1**).

In **Chapter 2**, the genome packaging process of RVFV and SBV was investigated. Contrary to what one could reasonably expect for three-segmented viruses, it was shown that the genome packaging of RVFV and SBV does not follow a tightly coordinated process. In fact, it is based on a stochastic process in which most virions assembled consist of empty or incomplete particles, and only a small fraction of the particles contains a complete set of the S, M and L genome

segments[6]. Besides considering the genomic composition of virus particles, the stochastic packaging notion is further supported by the absence of specific interactions between the three different bunyaviral RNAs, which complicates the incorporation of a three-segmented bundle[7].

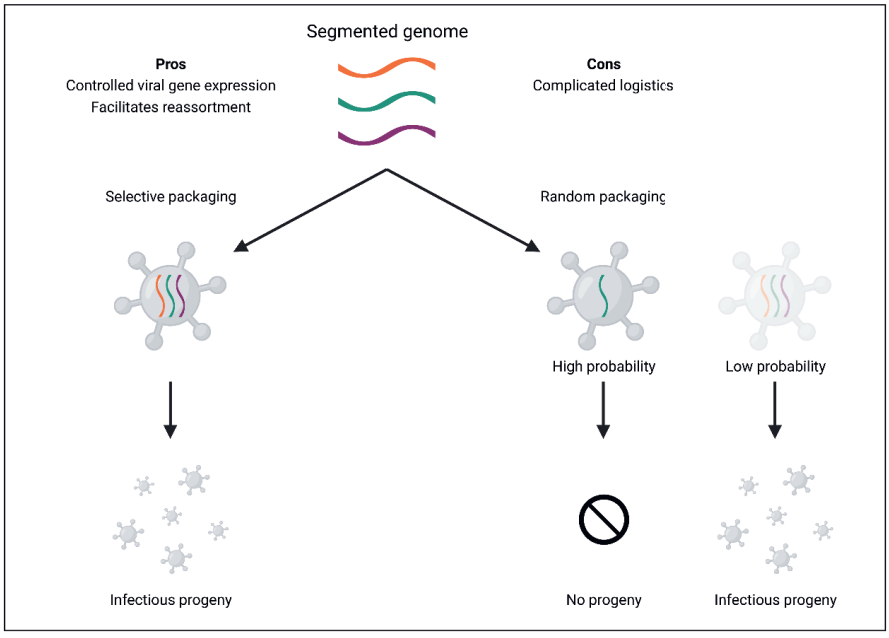

Figure 1. Genome packaging of segmented viruses. Segmented viruses employing a selective genome packaging mechanism incorporate a complete set of genome segments into virus particles. Complete virus particles are infectious on their own and able to generate progeny virions. On the other hand, segmented viruses that randomly incorporate the genome segments into virus particles have a low probability of generating complete virus particles but a high probability of generating empty (not shown) or incomplete particles unable to generate infectious progeny on their own.

The intra-virion genomic composition studies described in this thesis were all executed with cell culture-derived viruses. It remains important to verify if progeny bunyavirus virions generated during the natural course of infection (e.g., derived from an infected animal's blood or the saliva of an infected mosquito) show a similar particle composition frequency to the one observed *in vitro*. The challenge in analyzing blood- and saliva-derived samples is to develop a reliable method capable of dealing with the intrinsic complexity of these biological matrices.

How do (mechanistically) bunyaviruses package their segmented genome?

Previous work by others has shown that the RVFV N protein in the ribonucleoproteins (RNPs) interacts with the cytoplasmic tails of the viral glycoproteins to facilitate incorporation of the genome segments inside virus particles[8–11]. Such interaction proves crucial to ensure that the RNA molecules incorporated into the particles are viral genome segments and not the host's naked RNA. Nevertheless, this interaction should not necessarily be interpreted as a mechanism for a high degree of specificity. In this thesis was shown that complementary viral RNA (encapsidated by the N protein, similarly as viral genomic RNA) often also gets incorporated inside progeny virions[6] (**Chapter 2**). It has been previously suggested that incorporating the complementary RNA of the S segment may be beneficial for faster synthesis of NSs, and thus of innate immune antagonistic activity, within infected cells[12,13]. However, the fact that complementary RNAs of all three segments can be found within virions suggests that packaging of viral RNAs, whether genomic or anti-genomic, is not strictly controlled.

Multiple lines of evidence available thus far indicate that genome packaging of bunyaviruses is a random process. Yet, the exact mechanism by which bunyaviruses incorporate their segmented genome into virus particles remains a black box.

Is genome packaging of bunyaviruses host-dependent?

Bunyaviruses are known to have a very broad host range, being able to infect plants, birds, reptiles and mammals[14]. Specifically for arthropod-borne bunyaviruses, sustaining a productive infection cycle depends on successfully alternating between the arthropod vector and the vertebrate host. Studying key steps in the replication of the virus in the host and the vector is fundamental to gain insights into the dual viral life cycle. In **Chapter 2**, the genome packaging efficiency of RVFV was compared after replicating in mammalian and in insect cells. It was found that more genome segments (disregarding the S, M or L segment identity) are incorporated into virions when the virus replicates in insect cells. Moreover, insect-derived RVFV had a higher fraction of complete particles comprising the three genome segments than mammalian-derived RVFV[6]. This higher genome packaging efficiency in insect cells could possibly explain why RVFV grown in insect cells has shown to be more virulent than when grown in mammalian cells[15,16].

The cause underlying the different genome packaging efficiencies has not yet been addressed experimentally. Still, this difference may indicate that certain currently unknown host/vector factors are playing a role in the packaging process. Alternatively, it could be that the different ideal temperatures at which these cells are grown (28 ºC for insect cells and 37 ºC for mammalian

cells) also have an influence. The RNAs and N protein forming the RNPs might be subject to temperature-dependent conformational changes that facilitate or complicate their packaging. Moreover, the lower temperature at which insect cells are grown results in slower Brownian diffusion of intracellular molecules, which may benefit the unspecific inclusion of more RNPs within virions. This hypothesis of temperature influencing the packaging efficiency could in theory be tested by assessing genome packaging efficiencies after inverting the temperatures used to culture cells (e.g., maintaining mammalian cells at 28 ºC and insect cells at 37 ºC). However, this temperature change would probably modify regular cellular processes and negatively impact cellular homeostasis, rendering it very difficult to draw unbiased conclusions.

Regardless of the reason explaining the differences in genome packaging efficiency between the vertebrate host and the arthropod vector, the production of a larger fraction of complete particles in the vector likely contributes to maintaining high viral titers in its saliva, facilitating efficient vector to host virus transmission.

How do bunyaviruses cope with stochastic genome packaging?

It is intriguing that, albeit genome packaging of bunyaviruses is seemingly inefficient, it does not really hamper bunyaviruses from efficiently infecting their hosts and vectors. Based on the findings of stochastic genome packaging, the following study in this thesis focused on interrogating whether bunyavirus particles with an incomplete set of genome segments could contribute to within-host virus spread (**Chapter 3**). The results demonstrated that incomplete bunyavirus particles can co-infect individual cells and reconstitute, through genomic complementation, a complete viral genome capable of generating infectious progeny[17]. Thus, co-infection by complementing incomplete particles serves bunyaviruses as a mechanism to overcome, at least partially, the theoretical fitness cost of packaging its genome segments randomly.

These results confirmed that genome complementation by populations of incomplete bunyavirus particles is possible in cultured mammalian and insect cells but also *in vivo* in mosquitoes[17]. Even though there is no reason to believe that genome complementation could not occur in a mammalian host (*in vivo*), it would be valuable to perform such co-infection experiments to complement the observations presented in this thesis. Quantifying to what extent genome complementation is important for the efficiency of between-host transmission is a complex technical challenge to address. So far, simplified mathematical models only allow to deduct that genome complementation might be relevant under certain circumstances (e.g., at intermediate multiplicities of infection)[17].

Segmented viruses as a bohemian form of multipartitism

Multipartite and segmented viruses have in common that their genomes are divided over multiple segments. However, they differ in how the genome segments are packaged into virus particles. By definition, segmented viruses package all the genome segments inside a single particle. In contrast, multipartite viruses package each genome segment individually into separate particles. Multipartite viruses thereby rely on genome complementation via co-infection to complete their life cycle[1–3]. While the definition for segmented viruses holds true for those which employ a selective genome packaging (best exemplified by the eight-segmented influenza A virus[18]), segmented viruses with random genome packaging, like bunyaviruses, deviate from the formal definition.

In segmented viruses with random genome packaging, a large fraction of the progeny virions have an incomplete set of genome segments[6]. These incomplete particles are thus unable to establish a productive infection autonomously. Actually, some of the incomplete particles only contain one genome segment, closely resembling the condition of multipartite viruses. In that context, and considering that incomplete bunyavirus particles can co-infect a single cell to reconstitute a complete genome[17], similarly as multipartite viruses do, is that bunyaviruses with random genome packaging might be considered as a bohemian form of multipartitism (**Fig. 2**).

It is important to note though, that bunyaviruses also generate a fraction of particles with a complete set of genome segments, something that multipartite viruses cannot achieve. Another remarkable difference between segmented and multipartite viruses is the special feature of multipartite viruses being able to establish a productive infection in a cell in which not all genome segments are present. In that scenario, multipartite viruses can compensate for the absence of a genome segment through intercellular trafficking of the missing segment and/or the protein encoded by it[19].

A recent study with the plant-infecting octapartite faba bean necrotic stunt virus (FBNSV, family *Nanoviridae*) also demonstrated that genome complementation served as a mechanism to reconstitute the complete genome of a multipartite virus and mediate between-host transmission[20]. Interestingly, this genome reconstitution was possible after simultaneous incomplete genome transmission events by different individual aphid vectors (concomitant transmission), as well as through sequential transmission events by a single aphid vector infected with complementary sets of segments (non-concomitant transmission)[20]. Whether these

concomitant and non-concomitant transmission mechanisms are also possible for bunyaviruses remain to be investigated.

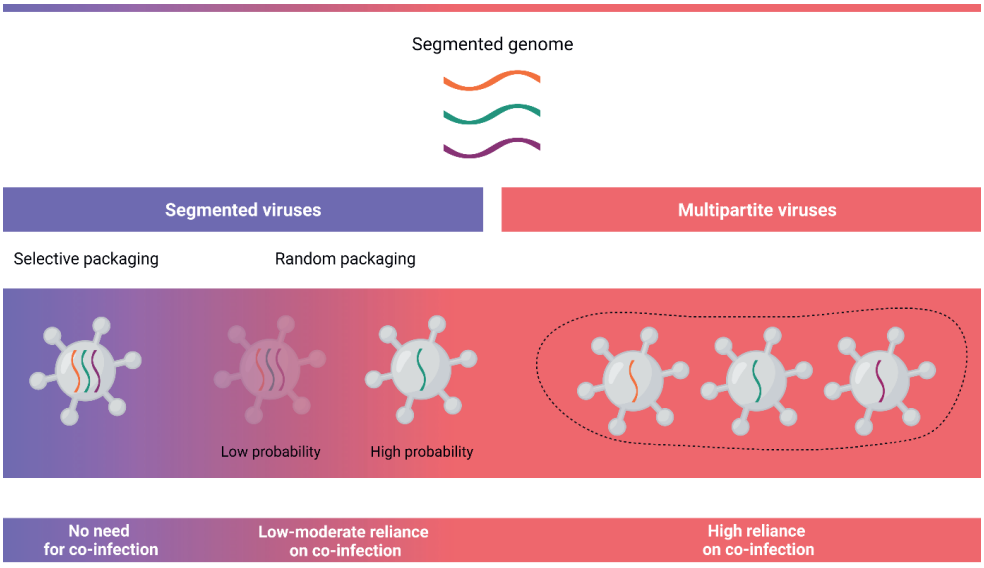

Figure 2. Segmented viruses as a bohemian form of multipartitism. Traditionally, clear differences in genome packaging allow the categorization of viruses with multiple segments either as segmented or multipartite. This classification seems to hold true for segmented viruses employing a selective genome packaging mechanism (no need for co-infection). At the opposite extreme of the spectra, multipartite viruses depend entirely on co-infection for a successful infection cycle. Although segmented viruses with random packaging sometimes manage to incorporate a complete set of segments in a single particle, they produce at the same time large amounts of incomplete particles that cannot establish a productive infection on their own. Segmented viruses with random packaging thus partially rely on co-infection by incomplete particles to reconstitute a complete genome. In this context, bunyaviruses display an unconventional way of infection that resembles the life cycle of multipartite viruses.

Do bunyaviruses have a genome formula?

The concept of a 'genome formula' originally arose from a study with FBNSV[21]. In this study, the researchers reported that FBNSV reproducibly accumulated the different genome segments at defined relative frequencies. This defined ratio of relative segment frequencies is now known as the genome formula[21]. To date, every multipartite virus species interrogated for its relative segment frequency has shown to accumulate to its own specific genome formula, which is dependent on the host plant species[22].

The concept of the genome formula is intriguing, as it comes along with the hypothesis that the multipartite nature of the virus allows it to differentially regulate viral gene expression in a context-dependent manner[21–23]. It should be noted though, that genome formulas of multipartite viruses reported so far are all based on bulk measurements from systemically infected host plant leaves, making it impossible to conclude if the genome formula per host is also maintained at the single-cell level.

The work in this thesis did not formally attempt to investigate if bunyaviruses also have a genome formula. However, the intracellular frequencies of the S, M and L genome segments in individual infected cells were assessed in **Chapter 2** and **Chapter 5**. Despite the extreme variability in the relative frequencies of the genome segments between individual cells[6], it might be possible that animal-infecting bunyaviruses also reach to a host-dependent setpoint genome formula. Similarly as reported with plant-infecting multipartite viruses, bulk measurements on infected samples could inform if animal-infecting bunyaviruses differentially regulate their gene expression depending if they are replicating in the vertebrate host or the arthropod vector.

Shedding light on RVFV-induced pathogenesis

The pathogenic effects of an RVFV infection have previously been studied following two distant approaches. On one side, infections of cultured cells have been critical to determine RVFV virulence factors and to start studying the cellular (immune) response upon infection[24–31]. On the other side, macro- and microscopic examination of tissues from natural and experimentally infected animals have revealed valuable knowledge on tissue tropism and pathology[32–35]. Nevertheless, a clear gap existed between those two approaches; the knowledge linking how the changes in the cellular environment induced by RVFV led to the pathological phenotype typically observed in infected animals was missing.

Profiling the transcriptome of target organs (liver and spleen) of lambs during RVFV infection provided new insights into the pathogenesis of RVFV and revealed changes in gene expression that can be associated with histopathological features (**Chapter 4**). As expected, it was shown that lambs responded to infection with a sharp upregulation of gene sets involved in the immune response, mainly those related to interferon-mediated pathways. However, the most interesting finding was that the RVFV-induced hepatocyte necrosis results in a strong downregulation of numerous liver enzymes, thereby severely compromising the normal functioning of the organ. This downregulation of liver enzymes possibly accounts for some clinical symptoms observed in RVFV-infected animals like icterus, hemorrhages and coagulation disorders[36]. Similar

transcriptomic studies in other target organs, such as in sheep placenta, ideally combined with complementary technologies like proteomics, would be extremely helpful to obtain a more complete picture of RVFV pathogenesis.

How is genome packaging interrelated with the host's response upon infection?

The research questions that motivated the work presented in this thesis transitioned from overseeing the genome packaging of bunyaviruses (**Chapter 2**), to exploring how genome packaging shapes the life cycle of bunyaviruses (**Chapter 3**), to studying how the host responds upon a bunyavirus infection (**Chapter 4**). But how is the genome packaging of bunyaviruses related to the host's response? The random process by which RVFV packages its genome segments not only impacts whether the infected cell will be able to generate infectious progeny but can also shape how the cell will respond to the infection.

In **Chapter 5**, the potential of single-cell RNA-seq technology to examine the responses in individual fetal liver cells upon RVFV infection was explored. The main interest was in comparing individual host cell responses depending on the nature of the incoming infecting virus particle (i.e., complete versus incomplete), or more accurately, based on the presence/absence of the different viral genome segments. One could anticipate that cells receiving a complete set (SML) of genome segments undergo a productive infection and therefore display a transcriptomic profile quite distinct from that of uninfected cells. However, it was completely unknown how a host cell would respond to the presence of only one or two types of viral genome segments and whether cells infected with the three different genome segments all respond the same.

Cells harboring one and two types of viral genome segments had transcriptomes resembling the profiles of either SML-infected or uninfected cells. The viral load, here referring to the combined (SML) viral expression level, was the main factor determining to which transcriptomic profile those cells resembled the most. A high viral load was associated with a SML infected phenotype, whereas a low viral load was associated with the uninfected phenotype, regardless of the number of segment types (one or two) or the identity of the segment (S, M, L or combinations thereof). The insights gained from this first single-cell RNA-seq study on fetal liver cells will be valuable to improve the design of future single-cell experiments.

Do incomplete bunyavirus particles interfere with the viral life cycle?

In many RNA virus families, error-prone viral replication leads to the generation of defective virus variants, often referring to defective viral genomes (DVGs) or defective interfering particles (DIPs).

DVGs are viral genomes with mutations or truncations that impede the virus from successfully completing a replication cycle. DIPs are morphologically and biochemically similar to regular viral infectious particles, but harbor DVGs instead of the wild-type genome[37,38]. As the terms suggest, these defective genomes/particles can interfere with the replication of the wild-type genome by competing for host and viral factors, and by being preferentially replicated due to their shorter length. Moreover, DIPs can influence viral pathogenesis by priming anti-viral immune responses[37,38].

Multiple studies have analyzed the production of bunyavirus DVGs and DIPs[39–43]. As covered throughout this thesis, bunyaviruses generate what is referred to as incomplete virus particles. Although incomplete bunyavirus particles are thought to harbor complete genome segments (i.e., consisting of the full-length sequence), it is reasonable to conceive incomplete bunyavirus particles as another type of defective virus variant, due to the lack of one or more full-length genome segments.

Intriguingly, under this conception, it is possible to argue that incomplete bunyavirus particles are DIPs that can potentially exert a dual effect: interference and/or assistance. Replication-competent but non-infectious incomplete bunyavirus particles could interfere with a regular replication cycle via the conventional mechanisms of competition for resources and innate immune activation. Alternatively, co-infection by incomplete bunyavirus particles can contribute to virus infection and spread through cooperative genome reconstitution, as demonstrated in **Chapter 3**[17]. The factors and context determining to which extent incomplete bunyavirus particles assist or interfere with a regular replication cycle remain to be elucidated. Nonetheless, the fact that genome reconstitution through co-infection readily occurred suggests that the balance leans more towards assisting the replication cycle than towards interfering with it.

Other avenues pending experimental exploration

Our knowledge of the molecular mechanisms underlying many biological processes in the life cycle of bunyaviruses is still limited. While the analysis of intracellular relative abundance of viral genome segments in mammalian cells at single-molecule resolution was possible in this thesis (**Chapter 2**), it is still uncertain what this relative abundance looks like in insect cells, since it proved to be technically challenging. It would be interesting to assess if a particular trend in the intracellular ratio of genome segments within insect cells can partially explain why genome packaging is more efficient in the vector. Furthermore, it is still unclear how two-segmented

bunyaviruses (family *Arenaviridae*) and three-segmented plant-infecting bunyaviruses (family *Tospoviridae* and genus *Tenuivirus* within the family *Phenuiviridae*) package their genome.

The work presented in this thesis focused on analyzing the genomic composition within virus particles while studying genome packaging. This intra-virion composition certainly is a major determinant of the infection outcome, although it may not be the only one. The protein and lipid composition of the viral particle can also influence the infection outcome. Work aimed at characterizing the content and architecture of the viral envelope using flow virometry, lipidomics and/or proteomics can reveal if specific lipid and protein compositions can result in improved infectivity[44,45]. Harnessing such experimental strategies to analyze the surface of three-segmented bunyavirus particles would be useful to further studying plausible host-dependent differences.

Superinfection exclusion and genetic reassortment are two other exciting topics around the biology of bunyaviruses that remained outside the scope of this thesis. Superinfection exclusion, a phenomenon in which a primary infection blocks a secondary infection with the same or a related virus[46], has previously been reported for viruses from several different families, including some belonging to the order *Bunyavirales*[47–50]. In the co-infection experiments presented in **Chapter 3**, co-infections were always performed simultaneously, thereby preventing the potential effects of superinfection exclusion. Whether incomplete bunyavirus particles can also lead to superinfection exclusion and influence the extent to which genome complementation contributes to infection remains undetermined. Further research could also explore if co-infection with incomplete particles, which appeared to occur without much restriction, could increase the chances of genetic reassortment with viruses infecting the same host or vector. Probably, a reassortant virus can only emerge when the polymerase, N protein and cytoplasmic tails of the glycoproteins are closely related to each other.

In recent years, refined structural biology techniques such as cryo-electron microscopy (cryo-EM) and cryo-electron tomography (cryo-ET) have taken the field by storm. The application of these structural virology methods has made it possible to gain a deeper and more detailed understanding of virus particles and intracellular biological processes at unprecedented levels of resolution[51–55]. For instance, obtaining a detailed structural map of the interaction between the N protein in RNPs and the cytoplasmic tails of the glycoproteins would be a significant step to better comprehend bunyavirus genome packaging. Either for analyzing host/viral protein complexes, characterizing the surface of virus particles, or studying the processes of viral

replication and virion assembly, it is expected that these techniques will continue to be applied to help researchers advance the current knowledge on bunyaviruses.

Concluding remarks

The bunyavirus ensemble: a flexible orchestration of solo, duo & trio acts

The results of this thesis make it necessary to reflect on how we normally think about bunyaviruses. Instead of the textbook representation of a bunyavirus particle typically depicting the three genome segments (for three-segmented bunyaviruses), we should be more inclined to think of bunyaviruses as a diverse population of empty, incomplete and complete particles, or as the title of this thesis metaphorizes: an ensemble (**Fig. 3**). Within the bunyavirus ensemble, particles comprise one segment, two segments or three segments. Analogous to a group of good musicians, individual bunyavirus particles might infect/play on their own performing a solo (one segment), act as a duo (two segments), a trio (three segments), or flexibly act together to play as a prominent infectious orchestra.

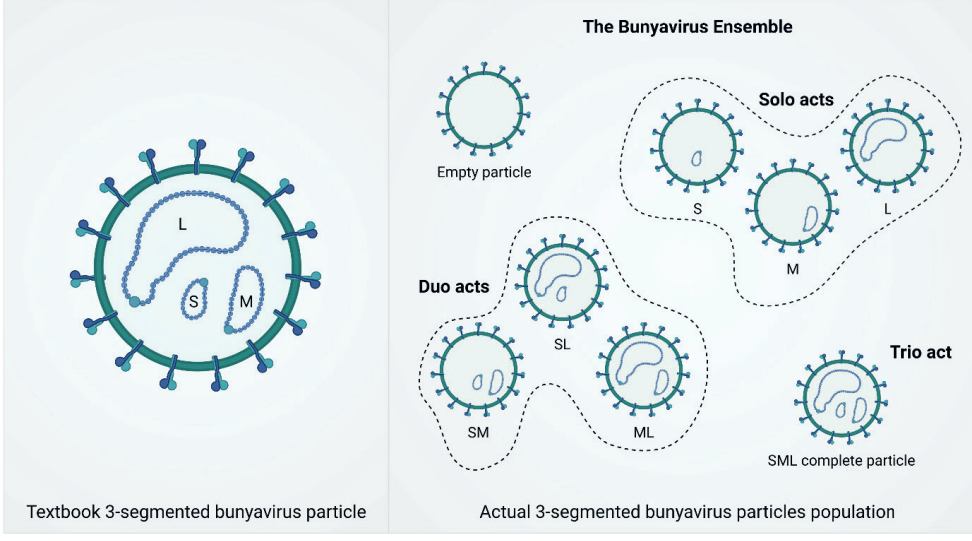

Figure 3. The bunyavirus ensemble. Bunyavirus populations consist of a mixture of empty, incomplete and complete particles. Upon co-infection within a single cell, diverse bunyavirus particles comprising solos (1-segment), duos (2-segments) or trios (3-segments) can complement genetically and reconstitute a complete genome, successfully establishing a productive infection.

Acknowledgements

Thanks to Paul J. Wichgers Schreur and Monique M. van Oers for providing valuable feedback on this chapter. Thanks also to Ingrid Cárdenas Rey for proofreading. Illustrations in **Figs. 1-3** were created with BioRender.com

References

1. Sicard A, Michalakis Y, Gutiérrez S, Blanc S. The strange lifestyle of multipartite viruses. *PLOS Pathogens* **2016**, *12* (11), e1005819. https://doi.org/10.1371/journal.ppat.1005819.
2. Michalakis Y, Blanc S. The curious strategy of multipartite viruses. *Annual Review of Virology* **2020**, *7* (1), 203–218. https://doi.org/10.1146/annurev-virology-010220-063346.
3. Lucía-Sanz A, Manrubia S. Multipartite viruses: adaptive trick or evolutionary treat? *npj Systems Biology and Applications* **2017**, *3* (1), 1–11. https://doi.org/10.1038/s41540-017-0035-y.
4. Lowen AC. It's in the mix: Reassortment of segmented viral genomes. *PLOS Pathogens* **2018**, *14* (9), e1007200. https://doi.org/10.1371/journal.ppat.1007200.
5. Iranzo J, Manrubia SC. Evolutionary dynamics of genome segmentation in multipartite viruses. *Proceedings of the Royal Society B: Biological Sciences* **2012**, *279* (1743), 3812–3819. https://doi.org/10.1098/rspb.2012.1086.
6. Bermúdez-Méndez E, Katrukha EA, Spruit CM, Kortekaas J, Wichgers Schreur PJ. Visualizing the ribonucleoprotein content of single bunyavirus virions reveals more efficient genome packaging in the arthropod host. *Communications Biology* **2021**, *4* (1), 1–13. https://doi.org/10.1038/s42003-021-01821-y.
7. Wichgers Schreur PJ, Kortekaas J. Single-molecule FISH reveals non-selective packaging of Rift Valley fever virus genome segments. *PLOS Pathogens* **2016**, *12* (8), e1005800. https://doi.org/10.1371/journal.ppat.1005800.
8. Överby AK, Pettersson RF, Neve EPA. The glycoprotein cytoplasmic tail of Uukuniemi virus (*Bunyaviridae*) interacts with ribonucleoproteins and is critical for genome packaging. *Journal of Virology* **2007**, *81* (7), 3198–3205. https://doi.org/10.1128/jvi.02655-06.
9. Ribeiro D, Borst JW, Goldbach R, Kormelink R. Tomato spotted wilt virus nucleocapsid protein interacts with both viral glycoproteins Gn and Gc *in planta*. *Virology* **2009**, *383* (1), 121–130. https://doi.org/10.1016/j.virol.2008.09.028.
10. Carnec X, Ermonval M, Kreher F, Flamand M, Bouloy M. Role of the cytosolic tails of Rift Valley fever virus envelope glycoproteins in viral morphogenesis. *Virology* **2014**, *448*, 1–14. https://doi.org/10.1016/j.virol.2013.09.023.
11. Tercero B, Narayanan K, Terasaki K, Makino S. Characterization of the molecular interactions that govern the packaging of viral RNA segments into Rift Valley fever phlebovirus particles. *Journal of Virology* **2021**, *95* (14), e00429-21. https://doi.org/10.1128/JVI.00429-21.
12. Simons JF, Hellman U, Pettersson RF. Uukuniemi virus S RNA segment: ambisense coding strategy, packaging of complementary strands into virions, and homology to members of the genus *Phlebovirus*. *Journal of Virology* **1990**, *64* (1), 247–255.

13. Ikegami T, Won S, Peters CJ, Makino S. Rift Valley fever virus NSs mRNA is transcribed from an incoming anti-viral-sense S RNA segment. *Journal of Virology* **2005**, *79* (18), 12106–12111. https://doi.org/10.1128/JVI.79.18.12106-12111.2005.

14. Wichgers Schreur PJ, Kormelink R, Kortekaas J. Genome packaging of the *Bunyavirales*. *Current Opinion in Virology* **2018**, *33*, 151–155. https://doi.org/10.1016/j.coviro.2018.08.011.

15. Nfon CK, Marszal P, Zhang S, Weingartl HM. Innate immune response to Rift Valley fever virus in goats. *PLOS Neglected Tropical Diseases* **2012**, *6* (4), e1623. https://doi.org/10.1371/journal.pntd.0001623.

16. Weingartl HM, Miller M, Nfon C, Wilson WC. Development of a Rift Valley fever virus viremia challenge model in sheep and goats. *Vaccine* **2014**, *32* (20), 2337–2344. https://doi.org/10.1016/j.vaccine.2014.02.066.

17. Bermúdez-Méndez E, Bronsvoort KF, Zwart MP, van de Water S, Cárdenas-Rey I, Vloet RPM, Koenraadt CJM, Pijlman GP, Kortekaas J, Schreur PJW. Incomplete bunyavirus particles can cooperatively support virus infection and spread. *PLOS Biology* **2022**, *20* (11), e3001870. https://doi.org/10.1371/journal.pbio.3001870.

18. Chou Y, Vafabakhsh R, Doğanay S, Gao Q, Ha T, Palese P. One influenza virus particle packages eight unique viral RNAs as shown by FISH analysis. *PNAS* **2012**, *109* (23), 9101–9106. https://doi.org/10.1073/pnas.1206069109.

19. Sicard A, Pirolles E, Gallet R, Vernerey M-S, Yvon M, Urbino C, Peterschmitt M, Gutierrez S, Michalakis Y, Blanc S. A multicellular way of life for a multipartite virus. *eLife* **2019**, *8*, e43599. https://doi.org/10.7554/eLife.43599.

20. Di Mattia J, Torralba B, Yvon M, Zeddam J-L, Blanc S, Michalakis Y. Nonconcomitant host-to-host transmission of multipartite virus genome segments may lead to complete genome reconstitution. *PNAS* **2022**, *119* (32), e2201453119. https://doi.org/10.1073/pnas.2201453119.

21. Sicard A, Yvon M, Timchenko T, Gronenborn B, Michalakis Y, Gutierrez S, Blanc S. Gene copy number is differentially regulated in a multipartite virus. *Nature Communications* **2013**, *4* (1), 1–8. https://doi.org/10.1038/ncomms3248.

22. Gallet R, Di Mattia J, Ravel S, Zeddam J-L, Vitalis R, Michalakis Y, Blanc S. Gene copy number variations at the within-host population level modulate gene expression in a multipartite virus. *Virus Evolution* **2022**, *8* (2), veac058. https://doi.org/10.1093/ve/veac058.

23. Zwart MP, Elena SF. Modeling multipartite virus evolution: the genome formula facilitates rapid adaptation to heterogeneous environments†. *Virus Evolution* **2020**, *6* (1), veaa022. https://doi.org/10.1093/ve/veaa022.

24. Bouloy M, Janzen C, Vialat P, Khun H, Pavlovic J, Huerre M, Haller O. Genetic evidence for an interferon-antagonistic function of Rift Valley fever virus nonstructural protein NSs. *Journal of Virology* **2001**, *75* (3), 1371–1377. https://doi.org/10.1128/JVI.75.3.1371-1377.2001.

25. Billecocq A, Spiegel M, Vialat P, Kohl A, Weber F, Bouloy M, Haller O. NSs protein of Rift Valley fever virus blocks interferon production by inhibiting host gene transcription. *Journal of Virology* **2004**, *78* (18), 9798–9806. https://doi.org/10.1128/JVI.78.18.9798-9806.2004.

26. Le May N, Dubaele S, De Santis LP, Billecocq A, Bouloy M, Egly J-M. TFIIH transcription factor, a target for the Rift Valley hemorrhagic fever virus. *Cell* **2004**, *116* (4), 541–550. https://doi.org/10.1016/S0092-8674(04)00132-1.

27. Habjan M, Pichlmair A, Elliott RM, Överby AK, Glatter T, Gstaiger M, Superti-Furga G, Unger H, Weber F. NSs Protein of Rift Valley fever virus induces the specific degradation of the double-stranded RNA-dependent protein kinase. *Journal of Virology* **2009**, *83* (9), 4365–4375. https://doi.org/10.1128/JVI.02148-08.

28. Ikegami T, Narayanan K, Won S, Kamitani W, Peters CJ, Makino S. Rift Valley fever virus NSs protein promotes post-transcriptional downregulation of protein kinase PKR and inhibits eIF2alpha phosphorylation. *PLOS Pathogens* **2009**, *5* (2), e1000287. https://doi.org/10.1371/journal.ppat.1000287.

29. Kainulainen M, Lau S, Samuel CE, Hornung V, Weber F. NSs virulence factor of Rift Valley fever virus engages the F-Box proteins FBXW11 and β-TRCP1 to degrade the antiviral protein kinase PKR. *Journal of Virology* **2016**, *90* (13), 6140–6147. https://doi.org/10.1128/JVI.00016-16.

30. Pinkham C, Dahal B, de la Fuente CL, Bracci N, Beitzel B, Lindquist M, Garrison A, Schmaljohn C, Palacios G, Narayanan A, Campbell CE, Kehn-Hall K. Alterations in the host transcriptome *in vitro* following Rift Valley fever virus infection. *Scientific Reports* **2017**, *7* (1), 14385. https://doi.org/10.1038/s41598-017-14800-3.

31. Havranek KE, White LA, Lanchy J-M, Lodmell JS. Transcriptome profiling in Rift Valley fever virus infected cells reveals modified transcriptional and alternative splicing programs. *PLOS ONE* **2019**, *14* (5), e0217497. https://doi.org/10.1371/journal.pone.0217497.

32. Odendaal L, Clift SJ, Fosgate GT, Davis AS. Lesions and cellular tropism of natural Rift Valley fever virus infection in adult sheep. *Veterinary Pathology* **2019**, *56* (1), 61–77. https://doi.org/10.1177/0300985818806049.

33. Odendaal L, Davis AS, Fosgate GT, Clift SJ. Lesions and cellular tropism of natural Rift Valley fever virus infection in young lambs. *Veterinary Pathology* **2020**, *57* (1), 66–81. https://doi.org/10.1177/0300985819882633.

34. Odendaal L, Clift SJ, Fosgate GT, Davis AS. Ovine fetal and placental lesions and cellular tropism in natural Rift Valley fever virus infections. *Veterinary Pathology* **2020**, *57* (6), 791–806. https://doi.org/10.1177/0300985820954549.

35. Oymans J, Wichgers Schreur PJ, van Keulen L, Kant J, Kortekaas J. Rift Valley fever virus targets the maternal-foetal interface in ovine and human placentas. *PLOS Neglected Tropical Diseases* **2020**, *14* (1), e0007898. https://doi.org/10.1371/journal.pntd.0007898.

36. Bermúdez-Méndez E, Angelino P, van Keulen L, van de Water S, Rockx B, Pijlman GP, Ciuffi A, Kortekaas J, Wichgers Schreur PJ. Transcriptomic profiling reveals intense host-pathogen dispute compromising homeostasis during acute Rift Valley fever virus infection. *Journal of Virology* **2023**, *97* (6), e00415-23. https://doi.org/10.1128/jvi.00415-23.

37. Vignuzzi M, López CB. Defective viral genomes are key drivers of the virus–host interaction. *Nature Microbiology* **2019**, *4* (7), 1075–1087. https://doi.org/10.1038/s41564-019-0465-y.

38. Ziegler CM, Botten JW. Defective interfering particles of negative-strand RNA viruses. *Trends in Microbiology* **2020**, *28* (7), 554–565. https://doi.org/10.1016/j.tim.2020.02.006.

39. de Oliveira Resende R, de Haan P, de Avila AC, Kitajima EW, Kormelink R, Goldbach R, Peters D. Generation of envelope and defective interfering RNA mutants of tomato spotted wilt virus by mechanical passage. *Journal of General Virology* **1991**, *72* (10), 2375–2383. https://doi.org/10.1099/0022-1317-72-10-2375.

40. de Oliveira Resende R, de Haan P, van de Vossen E, de Ávila AC, Goldbach R, Peters D. Defective interfering L RNA segments of tomato spotted wilt virus retain both virus genome termini and have extensive internal deletions. *Journal of General Virology* **1992**, *73* (10), 2509–2516. https://doi.org/10.1099/0022-1317-73-10-2509.

41. Patel AH, Elliott RM. Characterization of Bunyamwera virus defective interfering particles. *Journal of General Virology* **1992**, *73* (2), 389–396. https://doi.org/10.1099/0022-1317-73-2-389.

42. Inoue-Nagata AK, Kormelink R, Sgro J-Y, Nagata T, Kitajima EW, Goldbach R, Peters D. Molecular characterization of tomato spotted wilt virus defective interfering RNAs and detection of truncated L proteins. *Virology* **1998**, *248* (2), 342–356. https://doi.org/10.1006/viro.1998.9271.

43. Marchi A, Nicoletti L, Accardi L, Di Bonito P, Giorgi C. Characterization of Toscana virus-defective interfering particles generated *in vivo*. *Virology* **1998**, *246* (1), 125–133. https://doi.org/10.1006/viro.1998.9195.

44. Hutchinson EC, Charles PD, Hester SS, Thomas B, Trudgian D, Martínez-Alonso M, Fodor E. Conserved and host-specific features of influenza virion architecture. *Nature Communications* **2014**, *5* (1), 4816. https://doi.org/10.1038/ncomms5816.

45. Gaudin R, Barteneva NS. Sorting of small infectious virus particles by flow virometry reveals distinct infectivity profiles. *Nature Communications* **2015**, *6*, 6022. https://doi.org/10.1038/ncomms7022.

46. Folimonova SY. Superinfection exclusion is an active virus-controlled function that requires a specific viral protein. *Journal of Virology* **2012**, *86* (10), 5554–5561. https://doi.org/10.1128/jvi.00310-12.

47. Borucki MK, Chandler LJ, Parker BM, Blair CD, Beaty BJ. Bunyavirus superinfection and segment reassortment in transovarially infected mosquitoes. *Journal of General Virology* **1999**, *80* (12), 3173-3179. https://doi.org/10.1099/0022-1317-80-12-3173.

48. Bara JJ, Muturi EJ. Effect of mixed infections of Sindbis and La Crosse viruses on replication of each virus in vitro. *Acta Tropica* **2014**, *130*, 71–75. https://doi.org/10.1016/j.actatropica.2013.10.016.

49. Laureti M, Paradkar PN, Fazakerley JK, Rodriguez-Andres J. Superinfection exclusion in mosquitoes and its potential as an arbovirus control strategy. *Viruses* **2020**, *12* (11), 1259. https://doi.org/10.3390/v12111259.

50. Sims A, Tornaletti LB, Jasim S, Pirillo C, Devlin R, Hirst JC, Loney C, Wojtus J, Sloan E, Thorley L, Boutell C, Roberts E, *et al.* Superinfection exclusion creates spatially distinct influenza virus populations. *PLOS Biology* **2023**, *21* (2), e3001941. https://doi.org/10.1371/journal.pbio.3001941.

51. Lee KK, Gui L. Dissecting virus infectious cycles by cryo-electron microscopy. *PLOS Pathogens* **2016**, *12* (6), e1005625. https://doi.org/10.1371/journal.ppat.1005625.

52. Jiang W, Tang L. Atomic cryo-EM structures of viruses. *Current Opinion in Structural Biology* **2017**, *46*, 122–129. https://doi.org/10.1016/j.sbi.2017.07.002.

53. Quemin ERJ, Machala EA, Vollmer B, Pražák V, Vasishtan D, Rosch R, Grange M, Franken LE, Baker LA, Grünewald K. Cellular electron cryo-tomography to study virus-host interactions. *Annual Review of Virology* **2020**, *7* (1), 239–262. https://doi.org/10.1146/annurev-virology-021920-115935.

54. Li S. Cryo-electron tomography of enveloped viruses. *Trends in Biochemical Sciences* **2022**, *47* (2), 173–186. https://doi.org/10.1016/j.tibs.2021.08.005.

55. Modrego A, Carlero D, Arranz R, Martín-Benito J. CryoEM of viral ribonucleoproteins and nucleocapsids of single-stranded RNA viruses. *Viruses* **2023**, *15* (3), 653. https://doi.org/10.3390/v15030653.

Appendices

Summary

The taxonomical order *Bunyavirales* comprises a large and diverse group of negative-stranded RNA viruses. Several members of this group are on top priority lists of pathogenic microorganisms that threaten public health, as they are known to cause severe disease in plants, animals or humans. Comprehending the molecular basis of the biology of bunyaviruses is a critical task, as only then it will be possible to develop safe and effective countermeasures in the event of an outbreak. Nonetheless, our current knowledge of many aspects of the bunyavirus life cycle is still limited.

A peculiarity of bunyaviruses is that their genome is divided over multiple segments. Bunyaviruses thus face the logistics challenge of delivering a complete set of genome segments into host cells, since each genome segment is essential to establish a productive infection. This thesis aimed at gaining insights into the genome packaging process of bunyaviruses and its implications for their life cycle, along with revealing the molecular determinants underlying their pathogenesis. The three-segmented (SML) Rift Valley fever virus (RVFV), and in some cases Schmallenberg virus (SBV), were employed throughout this thesis as model viruses belonging to the families *Phenuiviridae* and *Peribunyaviridae*, respectively.

Direct visualization of viral RNA segments within virus particles at single-molecule resolution revealed that RVFV and SBV package their genome randomly, instead of following a selective process. Such random packaging yields a mixed population of progeny virions, or as the thesis title metaphorizes: an ensemble. The bunyavirus ensemble consists mostly of empty or incomplete particles (missing one or more segments), and only a minor fraction of complete three-segmented particles. Although apparently inefficient, genome packaging of RVFV was more efficient in insect cells than in mammalian cells. Virus particles produced upon replication in insect cells resulted in a higher absolute number of incorporated segments (regardless of the segment identity) and a higher fraction of complete three-segmented particles.

Incomplete particles are produced in large quantities but cannot establish a productive infection on their own. Co-infections with incomplete particles harboring complementing sets of genome segments proved to be a mechanism by which bunyaviruses can reconstitute a complete genome. Genome reconstitution via co-infection with incomplete particles occurred efficiently in cultured mammalian and insect cells over a range of multiplicities of infection. This phenomenon also occurred successfully *in vivo* in mosquitoes. The reconstituted genome was capable of generating

infectious progeny, suggesting that incomplete bunyavirus particles contribute, rather than interfere, to establish a productive infection. Remarkably, this cooperative strategy of bunyavirus virions relying on co-infection partly resembles the strategy employed by multipartite viruses to complete their infection cycle.

Profiling the transcriptome of target organs of lambs exposed to RVFV using RNA-sequencing technology recapitulated the important role that interferon-mediated immune pathways play in the host's response upon infection. Linking histopathology with transcriptomics unveiled how the RVFV-induced hepatic necrosis results in a drastic downregulation of numerous enzymes essential for metabolic homeostasis. Additionally, the elevated basal expression levels in the liver of *LRP1*, a recently discovered bunyavirus host entry factor, were correlated with the tropism that RVFV shows for this organ.

Finally, analysis of the intracellular levels of viral RNA in individual ovine liver cells using single-cell transcriptomics uncovered that the overall intracellular viral load is the main factor determining the host's mRNA profile and phenotype. Moreover, the analysis also exposed the extremely heterogeneous nature of the viral replication process, characterized by large variations in the intracellular S, M and L segment ratios across cells.

Altogether, the work presented in this thesis sheds new light on fundamental processes of the bunyavirus life cycle, further advances our understanding of bunyavirus pathogenesis and proposes new concepts in the biology of segmented viruses.

Resumen

El orden taxonómico *Bunyavirales* comprende un grupo grande y diverso de virus ARN de polaridad negativa. Varios miembros de este grupo se encuentran en listas priorizadas de microorganismos patógenos que amenazan la salud pública, ya que causan enfermedades graves en plantas, animales o humanos. Comprender las bases moleculares de la biología de los bunyavirus es una tarea crítica, ya que sólo así será posible desarrollar medidas seguras y eficaces para contrarrestar los embates en el caso de un brote. No obstante, nuestro conocimiento actual sobre muchos aspectos del ciclo de vida de los bunyavirus es limitado.

Una peculiaridad de los bunyavirus es que su genoma está dividido en múltiples segmentos. Ya que cada segmento del genoma es esencial para establecer una infección productiva, los bunyavirus enfrentan el desafío logístico de llevar un conjunto completo de segmentos del genoma a las células huésped. Esta tesis tuvo como objetivo estudiar el proceso de empaquetamiento del genoma de los bunyavirus y las implicaciones para su ciclo de vida, así como revelar los determinantes moleculares que explican su patogénesis. El virus tri-segmentado (SML) de la fiebre del Valle del Rift (RVFV, por sus siglas en inglés), y en algunos casos el virus Schmallenberg (SBV, por sus siglas en inglés), fueron empleados a lo largo de esta tesis como modelos de virus pertenecientes a las familias *Phenuiviridae* y *Peribunyaviridae*, respectivamente.

Estudios de microscopía a muy alta resolución en los que se visualizaron directamente los segmentos ARN dentro de las partículas virales (viriones) revelaron que RVFV y SBV empaquetan su genoma de manera aleatoria, y no emplean un proceso selectivo. Este empaquetamiento aleatorio produce una población mixta de viriones, o como metaforiza el título de esta tesis: un ensamble. El ensamble de bunyavirus consta principalmente de partículas vacías o incompletas (a las que les falta uno o más segmentos), y sólo una fracción menor de partículas completas que contienen los tres segmentos. Aunque en general el proceso de empaquetamiento aparenta ser ineficiente, se observó que el genoma de RVFV es empaquetado más eficientemente en células de insecto que en células de mamífero. Las partículas virales producidas tras la replicación en células de insecto resultaron con un mayor número absoluto de segmentos incorporados (independientemente de la identidad del segmento) y una mayor fracción de partículas completas de tres segmentos.

Los bunyavirus producen partículas incompletas en grandes cantidades, pero estas partículas no pueden establecer una infección productiva por cuenta propia. Sin embargo, los estudios

realizados en esta tesis demostraron que las co-infecciones con partículas incompletas pero que contienen sets complementarios de segmentos del genoma viral son un mecanismo mediante el cual los bunyavirus pueden reconstituir un genoma completo. La reconstitución del genoma mediante co-infección con partículas incompletas se produjo de manera eficiente en cultivos de células de mamífero y de insecto en una variedad de multiplicidades de infección. Este fenómeno también ocurrió de manera exitosa *in vivo* en mosquitos. El genoma viral reconstituido fue capaz de generar progenie infecciosa, lo que sugiere que las partículas incompletas de bunyavirus contribuyen, en lugar de interferir, a establecer una infección productiva. Notoriamente, esta estrategia cooperativa de los viriones de bunyavirus que dependen de la co-infección se asemeja en parte a la estrategia que los virus multipartitos emplean para completar su ciclo de infección.

Adicionalmente, estudiar el transcriptoma de órganos diana de corderos expuestos a RVFV utilizando tecnología de secuenciación de ARN recapituló el importante rol que desempeñan las vías inmunitarias mediadas por interferón en la respuesta del huésped ante la infección viral. Combinar histopatología con la transcriptómica reveló cómo la necrosis hepática inducida por RVFV resulta en una drástica regulación a la baja de numerosas enzimas esenciales para la homeostasis metabólica. Además, los elevados niveles de expresión basal en el hígado de *LRP1*, un factor para la entrada de bunyavirus al huésped descubierto recientemente, correlacionaron con el tropismo que RVFV muestra por este órgano.

Finalmente, el análisis de los niveles intracelulares de ARN viral en células hepáticas ovinas utilizando transcriptómica de células individuales mostró que la carga viral intracelular es el principal factor determinante del perfil de ARNm y del fenotipo de las células huésped. Además, este análisis también expuso la naturaleza extremadamente heterogénea del proceso de replicación viral, caracterizado por grandes variaciones en las proporciones intracelulares de los segmentos S, M y L entre las células.

En conjunto, el trabajo presentado en esta tesis brinda nuevas perspectivas sobre procesos fundamentales del ciclo de vida de los bunyavirus, avanzando aún más nuestra comprensión de su patogénesis y proponiendo nuevos conceptos en la biología de virus segmentados.

Publications

This thesis

Bermúdez-Méndez E, Angelino P, van Keulen L, van de Water S, Rockx B, Pijlman GP, Ciuffi A, Kortekaas J, Wichgers Schreur PJ. Transcriptomic profiling reveals intense host-pathogen dispute compromising homeostasis during acute Rift Valley fever virus infection. *Journal of Virology* **2023**, *97* (6), e00415-23. https://doi.org/10.1128/jvi.00415-23.

Bermúdez-Méndez E, Bronsvoort KF, Zwart MP, van de Water S, Cárdenas-Rey I, Vloet RPM, Koenraadt CJM, Pijlman GP, Kortekaas J, Wichgers Schreur PJ. Incomplete bunyavirus particles can cooperatively support virus infection and spread. *PLOS Biology* **2022**, *20* (11), e3001870. https://doi.org/10.1371/journal.pbio.3001870.

Bermúdez-Méndez E, Katrukha EA, Spruit CM, Kortekaas J, Wichgers Schreur PJ. Visualizing the ribonucleoprotein content of single bunyavirus virions reveals more efficient genome packaging in the arthropod host. *Communications Biology* **2021**, *4* (1), 1–13. https://doi.org/10.1038/s42003-021-01821-y.

Other

Wichgers Schreur PJ, Bird BH, Ikegami T, **Bermúdez-Méndez E**, Kortekaas J. Perspectives of next-generation live-attenuated Rift Valley fever vaccines for animal and human use. *Vaccines* **2023**, *11* (3), 707. https://doi.org/10.3390/vaccines11030707.

Wichgers Schreur PJ, van de Water S, Harmsen M, **Bermúdez-Méndez E**, Drabek D, Grosveld F, Wernike K, Beer M, Aebischer A, Daramola O, Rodriguez Conde S, Brennan K, Kozub D, Søndergaard Kristiansen M, Mistry KK, Deng Z, Hellert J, Guardado-Calvo P, Rey FA, van Keulen L, Kortekaas J. Multimeric single-domain antibody complexes protect against bunyavirus infections. *eLife* **2020**, *9*, e52716. https://doi.org/10.7554/eLife.52716.

Pucca MB, Cerni FA, Janke R, **Bermúdez-Méndez E**, Ledsgaard L, Barbosa JE, Laustsen AH. History of envenoming therapy and current perspectives. *Frontiers in Immunology* **2019**, *10*, 1598. https://doi.org/10.3389/fimmu.2019.01598

Bermúdez-Méndez E, Fuglsang-Madsen A, Føns S, Lomonte B, Gutiérrez JM, Laustsen AH. Innovative immunization strategies for antivenom development. *Toxins* **2018**, *10* (11) 452. https://doi.org/10.3390/toxins10110452

Laustsen AH, Gutiérrez JM, Knudsen C, Johansen KH, **Bermúdez-Méndez E**, Cerni FA, Jürgensen JA, Ledsgaard L, Martos-Esteban A, Øhlenschlæger M, Pus U, Andersen MR, Lomonte B, Engmark M, Pucca MB. Pros and cons of different therapeutic antibody formats for recombinant antivenom development. *Toxicon* **2018**, *146*, 151-175. https://doi.org/10.1016/j.toxicon.2018.03.004.

PE&RC Training and Education Statement

With the training and education activities listed below the PhD candidate has complied with the requirements set by the C.T. de Wit Graduate School for Production Ecology and Resource Conservation (PE&RC) which comprises of a minimum total of 32 ECTS (= 22 weeks of activities)

Review/project proposal (4.5 ECTS)

- Mix and match: how bunyaviruses package their segmented genomes

Post-graduate courses (3.6 ECTS)

- Emerging viruses; Institut Pasteur (2019)
- Intro to RNA-seq; Swiss Institute of Bioinformatics (2021)
- Single-cell transcriptomics; Swiss Institute of Bioinformatics (2021)
- Data visualization with R; Swiss Institute of Bioinformatics (2021)

Laboratory training and working visits (4.5 ECTS)

- Bulk and single-cell transcriptomics; Institute of Microbiology, Lausanne University Hospital and University of Lausanne (2021-2022)

Invited review of (unpublished) journal manuscripts (1 ECTS)

- Journal of Virology: RVFV reverse genetics (2020)

Competence strengthening/skills courses (2.7 ECTS)

- Project and time management; Wageningen Graduate Schools (2019)
- Scientific artwork, data visualization and infographics with Adobe Illustrator; Wageningen Graduate Schools (2020)
- Reviewing a scientific manuscript; Wageningen Graduate Schools (2021)
- Scientific publishing; Wageningen Graduate Schools (2022)
- Supervising BSc and MSc students; Wageningen Graduate Schools (2022)
- Last stretch of the PhD; Wageningen Graduate Schools (2022)
- Writing propositions; Wageningen Graduate Schools (2022)

Scientific integrity/ethics in science activities (0.6 ECTS)

- Scientific integrity; Wageningen Graduate Schools (2020)

PE&RC Annual meetings, seminars and the PE&RC weekend (2.4 ECTS)

- PE&RC First year's weekend (2019)
- PE&RC Day (2020)
- PE&RC Midterm weekend (2021)
- PE&RC Last year's retreat (2022)

Discussion groups/local seminars or scientific meetings (8.8 ECTS)

- European Congress of Virology (2019)
- Young NCOH masterclass (2019)
- Dutch Annual Virology Symposium (2019, 2021, 2022, 2023)
- Dutch Arboviral Research Network meeting (2019, 2021, 2022, 2023)
- Bunyavirus (2020)
- ZAPI Stakeholders final conference (2021)
- COGEM Symposium 'Vaccines, replicons and viruses' (2023)

International symposia, workshops and conferences (6.3 ECTS)

- Negative Strand Virus meeting; oral presentation; Braga, Portugal (2022)
- Bunyavirus; oral presentation; Cambridge, UK (2022)
- European Congress of Virology; poster presentation; Gdansk, Poland (2023)

Societally relevant exposure (1.5 ECTS)

- A colourful glimpse on a seemingly inefficient, yet highly successful viral life cycle; Nature Microbiology Community 'Behind the Paper' blog (2021)
- New molecular insights into the biology of bunyaviruses; WBVR news article (2021)
- Incomplete bunyavirus particles can collectively contribute to virus spread, WBVR news article (2022)

Committee work (2 ECTS)

- Dutch Young Virologists Symposium (2021, 2022)

Lecturing/supervision of practicals/tutorials (2.7 ECTS)

- Molecular virology (2019, 2020, 2021)

BSc/MSc thesis supervision of students (3 ECTS)

- MSc thesis: Role of incomplete particles in bunyavirus infection

Acknowledgements

Completing a doctoral degree is, in essence, an educational experience. In practice, it feels more like whitewater rafting, an extreme experience of navigating an unpredictable combination of rapids/obstacles. Completing this ride was only possible through a strong and sustained collective effort. To everyone who made this experience possible, listed here or not, I would like to express my appreciation. Big thank you for paddling along me to reach this stage!

Paul, in two words: you rock! I have had great fun working with you in each of our projects. You taught me what I know about viruses, kindly guiding me in the lab when I had barely got hands on a micropipette before. Thanks for openly sharing your knowledge, being extremely dedicated to this project and all the discussions about science and life in general. Your honest, constructive and timely feedback was highly appreciated. You gave me the freedom to explore my scientific interests and I am grateful for having your unconditional support. I believe the key to our camaraderie and academic development lies on understanding each other at a personal level. Whatever the reason or circumstance we had to discuss, especially on hard times, I always left your office with a smile, and to me that says it all. No matter how busy you were, you invariably found time. Your supervision was exceptional and precisely balanced. Right on spot! Many, many thanks!

Jeroen, thank you very much for having the courage to take bold decisions. Welcoming me in your group (not once but twice) despite my inexperience was a risky choice. I still do not understand exactly why, but I am very happy and grateful that it all worked out. You have a strong working ethic and a genuine interest in advancing science. Your contagious enthusiasm and optimism are a winning combination and a great dose of motivation to keep trying when things did not go our ways. It was a real pleasure working with you and knowing that you always had my back. Thanks a lot for your continuous support! I hope one day we will celebrate in sunnier environments while you enjoy the Costa Rican waves.

Gorben and Monique, thanks for stepping into my project given the unforeseen circumstances. I appreciate the scientific discussions and thoughtful feedback. Gorben, your recommendations and sharp eye were critical to improve our studies. Monique, your attentiveness was crucial to ensure a successful completion of this project. Thank you both! Claudius and staff at PE&RC, the support provided by the graduate school had a positive impact in my personal and professional development. Thanks for all the activities and retreats that made it possible and for funding my

PhD project. I extend my gratitude to the opponents: Wim, Ben, Izabela and Stéphane. Thanks a lot for taking your time to accept this role, evaluate my thesis and participate on the defense.

To our collaborators, thanks for bringing up to the table your expertise, resources, scientific interest and kindness. Your input enriched our investigations and provided new perspectives. A special mention to Mark, Paolo and Angela. Mark, thanks for your interest in our research and your willingness to share views, discuss science and work together. Paolo, I owe you most of what I know about RNA-seq and bioinformatics in general. Thanks for your patience, all the troubleshooting and for selflessly sharing your knowledge. Angela, many thanks for opening the doors of your team and lab in Lausanne for us to embark on single-cell experiments.

To my former and present colleagues at the Arbovirology group (Judith, Mirriam, Jet, Nadia, Rianka, Sandra, Lucien, José, Kirsten, Carine and Barry), many thanks for all your help throughout these years. Whether it has been in the lab helping me with your excellent technical/scientific skills or outside of it, I appreciate your patience and advice. Sandra, thanks for being caring and constantly checking up on me. Nadia, it was always nice to have our unexpected chats. Kirsten, working along you during your MSc thesis was both very enjoyable and productive. I learned a lot working together and you made supervision look easy. Judith, your positive energy and good mood are things more people should seek to replicate, including myself. You have helped me with so many things since the Edelhertweg days and up to my defence. Thanks for that and for all the group activities you organized! They were much needed and a lot of fun. Thanks also for being my paranymph and for all your kindness!

To my former and present colleagues at other groups within Wageningen Bioveterinary Research in Lelystad, at the Laboratory of Virology in Wageningen and elsewhere, thanks for the exchange of ideas, scientific discussions, help with administrative matters and informal chats. Em particular, quero agradecer muito ao Eduardo. Obrigado por tanta gentileza, pela excelente disposição em ajudar, pela amizade e por ser meu paranymph. Nossas conversas e almoço (tradicional) dos finais de semana sempre me fizeram passar momentos muito agradáveis. O tempo compartilhado na sala de ensaio serviu como uma válvula de escape perfeita para liberar o estresse e esquecer momentaneamente o trabalho. Eu me diverti muito de fazer o que tanto gostamos. ¡Muito obrigado amigo!

To Lawrence, Damián, Bjorn, Richard, Jeroen, Roy, Winfred, Patrick, Barry, Guus and Juan Carlos, many thanks for being so welcoming and generous! Guys, for you it might probably gone

unnoticed, but for me the time shared meant a formidable way of relaxing and enjoying my outside of work hours. I am convinced those moments played a crucial role in me being able to endure the obstacles of my project. Thanks for our friendship and all the good and fun times!

Although my ways have not led back to Denmark, I am grateful for the support I have received from Andreas. It is difficult to imagine how much I learned in such a short period of time around you. Andreas, you have contributed to my path towards becoming a scientist and I will always appreciate how much you believe in my capacities, even more than what I do myself. Keep up the great work and I wish you a lot of success with your research programs.

Con algunas personas no tenemos la suerte de compartir a menudo o de cerca, pero aun así, tienen la capacidad de influenciarlo a uno de manera positiva y duradera. Tal es el caso de Chema, que con su dedicación, trabajo incansable, humildad y brillantez ha sido fuente constante de inspiración. Chema, ¡muchísimas gracias por siempre estar disponible para leerme/escucharme y brindarme un consejo en mis momentos de mayor indecisión! Muchísimas gracias por darle tanto a la ciencia de nuestro país. Gracias también a la Facultad de Farmacia y OAICE de la Universidad de Costa Rica por el apoyo brindado para realizar mis estudios en el extranjero.

Extiendo mis agradecimientos a Mau, Luis, Germán, Cruz, Ronny, Catalina y José Alexis, quienes también se encuentran persiguiendo sus metas lejos de casa. ¡Muchas gracias por su amistad! A pesar de lo esporádico, aprecié cada una de las veces que pude compartir con algunos de ustedes visitándonos acá o allá. Esos momentos me brindaron un aire fresco y me hicieron sentir más cerca de casa. A Mau y Luis en especial, me sobran las razones para agradecerles. Luis, aprecio mucho el apoyo constante, la confianza y lo bien que nos llevamos. Mau, muchísimas gracias por todas las visitas, recibimientos, paseos, conversaciones, carcajadas y experiencias memorables. Nos la pasamos genial. Muchas gracias por su comprensión y por siempre apuntarse a todo. ¡Muchísimas gracias por tanto! A todos, les deseo el mayor de los éxitos en cada uno de sus proyectos personales y profesionales.

A mi familia en Costa Rica: Ma, Pa, Andrés, Beto, Dominique, Nicole y Luciana, para ustedes se me desbordan profundos sentimientos de gratitud y amor. Les agradezco y aprecio enormemente el cariño, palabras de aliento y apoyo incondicional que siempre me han brindado, aun cuando mis decisiones impliquen que estemos lejos físicamente o panoramas inciertos. El compartir con ustedes cada una de mis visitas a casa me renueva de energía e impulsa a seguir trabajando por mis metas. Siempre los pienso, los extraño y los llevo conmigo en mi corazón.

Ma y Pa, muchas gracias por priorizar nuestra educación. Todo lo que somos, se los debemos a ustedes. ¡Los admiro y amo demasiado! A Andrés, Dominique, Beto y Nicole, muchísimas gracias por la relación tan especial que tenemos. Me encanta reírme junto a ustedes y eso me da vida. Luciana, no sabes la alegría que trajiste a nuestras vidas. ¡Sos increíblemente especial! A todos, muchísimas gracias por aceptarme y valorarme tal y como soy. Solamente espero que en mi interacción con cada uno de ustedes, mis acciones transmitan más que mis palabras. ¡Muchísimas gracias por tanto amor!

Al resto de mis familiares (abuelita, tíos, tías, primos, primas) y amigos ticos, ¡muchísimas gracias por el apoyo y por todos los buenos deseos! El sentimiento siempre es recíproco. Una mención muy especial a tía Ana, que con su cuido y amor marcó por siempre mi vida y la de mis hermanos. ¡Muchísimas gracias por todo, tía!

De un tiempo acá, ese apoyo ahora también llega desde otras latitudes. A don Arturo y Cristhian, ¡muchísimas gracias por su gentileza y buenas vibras! Esperemos que sigamos teniendo oportunidades para compartir más momentos juntos. ¡La pasamos bien chévere!

Finalmente, agradezco incansablemente a Ingrid. Vos has tenido que lidiar conmigo de cerca y por cuenta propia lo que representa esta experiencia. Hemos compartido muchos momentos inolvidables, tanto asociados a nuestros proyectos como fuera de él. Has contribuido de mil y un formas a la culminación de este proyecto, siempre de manera genuina, creativa y entregada, dejando fluir naturalmente esa ayuda desinteresada que tanto te caracteriza. Ha sido muy grato y enriquecedor ir creciendo personal y profesionalmente de manera paralela. Muchísimas gracias por todo lo vivido y lo aprendido. Muchísimas gracias por estar ahí siempre, acompañándome y apoyándome en todo momento. ¡Muchísimas gracias por tanto amor!

Erick BM

Y para el tiempo de lluvia
Te guardo un poco de sol
Sepa que esta vida es suya
Métale corazón ♫

Mariposa de Abril, Señor Loop

About the author

Erick Bermúdez Méndez was born on Thursday the 31st of August, 1989. He studied Pharmacy at the University of Costa Rica, and finished his master's at Wageningen University & Research, The Netherlands, where his thesis was awarded the Virology Goldbach MSc Thesis Prize 2018. Between 2019 and 2023, he conducted his PhD studies in Wageningen University & Research. Writing this text, I assume he has excelled at this task. The following is a mixture of laudatory content and sentimental memory.

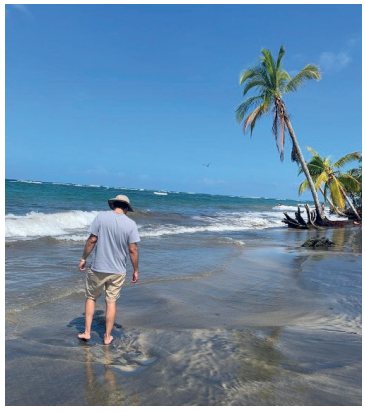

Photo by Beto

*

I don't remember the precise moment when I met Erick. We must have been both four years of age, since I am only two weeks older than him. We were probably sitting on a carpet before our kindergarten teacher, Ana Victoria. In our first day, I remember I cried a lot. If I know him well, I bet Erick came earlier and didn't shed a tear. Ever since that lost moment, a feeling of gratitude and genuine admiration has bonded me towards him. We easily became friends. We used to play soccer together. He was (I know he still is) a great midfielder, the kind of player every coach wants to have in his team. A foresighted player, always one step ahead, always with a planned solution. He had an elegant and precise touch, but he was also the strongest player to trust with a free-kick or a long shot. In fact, he was so talented that "Compa", our former coach, promoted him to the upper divisions in our school, since he was better than the older students.

Going into first grade, they separated us. It felt bad. I am sure I would have done better having him around. We never shared classrooms anymore, only recesses. In High School, I remember him talking about the possibility of switching to the Colegio Científico, where he would better prepare himself for the University. At that time, he wanted to be a doctor. When I visited his house, food was always awesome, and we would take any chance to turn the family living room into a soccer field.

Then came the University. He made the decision to study Pharmacy. It passed so quickly! After a while, we were both working at the University, which brought us together in a different way.

In 2017, when he was finishing his master's in Wageningen, I came to Germany and had the opportunity to visit him in Copenhagen. We had a great time discovering the city. When we bumped into anything big or interesting, he would scientifically affirm: "I don't know what that is, but it's important". Since we started our PhD studies almost at the same time, we have met every now and then in different places: Amsterdam, Göttingen, "Zwollywood" or "Osnabrooklyn". A 7 hour stroll around Göttingen and a bike tour between the Netherlands and Germany are definitely among the highlights.

Besides being a scientist and a sportsman, Erick is also a musician at heart. He plays the drums and, more recently, the piano. Some say he had to move out from Lelystad because his playing made locals afraid that something was finally about to happen in the ghost town... Jokes apart, he is a great listener, which is why he is so good at music.

I know I've praised him a lot on this text, and that is probably cliché. But he really is a great person to be near to, no matter if he is your friend or your colleague. Those who know him well will acknowledge that his academic achievements are no surprise given his hard work, but also his empathy, generosity, solidarity, understanding, good humor and clear mind. Coming from him, I am sure this book has a lot to teach, and that an even brighter career is ahead.

Written by Roy Mauricio Chaves Fernández

The research described in this thesis was financially supported by The Graduate School for Production Ecology & Resource Conservation (strategic funds PhD grant), Wageningen Bioveterinary Research, the Rob Goldbach Fund (laboratory visit grant) and Universidad de Costa Rica (grant OAICE-031-2019).

Financial support from Wageningen University and Wageningen Bioveterinary Research for printing this thesis is gratefully acknowledged.

Cover concept by Erick Bermúdez Méndez and Ingrid Cárdenas Rey

Cover design by Edo Brenes | edobrenes.com

Printed by ProefschriftMaken on FSC-certified paper